

DIVERSITY AND EVOLUTION OF THE
SAUROPSID TRIGEMINAL SENSORY SYSTEM

A Dissertation presented to
the Faculty of the Graduate School
at the University of Missouri-Columbia

In Partial Fulfillment
of the Requirements for the Degree
Doctor of Philosophy

by

EMILY J. LESSNER

Dr. Casey M. Holliday, Dissertation Supervisor

MAY 2022

The undersigned, appointed by the dean of the Graduate School, have examined
the dissertation entitled

DIVERSITY AND EVOLUTION OF THE
SAUROPSID TRIGEMINAL SENSORY SYSTEM

presented by Emily Lessner, a candidate for the degree of doctor of philosophy, and
hereby certify that, in their opinion, it is worthy of acceptance.

Professor Casey M. Holliday

Professor Kevin M. Middleton

Professor Kristina Aldridge

Professor Manuel Leal

Dedication

I dedicate my dissertation to all the communities that provided me everything I needed to succeed and to you, fearless reader.

I would like to express my deepest gratitude to the members of the Mizzou Integrative Anatomy Program, especially the students, and to Debbie Allen for support and guidance. To the rest of my academic family, thanks for kind words, PDFs, EXTERNAL email threads, and being goofy. Without my family of friends, I would never have stayed up so late, laughed so hard, or been so physically exhausted, and a dissertation in a pandemic would have been impossible. My family family, is the reason I am where I am today and I know I can count on them for interesting questions, articles on dinosaurs, and endless love. And finally, Erica really has no idea how hard it was to say 'I'm working' on all those working-from-home days since who even needs a PhD when they have her, nothing can compare. But wait, most of my writing happened in the physical presence of Yeager, Merlin, and Rascal, so I will dedicate this to them instead.

Acknowledgements

I thank the MU Life Sciences Fellowship Program, MU Graduate School, MU Graduate Professional Council, Missouri Research Board, Society of Vertebrate Paleontology, Evolving Earth, Geological Society of America, Society for Integrative and Comparative Biology, Paleontological Society, American Ornithological Society, Animal Behavioral Society, American Association for Anatomy, The Jurassic Foundation, and the National Science Foundation (IOS1457319, EAR1631684, IIS9874781, IIS0531767, EAR0617561, EAR0854218, EAR1525915) for funding.

This research would have been impossible without the assistance of museum and CT scanner personnel including: A. Atwater, J. Scannella, R. Irmis, C. Levitt-Bussian, T. Birthisel, R. Scheetz, R. Hunt-Foster, J. McHugh, A. Marsh, B. Parker, M. Smith, K. Mackenzie, J. Sertich, K. Bader, M. Brown, C. Sagebiel, A. Resetar, J. Maisano, D. Edey, M. Colbert, J. Schiffbauer, T. Selly, the MU Hospital Staff, and the Ashley Regional Medical Center Staff. This research was also made possible because of the generosity of those willing to share their data, specimens, and photos including: H. Tsai, A. Watanabe, M. Fabbri, J. Clark, N. Kley, P. Sereno, A. Turner, M. Norell, L. Witmer, P. O'Connor, J. Clarke, G. Bever, A. Balanoff, J. Choiniere, K. Dollman, K. Chapelle, V. Radermacher, L. Jacobs, M. Jones, B. Young, S. Nesbitt, the Florida Keys Wild Bird Center and S. Pierce, and The Rockefeller Wildlife Refuge and R. Elsey.

Thanks to C. Velhurst, K. Melstrom, N. Ong, and R. Ridgely, for additional assistance.

Table of Contents

Acknowledgements	ii
List of Figures	v
List of Tables	ix
Abbreviations	x
Abstract	xiii
Chapter 1 – Introduction	1
Trigeminal anatomy and physiology in sauropsids	1
Development of the sauropsid trigeminal system	6
Osteological correlates and inferences of sensation	7
Ecological, behavioral, and morphological transitions in sensation	10
Outline of dissertation chapters	12
Chapter 2 – A 3D ontogenetic atlas of <i>Alligator mississippiensis</i> cranial nerves and their significance for comparative neurology of reptiles	22
INTRODUCTION	22
MATERIALS AND METHODS	23
RESULTS	24
DISCUSSION	37
Chapter 3 – Ontogeny of the trigeminal system and associated structures in <i>Alligator mississippiensis</i>	71
INTRODUCTION	71
MATERIALS AND METHODS	75
RESULTS	77
DISCUSSION	84
CONCLUSIONS	93
Chapter 4 – Quantifying neurovascular canal branching patterns reveals a shared crocodylian arrangement	111
INTRODUCTION	111
MATERIALS AND METHODS	115

RESULTS	120
DISCUSSION	126
CONCLUSIONS	130
Chapter 5 – Ecomorphological patterns in trigeminal canal branching among sauropsids reveals a suchian sensory shift	149
INTRODUCTION	149
MATERIALS AND METHODS	151
RESULTS	154
DISCUSSION	167
CONCLUSIONS	179
Chapter 6 – Quantitative analysis of trigeminal osteological correlates among reptiles	201
INTRODUCTION	201
MATERIALS AND METHODS	202
RESULTS	204
DISCUSSION	222
CONCLUSIONS	231
Chapter 7 – Conclusions	245
References	251
Vita	290

List of Figures

Figure 1.1.: Trigeminal feature phylogenetic distribution	Page 18
Figure 1.2: Sauropsid crania	Page 19
Figure 1.3: Extant phylogenetic bracket of non-crocodylian pseudosuchians and non-avian avemetatarsalians with notable characters	Page 20
Figure 1.4: Features of the trigeminal system.....	Page 21
Figure 2.1: Brain	Page 51
Figure 2.2: Olfactory, Optic, Oculomotor, Abducens, and Trochlear Nerves.....	Page 52
Figure 2.3: Cross Sectional Data	Page 53
Figure 2.4: Eye Muscles.	Page 54
Figure 2.5: Autonomic Nerves.....	Page 55
Figure 2.6: Cranial Osteology.....	Page 56
Figure 2.7: Osteological and Nervous Relationships.....	Page 57
Figure 2.8: Osteological and Nervous Relationships (cont.)	Page 58
Figure 2.9: Trigeminal Nerve	Page 59
Figure 2.10: Trigeminal Nerve-Innervated Muscles.....	Page 60
Figure 2.11: Facial, Vestibulocochlear, Glossopharyngeal, Vagus, and Hypoglossal Nerves.	Page 61
Figure 2.12: Facial Nerve-Innervated Muscles.....	Page 62
Figure 2.13: Chorda Tympani.....	Page 63
Figure 2.14: Glossopharyngeal Nerve-Innervated Muscles.....	Page 64
Figure 2.15: Vagus Nerve-Innervated Muscles	Page 65
Figure 2.16: Hypoglossal Nerve-Innervated Muscles	Page 66
Figure 2.17: All segmented structures of yearling alligator MUV C AL031	Page 67

Figure 2.18: All cranial nerves and brain of yearling alligator MUVC AL031	Page 68
Figure 2.19: All segmented structures of stage 19 embryo MUVC AL089	Page 69
Figure 2.20: Color guide to segmented structures	Page 70
Figure 3.1: Developing brain and trigeminal nerves	Page 100
Figure 3.2: Developing musculature.....	Page 101
Figure 3.3: Developing epipterygoid region.....	Page 102
Figure 3.4 Developing cartilages	Page 103
Figure 3.5: Plot of relative growth of cerebral regions by skull width.....	Page 104
Figure 3.6: Plot of relative growth of trigeminal nerve ganglia and divisions by skull width	Page 105
Figure 3.7: Plot of relative growth of muscles by skull width.....	Page 106
Figure 3.8: Plot of relative growth of cranial nerve diameters by skull width	Page 107
Figure 3.9: Plot of growth of structures over time.....	Page 108
Figure 3.10 Plot of relative growth of structures by skull width	Page 109
Figure 3.11: Development of topologically informative structures.....	Page 110
Figure 4.1: Methods	Page 137
Figure 4.2: Ordering.....	Page 138
Figure 4.3: First segment order proportions	Page 139
Figure 4.4: Avizo parameters.....	Page 140
Figure 4.5: Topological complexity.....	Page 141
Figure 4.6: Topological center of mass and density metrics	Page 142
Figure 4.7: Segment count vs. order	Page 143
Figure 4.8: Mean segment lengths	Page 144

Figure 4.9: Density curves	Page 145
Figure 4.10: Boxplots and density peaks	Page 146
Figure 4.11: Preliminary comparative data.....	Page 147
Figure 4.12: Additional comparisons.....	Page 148
Figure 5.1: Sudan Black B staining of myelinated nerve branches	Page 186
Figure 5.2: Phylogenetic representation of study taxa.....	Page 187
Figure 5.3: Coronal CT scan slices of representative mandibles from contrast-enhanced, extant taxa and extinct taxa.....	Page 188
Figure 5.4: Dentaries.....	Page 189
Figure 5.5: Location of mandibular canal within the Meckelian fossa in fossil specimens and CT scan data of non-avian dinosaur taxa	Page 190
Figure 5.6: Location of mandibular canal within the Meckelian fossa in non-crocodylian suchian taxa.....	Page 191
Figure 5.7: Proximal and symphyseal canal contents of extant taxa	Page 192
Figure 5.8: Canal topology represented by counts of terminal topological segments	Page 193
Figure 5.9: Number of topological tips by dentary region by clade and ecology...	Page 194
Figure 5.10: Density metrics.....	Page 195
Figure 5.11: Strahler segment and Horton first segment counts.....	Page 196
Figure 5.12: Segment lengths	Page 197
Figure 5.13: Chronogram of non-crocodylian suchians and phylogeny of extant crocodylians	Page 198

Figure 5.14: Photographs of dentaries with neurovascular foramina of fossil pseudosuchians	Page 199
Figure 5.15: Photographs of dentaries with neurovascular foramina of fossil avemetatarsalians	Page 200
Figure 6.1: Lateral braincases of selected CT scanned taxa	Page 238
Figure 6.2: Dentaries of selected CT scanned taxa.....	Page 239
Figure 6.3: Relationships between soft tissue features and their osteological correlates	Page 240
Figure 6.4: Phylogenetic regression plots evaluating proxies for body size.....	Page 241
Figure 6.5: Ecological differences in relative osteological correlates	Page 242
Figure 6.6: Linear discriminant analysis used for ecological predictions for fossil taxa	Page 243
Figure 6.7: Relative sizes of cranial osteological correlates.....	Page 244

List of Tables

Table 2.1: Anatomical abbreviations and structure locations by figure	Page 43
Table 2.2: Individual URLs to 3D models of figures found in the Sketchfab collection (http://sketchfab.com/holliday/collections/alligator-cranial-nerve-atlas).....	Page 49
Table 3.1: Imaged specimens.....	Page 95
Table 3.2: Structure growth rates.....	Page 96
Table 3.3: Additional allometric relationships.....	Page 98
Table 3.4: Cranial nerve allometric relationships	Page 99
Table 4.1: Specimens used in this study	Page 132
Table 4.2: First segment order count and percentage summary for Avizo parameter test	Page 134
Table 4.3: Topological center of mass and density metrics.....	Page 135
Table 4.4: First segment order count and percentage summary	Page 136
Table 5.1: CT scan data	Page 181
Table 5.2: Specimens and prediction results.....	Page 183
Table 5.3: Neurovascular canal contents by clade.....	Page 185
Table 6.1: Correlations of soft tissue features and their osteological correlates. ...	Page 232
Table 6.2: Ecological predictions from linear discriminant analysis.....	Page 233

Abbreviations

Anatomical: (This list excludes additional abbreviations specific to Chapter 2, listed in Table 2.1.) **c**, canal; **cap. ot**, otic capsule; **C.j**, *Crocodylus johnstoni*; **CNV**, trigeminal nerve; **CNI**, olfactory nerve; **CNII**, optic nerve; **CNIII**, oculomotor nerve; **CNIV**, trochlear nerve; **CNVI**, abducens nerve; **CNVII**, facial nerve; **CNVIII**, vestibulocochlear nerve; **CNIX**, glossopharyngeal nerve; **CNX**, vagus nerve; **CNXII**, hypoglossal nerve; **cNv**, neurovascular canal; **G.g**, *Gavialis gangeticus*, **j**, jugal; **ls**, laterosphenoid; **mAMEM**, adductor mandibulae externus medialis; **mAMEP**, adductor mandibulae externus profundus; **mAMES**, adductor mandibulae externus superficialis; **mAMP**, adductor mandibulae posterior; **mc**, Meckelian groove; **MC**, Meckel's cartilage; **mDPi**, depressor palpebrae inferioris; **mIMA**, intermandibularis; **mIRA**, intramandibularis; **mLB**, levator bulbi; **Mm**, muscles; **mmf**, maxillomandibular foramen; **mPSTp**, pseudotemporalis profundus; **mPSTs**, pseudotemporalis superficialis; **mPTd**, pterygoideus dorsalis; **mPTv**, pterygoideus ventralis; **n**, nerve; **nAO**, angulus oris; **nL**, lingual nerve; **nM**, mandibular nerve; **nPTd**, pterygoid nerve to mPTd; **nPTv**, pterygoid nerve to mPTv; **O.t**, *Osteolaemus tetraspis*; **of**, ophthalmic foramen; **on**, ophthalmic notch; **P.p**, *Paleosuchus palpebrosus*; **pn**, prootic notch; **po**, postorbital; **pr**, prootic; **pr. asc. pq**, processus ascendens palatoquadrati; **pr. ot. pq**, processus otic palatoquadrati; **pr. ptg. pq**, processus pterygoideus palatoquadrati; **pr. ptq. pq**, processus pterygoquadrate palatoquadrati; **ptg**, pterygoid; **q**, quadrate; **qj**, quadratojugal; **sept. int**, interorbital septum **sq**, squamosal; **T.s**, *Tomistoma schlegelii*; **v**, vasculature; **vl. p. pi. aot**, ventrolateral process of the pila antotica; **V**, trigeminal nerve; **V₁**, trigeminal nerve ophthalmic division; **V_{1g}**, trigeminal nerve ophthalmic (profundal) ganglion; **V₂**,

trigeminal nerve maxillary division; **V_{2/3g}**, trigeminal nerve maxillomandibular (gasserian) ganglion; **V₃**, trigeminal nerve mandibular division; **Vf**, trigeminal foramen; **Vg**, trigeminal ganglion.

Institutional: **AMNH**, American Museum of Natural History, New York, New York, USA; **BMNH (NHMUK)**, British Museum of Natural History, London, England; **BP**, Bernard Price Institute for Paleontological Research, Johannesburg, South Africa; **BRLSI**, Bath Royal Literary and Scientific Institution, Bath, England; **BSPG**, Bayerische Staatssammlung für Paläentologie und Geologie, Munich, Germany; **BYU**, Brigham Young University Museum of Paleontology, Provo, Utah, USA; **CNRST-SUNY**, Centre National de la Recherche Scientifique et Technologique de Mali – Stony Brook University, New York, New York, USA; **CUP**, Catholic University of Peking, Beijing, China; **DINO**, Dinosaur National Monument, Jensen, Utah, USA; **DMNH**, Denver Museum of Nature and Science, Denver, Colorado, USA; **FMNH**, Field Museum of Natural History, Chicago, Illinois, USA; **GR**, Ghost Ranch, Abiquiu, New Mexico, USA; **IGM**, Institute of Geology, Ulaanbaatar, Mongolia; **IVPP**, Institute of Vertebrate Paleontology and Paleoanthropology, Beijing, China; **LACM**, Natural History Museum of Los Angeles County, Los Angeles, California, USA; **MAL**, Malawi Department of Antiquities, Malawi; **MCZ**, Museum of Comparative Zoology, Cambridge, Massachusetts, USA; **MNA**, Museum of Northern Arizona, Flagstaff, Arizona, USA; **MNN**, Muséum National du Niger, Niamey, République de Niger; **MOR**, Museum of the Rockies, Bozeman, Montana, USA; **MUO**, Museum of the University of Oklahoma, Norman, Oklahoma, USA; **MUVC**, University of Missouri Vertebrate Collection, Columbia, Missouri, USA; **MWC**, Museum of the West, Grand Junction, Colorado,

USA; **OUV**C, Ohio University Vertebrate Collection, Athens, Ohio, USA; **PEFO**, Petrified Forest National Park, Arizona, USA; **ROM**, Royal Ontario Museum, Toronto, Ontario, Canada; **SAM**, South African Museum, Cape Town, Western Cape Province, South Africa; **SAMA**, South Australia Museum, Adelaide, Australia; **SMNS**, State Museum of Natural History, Stuttgart, Germany; **TMM (TNHC)**, Texas Memorial Museum, Austin, Texas, USA; **UA** Université d'Antananarivo, Atntananarivo, Madagascar; **UADBA**, Université d'Antananarivo, Département de Biologie Animale, Atntananarivo, Madagascar; **UC**, University of Chicago, Chicago, Illinois, USA; **UCMP**, University of California Museum of Paleontology, Berkeley, California, USA; **UCR**, Universidade Estadual Paulista, Rio Claro, São Paulo, Brazil; **UF**, University of Florida, Gainesville, Florida, USA; **UMNH (UUVP)**, Utah Museum of Natural History, Salt Lake City, Utah, USA; **UNC**, University of North Carolina, Chapel Hill, North Carolina, USA; **USNM**, Smithsonian National Museum of Natural History, Washington, D.C., USA; **YPM**, Yale Peabody Museum, New Haven, Connecticut, USA; **ZPAL**, Institute of Paleobiology of the Polish Academy of Sciences, Warsaw, Poland.

Abstract

Understanding the evolution of sensory perception is essential in explaining organismal behavior. Organisms using environmental stimuli to navigate their environments, avoid predation, capture prey, and find a mate, have a selective advantage. One player in organismal fitness is how and how well organisms perceive, interpret, and react to signals from their environments. Perceptions are the organized properties of physical stimuli from the environment and are modulated by the nervous system.

Several key innovations in early vertebrate evolution, such as ectodermal placodes and neural crest cells, enhanced the nervous system and increased the range and types of stimuli organisms could perceive. The new body plan resulting from these innovations included a cranium capable of respiration, feeding, and information acquisition via numerous sensory organs and a segmental series of pharyngeal arches. The first pharyngeal arch includes the fifth cranial nerve, the trigeminal nerve (CN V), and its associated vasculature and is the primary somatosensory nerve of the vertebrate head. The trigeminal nerve mediates sensory perception in the first pharyngeal arch as the arch engages in feeding behavior.

The trigeminal system, though conserved in general form, is diverse across vertebrates, particularly sauropsids, which have evolved extreme forms of cranial somatosensation as in probe-feeding birds, infrared-sensing pit vipers, and touch-sensitive crocodylians. It remains to be understood how these adaptations for cranial sensation evolved among different clades of sauropsids, including specific lineages of lepidosaurs, crocodylians, and birds. Previous research has used osteological structures to predict nervous tissue anatomy in small ranges of extinct dinosaur and crocodylian

species. However, these hypotheses require thorough testing using modern imaging, morphometrics, and phylogenetic comparative methods. Overall, we still lack consistent anatomical means of comparing relative sensation across lineages of reptiles, and the origins of extreme forms of sensation in the clade remain largely unexplored.

This research identifies patterns in form, function, and evolution of the sauropsid trigeminal system. Osteological and soft tissue structures of the trigeminal system are compared in both embryonic and adult sauropsids to understand their relationship, physiology, and morphology. These data were compared to behavioral and ecological data from the literature and form-function relationships hypothesized across environments. From this knowledge, I draw conclusions on the presence of soft tissues in extinct taxa as well as their behaviors and ecologies and evolution of the system. This research will clarify the relationships between structure, function, behavior, and ecology of the extant reptilian trigeminal system to better understand evolutionary patterns of sensation.

Chapter 1 — Introduction

Trigeminal anatomy and physiology in sauropsids:

In vertebrates, the trigeminal nerve is the primary somatosensory nerve of the head and courses a largely conserved pathway from its origin in the hindbrain to nerve endings across the face. The trigeminal nerve and associated neurovasculature leave osteological correlates in the form of foramina, depressions, grooves, and canals which can be traced along this pathway through the skull. An in depth understanding of these pathways and their osteological correlates allow for better predictions of soft tissues in fossil organisms.

In sauropsids, the trigeminal nerve courses from the hindbrain (rhombencephalon), forms the trigeminal (semilunar) ganglion, and extends rostrally where it splits into three divisions. The structure typically referred to as the ‘trigeminal ganglion’ comprises two ganglia. The profundal ganglion holds the cell bodies of the ophthalmic division of the trigeminal nerve and the gasserian ganglion holds the cell bodies of the maxillomandibular divisions of the trigeminal nerve. These ganglia are often distinct in lepidosaurs but are typically fused in archosaurs into a single semilunar ganglion, similar to the case in mammals (Barbas-Henry and Lohman 1986, Oelrich 1956, Willard 1915) (Fig. 1.1). The ophthalmic and maxillary divisions of the trigeminal nerve transmit sensory signals from the upper face and jaw, whereas the mandibular division transmits both motor and sensory signals to and from the lower jaw.

Among sauropsids, the surrounding bone differs with respect to the trigeminal ganglion and divisions. In lepidosaurs, the trigeminal ganglion sits within the trigeminal

notch of the prootic bone just ventral to the prootic-eipterygoid suture (Fig. 1.2A; Barbas-Henry and Lohman 1986, Oelrich 1956). In most lepidosaurs the trigeminal notch is only bounded rostrally by a tendinous ligament creating a single foramen for the three trigeminal divisions (Evans 2008, Oelrich 1956). In pseudosuchians, the trigeminal ganglion is housed extracranially in a bony cavity lateral to the braincase, the trigeminal fossa, which is formed by the quadrate, prootic, laterosphenoid, and pterygoid (Hopson 1979, Witmer et al. 2008) (Fig. 1.2B, 1.3). Therefore, in pseudosuchians, a trigeminal foramen in the braincase allows transmission of the trigeminal nerve into the trigeminal fossa and the three divisions pass through bony foramina in their exit from the trigeminal fossa. The pseudosuchian ophthalmic division exits the ganglion rostrally via a foramen in the laterosphenoid, whereas the pseudosuchian maxillary and mandibular divisions exit the trigeminal ganglion laterally through the maxillomandibular foramen, bounded by the laterosphenoid and prootic (Holliday and Witmer 2009; Jollie 1962) (Fig. 1.3B, 1.4A-B). Trigeminal ganglion and division foramina are more variable in avemetatarsalians. In sauropod dinosaurs there is a single trigeminal foramen, indicating an extracranial (though not surrounded by bone) trigeminal ganglion (Hopson 1979, Witmer et al. 2008, Holliday 2009, Balanoff et al. 2010). This pattern contrasts with more derived avian-line condition in which the trigeminal ganglion is found within the braincase (Witmer et al. 2008). This intracranial placement is reflected by the presence of separate ophthalmic and maxillomandibular foramina within the braincase wall of many tetanuran dinosaurs (Witmer and Ridgely 2009). In extant birds, the trigeminal ganglion (occasionally partially divided) is located on the floor of the cranial cavity (Baumel & Witmer 1993). In avian-line archosaurs with an intracranial ganglion, the ophthalmic division exits the

braincase through a foramen between the laterosphenoid and basicranium (e.g., basisphenoid, parasphenoid, ethmoid), and the maxillary and mandibular divisions typically exit the braincase through the maxillomandibular foramen, bounded by the laterosphenoid and prootic (though some birds have separate maxillary and mandibular foramina) (Baumel & Witmer 1993) (Fig. 1.1, 1.2C).

From their exits, these divisions follow homologous pathways, occasionally excavate depressions in adjacent bone, and with vasculature, pass through musculature to extend through bony canals in the rostrum. The intermuscular pathways of trigeminal nerve divisions have been demonstrated to consistently divide muscles into homologous groups (Edgeworth 1935, Haas 1973, Holliday and Witmer 2007, Iordansky 2000, Lakjer 1926, Lubosch 1933, Säve-Söderbergh 1945, Zusi and Livezey 2000). The ophthalmic division passes into the orbit and innervates structures of the face and the maxillary division communicates with teeth and somatosensory receptors in the integument after passing through foramina perforating the mandibles (Fig. 1.4A). In addition to transmitting sensory signals from the mandibles, the mandibular division transmits motor signals to the musculature of the lower jaw. Muscular branches originate proximally from the mandibular division and include those to the divisions of the adductor, pterygoideus, and intermandibularis musculature (Holliday and Witmer 2007, Abdel-Kader et al. 2010, Lakjer 1926, Poglayen-Neuwall 1953, Schumacher 1973, Watanabe and Yasuda 1970, Watkinson 1926). Proximal sensory branches from the mandibular division include the anguli oris nerve to the corner of the mouth and the recurrent cutaneous nerve to the skin over the adductor mandibularis externus (Kader et al. 2010, Poglayen-Neuwall 1953, Watanabe and Yasuda 1970). Further distally, the mandibular division extends the large

caudal intermandibular or external cutaneous branch medially through the angular, which sends numerous cutaneous rami to the skin of the ventrolateral mandible (Kader et al. 2010, Poglayen-Neuwall 1953, Watanabe and Yasuda 1970). As the mandibular nerve enters the mandibles, medial and oral intermandibular branches extend to innervate epithelium of the mouth, dental lamina, and integument and the inferior alveolar nerve enters the dentary (Kader et al. 2010). Numerous lingual, mucosal, and dental branches extend from the intermandibular and inferior alveolar nerves to their terminations in the oral cavity, and foramina in the dentary transmit cutaneous branches to their terminations in the integument of the rostral mandibles.

Sensory receptors are present at the afferent terminations of the trigeminal nerve. In lepidosaurs integument sensory receptors are well known and morphology and distribution have been extensively studied (e.g., Ananjeva et al. 1991, Breyer 1929, Grace et al. 1999, Hiller 1968, Jackson 1977, Landmann 1975, Matveyeva and Ananjeva 1995, Orejas-Miranda et al. 1977, Schmidt 1920, Sherbrooke and Nagle 1996, Young and Wallach 1998, etc.). Function is less well known, but Hiller (1978) confirmed some receptors served a mechanosensitive function, and the infrared properties of snake pit-organs are well known (see Goris 2011 for a review). Trigeminal sense organs in extant archosaurs are well understood, especially in taxa considered highly sensitive. Extant crocodylians are known for having highly sensitive snouts covered with integumentary sensory organs (ISOs) (Fig. 1.4D). In *Alligator mississippiensis*, this sensory system is specialized for a semi-aquatic lifestyle, with the ability to sense minute changes in water pressure, temperature, and pH (Di-Poï and Milinkovitch 2013). Furthermore, somatosensory distribution differs across taxa in extant pseudosuchians (Leitch and

Catania 2012). Some extant birds are also specialized for trigeminal nerve-innervated somatosensation. Trigeminal supplied bill tip organs are known from multiple families of probe- and tactile-foraging birds (e.g., Baumel & Witmer 1993, Berkhoudt 1980, Cunningham et al. 2010). Turtles exhibit similar morphology to birds in distribution of sensory corpuscles around the edges of a keratinous rhamphotheca (Buchtová et al. 2009). The cell types responsible for mechanical sensation reception are morphologically similar across sauropsids as well (Baumel & Witmer 1993, vonDüring 1973, Landmann 1975, Leitch and Catania 2012).

Trigeminal neurons transmit signals proximally from receptors, through specific locations in ganglia to designated brain regions. These pathways and somatotopy (correspondence of a specific area of the body to a specific point in the central nervous system) have been examined in trigeminal ganglia of alligators (Leitch and Catania 2013), the trigeminal nucleus of turtles (Rhinn et al. 2012), and are well known in birds (see Wild 2015 for a review). These pathways allow identification of specific dermatomes or and receptive fields (Berkhoudt et al. 1981, Leitch and Catania 2013). Homology of such fields as been proposed (Holliday and Witmer 2007) and further understanding of rostral receptive fields will clarify hypotheses of homology regarding specific regions of beak, scale, or integument (e.g., Gauthier et al. 2008, Hieronymus and Witmer 2010). Holliday and Witmer (2007) described homology of adductor chamber musculature based on neurovascular patterns. However, they only investigated the homology of proximal branches of the trigeminal nerve. Dermatome size, shape, and density of innervation is expected to follow patterns of variation in sauropsid behavior and ecology.

Development of the sauropsid trigeminal system

Trigeminal system formation initiates early during development by 4 days (of 70) of incubation in alligator (Ferguson 1987), 3 days (of 21) of incubation in chicken (Hamburger & Hamilton 1951, Kuratani and Tanaka 1990), and 0 days (of 60) of incubation in bearded dragon (Ollonen et al. 2018). The trigeminal system forms from a combination of ectodermal placode and neural crest derived cells. The neural crest contributes peripheral glia and proximal sensory neurons to these ganglia whereas the profundal and trigeminal placodes contribute solely sensory neurons (D'Amico-Martel and Noden 1983, Barlow 2002, Park and Saint-Jeannet 2010, Steventon et al. 2014). Fusion of the ganglia occurs proximally in most vertebrate taxa during development leaving two lobes distally (Xu et al. 2008). The sensory neural crest and placode cells extend processes peripherally to terminate in sensory receptors and centrally to communicate with brain nuclei. The peripheral rami map to target tissues guided by multiple factors including chemoattractants from the first arch epithelium, inhibitory regions, and interactions with other rami (Scott 1992, Vogel 1992). With respects to the trigeminal system and sauropsids, this process has largely been studied in birds (e.g., Covell and Noden 1989, Kuratani and Tanaka 1990, Qureshi and Atkinson 2007).

The adult arrangement of the ganglia and nerve divisions is a result of organization during embryonic development. As the chondrocranium develops, the orbital cartilage (sphenolateral plate) comprises a number of cartilaginous processes. At the caudal extent of the orbital cartilage there is a vertically oriented process, the pila antotica, that ultimately ossifies to form the laterosphenoid and fuses to the basal plate (Bellairs and Kamal 1981, DeBeer 1937). In lepidosaurs, the pila antotica only ossifies

occasionally to form the rostral border of the prootic notch by which the trigeminal nerve exits the braincase (Jollie 1962). In pseudosuchians the ossified pila antotica contributes to the rostral border of the trigeminal fossa, which houses the trigeminal ganglion, and sometimes separates the ophthalmic and maxillary divisions of the trigeminal nerve (Bellairs and Kamal 1981, DeBeer 1937, Holliday and Witmer 2009, Jollie 1960). In birds, the pila antotica is resorbed and replaced by a laterally-located pila antotica spuria which fuses to the basal plate and creates a foramen for the ophthalmic division of the trigeminal nerve (Jollie 1960).

Myelination is an important developmental process that influences nerve morphology and physiology. During myelination, Schwann cells surround axons with concentric lipid-protein layers that both increase nerve size and conduction velocity (Kandel et al. 2000). Knowledge of myelination in sauropsids is limited, largely focuses on central nervous system development, and is lacking in description of timing and extent of myelination in the peripheral nerves (e.g., Hartman et al. 1979, Yanes et al. 1987, Dulac et al. 1988, Nadon et al. 1995, Santos et al. 2005) leaving a gap in knowledge regarding development of signal propagation. George and Holliday (2013) noticed a decrease in axon density as alligators grew and attributed this to the increasing diameter of the myelin sheath in younger animals.

Osteological correlates and inferences of sensation

Previous evolutionary studies of the sauropsid trigeminal system have mostly focused on pseudosuchians, the sister clade to bird-line archosaurs. Soares (2002) began with an investigation into the trigeminal system in crocodylians, discovering the sensory organs were receptive to pressure changes and hypothesizing that the foraminiferous jaws

representative of this system were only present in semiaquatic members present after the Early Jurassic. George and Holliday (2013) performed quantitative analyses, establishing that *Alligator mississippiensis* head length, brain size, and trigeminal nerve size are consistently related. This confirmed trigeminal ganglion size as an informative metric for trigeminal nerve size in crocodyliforms and as an informative proxy for sensitivity and supports the hypothesis that the unique system seen in extant crocodylians likely originated along the eusuchian line. Though extant crocodylians are conservative in morphology and ecology, occupying similar semi-aquatic niches, extinct pseudosuchians exhibited diverse forms and occupied terrestrial to aquatic habitats, navigating these environments with unknown sensory abilities.

Recent studies have applied these osteological correlates to avian-line taxa, both terrestrial and aquatic, inferring sensitivity based on the presence of foramina. The presence of neurovascular foramina is cited within Dinosauria as a proxy for trigeminal nerve-innervated sensitivity (Ibrahim et al. 2014, Barker et al. 2017, Rothschild and Naples 2017, etc.). However, these hypotheses remain qualitative, were based on presence or absence of foramina and canals, and have not been supported by quantitative analyses of trigeminal ganglia, neurovascular canals, or foramina.

Osteological correlates within the extant phylogenetic bracket of lepidosaurs, crocodylians, and birds indicate the potential for specialized trigeminal nerve-innervated sensation in additional members of Archosauria (as per Witmer & Thomason 1995). Witmer and Thomason (1995) demonstrated that soft tissue inference is necessary for forming hypotheses on functional morphology, behavior, ecology, and evolution and noted the importance of basing soft tissue inferences in extant organisms on osteological

data acquired from a sample of extant organisms. As such, there are multiple examples of research examining osteological structures as correlates for neural soft tissues to make further inferences of behavior and ecology.

The infraorbital foramen has long been used for ecological interpretations of fossil specimens (see Muchlinski et al. 2008 for an overview). Its relevance to inferences of sensitivity was verified, and cross-sectional area of the osteological infraorbital foramen may be used as proxies for infraorbital nerve cross-sectional area (Muchlinski et al. 2008). Previous studies indicated that nerve cross-sectional area may be used to estimate axon counts (Jonas et al. 1992, Mackinnon and Dellon 1995, Cull et al. 2003), that regions with high densities of sensory receptors require more innervation (Kandel et al. 2000, Oelschlager and Oelschlager 2002, Marino 2007), and that regions with higher receptor densities exhibit higher sensitivities (Dehnhardt and Kaminski 1995, Nicoletis et al. 1997). Therefore, it is possible to estimate the nerve cross-sectional area, axon count, and sensitivity of the region innervated all from the cross-sectional area of the infraorbital foramen. This reasoning has been confirmed in that mammals with higher vibrissae counts have larger infraorbital foramina, but the foramina area may not be used to predict exact numbers of vibrissae (Muchlinski et al. 2010).

A similar case was made for the hypoglossal canal as an indicator of speech capability because it innervates the tongue (Kay et al. 1998). However, no correlation was found between hypoglossal nerve size, axon count, and the size of the hypoglossal canal, and hypoglossal canal dimensions do not vary much across apes (DeGusta et al. 1999, Jungers et al. 2003). Therefore, this osteological feature is uninformative and

validation of correlation of soft tissue to bony correlates is required on a case by case basis.

The cribriform plate is another osteological feature that has been used to infer soft tissue structures and therefore sensory behavior. The robust cribriform plate has been used as an indicator of olfactory ability in fossil mammals in lieu of using the fragile ethmoturbinal bones previously used in extant mammals (see Bird et al. 2014 p. 2080 for a review). The cribriform plate allows passage of the olfactory nerves from the nasal passage to the olfactory bulb within the brain. Cribriform plate surface area and the total cross-sectional area of cribriform plate foramina are informative metrics in hypothesizing olfactory ability in mammals, increasing as olfactory ability increases (Bird et al. 2014, 2018). These metrics have even been tied to number of olfactory receptor genes present in extant mammals (Bird et al. 2018).

The trigeminal system has similar potential (Fig. 1.4). Using data collected in extant sauropsids, this project establishes statistically sound osteological correlates for trigeminal soft tissues in fossil archosaurs and follows with predictions of soft tissues, their function, and how these tie with behavior and ecology.

Ecological, behavioral, and morphological transitions in sensation

Because sensory systems provide adaptive advantages, they are subject to changes in form and function, especially over ecological transitions (e.g., Mason 2016, Nilsson et al. 2012, Stevens 2013). The environment affects signal receipt and transmission and therefore sensation. As such, organisms in different environments tend to possess different sensory organs. This has been well documented in multiple cases (e.g., electrosensitivity is more prominent in aquatic environments because of the conductivity

of water, vision is often exchanged for other modalities in low light environments, birds exhibit higher visual acuity than non-flighted animals, etc.) (Martin 2012, Stevens 2013).

Across sauropsid evolutionary history, there are a few key transitions, namely transitions to edentulism, a semiaquatic ecology, limblessness, flight, and several other smaller scale transitions within clades. Transitions to limblessness often occur in concert with eye reduction and enhanced chemosensation, whereas the transition to flight is tied with increased visual and spatial perception abilities (Alonso et al. 2004, Gans 1975). Although special senses (i.e., vision, hearing, smell, taste, balance) are commonly considered across transitions, investigation into trigeminal-specific adaptations has been limited to single clade or species-specific investigations.

Thewissen and Nummela (2008) summarize sensory adaptations to non-terrestrial ecologies (e.g., crocodylian mechanoreceptors, olfactory system regression in aquatic snakes, etc.). Aquatic taxa (e.g., crocodylians, ducks, probing birds) exhibit high densities of trigeminal soft tissue structures indicative of their trigeminal abilities. Similarly, these taxa are tactile-feeders but it is unknown if variation in feeding styles (e.g., active vs. sit and wait feeding, lingual vs. jaw prehension) among sauropsids corresponds with variation in amounts of trigeminal tissue or if these strategies integrate sensory information differently. Within Lepidosauria, at least 14 clades contain members that have independently transitioned to fully aquatic ecologies, within Avemetatarsalia numerous avian taxa have aquatic ecologies, and within Pseudosuchia, at least three clades contain members that have independently transitioned to fully aquatic ecologies (Thewissen and Nummela 2008, Wilberg et al. 2019).

Pseudosuchia proves a useful group in which to evaluate hypotheses of changing trigeminal tissues with shifting ecology. Osteological correlates in pseudosuchians are robust and habitat shifts are well known. Basal pseudosuchians occupied terrestrial habitats from their origins in the Early Triassic (+245 Ma) (Nesbitt 2011). Two habitat shifts by non-surviving clades include the transition from a terrestrial to marine habitat by the thalattosuchians in the Early Jurassic (~201.3 Ma) and a transition from a terrestrial to freshwater habitat by some notosuchian crocodyliforms in the Early Cretaceous (~130 Ma) (Wilberg et al. 2019). Along the neosuchian line to modern crocodylians, a transition from a terrestrial to semiaquatic habitat occurred in the Middle Jurassic (~174.1 Ma) (Wilberg et al. 2019). These ecological shifts are tied with morphological shifts and it is expected that these were accompanied by changes in sensory systems towards the extant condition (e.g., expanded trigeminal ganglion, numerous integumentary sensory organs). The following investigation of trigeminal osteological correlates along the pseudosuchian lineage reveals patterns of increased trigeminal tissue in the Jurassic as neosuchians invaded aquatic environments.

Outline of Dissertation Chapters

Chapter 2

Cranial nerves are key features of the nervous system and vertebrate body plan. However, little is known about the anatomical relationships and ontogeny of cranial nerves in crocodylians and other reptiles, hampering understanding of adaptations, evolution, and development of special senses, somatosensation, and motor control of cranial organs. In chapter two I share three dimensional (3D) models an of the cranial nerves and cranial nerve targets of embryonic, juvenile, and adult American Alligators

(*Alligator mississippiensis*) derived from iodine-contrast CT imaging, for the first time, exploring anatomical patterns of cranial nerves across ontogeny. These data reveal the tradeoffs of using contrast-enhanced CT data as well as patterns in growth and development of the alligator cranial nervous system. Though contrast-enhanced CT scanning allows for reconstruction of numerous tissue types in a non-destructive manner, it is still limited by size and resolution. The position of alligator cranial nerves varies little with respect to other cranial structures yet grow at different rates as the skull elongates. These data constrain timing of trigeminal and sympathetic ganglion fusion and reveal morphometric differences in nerve size and path during growth. As demonstrated by these data, alligator cranial nerve morphology is useful in understanding patterns of neurological diversity and distribution, evolution of sensory and muscular innervation, and developmental homology of cranial regions, which in turn, lead to inferences of physiology and behavior.

Chapter 3

From the appearance of the vertebrate head, the trigeminal system has played a role in behavioral and ecological adaptation. The trigeminal nerve is the primary cranial somatosensory nerve, also innervating the jaw muscles. In crocodylians the trigeminal nerve plays a role in modulating the high bite force and unique integumentary sensation. In association with these behaviors, crocodylians are known for large trigeminal nerves, a high volume of trigeminal-innervated musculature, and densely packed, specialized sensory receptors. These innovations also occurred in concert with a restructuring of the lateral braincase wall. These morphologies have previously been investigated in phylogenetic and evolutionary contexts, but an ontogenetic, whole-system investigation

of trigeminal tissue and associated musculature, cartilage, and bone is lacking, as is an understanding of developmental timing of evolutionarily significant morphologies. In chapter three I use contrast-enhanced CT imaging to provide description and analysis of the trigeminal system in an ontogenetic series of *Alligator mississippiensis* from embryonic to adult form. I explore growth rates and allometric relationships of structures and discuss significance to hypotheses of homology. I find a high growth rate and allometric trajectory of the trigeminal nerve in comparison to other cranial nerves, likely associated with the large volume of trigeminal musculature and high densities of sensory receptors. I identify a similar trend in the pterygoideus dorsalis muscle, the highest contributor to bite force. I narrow ontogenetic timing of features related to the trigeminal topological paradigm and the undeveloped epipterygoid. Overall, I provide a basis for understanding trigeminal development in crocodylians, which upon comparison across reptiles will reveal ontogenetic origins of morphological variation.

Chapter 4

Highly-branched dendritic structures are common in nature and often difficult to quantify and therefore compare. Cranial neurovascular canals, examples of such structures, are osteological correlates for somatosensory systems and have been explored only qualitatively. In chapter 4, adaptations of traditional stream-ordering methods are applied to representative structures derived from CT scan data. Applying these methods to crocodylian taxa, this clade demonstrates a shared branching pattern and exemplifies the comparative utility of these methods. Additionally, this pattern corresponds with current understanding of crocodylian sensory abilities and behaviors. The method is

applicable to many taxa and anatomical structures and provides evidence for morphology-based hypotheses of sensory and physiological evolution.

Chapter 5

Numerous types of somatosensation-enhancing, integumentary trigeminal sensory systems have evolved in vertebrates. In all extant reptiles, nerve branches course through bony canals and foramina in the face and mandibles terminating in sensory receptors, yet morphology varies by clade and ecology. High densities of trigeminal nerve-innervated receptors at the ends of nerve branches and large trigeminal features are present in species commonly engaging in tactile sensory behaviors (e.g., crocodylians, probing and dabbling birds), whereas those not engaging in tactile sensory behaviors share low receptor densities and small trigeminal features. The variation in soft tissue trigeminal features and behaviors is mirrored by the variation in the osteological correlates of the reptilian trigeminal system, specifically the mandibular canal, allowing for inferences of facial sensation and tactile sensory behaviors in extinct taxa. In chapter 5, using measurements from CT scans of extant data, I performed morphometric analysis of the mandibular canal of several extant sauropsids, building a robust phylogenetic bracket for extinct archosaurs and establishing morphologies associated with enhanced sensory abilities. Employing the same techniques, I investigated extinct archosauromorph taxa including a diverse sampling of pseudosuchians from across the clade and several theropod dinosaurs. Results reveal diversity in mandibular canal morphology and thus trigeminal nerve distribution and facial sensory abilities in extinct archosaurs. Comparisons show reduced branching in most dinosaurian taxa and an increase in hypothesized tactile sensory abilities towards crown Crocodylia. The increase along the

pseudosuchian line precedes the transition from the terrestrial to semi-aquatic environment within the clade. Overall, using quantitative methods, I provide support for ecomorphological categories associated with trigeminal sensory behaviors allowing for predictions in extinct reptiles.

Chapter 6

Vertebrate sensory systems are in close contact with surrounding tissues, often leaving bony signatures behind. These bony features are the keys to assessing variation in sensory systems in fossil taxa. The trigeminal sensory system (e.g., trigeminal ganglion, ophthalmic, maxillary, and mandibular divisions) has osteological correlates throughout the skull including the braincase (e.g., trigeminal fossa, prootic notch, ophthalmic and maxillomandibular foramina) and rostrum (e.g., mandibular canal, neurovascular foramina). Here, I measured and compared these features among a morphologically, phylogenetically, and ecologically diverse sample of sauropsids to determine strength of osteological correlates and to explore ecomorphological trends. I determined several suitable osteological correlates for trigeminal soft tissue features and discounted foramen count alone as a suitable osteological correlate. However, when size was accounted for, foramen count becomes a useful indicator of sensory ecology. Among extant taxa, those engaging in tactile-sensory behaviors exhibit relatively larger trigeminal tissues and osteological correlates than those not engaging in tactile-sensory behaviors. Though trends are unclear among several clades, both relative feature sizes and models used to predict sensory ability reveal a trend of increasing tactile sensitivity along the pseudosuchian lineage. Overall, quantitative assessment of ecomorphological trends of trigeminal osteological correlates proves informative for hypotheses of behavior in

extinct taxa, and supports use of similar assessment methods for other osteological correlates.

Figure 1.1. Trigeminal feature phylogenetic distribution.

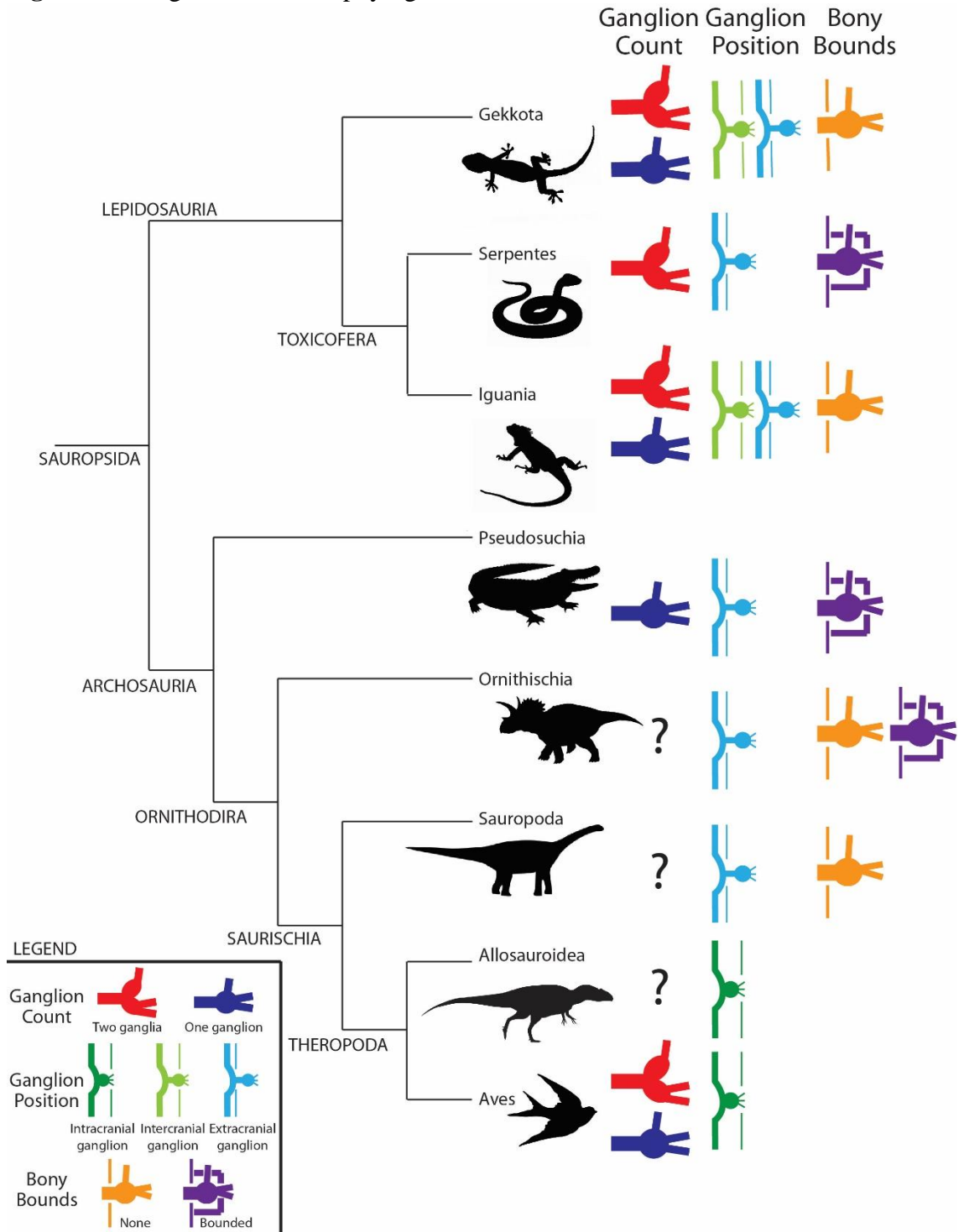


Figure 1.2. Sauropsid crania. Anole (MUVCL I089) (A), alligator (MUVCL AL031) (B), and parrot (MUVCL AV042) (C) crania with lateral skull removed showing locations of trigeminal nerve foramina and branches with respect to skeletal elements.

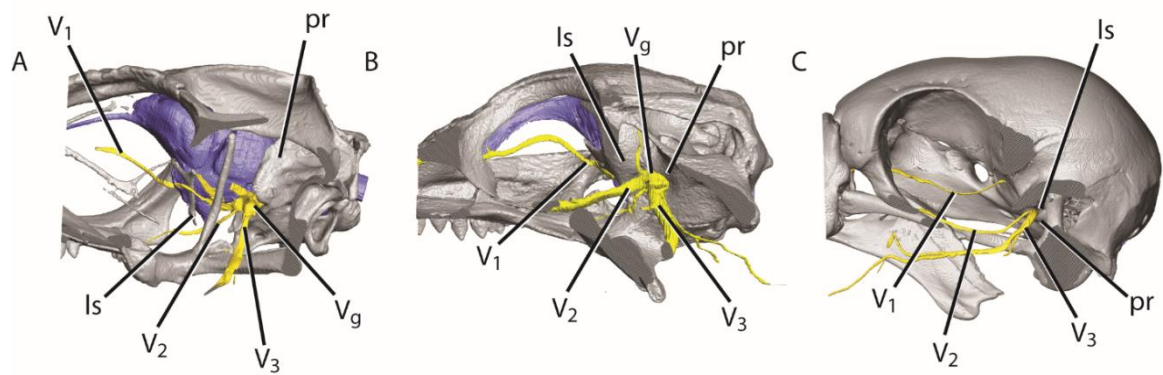


Figure 1.3. Extant phylogenetic bracket of non-crocodylian pseudosuchians and non-avian avemetatarsalians with notable characters. Fossil pseudosuchian and avemetatarsalian taxa (*Simosuchus*: UA 8679; *Tsaagan*: IGM100/1015) are bracketed by contrast-enhanced and CT scanned lepidosaurs (brown anole: MUVCL1089), crocodylians (American alligator: MUVCL031), and avians (grey parrot: MUVCL092).

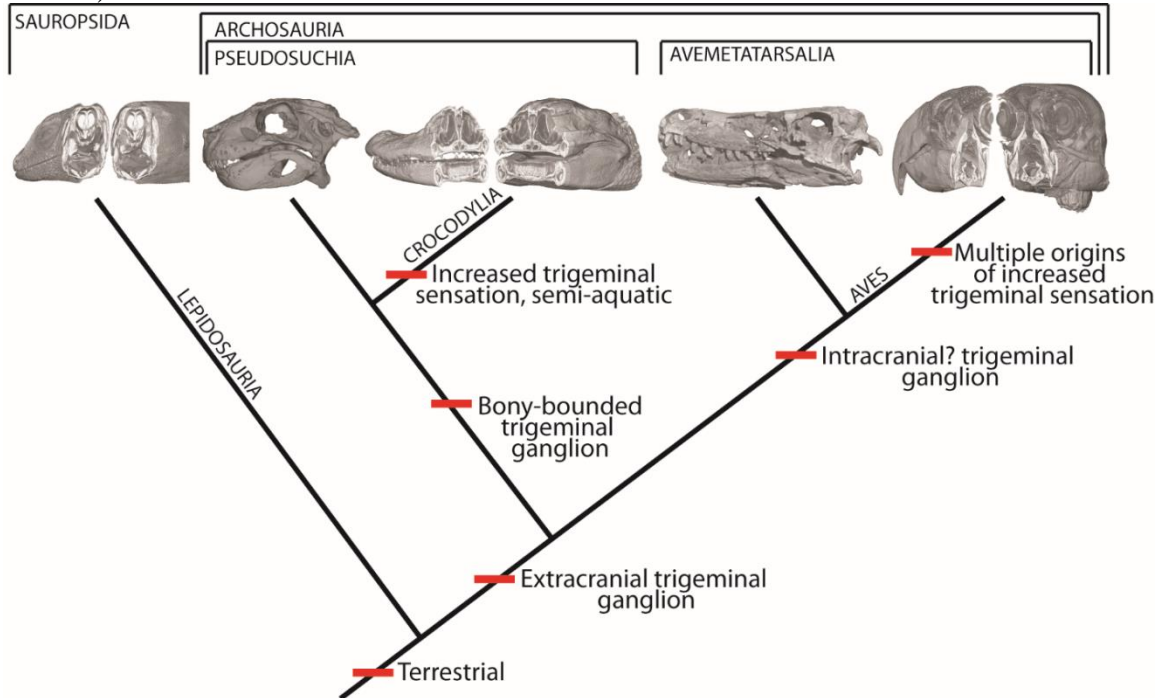
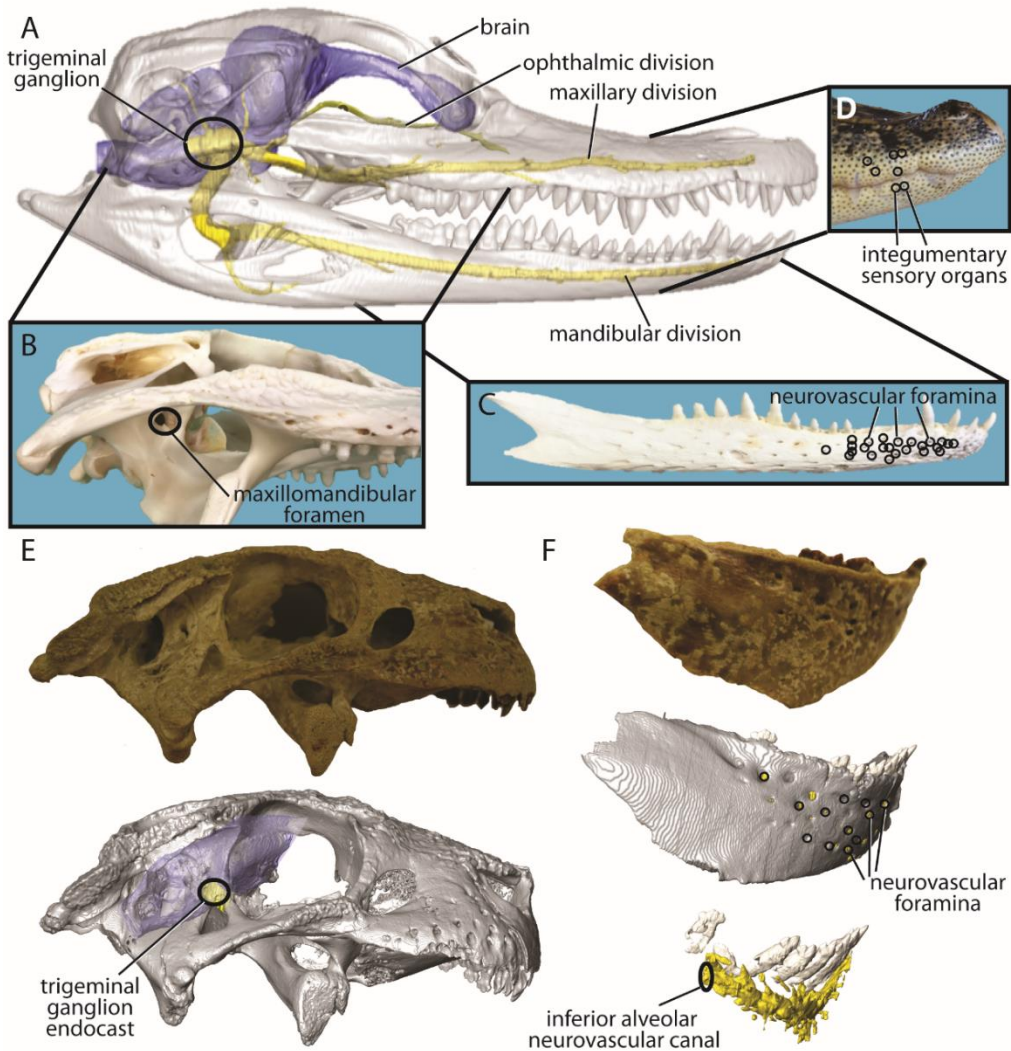


Figure 1.4. Features of the trigeminal system as exemplified by *Alligator mississippiensis* and *Simosuchus clarki*. 3D reconstruction of a CT scanned alligator (MUV C AL031) with brain in blue and nerves in yellow showing positions of the trigeminal ganglion and inferior alveolar canal (A). Alligator skull showing the position of the trigeminal foramen (B). Alligator dentary showing the position of neurovascular foramina (C). Integumentary sensory organs on the alligator rostrum (D). *Simosuchus* (UA 8679) cranium and CT reconstruction of cranium and endocast (E). *Simosuchus* (UA 8679) dentary and CT reconstruction of dentary, neurovascular canal, and teeth (F).



Chapter 2 — A 3D ontogenetic atlas of *Alligator mississippiensis* cranial nerves and their significance for comparative neurology of reptiles

INTRODUCTION

The American alligator (*Alligator mississippiensis*) has long been the subject of numerous anatomical studies focusing on all aspects of form and function (e.g., Wedin, 1953; Ferguson, 1984; Busbey, 1989; Rieppel, 1993; Erickson et al., 2003; Allen et al., 2010; Holliday et al., 2013; Dufeau and Witmer, 2015) and as an accessible member of the pseudosuchian line, has also been used as an evolutionary model for the extant crocodylian condition (e.g., Colbert et al., 1946; Müller and Alberch, 1990; Tsai and Holliday, 2011; George and Holliday, 2013; Gignac and Erickson, 2016). Alligators and other crocodylians experience marked changes in the shape of the skull, sensory capsules, cranial musculature, and other cranial organ systems during development from dorsoventrally tall-skulled hatchlings to flat-skulled adults (e.g., Dodson, 1975; Monteiro et al., 1997; Tsai and Holliday, 2011; Dufeau and Witmer, 2015; Fabbri et al., 2017; Sellers et al., 2017). Yet we know little about how the cranial nerves accompany these ontogenetic changes in passage to and from cranial organs. Crocodylian cranial nerve morphology, has been described previously (e.g., Shiino, 1914; Reese, 1915; Lakjer, 1926; Bellairs and Shute, 1953; Poglayen-Neuwall, 1953; Schumacher, 1973; Shaker and El-Bably, 2015) but illustrations have been limited to two-dimensional projections usually following dissection. New contrast-enhanced imaging approaches offer holistic views of the peripheral cranial nervous system and reveal morphological changes during ontogeny.

Here I provide a three-dimensional anatomical atlas of *Alligator mississippiensis* cranial nerves to better describe their relative positions, topology, and targets and show

how these change through ontogeny. Using these new data, I discuss the tradeoffs of the method and caution against using contrast-enhanced CT data without supplementary dissection or histological comparison. These new morphological data from cranial nerves are critical to resolving questions in crocodylian biology and vertebrate evolution including: what patterns of neurological diversity exist in crocodylians, archosaurs, and tetrapods; when the acquisition of extreme somatosensation occurred in the pseudosuchian and avian lineages and whether similar acquisition occurred in other lineages (Soares, 2002; Cunningham et al., 2007; Leitch and Catania, 2012; George and Holliday, 2013); patterns of neurological distribution to cranial dermatomes in crocodylians, archosaurs, and tetrapods (Holliday and Witmer, 2007; Hieronymus and Witmer, 2010); and the developmental biology of various skull regions (Klembara, 2001; Holliday and Witmer, 2007, 2009). Finally, I offer an accompanying library of 3D interactive models of the head and cranial nerves of *Alligator* for use in research and public education.

MATERIALS AND METHODS

This project features four *Alligator mississippiensis* specimens from Rockefeller State Refuge, Grand Chenier, Louisiana, USA. The first is an adult specimen with a skull length of 25.4 cm (MUVCL606). The removed head was fixed in 10% neutral buffered formalin and immersed in 12.3% I₂KI (Lugol Solution, Carolina Biological Supply Company, NC) for 3 years and 7 months. The scan for this specimen was conducted on a NSI scanner using 220 kV, 0.14mA, and a voxel size of 87.5µm.

The second is a 12-month-old specimen (MUVCL031; also used in Holliday et al., 2013; Sellers et al., 2017; Lessner et al., 2019) with a skull length of 5.7 cm. The removed head was fixed in 10% neutral buffered formalin, stored in 70% ethanol, and

immersed in 12.3% (w/v) I₂KI (Lugol Solution, Carolina Biological Supply Company, NC) for 5 weeks. The scan for this specimen was conducted on a Zeiss Xradia Versa 510 using 120kV, 0.083 mA, and a voxel size of 39.42μm.

The third is an embryonic, stage 19, 27-28 day specimen (MUVC AL089) (Ferguson 1985) with a head length of 1.4 cm. The entire embryo was fixed in 10% neutral buffered formalin and stabilized using the modified STABILITY protocol (Wong et al.,F 2013) of Carlisle and Weisbecker (2016). The specimen was then stained overnight in 1% (w/v) I₂KI (Lugol Solution, Carolina Biological Supply Company, NC) and embedded in 1% agarose gel for stabilization during CT scanning. The scan for this specimen was conducted on a Zeiss Xradia Versa 510 using 80kV and a voxel size of 20.723μm.

The fourth is a specimen with a 9.8 cm skull length (MUVC AL623). The removed head was bisected, fixed in 10% neutral buffered formalin, and scanned with a voxel size of 51.92μm on a Siemens Inveon MicroCT scanner at the University of Missouri Biomolecular Imaging Center.

Scan data were imported as DICOM files into Avizo v.9 for segmentation. Structures of interest (see Table 2.1) were segmented manually using thresholding and the magic wand and paintbrush tools.

RESULTS

Specimen suitability

Of the three contrast-enhanced and scanned specimens, MUVC AL031 provided the most data. The specimen was fully stained (partially overstained, specifically in the middle-ear region) allowing for contrast between muscles, nerves, bone, cartilage, and some vasculature. The embryonic specimen (MUVC AL089) was scanned at a higher

resolution than the others because of its small size but it was unclear whether stain had not bound to finer nerve branches, higher resolution is required, or these branches have not yet formed. The STABILITY protocol discussed above and embedding in 1% agarose noticeably enhanced the scan (e.g., eliminated shrinkage, increased staining) in comparison to a previously stained and scanned embryo that was not subjected to this protocol. The largest specimen (MUVC AL606), even after years of staining, exhibited lower contrast between structures either because of incomplete stain penetration and binding to the deepest structures or limited x-ray penetration. Because it was scanned as a whole, its size also limited the minimum resolution of the resulting data. Generally, in the embryo, because the brain has not yet elongated to the adult morphology, nor have the muscles and bones fully formed, the relationships between the nerves and other structures are less clear. Conversely, in the large specimen, because scan resolution is limited by stain penetration and specimen size, relationships between tissues are less clear.

Cranial nerve I: Olfactory

The olfactory nerve (CN I) transmits purely sensory signals from air-borne stimuli from olfactory sensory neurons in the nasal cavity to the olfactory bulbs via unmyelinated fibers (Crosby, 1917; Hansen, 2007). The neurons comprising the first cranial nerve are visible as a series of short ventral extensions of the rostral end of the olfactory bulbs (Figs. 2.1,2.2). From the olfactory bulbs, these bundles extend rostroventrally to contact the olfactory epithelium of the nasal cavity (Fig. 2.3). There are no visible ontogenetic differences in the olfactory nerve.

Cranial nerve II: Optic

The optic nerve (CN II) transmits purely visual sensory signals. The optic nerve is a short, thick nerve extending from the midline of the telencephalon (Figs. 2.1,2.2). Shortly after its origin from the brain, it passes through the optic chiasm in close contact with the opposing optic nerve. The optic nerve then extends by the rostroventral border of the laterosphenoid. From there it passes dorsal to the m. rectus ventralis (mRv, m. inferior rectus), medial to the m. rectus dorsalis (mRd, m. superior rectus), and bends ventrally around the m. levator bulbi (mLB) to enter the caudomedial aspect of the eye (Fig. 2.4). During ontogeny, the optic nerve elongates rostrocaudally in response to the lengthening of the skull and the more rostral position of the orbits (i.e., with respect to the origin of the nerve from the telencephalon) in the adult.

Cranial nerve III: Oculomotor

The oculomotor nerve (CN III) transmits only motor signals and is a long, nerve emerging from the mesencephalon-pontine junction (Figs. 2.1,2.2). It passes through a notch in the ventral border of the laterosphenoid (fCN III) caudoventral to the optic nerve before extending through the ciliary ganglion (C_g) to its destinations (Romer, 1956) (Figs. 2.5-8). In the embryo and yearling alligators (but not the adult), the oculomotor nerve passes laterally around the diencephalon (Fig. 2.2). The ciliary ganglion (Fig. 2.5) of the oculomotor nerve is located dorsal to m. levator bulbi and m. lateral rectus (mRl, m. rectus lateralis) and inferior to the ophthalmic division of the trigeminal nerve (V_1) where the oculomotor nerve sends a short branch (superior branch, nRd) to the ventral border of the m. rectus dorsalis (Fig. 2.4,2.5). The next branch passes laterally, between the m. levator bulbi and m. lateral rectus, though its destination is unknown (potentially carrying parasympathetic neurons). A third branch (inferior branch) innervates the m. rectus

ventralis at its ventral surface, passing dorsal to the m. lateral rectus and extends two more branches. One of these (nRm) innervates the m. medial rectus (mRm, m. rectus medialis) and the other (nOv) passes ventral to the eye before innervating the m. obliquus ventralis (mOv, m. inferior oblique) (Fig. 2.4). There are no obvious differences in oculomotor nerve anatomy during ontogeny.

Cranial nerve IV: Trochlear

The trochlear nerve (CN IV) transmits only motor signals as well and is a long, thin nerve extending from the dorsolateral surface of the caudal midbrain (Figs. 2.1,2.2). It extends laterally around the brain, ventral to the cerebrum. In the yearling and adult alligator, the nerve passes in close proximity to the ventral cerebrum, whereas in the embryo the cerebrum has not completed growth and therefore the trochlear nerve is well ventral to it. From there, it passes through a foramen in the laterosphenoid (fCN IV) caudal to the optic nerve (Fig. 2.6-8). The trochlear nerve continues rostrally to innervate the m. obliquus dorsalis (mOd, m. superior oblique) from a ventral aspect, passing caudal to the m. rectus dorsalis, dorsal to the m. medial rectus, superior to the ophthalmic division of the trigeminal nerve, and medial to the eye (Fig. 2.3,2.4). As with the oculomotor nerve, there are no obvious ontogenetic differences in trochlear nerve anatomy.

Cranial nerve V: Trigeminal

The path of the *Alligator* trigeminal nerve (CN V) has been covered extensively in the literature (e.g., Poglayen-Neuwall, 1953; Iordansky, 1964; Schumacher, 1973; Holliday and Witmer, 2007; Holliday and Witmer, 2009; Leitch and Catania, 2012; George and Holliday, 2013) and so will be summarized here. The trigeminal nerve

transmits both motor and sensory signals, beginning at the pons, and extending roots to the trigeminal ganglion (V_g) through a large foramen (fCN V) bounded by the prootic and laterosphenoid (Figs. 2.1,2.6,2.9). The trigeminal ganglion sits within the trigeminal fossa, formed by the prootic, laterosphenoid, quadrate and pterygoid (Figs. 2.6-8) and comprises two smaller ganglia. The maxillomandibular ganglion ($V_{g2/3}$) is larger, and more caudoventral than the smaller, rostradorsally located ophthalmic ganglion (Fig. 2.9, V_{g1}). Through ontogeny, there is less distinction between the ophthalmic and maxillomandibular ganglia; two distinct ganglia are visible in the embryonic alligator, less so in the yearling, and not at all in the adult alligator. Also, the merged trigeminal ganglion becomes larger relative to brain size as specimen size increases.

The ophthalmic division of the trigeminal nerve (V_1) extends rostrally through a foramen in the laterosphenoid and passes along the ventral surface of the laterosphenoid dorsal to the m. levator bulbi and m. lateral rectus and lateral to the oculomotor nerve (Fig. 2.5). Before continuing rostrally, a branch (nFR) extends dorsally from the ophthalmic ganglion, passing caudal to the orbit and extending to the frontal (Fig. 2.9). The ophthalmic nerve continues rostrally, passing through the m. rectus dorsalis and dorsal to the optic nerve. From there it courses rostrally, medial to the eye, ventral to the trochlear nerve, dorsal to the m. medial rectus, then ventrolateral to the m. obliquus dorsalis before paralleling the olfactory bulbs. The terminal ophthalmic branches, the medial and lateral nasal branches (nNm, nNl), extend rami through various foramina on the surface of the nasals and premaxillae to innervate the integument of the dorsomedial portion of the rostrum. The lateral nasal branch also carries parasympathetic fibers rostrally to the narial musculature (nN).

Two small branches extend dorsally from the trigeminal ganglion, the tympanic branch (nTYM), passing through a foramen in the prootic, and the supraorbital ramus (nSO) of the maxillary division (Fig. 2.9). The maxillary (V₂) and mandibular (V₃) divisions extend laterally from the trigeminal ganglion through the trigeminal (maxillomandibular) foramen, formed by the quadrate, pterygoid, and laterosphenoid (Fig. 2.8). The maxillary division passes rostrally, dorsal to the m. pterygoideus dorsalis (mPTd) through the ventrolateral portion of the orbit (Fig. 2.10). Before entering the superior alveolar canal in the maxilla, a branch (nJU) extends laterally, perforating the jugal to innervate integumentary receptors. From there it enters the maxilla as the superior alveolar nerve (nAs) and extends branches through various foramina to terminate in sensory receptors in the integument (nCU), gingiva (nGV), and alveoli (nA). Several palatine branches (nP) descend to innervate the palatal mucosa. The superior alveolar nerve continues into the premaxilla lateral to the nasal mucosa.

The mandibular division extends ventrolaterally after exiting the trigeminal foramen (Fig. 2.10; see the following for detailed descriptions: Poglayen-Neuwall, 1953; Schumacher, 1973; Holliday and Witmer, 2007). Immediately, short branches extend laterally, one (nAMEP) to the m. adductor mandibulae externus profundus (mAMEP), followed by two (nAMEM) to the m. adductor mandibulae externus medialis (mAMEM). The pterygoid ramus (nPT) extends rostroventrally and divides (extending the nPTd and nPSTs) to innervate the m. pterygoideus dorsalis (mPTd) and the m. pseudotemporalis superficialis (mPSTs) (Fig. 2.10). Another branch (nPTv) extends caudoventrally to the m. pterygoideus ventralis (mPTv). Further ventrally along the mandibular division, the ramus caudalis (nCA) extends laterally and curves rostrally, passing between the m.

adductor mandibulae externus superficialis (mAMES) and the m. adductor mandibulae posterior (mAMP). Another small branch extends caudolaterally to the m. adductor mandibulae posterior (nAMP). A sensory branch, the angulus oris (nAO), then extends rostrally, receiving sensory input from the caudal border of the oral cavity (Fig. 2.10). From there, the mandibular division loops ventrolaterally bounded by the m. adductor mandibulae posterior and the m. adductor mandibulae internus medially and the m. adductor mandibulae externus laterally. The recurrent cutaneous branch (nRC) extends caudally just before the rostral extension of the mandibular division. As the mandibular division extends rostrally, a caudal intermandibular branch (nMp) passes ventromedially, extending rami (nIMA) to the m. intermandibularis (mIMA) and integument. As the mandibular division passes dorsal to the m. intramandibularis (mIRA) and lateral to the m. intermandibularis, it extends branches to each (nIMA, nIRA) before entering the inferior alveolar canal (Fig. 2.10). Here a branch to the m. constrictor colli pars anterior (mCCCa) is expected, but not visible in the data. The middle intermandibular branch (nMa) extends medially, followed by the oral intermandibular branch (nIO), and a branch that travels rostrally with Meckel's cartilage (nMK). Lingual (nLG) and mucosal (nM) rami extend from the oral intermandibular branch. Rostrally, numerous lingual, mucosal, and dental branches (nCU, nA, nM) extend from the inferior alveolar nerve (nAi) to their terminations in the oral cavity, and foramina in the dentary transmit cutaneous branches to their terminations in sensory receptors of the integument of the rostral mandibles (Fig. 2.9).

In the embryonic alligator, the three trigeminal divisions are similar in diameter. However, in the yearling and adult alligator, the ophthalmic division is the smallest and

the mandibular division the largest. Additionally, because of the lengthening of the skull and brain, the ventrolateral loop of the mandibular division becomes more defined during ontogeny.

Cranial nerve VI: Abducens

The abducens nerve (CN VI) is a short, motor-only nerve, extending from the pontine-medulla junction on the ventral surface of the brain (Figs. 2.1,2.2). It does so by passing through a canal and foramen (fCN VI) in the basisphenoid lateral to the canal and foramen for the internal carotid artery (Fig. 2.3) (foramen caroticum anterius of Iordansky [1973]) (Figs. 2.6,2.8). One third of the extent of the abducens nerve is just dorsal to the endocranial surface of the basisphenoid, a second third within the basisphenoid, and the final third within the orbit approaching the ophthalmic division of the trigeminal nerve and the innervating the m. lateral rectus (Fig. 2.4, mRI). The abducens nerve also innervates the m. quadratus, which is responsible for movement of the nictitating membrane of the eye (Stibbe, 1928), but neither this branch nor this muscle are visible in these data. The abducens nerve lengthens rostrocaudally as specimen size increases in response to the lengthening of the skull and brain and the more rostral position (i.e., with respect to the origin of the nerve from the pontine-medulla junction) of the orbits in the adult.

Cranial nerve VII: Facial

The facial nerve (CN VII) transmits both motor and sensory signals and extends rostrally and laterally from the pontine-medulla junction through a foramen (fCN VII) in the prootic before immediately passing through the geniculate ganglion (Figs. 2.1,2.11, VII_g). The palatine division (nPAL) extends rostrally and ventromedially from the

ganglion where the hyomandibular division (nHYM) extends caudally. The palatine division passes ventrally across the lateral border of the prootic and basipterygoid before extending between the basipterygoid-palatine suture and continuing dorsally along the lateral border of the palatine to the palatine-maxillary suture (Figs. 2.3,2.6-8). The hyomandibular division passes dorsolaterally along the lateral border of the prootic to the prootic-opisthotic suture. Here it passes nearby the m. levator auriculae (mLA) and m. depressor auriculae (mDA) (Fig. 2.12) via a canal to the paraoccipital process of the exoccipital at the junction of the exoccipital and quadrate (Fig. 2.6, cCQ) (cranioquadrate canal and fissure of Jollie [1962] and Iordansky [1973]). The hyomandibular division splits into two smaller rami (Shiino, 1914; Bellairs and Shute, 1953), the hyoid ramus of the hyomandibular division (ramus communicans of Shiino, 1914) and the chorda tympani (nCHT), but only the beginning of the hyomandibular division and the hyoid ramus are clearly visible in these data, the chorda tympani being too small. The path of the chorda tympani was approximated using the associated vasculature with which it travels (external carotid artery and mandibular vein and artery [Porter et al., 2016]) and the description of Shiino (1914) (Fig. 2.12). The hyomandibular division splits at the level of the foramen magnum and the hyoid ramus extends rami (nDM, nCCp) to innervate the m. depressor mandibulae (mDM) and the m. constrictor colli profundus (Figs. 2.12,2.13, mCCp). The chorda tympani loops rostr dorsally, ventral to the otic process of the quadrate and dorsomedial to the stapes before continuing ventrally, first lateral to the quadrate and rostral to the stapes along the rostral wall of the tympanic cavity, then medial to the mandibular joint (Shiino, 1914 [see Text-fig. 33]; Goodrich, 1915; Hotton, 1960). This loop is followed by a ventral loop and rostral approach to the

mandibular division of the trigeminal nerve (Fig. 2.13). The bend in the paths taken by the branches of the facial nerve become more defined during ontogeny in response to the lengthening of the skull and brain in the adult.

Cranial nerve VIII: Vestibulocochlear

The vestibulocochlear nerve (CN VIII) transmits only sensory signals and extends laterally from the pontine-medulla junction, just caudal to the root of the facial nerve (Figs. 2.1,2.11). The vestibular divisions (nV) and the cochlear branch (nC) pass through individual foramina (fCN VIII) on the medial surface of the prootic before extending to the ampullae of the semicircular canals (nAc, nAl, nAr) and cochlea, respectively (Figs. 2.6,2.11). In the larger specimens, the vestibulocochlear branches are shorter and less defined as the middle and inner ear increase in size and proximity to the root of the nerve.

Cranial nerve IX: Glossopharyngeal

The glossopharyngeal nerve (CN IX) transmits both motor and sensory signals and originates from the medulla, extending laterally to exit the cranial cavity via the jugular foramen (fCN IX) in the exoccipital (Figs. 2.1,2.6,2.8,2.11). Just after exiting the jugular foramen, it forms the petrosal ganglion (IX_g) then extends ventrally passing by the external carotid artery. Extending further ventrally, the glossopharyngeal nerve passes along the dorsal border of the m. constrictor colli profundus and between the m. branchiohyoideus dorsalis (mBHd) and m. branchiohyoideus ventralis (mBHv) (Fig. 2.14) (innervating these two; Li and Clarke, 2015) and lateral to the hyoid. Then it passes medial to the m. geniohyoideus (mGH) to the ventral border of the tongue. This nerve takes an increasingly tortuous path to its destinations during ontogeny in response to the increasingly horizontal orientation of the hindbrain.

Cranial nerve X: Vagus

The vagus nerve (CN X) transmits both motor and sensory signals and originates from the medulla extending laterally to exit the cranial cavity via the jugular foramen (fCN X) in the exoccipital (Figs. 2.1,2.6,2.8,2.11). Just after exiting the jugular foramen, it forms a ganglion (dorsal to the sympathetic ganglion [S_g], the jugular and/or nodose ganglion, X_g) before passing ventrally with the internal carotid. The vagus nerve then takes a tortuous ventral path medial to the glossopharyngeal nerve before splitting at the dorsal extent of the m. constrictor colli profundus (Li and Clarke, 2015). The pharyngolaryngeal branch (of Shiino, 1914, nPHL) passes rostrally, medial to the m. constrictor colli profundus and medial to the hyoid along the dorsal border of the m. omohyoideus (Li and Clarke, 2015). Then the pharyngolaryngeal branch passes medially, ventral to the m. constrictor larynges (mCL) and the m. cricoarytenoid (Fig. 2.15, mCR) (innervating them; see Riede et al. [2015] for laryngeal musculature details). The vagal branch (of Shiino, 1914) extends caudally from the division alongside the lateral border of the esophagus into the thorax. Like the glossopharyngeal nerve, the vagus nerve also takes an increasingly tortuous path to its destinations as specimen size increases in response to the increasingly horizontal orientation of the hindbrain.

Cranial nerve XI: Accessory

I skip discussion of the accessory nerve as it originates outside of the skull from cervical nerve roots and targets cervical musculature and is therefore, though passing through the jugular foramen from the cranial cavity, not a “cranial” nerve (Benninger and McNeil, 2010).

Cranial nerve XII: Hypoglossal

The hypoglossal nerve (CN XII) transmits motor signals and originates from the medulla and extends laterally through the hypoglossal foramen (fCN XII) in the exoccipital (Figs. 2.1,2.6,2.8,2.11). The hypoglossal nerve passes rostral to the first cervical nerve before extending ventrally through the m. longissimus capitis (Al-Hassawi, 2004). From there, it follows a tortuous path, paralleling the vagus nerve medial to the m. constrictor colli profundus before turning rostrally at the dorsal extent of the m. omohyoideus (Li and Clarke, 2015). The hypoglossal nerve then extends rostromedially, paralleling the glossopharyngeal nerve lateral to the hyoid and medial to the m. branchiohyoideus dorsalis (Li and Clarke, 2015). The nerve continues rostrally along the floor of the mouth, innervating the m. hyoglossus (mHG), m. genioglossus (mGG), m. geniohyoideus (mGH), m. episternobranchiotendineus (mEBT) and the m. episternobranchialis (Fig. 2.16, mEB) (see Li and Clarke, 2015) before anastomosing with the opposing hypoglossal nerve at the level of the fourteenth dentary tooth (counted from rostral). The hypoglossal nerve has numerous caudal extensions (nCV) before its rostromedial curve, which extend to meet the cervical nerves. The hypoglossal nerve, like the glossopharyngeal and vagus nerves, increases in tortuosity during ontogeny in response to the increasingly horizontal orientation of the hindbrain.

Cranial autonomic nerves:

The autonomic system is discussed here because of its many cranial targets and shared pathways with cranial nerves. Where nerves are untraceable in these data, this description relies on that of Shiino (1914) and Bellairs and Shute (1953, esp. Text-fig. 5.).

The most evident autonomic nerves in the alligator cranium are those of the sympathetic system. The sympathetic nerve (nSYM) travels cranially lateral to the cervical vertebrae until forming a sympathetic ganglion (S_g) just outside the jugular foramen (Shiino, 1914; Bellairs and Shute, 1953). The ganglion is in close contact with the petrosal ganglion of the glossopharyngeal nerve and the vagus ganglion of the vagus nerve (Fig. 2.3,2.4,2.8,2.11). From there, the thick cranial sympathetic nerve extends through the jugular foramen into the exoccipital, around the round window of the otic capsule, across the secondary tympanic membrane, medial to the facial nerve, around the lateral semicircular duct, dorsal to the geniculate ganglion to the maxillomandibular ganglion of the trigeminal nerve (Bellairs and Shute, 1953). Bellairs and Shute (1953) reported a communicating branch to the hyoid ramus of the facial nerve (too small to see in these data) which ultimately innervates the m. constrictor colli profundus, m. levator auriculae, m. depressor auriculae, m. levator palpebrae (mLP), and m. depressor palpebrae (Fig. 2.12, mDP). The sympathetic nerve contacts the maxillomandibular ganglion of the trigeminal nerve, and in our dataset, further branches are not visible. Bellairs and Shute (1953) reported communicating branches with the maxillomandibular and ophthalmic ganglia and nerves that travel with the ophthalmic nerve eventually innervating the nasal gland and nasal muscles via the lateral nasal (ethmoidal) ramus (Fig. 2.9, nN). The sympathetic nerve is large in diameter in the embryo, but too small to locate in the yearling and adult specimens.

The alligator parasympathetic nervous system is represented by three ganglia along the course of cranial nerves (Bellairs and Shute, 1953). The oculomotor nerve holds the ciliary ganglion (C_g) just caudal to the branch to the rectus dorsalis muscle (Fig.

2.2,2.3). The parasympathetic nerves of the ciliary ganglion innervate the ciliary and sphincter muscles responsible for focusing the eye via constricting the pupil and adjusting the lens. The maxillary division of the trigeminal nerve holds the palatine ganglion (P_g) rostrally, at the location of a communicating branch with the palatine division of the facial nerve (Fig. 2.3). These two ganglia are evident in the embryonic alligator, but not visible in the yearling or adult specimens. The parasympathetic nerves of the palatine ganglion innervate the orbital glands and mucosa of the nasal cavity and palate. Bellairs and Shute (1953) reported a mandibular (submandibular) ganglion along the chorda tympani but the presence of this ganglion is unclear in these data. The parasympathetic nerves of the mandibular ganglion innervate the submandibular and sublingual glands.

DISCUSSION

This study provides a three-dimensional view of alligator cranial nerve anatomy. It adds to the growing collection of 3D alligator data and those of other crocodylians (e.g., Rowe et al., 1999; Holliday et al., 2013; Dufeu and Witmer, 2015; Li and Clarke, 2015; Riede et al. 2015; Porter et al., 2016) also contributing to the numerous imaging resources available for download. Also, data from extant taxa provide detailed, necessary phylogenetic brackets for the increasingly common studies of paleoneurology from endocasts of extinct pseudosuchian species (e.g., Sereno and Larsson, 2009; von Baczko et al., 2018; Mastrantonio et al., 2019). These datasets are available from Sketchfab as annotated, 3D interactive models (see Table 2.2) (<https://sketchfab.com/holliday/collections/alligator-cranial-nerve-atlas>). Sketchfab also provides a model inspector (<https://labs.sketchfab.com/experiments/model-inspector>) in which model objects may be toggled on or off using “Scene” to further explore structure

relationships in three dimensions. Raw datasets are available when possible from Open Science Framework (<https://osf.io/jmpck/>).

Anatomy

Overall, there are not many gross anatomical differences among alligator cranial nerves at these ontogenetic stages. The absence of differences is itself significant. Any changes occur largely as a result of the changing skull and brain shapes during ontogeny. The cranial nerves are brought along as they maintain their pathway from origin to destination. The cranial modules grow at different rates (Goswami, 2006; Watanabe et al., 2019), yet the cranial nerves maintain their origins and targets during development regardless of the distance between (Vogel, 1992). At stage 19 in the alligator the placode-derived sensory neurons have all contacted the hindbrain and their targets. As hindbrain becomes horizontal and the skull elongates, the trigeminal, facial, glossopharyngeal, vagus, and hypoglossal nerves all must grow at a faster rate than the nerves to the ears, eye, and extraocular muscles. The olfactory nerve maintains close contact between the olfactory bulbs and the nasal mucosa and therefore grows at the slowest rate.

There are some noteworthy differences with respect to the trigeminal nerve among datasets. The embryonic specimen has two distinct ganglia (i.e., ophthalmic [profundal] and maxillomandibular [Gasserian]) that have not yet fused into a single trigeminal ganglion at stage 19, day 27-28 of in ovo development, rather than a single-fused trigeminal ganglion as seen in the yearling and adult specimens. With more embryonic sampling, it will be possible to pinpoint the developmental stage at which these ganglia merge, adding a character not typically used in embryonic staging, though potentially useful in evolutionary and developmental neurological comparisons. The

trigeminal nerve ganglion also increases in size with respect to the brain during ontogeny, perhaps tied to the increase in diameter of the maxillary and mandibular divisions in comparison to the ophthalmic division. The maxillary and mandibular regions receive sensory input from most of the rostral sensory organs, which are responsible for fine sensation and orientation to prey (Leitch and Catania, 2012). Increase in nerve and ganglion size implies an increase in myelination of neurons, which leads to an increase in signal propagation, and therefore faster sensory speeds and increased performance in larger specimens (Kandel et al., 2000). This is supported by the observation of George and Holliday (2013) that axon density decreases in larger alligators, likely because myelin sheaths increase in size. I suspect that histological investigation of the merged trigeminal ganglia would show a larger increase in maxillomandibular ganglion size than ophthalmic ganglion size during alligator ontogeny.

Another noteworthy difference between the embryonic and larger individuals is the increasing tortuosity of the glossopharyngeal, vagus, and hypoglossal nerves. These likely reflect the extra length of nerve required for the range of head movements alligators engage in and therefore, with the elastic properties of nerves (e.g., Vogl et al., 2015), could be used as constraints in biomechanical investigations of head orientation, gape, and other movements.

These data show a single cranial sympathetic ganglion (the rostral [superior] cervical ganglion, S_g), even in the embryonic specimen. This is actually a fusion of the primary and secondary cervical ganglia (Shiino, 1914; Bellairs and Shute, 1953), only visible using histology. These two ganglia ultimately fuse with the petrosal (IX_g) and vagus (X_g) ganglia during ontogeny. As with the fusion of the trigeminal ganglia,

pinpointing the developmental stage at which these ganglia merge could be a potentially useful character for comparison across reptiles. Reptilian autonomic systems are not well researched in general, so unraveling sympathetic distribution along the other cranial nerves is the first step in understanding autonomic components of cranial nerves and autonomic function in the reptile head.

Homology

Nerve homology guides our understanding of the origins of cranial bones, dermatomes, muscles, glands, and other structures. Nerves and their branches maintain conserved pathways through structures and tracing nerves and their branches from origin to target through development is a successful method of testing for structure homology (e.g., trigeminal nerve and jaw muscle topology [Holliday and Witmer, 2007] and the hypoglossal nerve and craniocervical homology [Maddin et al., 2020]). Data provided here can further understanding of homologous structures and their evolutionary and developmental origins. Cranial element homology is usually traced by fate mapping of embryonic precursors (e.g., Maddin et al., 2016), but nerves with identical origins could be traced to targets of questionable origin. Also, it has been suggested that the skull roof tracks with the brain during evolution and development in reptiles (Fabbri et al., 2017), but it may also track with cranial nerve innervation. Similarly, as suggested by Holliday and Witmer (2007), there are conserved muscle groups traceable through trigeminal motor nerves and conserved trigeminal dermatomes traceable through trigeminal sensory nerves. For example, the integument over the interorbital region, formed by the frontal bone, is innervated by the frontal branch of the ophthalmic division of the trigeminal nerve in the alligator, whereas the integument over the postorbital region, formed by the

frontal, postorbital, and parietal bones, is innervated by the supraorbital ramus of the maxillary division of the trigeminal nerve. Therefore, homologous nerves are expected to arise from the ophthalmic and maxillary division in other taxa and would distinguish between homologous regions (e.g., interorbital vs. postorbital) and elements (e.g., frontal vs. postorbital vs. parietal) in those taxa. The other sensory nerves should follow similar patterns, defining homologous muscle groups and sensory regions when explored across multiple taxa. Finally, the origins of cranial glands are often discussed (e.g., Jarrar and Taib, 1987; Fry et al., 2006; Kardong et al., 2009) especially when investigating origins of venom (e.g., McDowell, 1986; Fry et al., 2012), and nerve innervation (by autonomic nerves along CN VII or CN V) is a possible method to confirm homology.

Methods

This study highlights both the utility and drawbacks of contrast-enhanced CT imaging and 3D reconstruction. Numerous structures of various tissue types (e.g., muscle, bone, nerve, including both myelinated (e.g., CN V) and unmyelinated (CN I) nerves, were identified in multiple specimens of various sizes making it possible to track growth and development of structures. The interconnected anatomy of the flat crocodylian skull is difficult to approach in traditional dissection, and this method allows for a non-destructive view into a complex region. Unfortunately, though resolution has increased since CT scanning for anatomical purposes began in the late 20th century, it is still one of the largest limiting factors. Many finer nerve branches that supply muscles or are parts of the autonomic system are still only visible using histology and sometimes dissection. These branches remain missing from this CT data either because these branches are too fine for contrast particles to bind to or because the specimens were scanned with a lower

resolution than necessary to see them. Similarly, thin muscles with few muscle fascicles are also not visible with this method. Specific examples in this dataset include the m. constrictor internus dorsalis (mCID) and the trigeminal ramus that innervates these muscles (nCID), the trigeminal ramus (nCCa) to the m. constrictor colli pars anterior (mCCa), the m. quadratus (muscle of the nictitating membrane) and its motor ramus from the abducens nerve, and communicating branches from the sympathetic nerve to other cranial nerves. However, in the case that branches are missing from a dataset, occasionally, they were discernible in another, such as the case with the frontal branch (nFR) from the trigeminal nerve and the sympathetic nerve (nSYM), which were only visible in the embryonic dataset. This method of contrast is also limited in highlighting the vasculature accompanying nerves and supplying structures. Finally, details on the cellular level are absent and require complementary histology to visualize, such as fiber decussation in the optic chiasm, distinction between fused ganglia, somatotopy, axon counts, and extent of myelination.

I also caution against drawing conclusions before careful comparison of 3D-reconstructed data and dissected and histologically processed specimens. When presented with such a large amount of complicated structures, familiarization with 3D relationships can prove difficult to untangle and misidentification is quite easy. Before structure identification, it is necessary to explore the structure from origin to target and confirm its topological relationships with other structures (often conserved) with the literature, dissection, and other available 3D resources.

Table 2.1. Anatomical abbreviations and structure locations by figure.

Abbrev.	Structure	Figure 2.:
CN I	Cranial nerve 1 (N. olfactorius)	3,4A,6,8,9(A)
CN II	Cranial nerve 2 (N. opticus)	3,4B,5(A,D),6,8,9 (A)
CN III	Cranial nerve 3 (N. oculomotorius)	3,4B,5(A,D),6,8,9 (A)
mOv	Inferior oblique muscle (m. obliquus ventralis)	5
mRd	Superior rectus muscle (m. rectus dorsalis)	5
mRm	Medial rectus muscle (m. recuts medialis)	4B,5
nRv	Inferior rectus muscle (m. rectus ventralis)	4B,5
nOv	Branch to inferior oblique muscle (n. obliquus ventralis)	3
nRd	Branch to superior rectus muscle (n. rectus dorsalis)	3
nRm	Branch to medial rectus muscle (n. recuts medialis)	3
CN IV	Cranial nerve 4 (N. trochlearis)	3,4,5(A,D),6,8,9(A)
mOd	Superior oblique muscle (m. obliquus dorsalis)	5
CNV	Cranial nerve 5 (N. trigeminus)	4B,5(A,D),6,8,9(A),10,11(A,D),14
mAMEM	Adductor mandibulae externus medialis	11
mAMEP	Adductor mandibulae externus profundus	11
mAMES	Adductor mandibulae externus superficialis	11
mAMP	Adductor mandibulae posterior	11

mCN	Constrictor nares	10
mDN	Dilator nares	10
mIRA	Intramandibularis	11
mLB	Levator bulbi	4B,5,11
mPSTp	Pseudotemporalis profundus	11
mPSTs	Pseudotemporalis superficialis	11
mPTd	Pterygoideus dorsalis	11
mPTv	Pterygoideus ventralis	11
nA	Branch to alveoli (R. alveolares)	10
nAi	Inferior alveolar branch	10
nAMEM	Branch to Adductor mandibulae externus medialis	11
nAMEP	Branch to Adductor mandibulae externus profundus	11
nAMP	Branch to Adductor mandibulae posterior	11
nAO	Angulus oris	10B,11
nAs	Superior alveolar branch	10
nCA	Ramus caudalis	11
nCU	Cutaneous branch (R. cutanei)	10,11C
nGV	Gingival branch	10
nIMA	Branch to intermandibularis	10B,11
nIO	Oral intermandibular branch	10B
nIRA	Branch to intramandibularis	10B,11
nJU	Jugal branch	10B,11
nLG	Lingual branch (R. lingualis)	10

nM	Mucosal branch	10B
nMa	Middle intermandibular branch (R. mylohyoideus anterior)	10B
nMK	Meckelian branch	10B
nMp	Caudal intermandibular branch (R. mylohyoideus posterior)	10,11
nN	Branch to narial musculature	10B
nNI	Lateral nasal branch (R. lateralis nasi)	10
nNm	Medial nasal branch (R. medialis nasi)	10
nPAL	Palatine branch	10
nPSTs	Branch to pseudotemporalis superficialis	11
nPT	Branch to pterygoideus muscles (R. pterygoideus)	11
nPTd	Branch to pterygoideus dorsalis	10,11
nPTv	Branch to pterygoideus ventralis	10B,11
nRC	Recurrent cutaneous branch	10B
nSO	Supraorbital branch (N. supraorbitalis)	10,11
nTYM	Tympanic branch	10,11
V ₁	Ophthalmic division (N. ophthalmicus)	4B,5,10,11,14
V ₂	Maxillary division (N. maxillaris)	4B,5,10,11,14
V ₃	Mandibular division (N. mandibularis)	4,5,10,11,14
V _g	Trigeminal ganglion (Ganglion trigeminale)	10,11,14A
V _{g1}	Ophthalmic ganglion (Ganglion profundal)	6,10C,11D,14B
V _{g2/3}	Maxillomandibular ganglion (Ganglion gasserian)	6,10C,11D,14B

CN VI	Cranial nerve 6 (N. abducens)	3,4C,5(A,D),8,9(A)
mRl	Lateral rectus muscle (m. rectus lateralis)	5
CNVII	Cranial nerve 7 (N. facialis)	4C,6,8,9(A),12,13(A,E),14
VII _g	Geniculate ganglion (Ganglion geniculi)	12,13,14
mCCa	Constrictor colli pars anterior	13
mCCp	Constrictor colli profundus	13
mDA	Depressor auriculae	13
mDM	Depressor mandibulae	13
mDP	Depressor palpebrae	13
mIMA	Intermandibularis	13
mLA	Levator auriculae	13
mLP	Levator palpebrae	13
nCC	Branch to constrictor muscles	12C
nCHT	Chorda tympani	14
nDM	Branch to depressor mandibulae	12C
nHYM	Hyomandibular division (N. hyomandibularis)	6,12,14
nPAL	Palatine division (N. palatinus)	12,14
CNVIII	Cranial nerve 8 (N. vestibulocochlearis)	6,8,9(A),12
nC	Cochlear branch (N. cochlearis)	12
nAc	Branch to caudal ampulla (N. ampullaris caudalis)	12
nAl	Branch to lateral ampulla (N. ampullaris lateralis)	12
nAr	Branch to rostral ampulla (N. ampullaris rostralis)	12
nV	Vestibular branch (Pars vestibularis/ampullaris)	12

CN IX		Cranial nerve 9 (N. glossopharyngeus)	4,6,8,9(A),12,15(A,C)
IX _g	Petrosal ganglion		4D,9,12
mBHd	Branchiohyoideus dorsalis		15
mBHv	Branchiohyoideus ventralis		15
nTYM	Tympanic branch		12B
CN X		Cranial nerve 10 (N. vagus)	4,6,8,9(A),12,16(A)
mCL	Laryngeal constrictors (Constrictor larynges)		16
mCR	Cricoarytenoid (Cricoarytenoideus)		16
nPHL	Pharyngolaryngeal branch		12
nTYM	Tympanic branch		12
nX	Vagal branch		12
X _g	Vagus ganglion		4D,12
CNXII		Cranial nerve 12 (N. hypoglossus)	4,6,8,9(A),12,17(A,D)
mEB	Episternobranhialis		17
mEBT	Episternobranhiotendineus		17
mGG	Genioglossus		17
mGH	Geniohyoideus		17
mHG	Hyoglossus		17
mT	Intrinsic muscles of the tongue		17
nCV	Cervical branch (R. cervicalis)		12B
OTHER			
aCO	Carotid artery		7C
cCQ	Cranioquadrate canal		7C

C _g	Ciliary ganglion	6
CT	Cartilago transiliens	11A
dBS	Basisphenoid diverticulum	7D
dITY	Intertympanic diverticulum	7D
dPA	Parietal diverticulum	7D
dPT	Pterygoid diverticulum	7D
f	Foramen	7
fL	Lymphatic foramen	7D
fMAG	Foramen magnum	7
fPS	Foramen from basisphenoid diverticulum to pharyngotympanic sinus	7D
nSYM	Sympathetic nerve	6
P _g	Palatine ganglion	6
S _g	Sympathetic ganglion	6,9
vJG	Jugular vein	7C

Table 2.2. Individual URLs to 3D models of figures found in the Sketchfab collection (<https://sketchfab.com/holiday/collections/alligator-cranial-nerve-atlas>).

Figure(s)	URL
2.:	
5A	https://sketchfab.com/3d-models/yearling-alligator-extraocular-muscles-832ea36447394124b9fa51fbed6bcd9b
5D	https://sketchfab.com/3d-models/embryonic-alligator-extraocular-muscles-03ccd7cc21fd40608d6bb4dbd6e61578
6	https://sketchfab.com/3d-models/embryonic-alligator-cranial-nerves-b14a75f97da74cd89e402d118ba38e59
7B and 9A	https://sketchfab.com/3d-models/alligator-skull-and-cranial-nerves-98c9ca48f3a3408f8c64d6c6d4256aee
11A	https://sketchfab.com/3d-models/yearling-alligator-cn-v-innervated-muscles-538568dea57041628e8a5b564b30b2eb
11D	https://sketchfab.com/3d-models/embryonic-alligator-cn-v-innervated-muscles-3a7d93f76545415da07e60d46d03c346
13A	https://sketchfab.com/3d-models/yearling-alligator-cn-vii-innervated-muscles-c2d269b76ef9402480ab296feda0f675
13E	https://sketchfab.com/3d-models/embryonic-alligator-cn-vii-innervated-muscles-278d5ba701ff43aa898915e52ae049c7
15A	https://sketchfab.com/3d-models/yearling-alligator-cn-ix-innervated-muscles-fd0d25c386494e719ca17cc742e76443

15C	https://sketchfab.com/3d-models/embryonic-alligator-cn-ix-innervated-muscles-61720901bf684060aa0c1fba74475f5e
16A	https://sketchfab.com/3d-models/yearling-alligator-cn-x-innervated-muscles-c05d83b85d6247c1a97f360f144c5c37
17A	https://sketchfab.com/3d-models/yearling-alligator-cn-xii-innervated-muscles-f116e8e8222d4607a998107d06e45f50
17D	https://sketchfab.com/3d-models/embryonic-alligator-cn-xii-innervated-muscles-764fd8ced1e545668930938b39dd9de5
3B, 5A, 10B, 11A, 12B, 13A, 14A, 15A, 16A, 17A	https://sketchfab.com/3d-models/yearling-alligator-cranial-nerve-and-muscles-6563d92576ab475ca31f2752ea710248
3B, 10B, 12B, 14A	https://sketchfab.com/3d-models/yearling-alligator-cranial-nerve-and-muscles-51dbdca420454effb324a88753b047f9
3C, 5D, 6, 10C, 11D, 12C, 13E, 14B, 15C, 17D	https://sketchfab.com/3d-models/embryonic-alligator-cranial-nerve-and-muscles-3c844a3b122044c6b533ac2de8a5fb7b

*Load model URL into the model inspector

(<https://labs.sketchfab.com/experiments/model-inspector>) to toggle layers using “Scene.”

Figure 2.1. Brain. 3D reconstruction of the brain, brain regions, and head of alligator MUV C AL606 (A), yearling alligator MUV C AL031 (B), and stage 19 embryo MUV C AL089 (C, mirrored) in right lateral view.

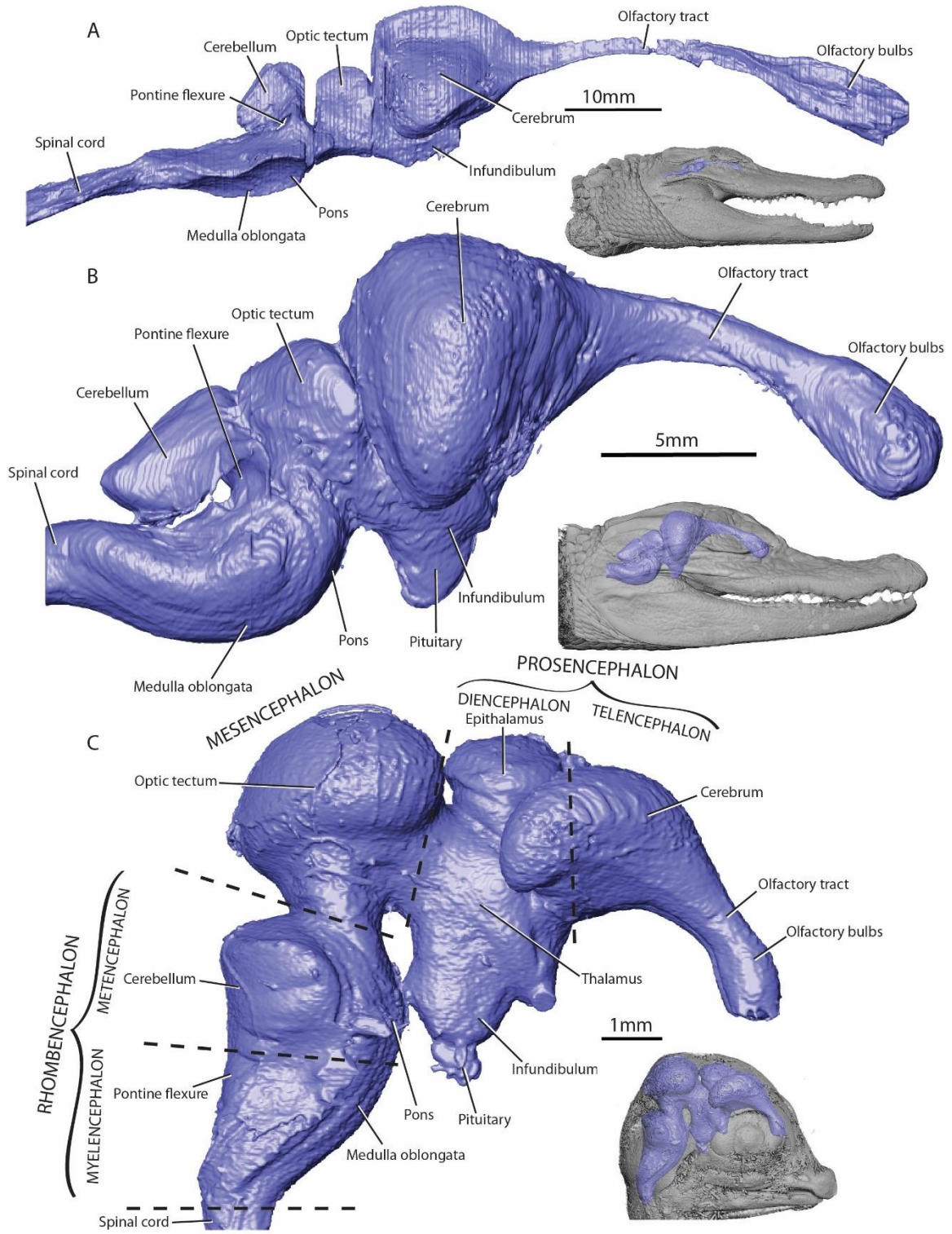


Figure 2.2. Olfactory, Optic, Oculomotor, Abducens, and Trochlear Nerves. 3D reconstruction of the brain, cranial nerves I to VI (excluding V), and head of alligator MUVc AL606 (A), yearling alligator MUVc AL031 (B), and stage 19 embryo MUVc AL089 (C, mirrored) in right rostralateral view.

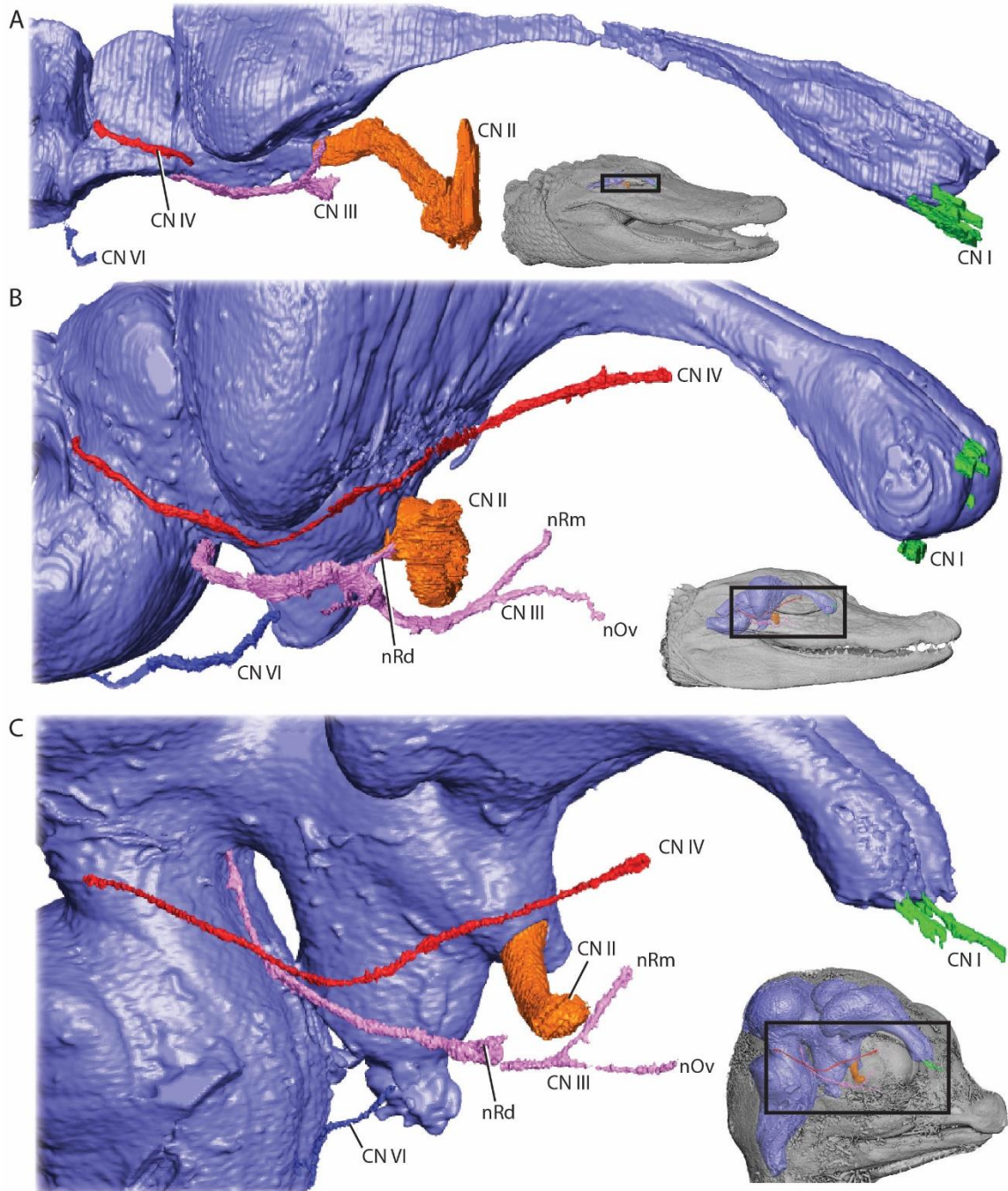


Figure 2.3. Cross Sectional Data. Axial slices through segmented CT data of alligator MUVC AL606 (A), stage 19 embryo MUVC AL089 (B), and yearling alligator MUVC AL031 (C,D).

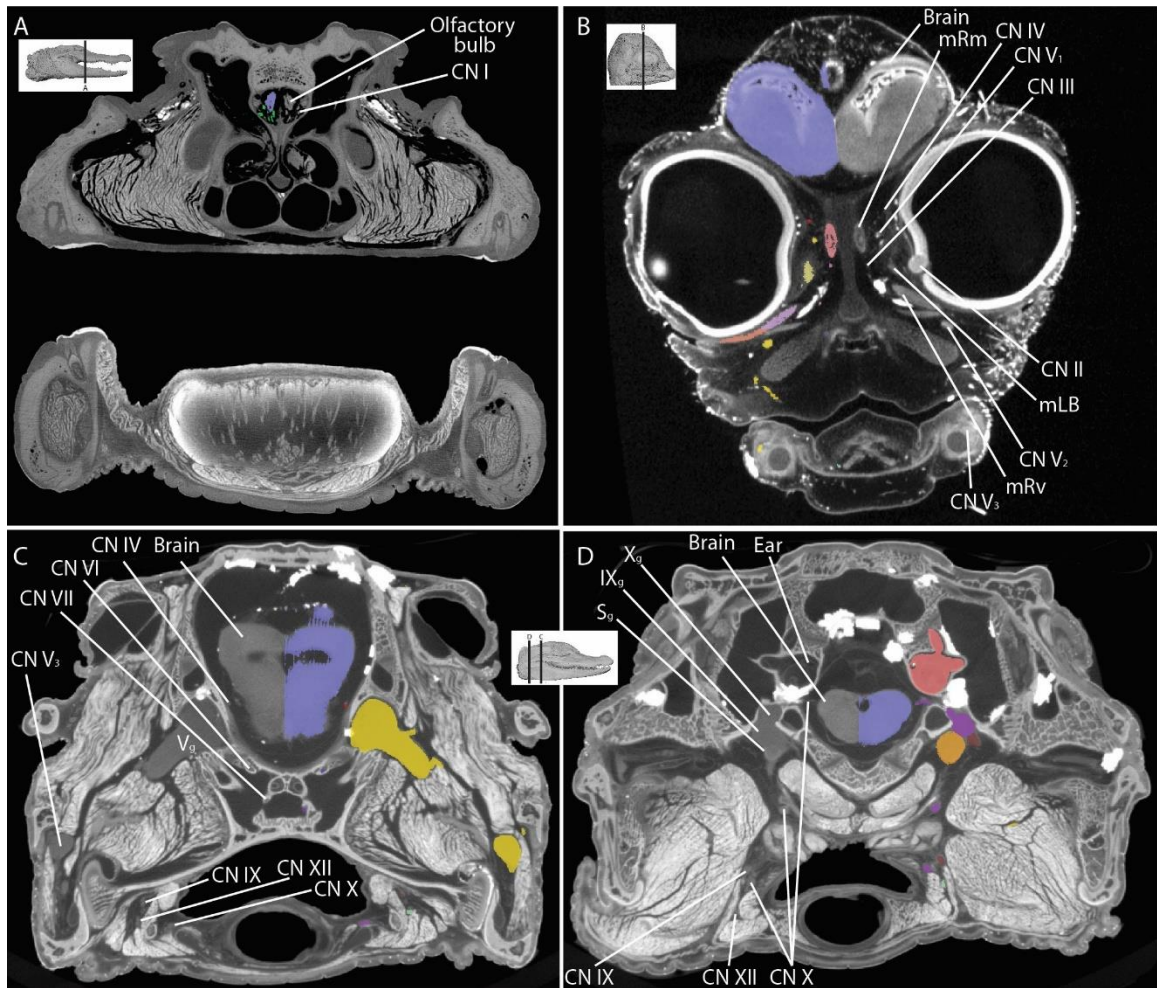


Figure 2.4. Eye Muscles. 3D reconstruction of the brain, cranial nerves I to VI (excluding V), extraocular muscles, and head of yearling alligator MUVC AL031 (A) and stage 19 embryo MUVC AL089 (D, mirrored) in right rostralateral view with axial CT slices of MUVC AL031 (B,C). A 3D model of figure 4A may be found at: <https://sketchfab.com/3d-models/yearling-alligator-extraocular-muscles-832ea36447394124b9fa51fbed6bcd9b> and a 3D model of figure 4D may be found at: <https://sketchfab.com/3d-models/embryonic-alligator-extraocular-muscles-03ccd7cc21fd40608d6bb4dbd6e61578>.

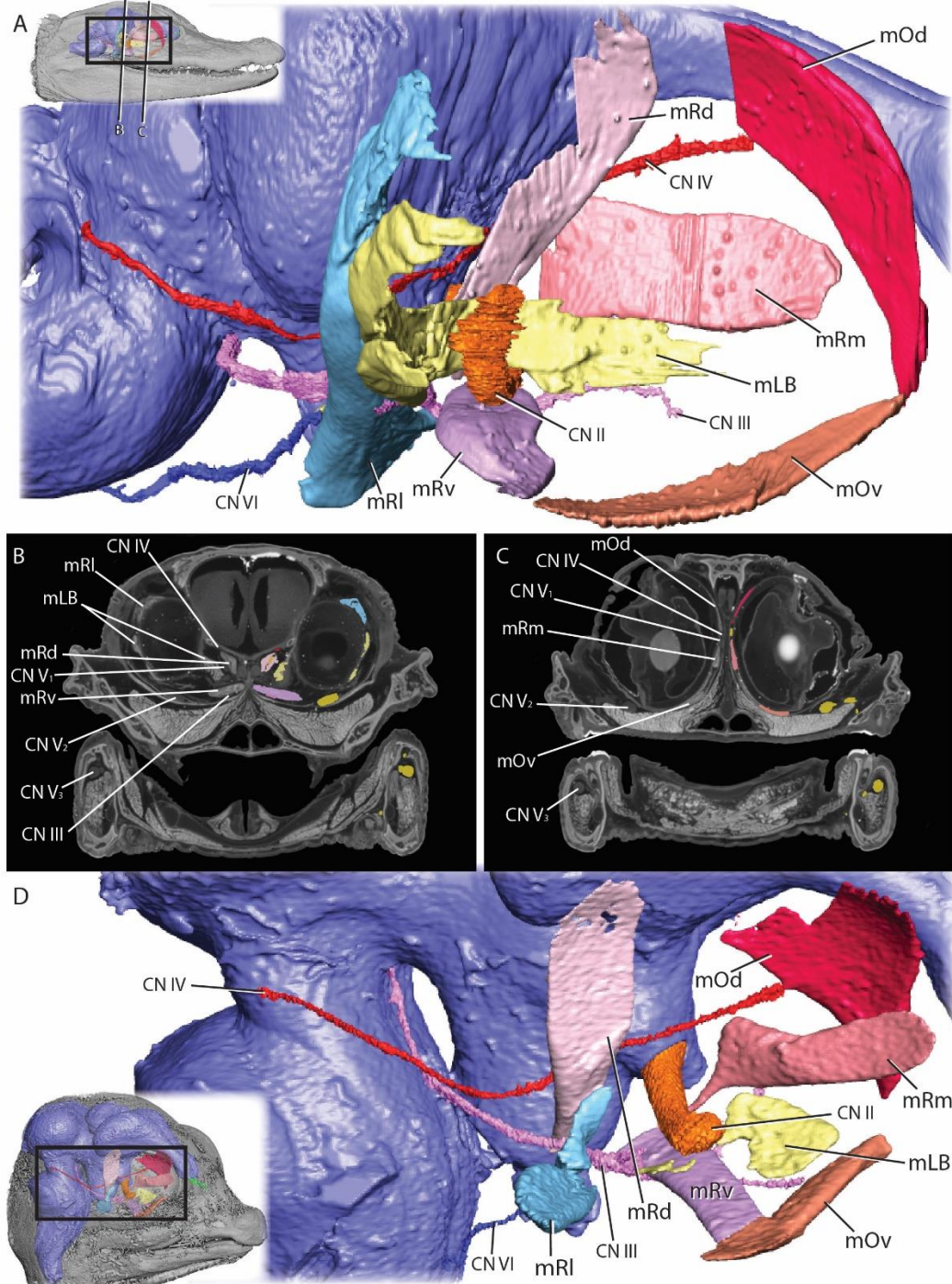


Figure 2.5. Autonomic Nerves. 3D reconstruction of the brain, cranial nerves, autonomic structures, and head of stage 19 embryo MUVc AL089 (mirrored) in right lateral view. A 3D model of figure 5 may be found at: <https://sketchfab.com/3d-models/embryonic-alligator-cranial-nerves-b14a75f97da74cd89e402d118ba38e59>.

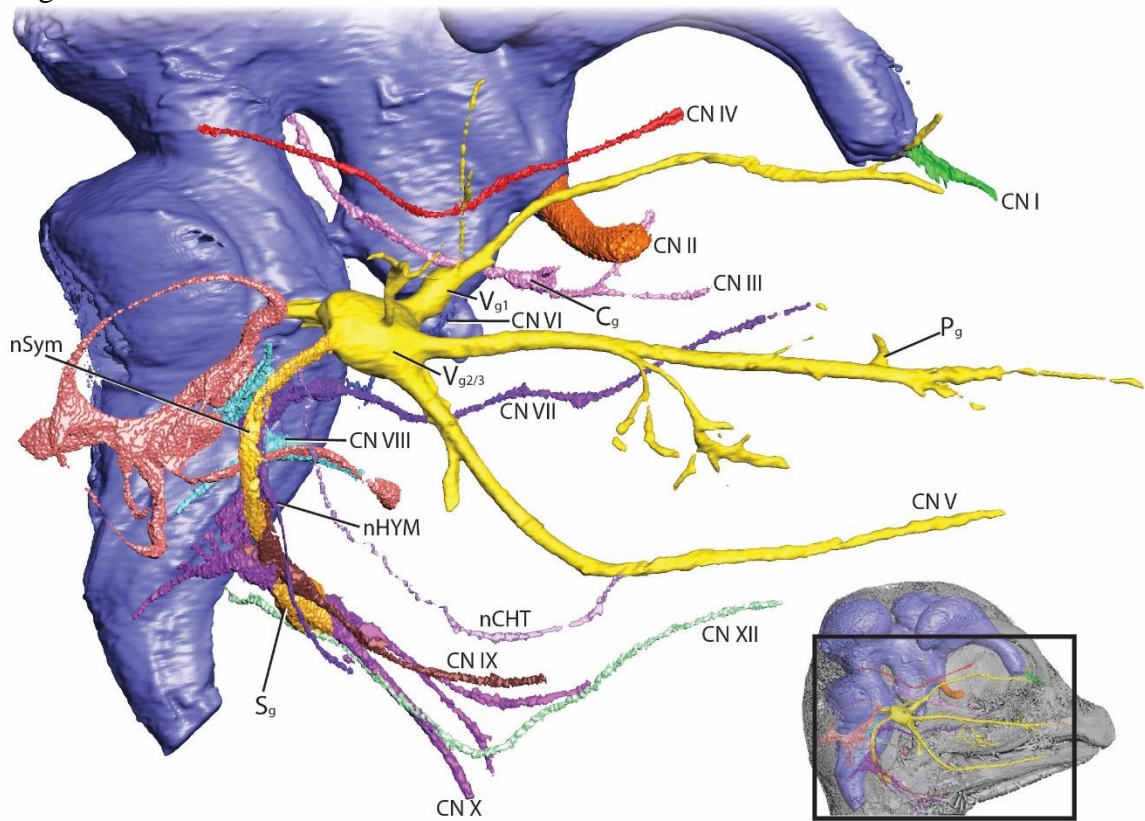


Figure 2.6. Figure 6: Cranial Osteology. 3D reconstruction of alligator (MUVCL623) cranial elements in left lateral (A), left medial (B), bisected caudal (C), and left medial (D) view. Location of D marked in B. A 3D model of figure 6B may be found at: <https://sketchfab.com/3d-models/alligator-skull-and-cranial-nerves-98c9ca48f3a3408f8c64d6c6d4256ae>

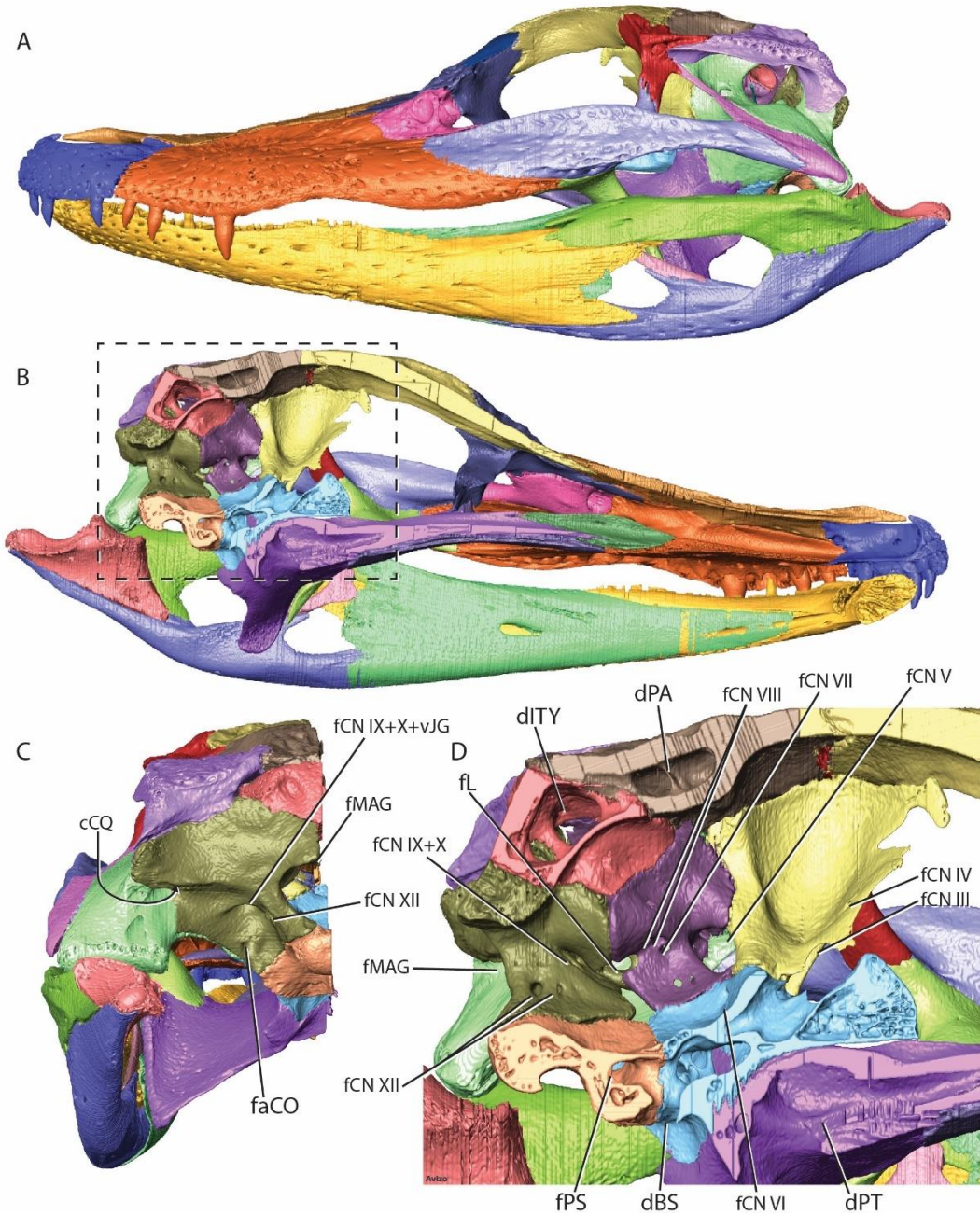


Figure 2.7. Osteological and Nervous Relationships. 3D reconstruction of alligator cranial elements (MUVC AL623), cranial nerves (MUVC AL031), and the brain (MUVC AL031) in left lateral (A) and left medial (B) view. Cranial nerves and brain from MUVC AL031 have been mirrored and transformed to fit the skull of MUVC AL623.

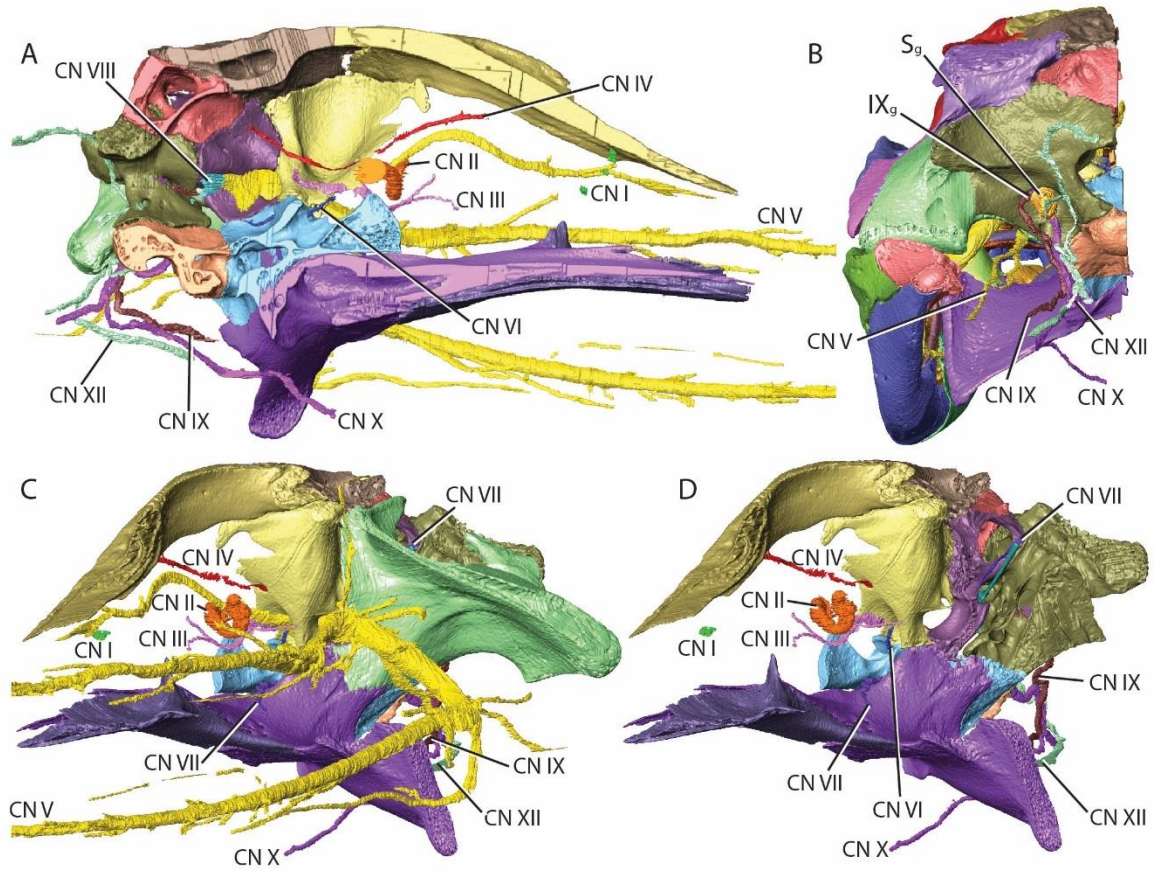


Figure 2.8. Osteological and Nervous Relationships (cont.). 3D reconstruction of alligator cranial elements (MUVc AL623) and nerves (MUVc AL031) in left medial (A), caudal (B), and left rostralateral (C) views and left rostralateral view with CNV and the quadrate removed (D). Cranial nerves from MUVc AL031 have been mirrored and translated to fit the skull of MUVc AL623. A 3D model of figure 8A may be found at: <https://sketchfab.com/3d-models/alligator-skull-and-cranial-nerves-98c9ca48f3a3408f8c64d6c6d4256aee>.

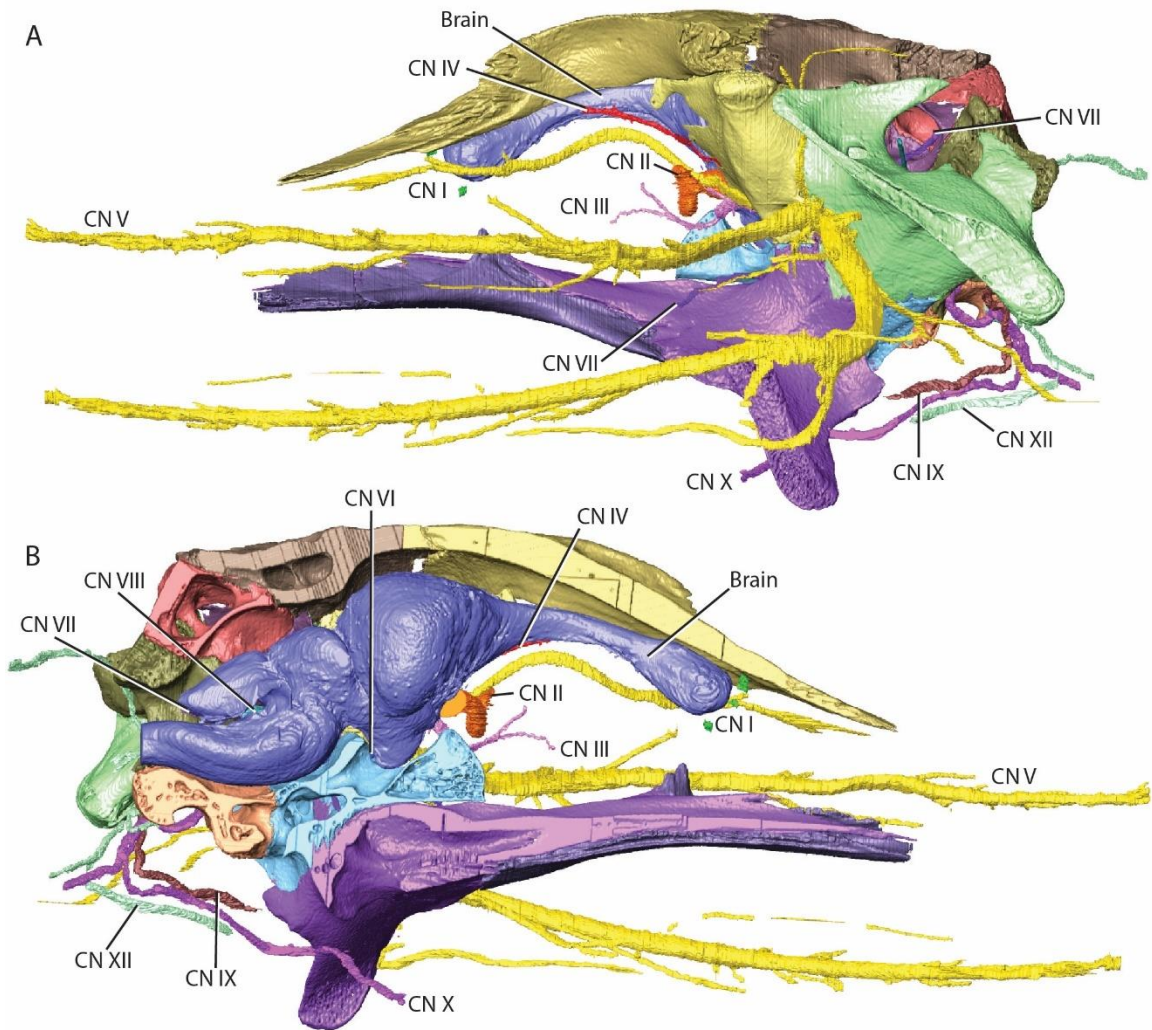


Figure 2.9. Trigeminal Nerve. 3D reconstruction of the brain, cranial nerve V, narial muscles, and head of alligator MUVc AL606 (A), yearling alligator MUVc AL031 (B), and stage 19 embryo MUVc AL089 (C, mirrored) in right lateral view

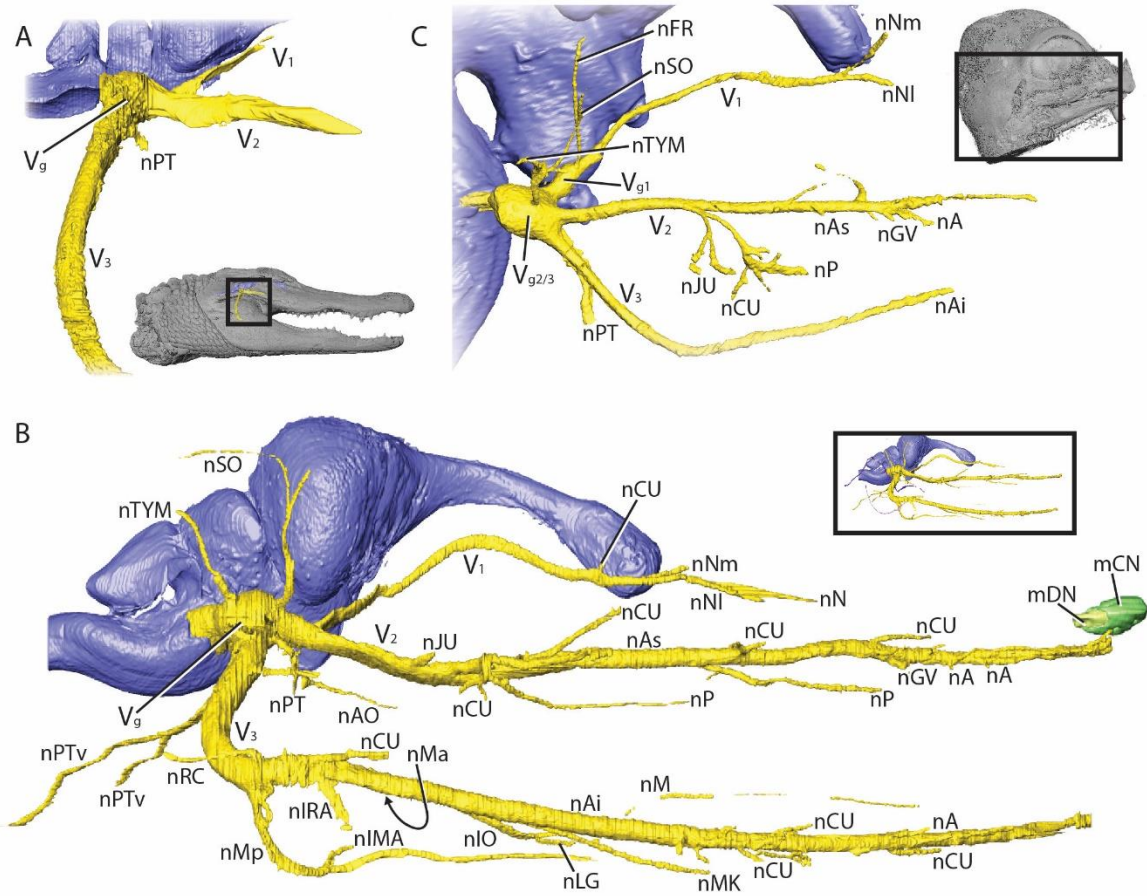


Figure 2.10. Trigeminal Nerve-Innervated Muscles. 3D reconstruction of cranial nerve V, the trigeminal nerve-innervated muscles, and head of yearling alligator MUVc AL031 (A) and stage 19 embryo MUVc AL089 (D) in dorsolateral view with muscular branches of MUVc AL031 in left caudolateral (B) and left rostralateral (C) views. (Colors follow Holliday et al., 2013). A 3D model of figure 10A may be found at: <https://sketchfab.com/3d-models/yearling-alligator-cn-v-innervated-muscles-538568dea57041628e8a5b564b30b2eb> and a 3D model of figure 10D may be found at: <https://sketchfab.com/3d-models/embryonic-alligator-cn-v-innervated-muscles-3a7d93f76545415da07e60d46d03c346>.

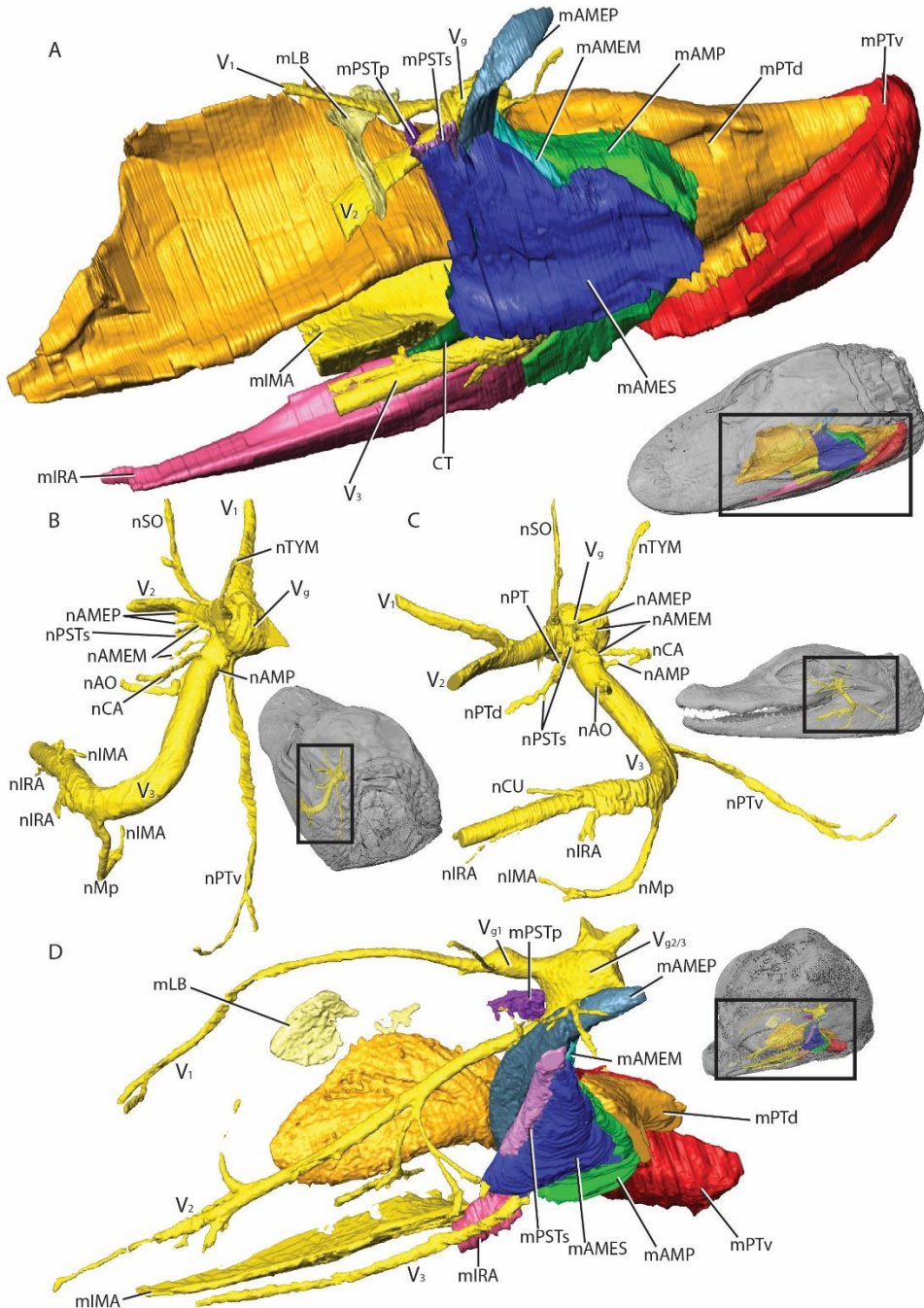


Fig. 2.11. Facial, Vestibulocochlear, Glossopharyngeal, Vagus, and Hypoglossal Nerves. 3D reconstruction of the brain, cranial nerves VII to XII (excluding XI), inner and middle ear (transparent), and head of alligator MUVC AL606 (A), yearling alligator MUVC AL031 (B), and stage 19 embryo MUVC AL089 (C, mirrored) in right caudolateral (A,B) and ventrolateral (C) view.

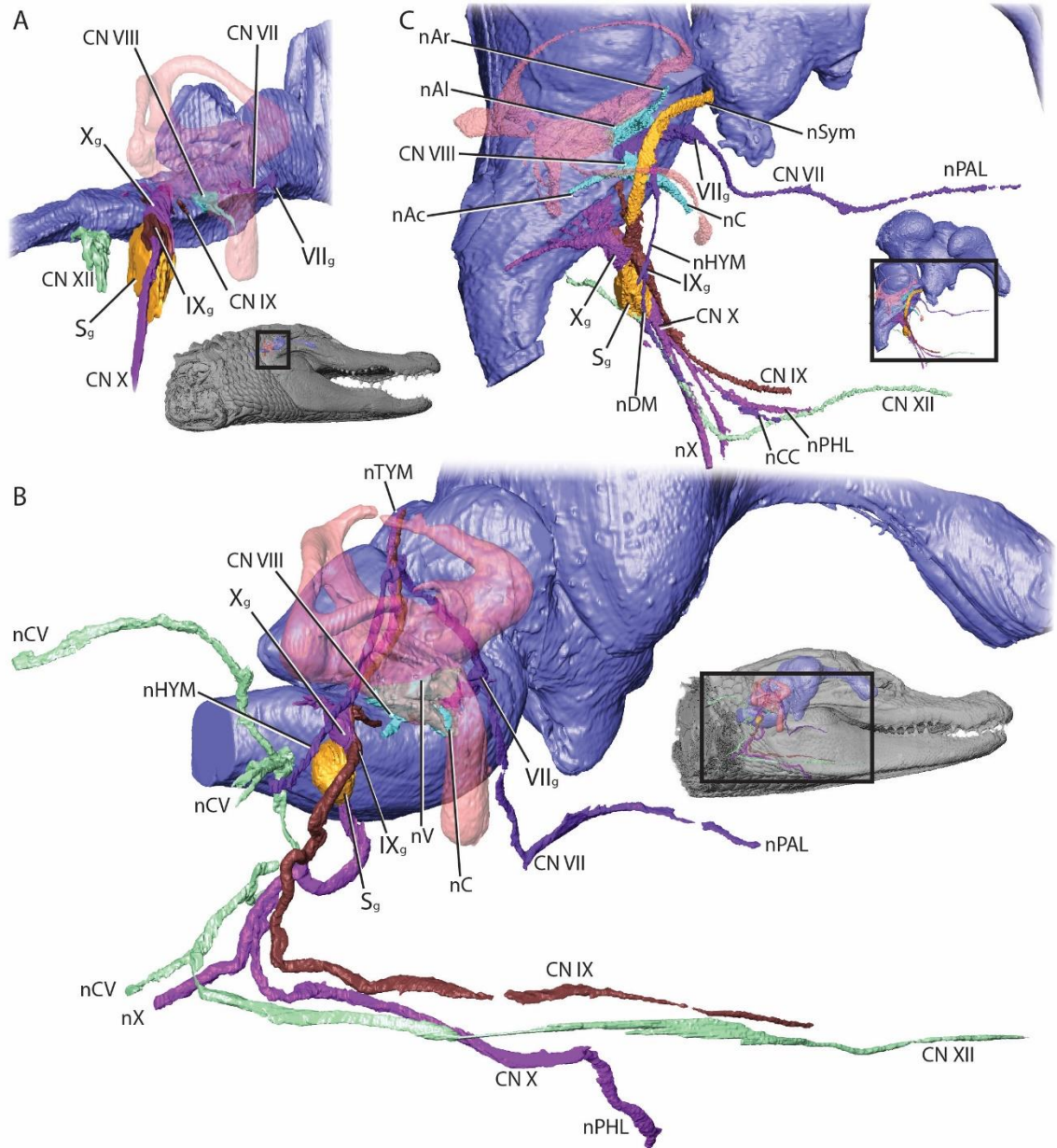


Fig. 2.12. Facial Nerve-Innervated Muscles. 3D reconstruction of the brain, cranial nerve VII, the facial nerve-innervated muscles, and head of yearling alligator MUVC AL031 (A) and stage 19 embryo MUVC AL031 (E) in right lateral (A) and right dorsolateral views (B) with axial CT slices of MUVC AL031 (B-D). A 3D model of figure 12A may be found at: <https://sketchfab.com/3d-models/yearling-alligator-cn-vii-innervated-muscles-c2d269b76ef9402480ab296feda0f675> and a 3D model of figure 12E may be found at: <https://sketchfab.com/3d-models/embryonic-alligator-cn-vii-innervated-muscles-278d5ba701ff43aa898915e52ae049c7>.

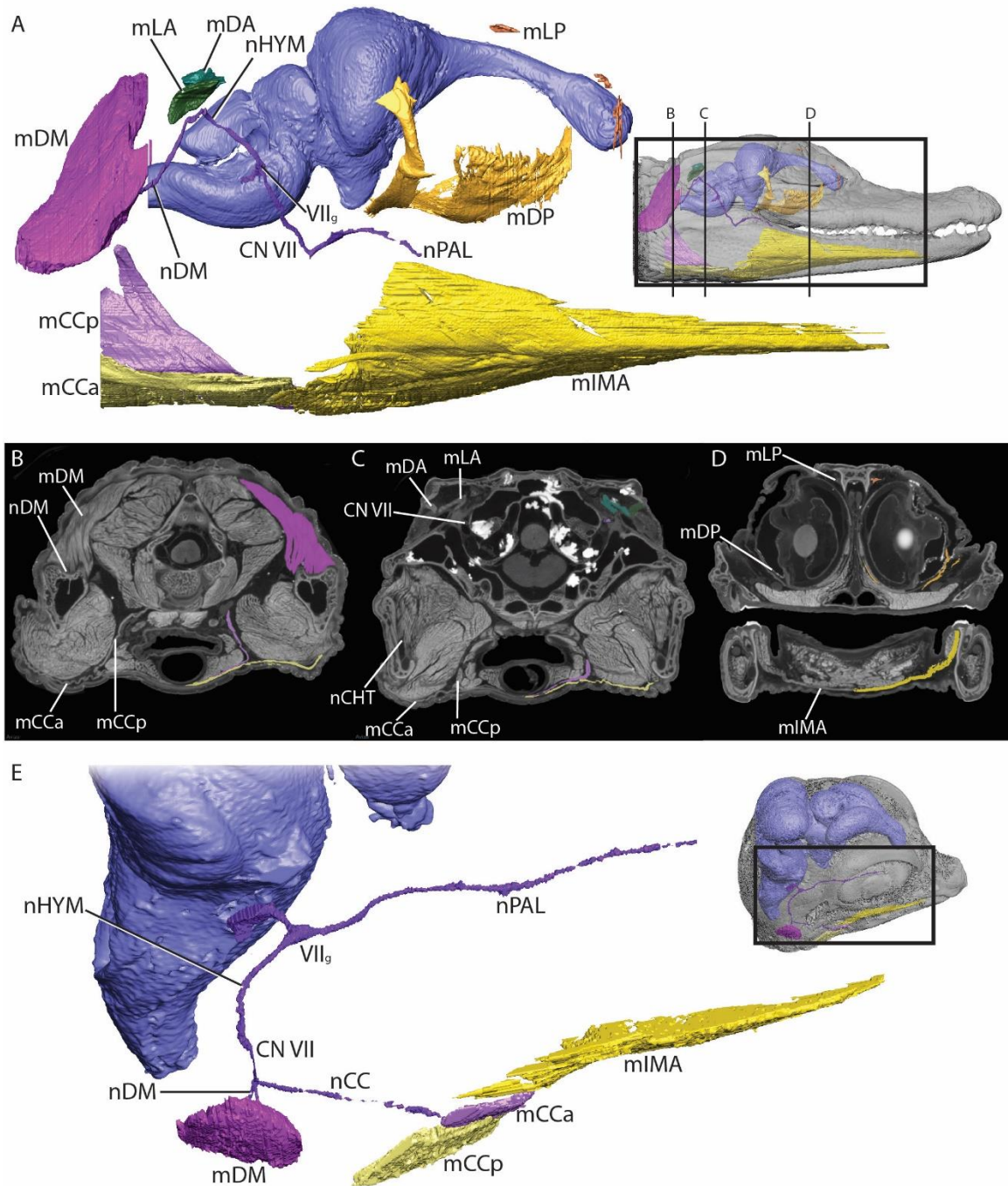


Fig. 2.13. Chorda Tympani. 3D reconstruction of the brain, cranial nerves V and VII, potential path of the chorda tympani branch of CN VII, and head of yearling alligator MUVc AL031 (A) and embryo MUVc AL089 (B, mirrored) in right lateral (A) and right rostralateral (B) views. Developing quadrate is included in green for the embryonic alligator (B).

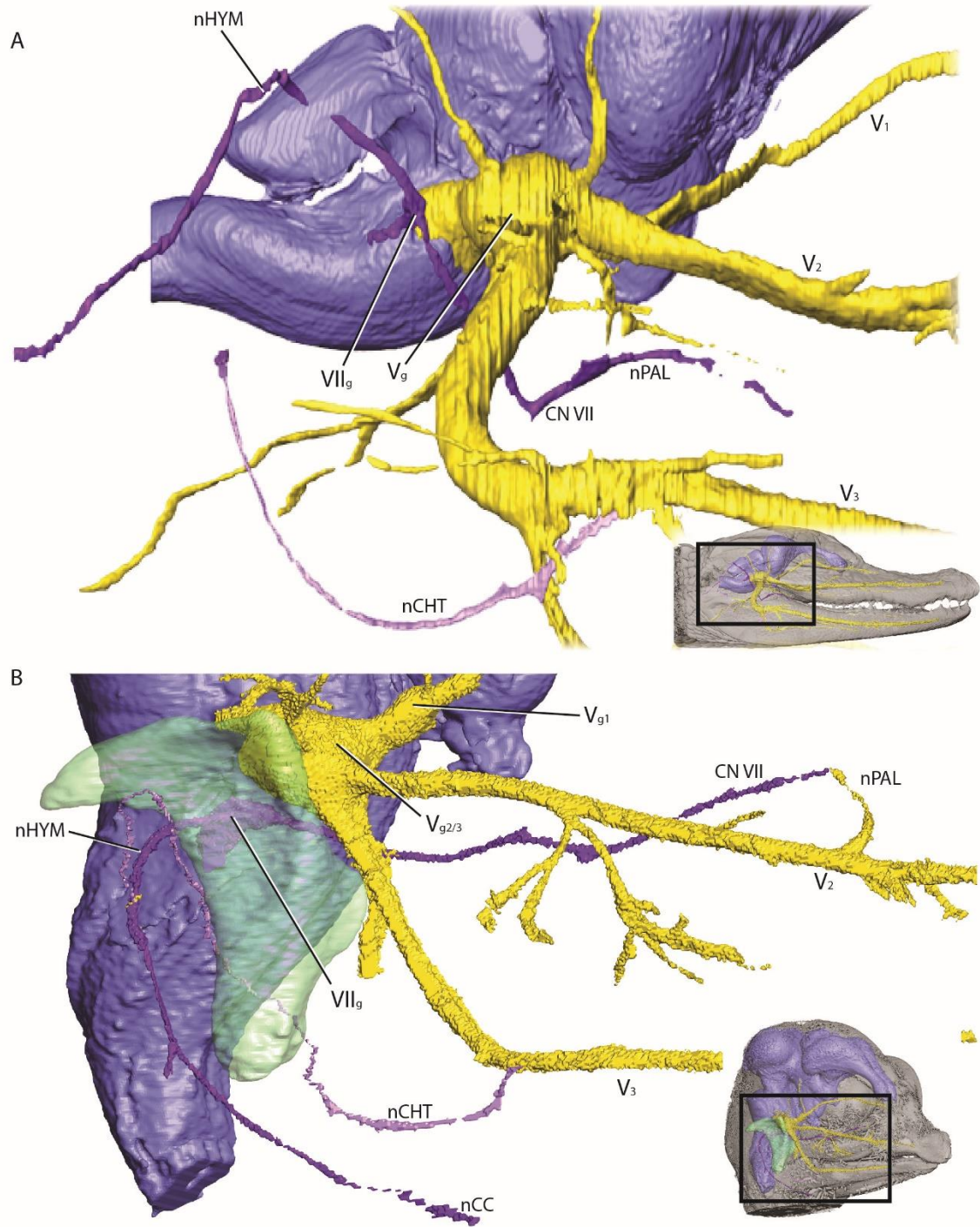


Fig. 2.14. Glossopharyngeal Nerve-Innervated Muscles. 3D reconstruction of the brain, head, cranial nerve IX, and glossopharyngeal nerve-innervated muscles of yearling alligator MUV C AL031 (A) and stage 19 embryo MUV C AL089 (C, mirrored) in right lateral view with an axial CT slice (B). (Colors follow Li and Clarke, 2015). A 3D model of figure 14A may be found at: <https://sketchfab.com/3d-models/yearling-alligator-cn-ix-innervated-muscles-fd0d25c386494e719ca17cc742e76443> and a 3D model of figure 14C may be found at: <https://sketchfab.com/3d-models/embryonic-alligator-cn-ix-innervated-muscles-61720901bf684060aa0c1fba74475f5e>.

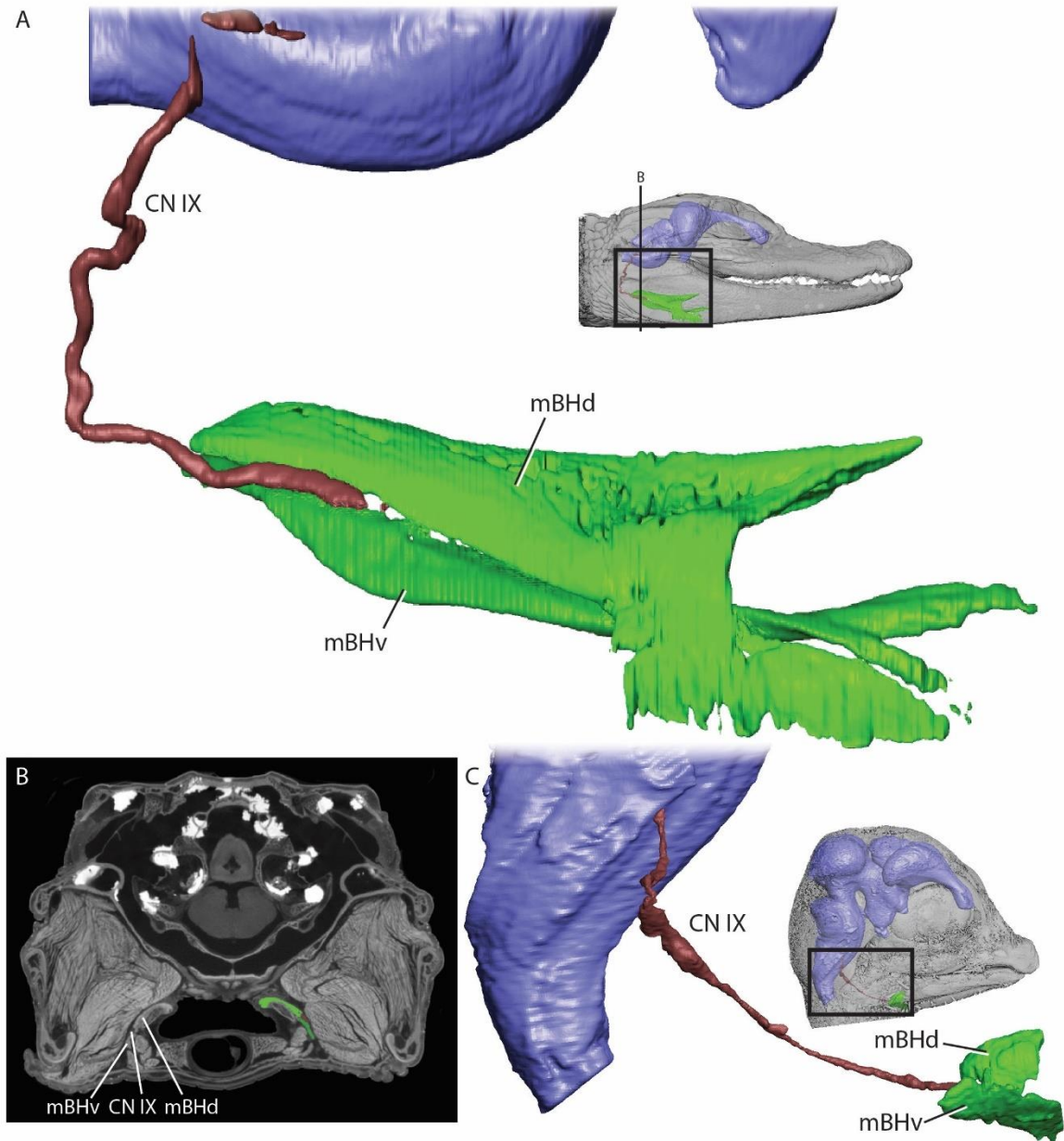


Fig. 2.15. Vagus Nerve-Innervated Muscles. 3D reconstruction of the brain, head, cranial nerve X, and vagus nerve-innervated muscles of yearling alligator MUVC AL031 (A) in right lateral view with an axial CT slice (B). (Colors follow Riede et al., 2015). A 3D model of figure 15A may be found at: <https://sketchfab.com/3d-models/yearling-alligator-cn-x-innervated-muscles-c05d83b85d6247c1a97f360f144c5c37>.

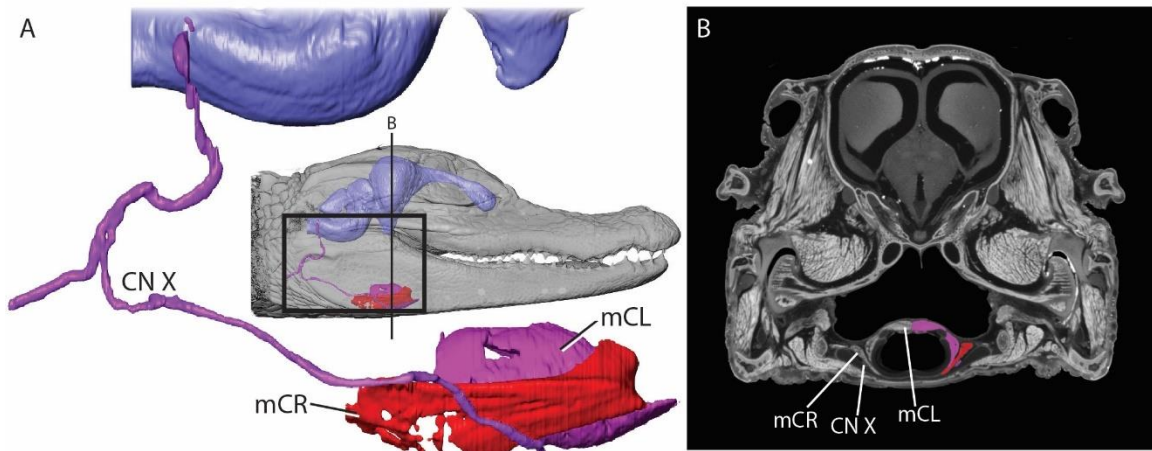


Fig. 2.16. Hypoglossal Nerve-Innervated Muscles. 3D reconstruction of the brain, head, cranial nerve XII, and the hypoglossal-innervated muscles of yearling alligator MUV C AL031 in right dorsolateral view (A) and stage 19 embryo MUV C AL089 in right ventrolateral view (D, mirrored) with axial CT slices of MUV C AL031 (B,D). (Colors follow Li and Clarke, 2015). A 3D model of figure 16A may be found at: <https://sketchfab.com/3d-models/yearling-alligator-cn-xii-innervated-muscles-f116e8e8222d4607a998107d06e45f50> and a 3D model of figure 16D may be found at: <https://sketchfab.com/3d-models/embryonic-alligator-cn-xii-innervated-muscles-764fd8ced1e545668930938b39dd9de5>.

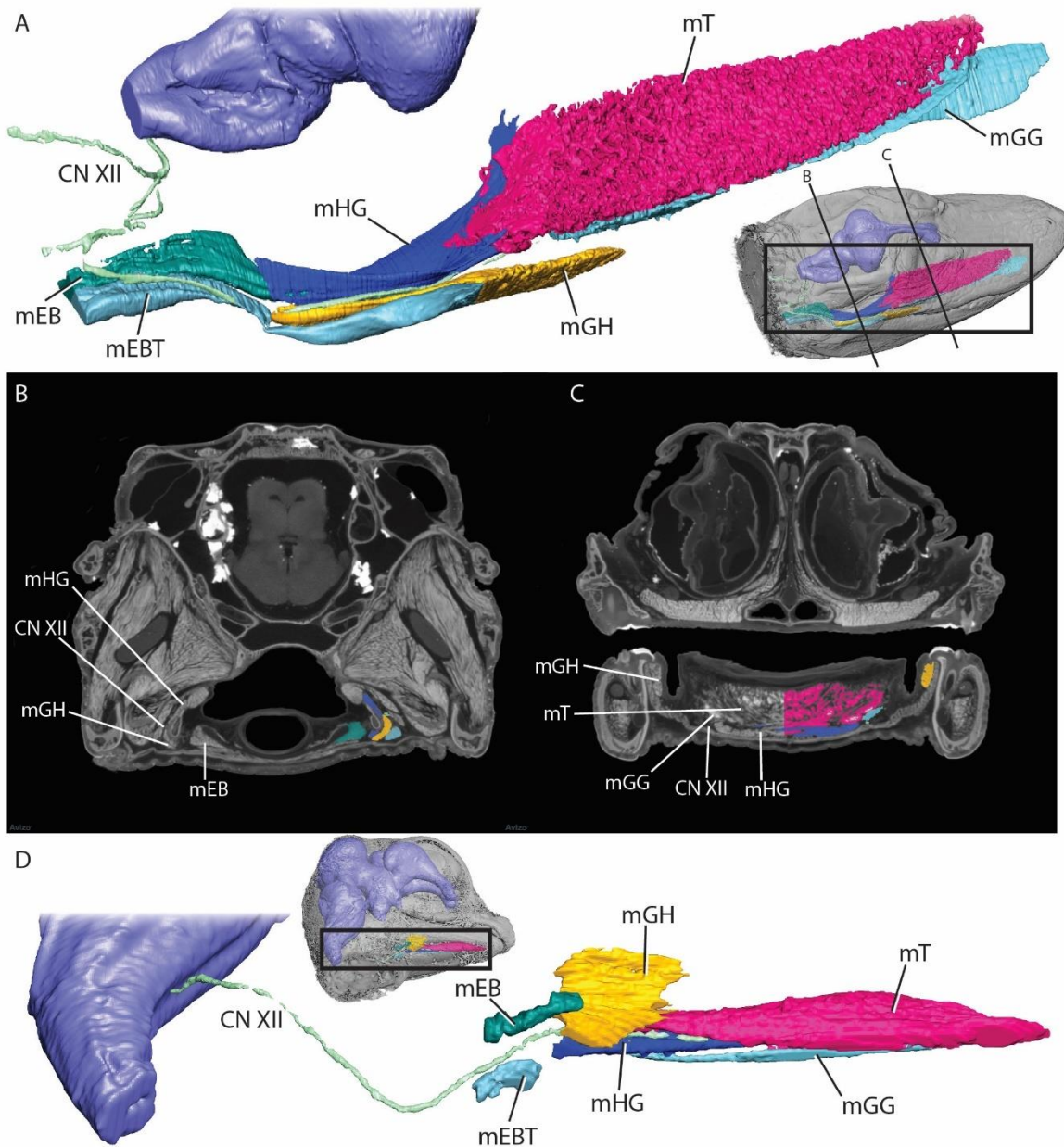


Fig. 2.17. All segmented structures of yearling alligator MUVC AL031. A 3D model of figure S1 may be found at: <https://sketchfab.com/3d-models/yearling-alligator-cranial-nerves-and-muscles-6563d92576ab475ca31f2752ea710248>.

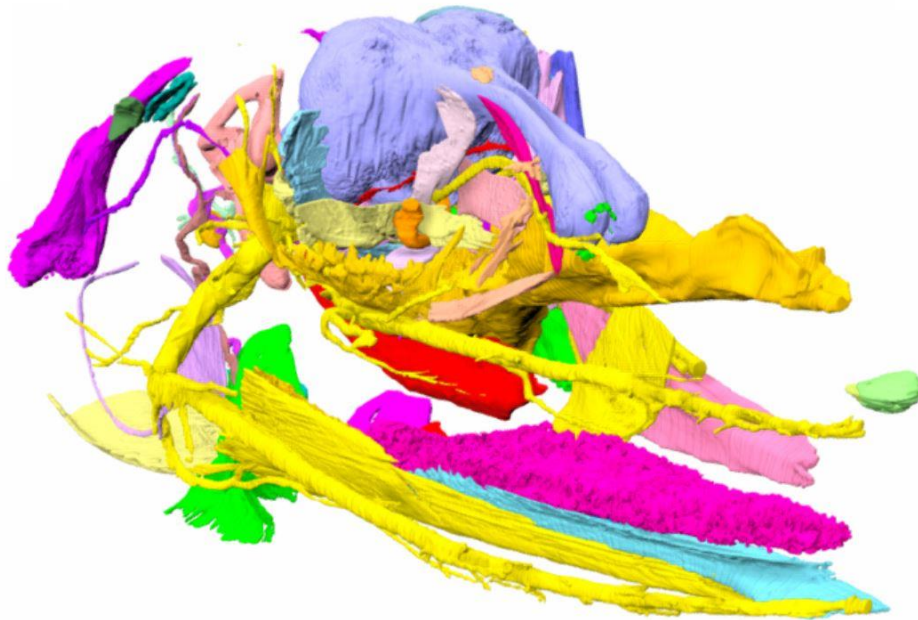


Fig. 2.18. All cranial nerves and brain of yearling alligator MUVc AL031. A 3D model of figure S2 may be found at: <https://sketchfab.com/3d-models/yearling-alligator-cranial-nerves-51dbdca420454effb324a88753b047f9>

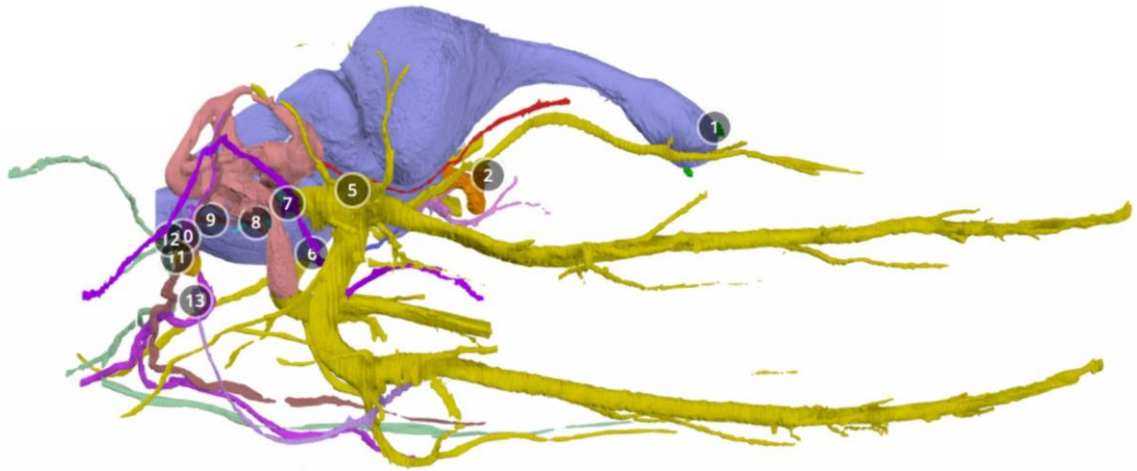


Fig. 2.19. All segmented structures of stage 19 embryo MUVc AL089. A 3D model of figure S3 may be found at: <https://sketchfab.com/3d-models/embryonic-alligator-cranial-nerves-and-muscles-3c844a3b122044c6b533ac2de8a5fb7b>.

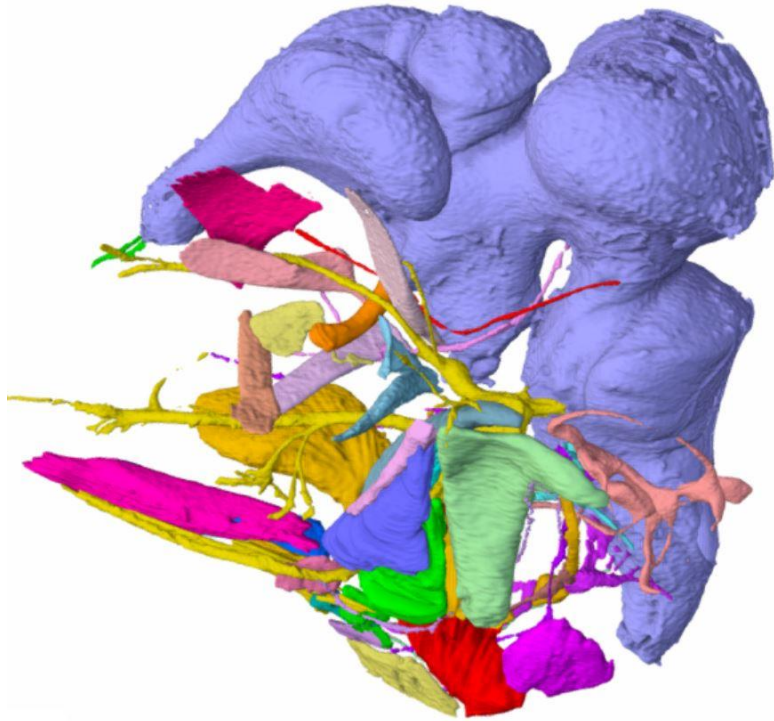

























Fig. 2.20. Color guide to segmented structures.







































NERVOUS

 Brain	 CN III	 CN VI	 CN VIII	
 CN I	 CN IV	 CN VII	 CN IX	 CN XII
 CN II	 CN V	 potential CN VII	 CN X	 Sympathetics

SKELETAL

 Angular	 Ectopterygoid	 Maxilla	 Prearticular	 Quadratojugal
 Articular	 Exoccipital	 Nasal	 Prefrontal	 Splenial
 Basisoccipital	 Frontal	 Palatine	 Premaxilla	 Squamosal
 Basisphenoid	 Jugal	 Palpebral	 Prootic	 Stapes
 Coronoid	 Lacrimal	 Parietal	 Pterygoid	 Supraoccipital
 Dentary	 Laterosphenoid	 Postorbital	 Quadrate	 Vomer

MUSCULAR

 Superior rectus	 Adductor mandibulae externus superficialis	 Depressor mandibulae	 Cricoarytenoid
 Inferior rectus	 Adductor mandibulae externus profundus	 Levator auriculae	 Laryngeal constrictors
 Medial rectus	 Adductor mandibulae externus medialis	 Depressor auriculae	
 Inferior oblique	 Adductor mandibulae posterior	 Levator palpebrae	 Geniohyoideus
	 Pseudotemporalis superficialis	 Depressor palpebrae	 Hyoglossus
 Superior oblique	 Pseudotemporalis profundus	 Intermandibularis	 Genioglossus
	 Pterygoideus dorsalis	 Constrictor colli profundus	 Tongue
 Levator bulbi	 Pterygoideus ventralis	 Constrictor colli pars anterior	 Episternobranchio-tendineus
 Intramandibularis		 Branchiohyoideus dorsalis	 Episternobranchialis
 Constrictor naris	 Lateral rectus	 Branchiohyoideus ventralis	
 Dilator naris			
OTHER			
 Middle/inner ear	 Cartilago transiliens		

Chapter 3 — Ontogeny of the trigeminal system and associated structures in *Alligator mississippiensis*

INTRODUCTION

Trigeminal system in crocodylians

In vertebrates, the trigeminal nerve is the primary somatosensory nerve of the head and courses a largely conserved pathway from its origin in the hindbrain to nerve endings across the face. It also provides innervation to the extensive jaw musculature. Trigeminal system formation initiates early during development by 4 days of incubation in *Alligator* (Ferguson 1987). The trigeminal system forms from a combination of ectodermal placode and neural crest derived cells. The neural crest contributes peripheral glia and proximal sensory neurons to the two trigeminal ganglia whereas the profundal and trigeminal placodes contribute solely sensory neurons (D'Amico-Martel and Noden 1983, Barlow 2002, Park and Saint-Jeannet 2010, Steventon et al. 2014). Fusion of the ganglia occurs proximally in most vertebrate taxa during development leaving two lobes distally (Xu et al. 2008). The sensory neural crest and placode cells extend processes peripherally to terminate in sensory receptors and centrally to communicate with brain nuclei. The peripheral rami map to target tissues guided by multiple factors including chemoattractants from the first arch epithelium, inhibitory regions, and interactions with other rami (Scott 1992, Vogel 1992).

Myelination is an important developmental process that influences nerve morphology and physiology. During myelination, Schwann cells surround axons with concentric lipid-protein layers that both increase nerve size and conduction velocity (Kandel et al. 2000). Myelination of the peripheral nervous system starts embryonically in reptiles (Dulac et al. 1988, Santos et al. 2005). George and Holliday (2013) noticed a

decrease in axon density as alligators grew and attributed this to the increasing diameter of the myelin sheath in younger animals.

In *Alligator* the trigeminal nerve courses from the hindbrain (rhombencephalon), forms the trigeminal (semilunar) ganglion, and extends rostrally where it splits into three divisions. The structure typically referred to as the 'trigeminal ganglion' comprises two ganglia. The profundal ganglion holds the cell bodies of the ophthalmic division of the trigeminal nerve and the gasserian ganglion holds the cell bodies of the maxillomandibular divisions of the trigeminal nerve. These ganglia are typically fused into a single semilunar ganglion in adults. The ophthalmic and maxillary divisions of the trigeminal nerve transmit sensory signals from the upper jaw, whereas the mandibular division transmits both motor and sensory signals to and from the lower jaw.

The adult arrangement of the ganglia and nerve divisions is a result of organization during embryonic development. As the chondrocranium develops, the orbital cartilage (sphenolateral plate) comprises a number of cartilaginous processes. At the caudal extent of the orbital cartilage there is a vertically oriented process, the pila antotica, that ultimately ossifies to form the laterosphenoid and fuses to the basal plate (Bellairs and Kamal 1981, DeBeer 1937). In pseudosuchians the ossified pila antotica contributes to the rostral border of the trigeminal fossa, which houses the maxillomandibular ganglion, and sometimes separates the ophthalmic and maxillary divisions of the trigeminal nerve (Bellairs and Kamal 1981, DeBeer 1937, Holliday and Witmer 2009, Jollie 1960). Thus, in hatched crocodylians, the maxillomandibular ganglion is housed extracranially in a bony cavity alongside the braincase, the trigeminal fossa, formed by the quadrate, prootic, laterosphenoid, and pterygoid (Hopson 1979,

Witmer et al. 2008). Therefore, in crocodylians, a trigeminal foramen allows transmission of the trigeminal nerve into the trigeminal fossa and the three divisions pass through bony foramina in their exit from the trigeminal fossa. The crocodylian ophthalmic division exits the ganglion rostrally via a foramen in the laterosphenoid, whereas the crocodylian maxillary and mandibular divisions exit the trigeminal ganglion laterally through the maxillomandibular foramen, bounded by the laterosphenoid and prootic (Holliday and Witmer 2009; Jollie 1962).

From their exits, these divisions follow homologous pathways, occasionally excavate depressions in adjacent bone, and with vasculature, pass through musculature to extend through bony canals in the rostrum. The intermuscular pathways of trigeminal nerve divisions have been demonstrated to consistently divide muscles into homologous groups (Edgeworth 1935, Haas 1973, Holliday and Witmer 2007, Iordansky 2000, Lakjer 1926, Lubosch 1933, Säve-Söderbergh 1945, Zusi and Livezey 2000). The ophthalmic division passes into the orbit and innervates structures of the face and the maxillary division communicates with teeth and somatosensory receptors in the integument after passing through foramina perforating the mandibles. In addition to transmitting sensory signals from the mandibles, the mandibular division transmits motor signals to the musculature of the lower jaw. Muscular branches originate proximally from the mandibular division and include those to the divisions of the adductor, pterygoideus, and intermandibularis musculature (Holliday and Witmer 2007, Lakjer 1926, Poglayen-Neuwall 1953, Schumacher 1973). Proximal sensory branches from the mandibular division include the anguli oris nerve to the corner of the mouth and the recurrent cutaneous nerve to the skin over the adductor mandibularis externus (Poglayen-Neuwall

1953). Further distally, the mandibular extends the large caudal intermandibular or external cutaneous branch medially through the angular, which sends numerous cutaneous rami to the skin of the ventrolateral mandible and (Poglayen-Neuwall 1953). As the mandibular nerve enters the mandibles, medial and oral intermandibular branches extend to innervate epithelium of the mouth, dental lamina, and integument and the inferior alveolar nerve enters the dentary (Poglayen-Neuwall 1953). Numerous lingual, mucosal, and dental branches extend from the intermandibular and inferior alveolar nerves to their terminations in the oral cavity, and foramina in the dentary transmit cutaneous branches to their terminations in the integument of the rostral mandibles.

Sensory receptors are present at the afferent terminations of the trigeminal nerve. Extant crocodylians are known for having highly sensitive snouts covered with integumentary sensory organs (ISOs). In *Alligator mississippiensis*, this sensory system is specialized for a semi-aquatic lifestyle, with the ability to sense minute changes in water pressure, temperature, and pH (Di-Poï and Milinkovitch 2013). Furthermore, somatosensory distribution differs across taxa in crocodylians (Leitch and Catania 2012).

Here I provide a four-dimensional anatomical model of the trigeminal system in *Alligator* including the ganglia and nerves, the cartilaginous-skeletal braincase wall, and the musculature. In addition to providing gross anatomical description and growth rates of trigeminal-associated structures, I expected and therefore explored developmental covariation between structures. The trigeminal nerve targets the associated musculature and integument across the rostrum, thus isometric relationships were expected between trigeminal nerve dimensions and target structure dimensions. The motor and sensory nuclei of the trigeminal nerve are located within the pons and thus an isometric

relationship between trigeminal nerve dimensions and pontine dimensions were expected as well. Additionally, the trigeminal nerve and associated neurovasculature leave osteological correlates in the form of foramina, depressions, grooves, and canals which can be traced along this pathway through the skull. An in depth understanding of the development of these tissues, pathways, and their osteological correlates allow for better predictions of soft tissues in fossil organisms.

MATERIALS AND METHODS

Specimens and imaging

This project features several *Alligator mississippiensis* specimens from Rockefeller State Refuge, Grand Chenier, Louisiana (Table 3.1). The removed heads of MUV C AL606, MUV C AL096, MUV C AL095, and MUV C AL031 and the entire embryo of MUV C AL 089-094, Henry 1, and Henry 2 were fixed in 10% neutral buffered formalin, and the FMNH specimens in 70% ethanol. All were immersed in I₂KI (Lugol Solution, Carolina Biological Supply Company, NC). These specimens were all micro-CT scanned at the highest resolution at the University of Missouri MizzoμX facility except for MUV C AL606, which was CT scanned at the University of Texas High-Resolution X-Ray Computed Tomography facility in Austin, TX. Five non-*Alligator* crocodylians were included (Table 3.1) and underwent the same treatment as MUV C AL606 with the exception of *Gavialis* which went unfixed and was injected with I₂KI rather than immersed. Other *Alligator* specimen data were acquired from Fabbri et al. (2017), and Watanabe et al. (2019).

3D reconstruction and data collection

Scan data were imported as DICOM and TIFF files into Avizo v.9 for segmentation. Structures of interest (see Table 1 and Figure 1) were segmented manually

using thresholding and the magic wand and paintbrush tools. Volumes of structures were collected in Avizo using the 'Material Statistics' module, lengths using the 'Measure: 2D length' tool, and areas using the 'Surface Editor'. Nerve division diameters were taken at their departure from the brain or associated ganglia. The diameter of the motor portion of the trigeminal nerve was calculated by subtracting the diameter of the mandibular nerve rostral to the extent of the motor branches (i.e., rostral to the bend in the nerve) from the mandibular nerve at its departure from the maxillomandibular ganglion. Brain regions were defined as follows: 'olfactory' included bulbs and tracts until the rostral arc of the cerebrum; 'cerebrum' included from the olfactory tracts rostrally to the recess before the diencephalon or optic tectum caudally; 'optic tectum' included from the cerebrum-optic tectum/diencephalon recess rostrally to the recess before the cerebellum caudally and its ventral border is a shallow depression before the diencephalon; 'cerebellum' included from the optic tectum-cerebellum recess rostrally to the pontine flexure caudally and its ventral border is a shallow depression before the diencephalon; the 'pons and medulla' included from the pontine flexure and a shallow depression along the diencephalon rostrally to the foramen magnum caudally; the 'diencephalon' included all non-optic tectum, non-cerebellum, and non-pons and medulla brain tissue. Jaw surface area was taken as the lateral integumentary surface receiving trigeminal nerve innervation.

Analyses

Increase in size of structures over time was explored, both embryonically (i.e., *in ovo*) and post-hatching. Size of structures were also compared to body size and one another to determine allometric relationships. Linear modelling and two-tailed T-tests

were used in R to test for isometry. In this case, skull width was used as a proxy for body size, an appropriate method for crocodylians as determined by O'Brien et al. (2019).

RESULTS

Description

Nerve development

Ferguson (1985) reports the cranial nerves to the first branchial arch are visible during stage 4; however, our dataset begins at Ferguson stage 10 (F10).

At stage F10 (Fig. 3.1a) there is clear separation between the two trigeminal ganglia (i.e., maxillomandibular and ophthalmic). All three trigeminal divisions are present in the stage F10 embryo, extending rostrally from the ganglia. The rostralmost extent of the ophthalmic division (V_1) is just posterodorsal to the eye. The mandibular division (V_2) is the longest of the three trigeminal divisions at stage F10, extending just ventral to the eye. The maxillary division (V_3) is short because the first pharyngeal arch is also short but extends to the rostral end of the developing mandible. In lateral view, the angle between the ophthalmic and maxillary divisions is about 50° , and the angle between the maxillary and mandibular division is about 20° .

At stage F13 (Fig. 3.1b) the two trigeminal ganglia are still clearly separated, though there is some proximal fusion. The ophthalmic division is now the longest, extending to the frontonasal process, far rostral to the eye. The maxillary division also extends just rostral to the eye, entering the maxillary process. The mandibular division remains short, extending to the now-present rostral jaw margin. In lateral view, the angle between the ophthalmic and maxillary divisions is still about 50° , but the angle between the maxillary and mandibular division has now increased to about 30° .

At stage F16 (Fig. 3.1c) besides increasing in size, the two trigeminal ganglia are unchanged (i.e., still barely fused proximally). The ophthalmic and maxillary divisions hook rostroventrally with the maxillary process. The mandibular division is now rostrally lengthened, present ventral to the eye. In lateral view, the angle between the ophthalmic and maxillary divisions has now decreased to about 40° , but the angle between the maxillary and mandibular division is still about 30° .

The separation between the two trigeminal ganglia is still present at stage F19 (Fig. 3.1d). The rostral nasal branches of the ophthalmic division are present. The maxillary division extends to the rostralmost tip of the jaw. The mandibular division extends the length of the lower jaw, now just posterior to the upper jaw. At stage F19, the two trigeminal ganglia remain unfused distally. There is now a distinct 120° bend in the mandibular division in lateral view. In lateral view, the angle between the ophthalmic and maxillary divisions has decreased further to about 35° , and the angle between the maxillary and mandibular division has increased to about 50° .

In stage F22 (Fig. 3.1e), the trigeminal ganglia are still distinct, but the ophthalmic ganglion has now moved ventrally and is barely visible in lateral view, being located just dorsal to the mandibular division and rostral to the maxillomandibular ganglion. In lateral view, the angle between the ophthalmic and maxillary divisions has now decreased to 30° , and the angle between the maxillary and mandibular division is still about 50° . The bend in the mandibular division has sharpened, but the angle is still 120° in lateral view.

The position and extent of the trigeminal nerve divisions and ganglia after F24 (Fig. 3.1f), and F25 (Fig. 3.1g) is similar to that of the hatched specimens (yearling, Fig

3.1h and juvenile, Fig 3.1i). The ophthalmic ganglion is no longer visible in lateral view and is now located medial to the maxillary division. It is also slightly fused with the maxillomandibular ganglion. The bend in the mandibular division has decreased to 100° in F24, but has achieved the adult position of 90° by F25. In lateral view, the angle between the ophthalmic and maxillary divisions is consistently about 25°, and the angle between the maxillary and mandibular division is about 85-90°.

Muscle development

At stage F10 there is no evidence of muscular development. By stage F13 (Fig. 3.2a), the m. adductor mandibulae externus (mAME) is present though differentiation between the distinct muscles (i.e., profundus [mAMEP], superficialis [mAMES], and medialis[mAMEM]) is not possible. The m. pterygoideus dorsalis (mPTd) and m. intramandibularis (mIRA) are also present. At stage F16 (Fig. 3.2b) the m. levator bulbi (mLB of the constrictor I dorsalis group), m. intermandibularis (mIMA), and m. adductor mandibulae posterior (mAMP) are present. It is still not possible to distinguish between the m. adductor mandibulae externus muscles. The m. pterygoideus ventralis (mPTv) is just forming. In stage F17 (Fig. 3.3a), there is a well-defined, flat muscle present medial to the maxillary division of the trigeminal nerve, the m. depressor palpebrae inferioris (mDPi). The mDPi originates at from a cartilaginous bar dorsal to the trigeminal ganglion (columella prootica, described below) and attaches to the ventral surface of the eye. By stage F19 (Fig. 3.2c), all muscles are present and distinct. This includes the m. pseudotemporalis profundus (mPSTp) and m. pseudotemporalis superficialis (mPSTs) in addition to those described above. At stage F22 (Fig. 3.2d), the mPTv, mLB, mIRA, and mPTd are present in their adult shape, lengthening in response to the lengthening of the

skull. The mPSTp has also noticeably increase in size. Up to hatching, the musculature remains the same, just changing shape in response to further lengthening of the skull (Fig. 3.2e-f). Between hatching and one year (Fig. 3.2g), the mPSTs and mAMEP muscle fibers appear to switch medio-lateral positions so that the mAMEP is lateral to the mPSTs in the adult form (Fig. 3.2h).

Cartilage and Skeletal Development

In adult *Alligator* the trigeminal fossa is bounded by the quadrate, prootic, laterosphenoid, and pterygoid (Hopson 1979, Witmer et al. 2008), the maxillomandibular divisions passing laterally through a foramen bounded by the laterosphenoid and prootic and the ophthalmic division passing rostrally through a foramen in the laterosphenoid (Holliday and Witmer 2009; Jollie 1962). As such, development of these elements is discussed below. It is possible to trace the development of these structures through embryonic development as the cartilaginous precursors lay the foundation for the adult morphology. Crocodylian chondrification commences around stage F9 (Viera et al. 2018, Goldby 1925, Parker 1883) and shadows of chondrified elements are visible in our data at stages F11, F13, and F15. By stage F16 (Fig. 3.4a) the ventral portion of the developing cartilaginous otic capsule is visible. This is followed by an expansion of the otic capsule and initiation of quadrate and nasal capsule chondrification by stage F17. Only during stage F17, a cartilaginous rod (columella prootica of Klembara [2004], see discussion below) is present, spanning from the trigeminal ganglion between the ophthalmic and maxillary divisions to the anterodorsal otic region (Fig. 3.3a). Before stage F22 the rostral pterygoid process of the quadrate exists as a narrow rod (Fig. 3.3b, 3.4b). In the stage F22 embryo, the process has thickened and become relatively shorter (Fig. 3.4c). In stage F22

there is also a dorsoventrally-oriented cartilaginous process between the ophthalmic and maxillomandibular divisions of the trigeminal nerve as they extend from the trigeminal ganglion (Fig. 3.4c). This outgrowth is the perichondral outgrowth from the antotica pila ventrolateral region noted in Klembara's (2004) stage 10A (equivalent to F27). There is also a small cartilaginous process present between the maxillary and mandibular divisions that is only present in F22 (asterisk in Fig. 3.4c). The outgrowth between the ophthalmic and maxillary divisions begins ossification by stage F24 (Fig. 3.4d) as do the other lateral cartilaginous structures. During stage F24 (Fig. 3.4d) the otic capsule of the exoccipital and the distal end of the quadrate remain cartilaginous, and the precursors of the prootic and laterosphenoid are distinguishable as individual elements. By stage F25 (Fig. 3.4e), ossification is nearly complete for all cranial elements.

Quantification

Skeletal development

Skeletal development occurs rapidly *in ovo* and slows post-hatching. Skull width initially occurs at a rate of 0.33 mm/day and slows to 0.033 mm/day. Skull length rates are similar, decreasing from a rate of 0.61 mm/day to 0.050 mm/day. Skull length grows isometrically to body size both pre- and post-hatching (Table 3.2).

Central nervous system development (Figs. 3.1,3.5)

Until hatching, spinal cord width and height are within 0.67 mm in all specimens. Post-hatching, the spinal cord widens more rapidly than it increases in height. Spinal cord width and height grow rapidly *in ovo* and slow post-hatching (0.042 mm/day to 0.001 mm/day; 0.023 mm/day to 0.0004 mm/day, respectively). The spinal cord grows with negative allometry to body size both pre- and post-hatching. Total brain volume follows

the same trend (9.515 mm³/day to 4.032 mm³/day), as does olfactory bulb volume (0.447 mm³/day to 0.287 mm³/day), cerebrum volume (4.037 mm³/day to 2.123 mm³/day), cerebellum volume (0.423 mm³/day to 0.185 mm³/day), diencephalon volume (0.756 mm³/day to 0.273 mm³/day), optic tectum volume (1.587 mm³/day to 0.305 mm³/day), and pontine-medulla volume (2.333 mm³/day to 0.858 mm³/day). All brain sections grow with negative allometry to body size as well (except for the olfactory bulbs and cerebrum pre-hatching, which grow isometrically; Table 3.2) and nearly isometrically to total brain volume (Fig. 3.1).

Nerve development (Figs. 3.1,3.6)

The mandibular division consistently has the largest volume followed by the maxillary and ophthalmic divisions, respectively. Volume of the ophthalmic nerve division increases *in ovo* at a rate of 0.015 mm³/day. The maxillary and mandibular division volumes increase at higher rates during this period of development ($V_2=0.077$ mm³/day; $V_3=0.117$ mm³/day, Fig. 3.1). A similar trend is present when exploring nerve division diameter ($V_1= 0.006$ mm/day; $V_2=0.016$ mm/day; $V_3=0.020$ mm/day). When hatched, volume of the nerve division increases steadily at a higher rate than *in ovo*, increasing across all divisions ($V_1= 0.060$ mm³/day; $V_2= 0.40$ mm³/day; $V_3= 0.83$ mm³/day). Post-hatching, diameter increases at a lower rate than *in ovo*, but also increasing across all divisions ($V_1= 0.0005$ mm³/day; $V_2= 0.0008$ mm³/day; $V_3= 0.0009$ mm³/day). The ophthalmic division volume grows isometrically to body size pre-hatching, but pre-hatching diameter and both pre- and post-hatching volume grow with a negative allometric relationship to body size. The maxillary division grows isometrically to body size pre-hatching whereas post-hatching, it grows with a positive allometric

relationship to body size. The mandibular division diameter grows isometrically to body size pre-hatching and the pre-hatching volume positively allometric to body size, but post-hatching, both volume and diameter have a negative allometric relationship with body size (Table 3.2).

The maxillomandibular ganglion consistently has a larger volume than the ophthalmic ganglion. Volume of the maxillomandibular ganglion increases rapidly, and steadily during *in ovo* development (0.090 mm³/day) and continues at the same rate post-hatching (Fig. 3.1). The ophthalmic ganglion follows a similar trend (0.009 mm³/day, 0.004 mm³/day respectively), however, it becomes impossible to distinguish the ophthalmic ganglion from the maxillomandibular ganglion in adult specimens. Both ganglia grow with a negatively allometric relationship to body size.

The ganglia volumes and nerve heights increase in concert with the lengthening jaw. The relationship between these variables and skull width is stronger than the relationship between these variables and skull length both as a whole and embryonically and post-hatching individually.

Muscle development (Figs. 3.2,3.7)

As with the above structures, muscular development is slow *in ovo* and increases post-hatching. Overall muscle volume increases at a rate of 5.140 mm³/day pre-hatching, and 118.97 mm³/day post-hatching, growing at a positively allometric relationship to body size post-hatching. Individual muscles range from rates of 0.087 to 1.940 mm³/day *in ovo* but this range increases as the rate increases post-hatching to 0.183 to 90.91 mm³/day (Table 3.2, Fig. 3.9). Pre-hatching, all muscles grow with a negatively allometric relationship to body size except for pterygoideus ventralis, intramandibularis,

and intermandibularis, which grow isometrically. Post-hatching all muscles grow isometrically except adductor mandibulae externus medialis, pterygoideus ventralis, and intramandibularis, which grow with a positively allometric relationship to body size and levator bulbi, which grows with a negatively allometric relationship to body size.

Cross-system allometric relationships

Additional potentially informative allometric relationships were explored (Table 3.3). Muscle volume was found to increase faster than diameter of the mandibular nerve, maxillomandibular ganglion volume, and skull length. Both maxillomandibular ganglion volume and diameter of the mandibular nerve increased slower than skull length, but only mandibular nerve diameter increased slower than surface area of the mandible. The maxillary and mandibular nerve diameters together increased faster than the volume of the maxillomandibular ganglion. Additively, the trigeminal-innervated muscle volume and surface area of the mandible increased faster than the individual maxillomandibular ganglion volume and mandibular division diameter. The maxillomandibular ganglion volume increased faster than both the total brain volume and the pontine-medulla volume, which increase in size isometrically when compared.

DISCUSSION

General anatomical observations

The nervous anatomy largely reflects the changing anatomy of the head (i.e., lengthening and flattening). There is a general trend of a decreasing angle between the ophthalmic and maxillary divisions and an increasing angle between the maxillary and mandibular divisions (Fig. 3.1). The overall angle between the ophthalmic and mandibular divisions increases as well. The shapes and orientations of the musculature similarly reflect the changing cranial orientation (Fig. 3.2). Interestingly, a transition

from a tall, narrow skull to a broad and flat skull occurs during along the evolutionary lineage to extant crocodylians in concert with reorientation of the trigeminal-innervated jaw musculature (Sellers 2021). The developmental reorientation of the skull is most drastic between stage F22 and F24 implying this time period will be important for future investigation of ontogenetic shifts resulting in the evolution of a flat skull. I note that mPSTs is quite distinct from mPSTp from appearance in stage F19. Development of specific cartilaginous and skeletal structures are discussed below.

Cranial integumentary sensory organs become visible at F23 (e41-45) in *Alligator* (Ferguson 1987). These begin developing in *C. niloticus* at e38 and complete by e55 (Di-Poï and Milinkovitch 2013) and display the same relative timing in caimans, appearing at e27 in *Caiman latirostris* (Iungman et al. et al. 2008). However, the developmental timing of the sensory cells that are part of these structures is unknown. The sensory cells comprising these structures (i.e., Merkel discs and cells and lamellated [Herbst] corpuscles, Leitch and Catania 2012) have been shown to initiate growth in avians at e11-19 and complete development by hatching (~e28) (Saxod 1996). It has also been demonstrated that sensory organ formation relies on the presence of development of these cells (Saxod 1996), therefore further understanding of developmental timing can inform placement and distribution of sensory receptors in reptiles.

Allometric implications

The negatively allometric growth of the majority of the nervous structures (Figs. 3.5,3.6,3.8,3.10) is expected, as this is a trend seen across vertebrate central nervous systems (Gould 1966, Jerison 1969, Armstrong 1990) and sensory tissues (Bird et al. 2014, Jerison 1973, Menco 1980, Nummela 1995). However, the maxillary and

mandibular divisions (i.e., diameter and volume) grow with positive allometry pre-hatching (Table 3.2), which is concurrent with the large relative size of these features by time of hatching. The rapid growth of the maxillary and mandibular divisions may be reflecting the early formation, rapid growth, and large size of the first pharyngeal arch and its contents (e.g., jaw musculature, tongue, etc.) (Tan and Morriss-Kay 1985, Graham 2003). If so, the slower growth of the ophthalmic division is also reflected by the slower and later-growing frontonasal prominence. Another potential factor playing a role is the length of the rostrum in Alligator and the associated increase in surface area.

Crocodylians have elongate rostra, requiring the nerves to be similarly elongate. Because the maxillary and mandibular divisions innervate the rostral-most points of the rostrum, their growth reflects the growth of the elongate dentary, tongue, and maxilla. The ophthalmic division does not extend rostrally in crocodylians, nor does it provide innervation to an increased surface area (Leitch and Catania 2012).

Perhaps more interestingly, of all cranial nerves (Fig. 3.8), the trigeminal nerve is the largest, and its growth is the least negatively allometric with respect to skull width (CNV slope = 0.857, Table 3.4). Only the oculomotor, glossopharyngeal, and hypoglossal nerves grow with similar allometry (CNIII = 0.746, CNIX = 0.766, CNXII = 0.778) followed by the optic and vestibulocochlear nerves (CNII = 0.607, CNVIII = 0.673). The other sensory nerves (i.e., olfactory, optic, vestibulocochlear) and the other mixed nerves have observably lower allometric relationships (CNI = 0.447, CNIV = -0.024, CNVI = -0.244, CNVII = 0.186, CNX = 0.472). With the exception of the vagus nerve, the glossopharyngeal and hypoglossal nerves take the longest, most tortuous path to their targets (i.e., throat and tongue), which also elongate with the rostrum (Lessner &

Holliday 2020). If the high growth rate exhibited by the trigeminal nerve is because of an elongate rostrum, this would explain similar rates in these nerves. The high growth rate of these nerves may also relate to extent and timing of myelination, which initiates embryonically and continues post-hatching in reptiles (Yanes et al. 1987, Nadon et al. 1995, Champoux et al. 2020). Though it extends further than the hypoglossal and glossopharyngeal nerves, the vagus nerve contains a large amount of unmyelinated, autonomic nerve fibers, which would also contribute to the slower growth rate when compared with more myelinated nerves (Pereyra et al. 1992, Arcilla and Tadi 2020).

Individually investigated and taken together, the targets of the mandibular division of the trigeminal nerve innervation (i.e., trigeminal-innervated muscles and surface area of the mandible) increase faster than the diameter of the mandibular division (Table 3.3). Absence of isometric relationships in these instances suggest that parallel development is not occurring between these structures or that an additional factor is influencing the relationship. In addition to the jaw musculature and integumentary surface, the mandibular division targets alveoli, oral tissues, and the tongue, so further exploration of growth of individual structures and nerves is necessary to untangle these relationships. Pontine-medulla and trigeminal metrics are also uncoupled with pontine-medulla volume development paralleling that of the brain rather than the trigeminal nerve. As with the trigeminal nerve, the pontine-medulla region is responsible for integrating many processes and there is likely more at play in this relationship than just the influence of the trigeminal nerve. The allometric relationship between maxillary and mandibular division diameters and maxillomandibular ganglion volume also non-isometric as is the relationship between the ophthalmic division diameter and the

ophthalmic ganglion volume, again indicative of additional factors playing a role (Table 3.3). This is potentially the result of variation in ganglionic and peripheral nerve myelination. Previous investigation into myelination of vestibulocochlear ganglia in goldfish and rats has demonstrated that cranial nerve ganglia myelin is often thinner and more compact than peripheral nerve myelin upon completion of myelination (Toesca 1996, Rosenbluth and Palay 1961, Rosenbluth 1962). Thus, the more rapid growth of peripheral trigeminal nerves in comparison to their associated ganglia may be instead reflecting the more extensive myelination of these axons than their associated cell bodies.

Many muscles grow with negative allometry pre-hatching and with positive allometry post-hatching. The muscles with the highest allometric trajectories during embryonic development include mPTd, mPTv, and mIMA (Table 3.2). The high pre-hatching trajectories of mPTd, mPTv, and mIMA might suggest these muscles are the most necessary for feeding immediately upon hatching. This is expected at least for mPTd, which plays a major role in jaw adduction and generates the highest proportion of jaw muscle forces from yearling onward (Sellers et al. 2017). The reason for high trajectories in mPTv could be because of close relationship with mPTd, but the cause for mIMA's high trajectory is unknown. The increase to isometry or positive allometry in the muscles post-hatching indicates the rapid need for high volume muscles to produce the necessary forces for tackling large prey (Neill 1971, Erickson 2003, Sellers et al. 2017). The negatively allometric trajectory of mLB post-hatching is thus potentially explained by the fact that it does not play a role in jaw adduction.

Other crocodylians

I included four non-*Alligator* crocodylians in the study to determine whether the patterns could be observed more broadly (labelled in Figs. 3.5-8). I found that trends held when including *Crocodylus johnstoni*, *Tomistoma schlegelii*, *Gavialis gangeticus*, *Osteolaemus tetraspis*, and *Paleosuchus palpebrosus* (Table 3.1). The *C. johnstoni* specimen is labelled as an embryonic specimen because of the incomplete ossification observed in its skull and the curled arrangement in which it is preserved.

Nervous topology

It has been repeatedly demonstrated that the path of the trigeminal nerve divisions separates the trigeminal muscles into homologous groups across reptiles (Edgeworth 1935, Haas 1973, Holliday and Witmer 2007, Iordansky 2000, Lakjer 1926, Lubosch 1933, Säve-Söderbergh 1945, Zusi and Livezey 2000). Crocodylians, however, exhibit a unique morphology that has brought attention to the origins of potentially homologous structures. Holliday and Witmer (2007) identified three topological changes (i.e., 1. mPSTs and V₂ switch positions, 2. nAO (angulus oris) and mAMEP switch positions, and 3. mPSTs and nPT (pterygoid) switch positions) between crocodylians and other reptiles that are the keys to understanding structure homology. Here I tracked ontogenetic appearance of these changes in order to determine the heterochronic differences resulting in the variation among reptiles:

1. From its appearance in stage F19, mPSTs is located lateral to the maxillary division of the trigeminal nerve (Fig. 3.11a). Therefore, in agreement with Holliday and Witmer (2007), *Alligator* does not meet the criterion of the traditional trigeminal topological paradigm, which states that the maxillary division separates mPSTs from

mAMEP. As such, I conclude that this organization is a result of a change in signaling that occurs before development of the structures involved.

2. In stage F16 the angulus oris (nAO) is not visible, but it becomes barely visible in stage F17 before individual muscles are distinguishable. In stage F19, the nerve does not quite split the mAMEP and mAMEM (Fig 3.11b). Instead, it follows the caudal border of the mAME muscles. By stage F24, the nerve is just visible separating the mAMEP and mAMEM as it does in the adult form (Fig 3.11c). This organization therefore occurs as a result of signaling between stage F19 and stage F24.

3. Again, from its appearance in stage F19, mPSTs is located in its adult position (i.e. rostral and lateral to the pterygoid nerves [nPT], Fig 3.11d). I do note a nerve that passes straight from the origin of the mandibular division to the mPTd in F19 in addition to the innervation received from the nPT. As the maxillomandibular ganglion increases in size, in the yearling alligator, this mPTd specific branch appears to come directly from the maxillomandibular ganglion.

Epipterygoid homology

The epipterygoid is a cranial element found lizards though not in crocodylians and birds (Klembara 2004). Our data provides further explanation for homologies and developmental origins of the structure. In the stage F17 alligator (Fig 3.3a), I describe a trigeminal-innervated muscle (m. depressor palpebrae inferioris) with origins in close proximity to the trigeminal ganglion and seeming to originate from the cartilaginous rod I identify as the columella prootica of Klembara (2004). The structure is situated between the ophthalmic and maxillary divisions of the trigeminal nerve as described by DeBeer (1937) and lies in the anterodorsal portion of the vestibular part of the otic region as

described by Klembara (1991, Fig. 3.3d) with the rostralmost end immediately dorsal to the anterior portion of the trigeminal ganglion (Klembara 2004). Klembara (2004) notes the columella prootica as present in Stage 1 and Stage 1A, also Ferguson stage 17.

The m. depressor palpebrae inferioris (ventralis) (mDPi) is one of the first dorsal constrictor muscles (CID, C₁D), those muscles originating from the mandibular myotome dorsal to the pterygoid process of the palatoquadrate (Edgeworth 1907, Fig. 3.3c). The others include the m. levator bulbi (pars dorsalis), m. depressor auriculae inferior, m. tensor periorbitae, and the m. levator pterygoideus (Lakjer 1926, Iordansky 1964, 2000, Poglayen-Neuwall 1953, Shute and Bellairs 1955, Schumacher 1973). In crocodylians, these muscles have been reported to have numerous origins including the cartilaginous interorbital septum (Wedin 1953, Shute and Bellairs 1955), dorsal part of the medial palatoquadrate (Lakjer 1926), pterygoid process of the quadrate (Edgeworth 1907), anterodorsal corner of the basisphenoid rostrum or caudal parasphenoid (Schumacher 1973, Poglayen-Neuwall 1955, Iordansky 1964, 2000), and laterosphenoid (Holliday and Witmer 2007). In birds, this muscular group is also reported to attach to the interorbital septum (Baumel and Witmer 1993), and in lizards, the epipterygoid (Lakjer 1926). Klembara (2004) hypothesizes that the columella prootica is the embryonic precursor of the ascending process of the palatoquadrate in crocodylians and epipterygoid in lizards. As such, evidence of a CID muscle originating from the columella prootica in a crocodylian embryo when CID musculature originates from the epipterygoid in lizards (Lakjer 1926), and the observation of CID muscle attachment to the dorsal portion of the palatoquadrate (Lakjer 1926) corroborates Klembara's (2004) evidence that the columella prootica is embryonic evidence of the un-developed epipterygoid in crocodylians. Its

disappearance leaves the musculature to attach to the rostradorsal portion of the palatoquadrate (i.e., pterygoid portion of pars pterygoquadrate of Klembara [2004]) and surrounding structures (i.e., interorbital septum, pterygoid process of the quadrate, parabasisphenoid, and laterosphenoid). Specific investigation into the CID musculature and attachments is expected to reveal more.

Perhaps similarly, the mPSTp attaches to the epipterygoid and prootic in lepidosaurs but the laterosphenoid in archosaurs (Holliday and Witmer 2007). In stage F17, there is a small mass at the base of mDPi, which is located similarly to the mPSTp in stage F19 and therefore may be the developing mPSTs (Fig. 3.3a-b). If so, there may be a developmental relationship between mDPi, mPSTp, and the epipterygoid.

Evolutionary implications

Ontogenetic investigation often has evolutionary implications, specifically assisting in identification of heterochronic shifts resulting in variation in morphology. Notable areas of focus with respect to evolution of the crocodylian trigeminal system are:

1. Evolution and restructuring of the lateral braincase wall in crocodylians.

This research has confirmed yet again that ontogenetic study is necessary in understanding phylogenetic and evolutionary differences. For example, the disappearance of the columella prootica after stage F17 of development or the appearance of tissue dividing the ophthalmic and maxillomandibular divisions of the trigeminal nerve by stage F22 are both key events in understanding homologies and timing of development. Disappearance of the columella prootica helps identify developmental timing of the loss of the epipterygoid in crocodylians. Identification of the timing of the origins of tissue

separating the trigeminal divisions can help narrow in timing of development of similar morphologies in other taxa (e.g., avians, non-avian theropod dinosaurs, snakes, etc.).

2. Evolution of the trigeminal-innervated jaw musculature as the crocodylian skull flattens.

The organization of crocodylian musculature and cranial elements allows for a low profile in the water while maintaining a hard bite (Iordansky 1973, Sellers et al. 2017). Ontogenetic study allows for identification of growth events upon which the adult morphology is reliant. For example, I reveal mPTd demonstrates the least-negative allometric growth pre-hatching thus identifying it as likely the most essential muscle for initial feeding behaviors in *Alligator*. Further comparison among reptiles can lead to understanding of heterochronic differences leading to biomechanical variation.

3. Evolution of the trigeminal-innervated rostral sensory system as crocodylians invade semi-aquatic habitats.

The transition from a terrestrial to semiaquatic habitat is well documented along the lineage to extant crocodylians (Wilberg et al. 2019). In addition to morphological changes, crocodylians also evolved trigeminal-innervated integumentary sensory organs (ISOs), suiting them well for a semiaquatic lifestyle (Soares 2002, Leitch and Catania 2012). This system requires abundant trigeminal tissue and a complexly branched nerve (George and Holliday 2013, Lessner 2020). Thus, investigation of the rate and timing of appearance of trigeminal tissues, and further comparison with other reptiles can shed light on sensory differences that are present because of differing developmental timing.

CONCLUSIONS

Ontogeny of the *Alligator* trigeminal system has received some previous attention in the context of biomechanics (e.g., Erickson 2003, Sellers et al. 2017) and sensory

biology (e.g., Di-Poï and Milinkovitch 2013), but overall development of the system is typically ignored in embryonic studies. This investigation filled embryonic gaps and provided a complete picture of development of nervous, muscular, cartilaginous, and skeletal structures associated with the trigeminal system using CT acquired data. Further combination of CT data with different techniques will lead to a more in-depth understanding of the system. Potential next steps include histological investigation of differences in myelination or analysis of muscle fiber orientation as by Sullivan et al. (2019). Additionally, cross-taxa ontogenetic comparisons have the potential to increase understanding of biomechanical and sensory biology. Similar patterns of cranial nerve growth (i.e., more positively allometric and larger size of the trigeminal nerve in comparison to all other cranial nerves) is expected in other trigeminal specialists (e.g., dabbling and probing birds) and similar analyses across sensory niches are expected to reveal links between relative nerve size and growth and identification of the most relied upon senses. This investigation has assisted in identifying and narrowing the range in which trigeminal-related structures develop. Targeted exploration of ontogenetic series in additional taxa could confirm homology of structures and reveal developmental origins of morphological differences.

Table 3.1. Imaged specimens.

Specimen	Species	Embryonic Stage*	Time	Skull Length (mm)	Source	Stain	Stain Duration	Scanner	Resolution (mm)
MUVC AL091	<i>Alligator mississippiensis</i>	10	10-11 days	3.84	Rockefeller Refuge	1% I ₂ KI (agarose)	overnight	Zeiss Xradia Versa 510 CT	0.013123
Alligator_Stage11_2	<i>Alligator mississippiensis</i>	11	12	7.41	Watanabe				0.0204059
MUVC AL092	<i>Alligator mississippiensis</i>	13	15 days	6.26	Rockefeller Refuge	1% I ₂ KI (agarose)	overnight	Zeiss Xradia Versa 510 CT	0.013133
Alligator_Stage15_2	<i>Alligator mississippiensis</i>	15	18-20	10.19	Watanabe				0.0226869
MUVC AL093	<i>Alligator mississippiensis</i>	16	21 days	8.61	Rockefeller Refuge	1% I ₂ KI (agarose)	overnight	Zeiss Xradia Versa 510 CT	0.01917
Alligator_Stage17.5_2	<i>Alligator mississippiensis</i>	17	22-23	11.53	Watanabe				0.0255872
MUVC AL089	<i>Alligator mississippiensis</i>	19	27-28 days	14.34	Rockefeller Refuge	1% I ₂ KI (agarose)	overnight	Zeiss Xradia Versa 510 CT	0.020723
Henry 1	<i>Alligator mississippiensis</i>	20	29-30 days	14.51	Rockefeller Refuge	I ₂ KI		Zeiss Xradia Versa 510 CT	0.0294
Alligator_Stage20_2	<i>Alligator mississippiensis</i>	20	29-30	13.15	Watanabe	I ₂ KI			0.0280057
Henry 2	<i>Alligator mississippiensis</i>	21	31-35 days	16.14	Rockefeller Refuge	I ₂ KI		Zeiss Xradia Versa 510 CT	0.0294
Fabfri secondsmallest	<i>Alligator mississippiensis</i>	21	32 days	14.62	Fabfri et al. 2017	5% phosphomolybdic acid	unknown	Harvard Center for Nanoscale Systems (CNS)?	0.0088
MUVC AL094	<i>Alligator mississippiensis</i>	22	36-40 days	21.2	Rockefeller Refuge	1% I ₂ KI (agarose)	overnight	Zeiss Xradia Versa 510 CT	0.028147
Fabfri alligators_smallerhead	<i>Alligator mississippiensis</i>	22	40 days	19.28	Fabfri et al. 2017	5% phosphomolybdic acid	unknown	Harvard Center for Nanoscale Systems (CNS)?	0.0275
MUVC AL153	<i>Alligator mississippiensis</i>	22	36-40 days		Rockefeller Refuge				0.021037
MUVC AL114	<i>Alligator mississippiensis</i>	22	36-40 days		Rockefeller Refuge				0.021037
MUVC AL095	<i>Alligator mississippiensis</i>	24	46-50 days	26.56	Rockefeller Refuge	1% I ₂ KI	emails	Zeiss Xradia Versa 510 CT	0.028147
MUVC AL096	<i>Alligator mississippiensis</i>	25	51-60 days	31.24	Rockefeller Refuge	1% I ₂ KI	emails	Zeiss Xradia Versa 510 CT	0.028147
Fabfri Camacho_alligator	<i>Alligator mississippiensis</i>	28	60+ days	33.80	Fabfri et al. 2017	5% phosphomolybdic acid	unknown	Harvard Center for Nanoscale Systems (CNS)?	0.0235113
FMNH 16162	<i>Crocodylus johnstoni</i>	-	hatchling	35.33	Field Museum	8% I ₂ KI	77 days	NSI CT scanner	0.227
FMNH 22817	<i>Paleosuchus palpebrosus</i>	-	hatchling	39.31	Field Museum	8% I ₂ KI	77 days	NSI CT scanner	0.0589
AlligatorStained_Hatchling_2	<i>Alligator mississippiensis</i>	-	hatchling	43.6	Watanabe				0.0404325
FMNH 53632	<i>Osteolaemus tetraspis</i>	-	juvenile	49.87	Field Museum	8% I ₂ KI	77 days	NSI CT scanner	0.0457
AlligatorStained_Hatchling_1	<i>Alligator mississippiensis</i>	-	hatchling	50.4	Watanabe	I ₂ KI			0.0455933
MUVC AL031	<i>Alligator mississippiensis</i>	-	1 year	57.05	Rockefeller Refuge	12.3% I ₂ KI	35 days	Zeiss Xradia Versa 510 CT	0.03942
AlligatorStained_Yearling_1	<i>Alligator mississippiensis</i>	-	yearling	87.39	Watanabe	I ₂ KI			0.0645218
FMNH 11085	<i>Tomistoma schlegelii</i>	-	juvenile	105.64	Field Museum	8% I ₂ KI	77 days	NSI CT scanner	0.0556
AlligatorStained_Yearling_2	<i>Alligator mississippiensis</i>	-	yearling	108.31	Watanabe	I ₂ KI			0.0797908
AlligatorStained_Juvenile_2	<i>Alligator mississippiensis</i>	-	juvenile	119.15	Watanabe	I ₂ KI			0.0900018
AlligatorStained_Juvenile_1	<i>Alligator mississippiensis</i>	-	juvenile	131.92	Watanabe	I ₂ KI			0.0898367
AlligatorStained_Subadult_2	<i>Alligator mississippiensis</i>	-	subadult	251.92	Watanabe	I ₂ KI			0.133077
MUVC AL606	<i>Alligator mississippiensis</i>	-	adult	254	Rockefeller Refuge	12.3% I ₂ KI	1319	NSI CT scanner	0.0875
TMM	<i>Gavialis gangeticus</i>	-	adult	443.55	Texas Memorial Museum	12.3% I ₂ KI	injection	NSI CT scanner	0.1195

*Embryonic stages are based on Ferguson 1987

Table 3.2. Structure growth rates (all measurements were log-transformed for allometric slopes).

Metric	Embryonic (mm ³ /day)	Post-hatch (mm ³ /day)	Isometric slope	Embryonic allometric slope	p-value	Post-hatch allometric slope	p-value	Difference (embryonic-post-hatch)	Overall allometric slope	p-value
Skull width	0.33	0.033	Body size proxy	-	-	-	-	-	-	-
Skull length	0.61	0.050	1	1.01	0.92	1.05	0.30	0.04	1.00	0.92
Spinal cord width	0.042	0.001	1	0.81	0.08	0.55	1.4e-04**	-0.26	0.680	2.7e-10*
Spinal cord height	0.023	0.0004	1	0.53	3.3e-05*	0.45	1.0e-06**	-0.08	0.574	7.9e-16*
Brain volume	9.515	4.032	3	2.18	1.7e-03*	1.20	3.5e-10**	-0.98	1.65	2.2e-17*
Olfactory bulb volume	0.447	0.287	3	2.28	0.24	1.48	2.9e-07**	-0.80	2.06	1.2e-06*
Cerebrum volume	4.037	2.123	3	2.59	0.10	1.20	5.9e-09**	-1.39	1.87	1.4e-12*
Cerebellum volume	0.423	0.185	3	1.79	6.5e-04*	1.21	9.4e-09**	-0.58	1.58	1.4e-16*
Diencephalon volume	0.756	0.273	3	1.68	2.3e-06*	1.23	2.0e-06**	-0.45	1.30	3.6e-20*
Optic tectum volume	1.587	0.305	3	2.06	1.7e-03*	0.92	3.6e-09**	-1.14	1.33	1.3e-17*
Pontine-medulla volume	2.333	0.858	3	2.23	1.8e-04*	1.13	1.6e-11**	-1.10	1.63	8.4e-18*
V ₁ volume	0.015	0.060	3	2.53	0.42	2.35	6.8e-03**	-0.18	2.56	1.1e-02*
V ₂ volume	0.077	0.40	3	3.43	0.15	2.62	2.0e-02**	-0.81	3.07	0.48
V ₃ volume	0.117	0.83	3	3.44	1.8e-02*	2.74	2.9e-02**	-0.70	3.20	3.3e-03*
V ₁ diameter	0.006	0.0005	1	0.58	1.13e-03*	0.48	5.1e-05**	-0.10	0.735	5.3e-07*
V ₂ diameter	0.016	0.0008	1	1.08	0.55	0.68	2.1e-03**	-0.40	0.870	3.9e-03*
V ₃ diameter	0.020	0.0009	1	1.01	0.92	0.80	2.8e-03**	-0.21	0.900	2.1e-

										03*
V ₁ ganglion volume	0.009	0.004	3	1.68	1.1e-03*	1.55	3.0e-02**	-0.13	1.84	3.2e-15*
V _{2/3} ganglion volume	0.090	0.090	3	1.85	1.0e-04*	1.98	2.76e-06**	0.13	2.00	1.2e-18*
Muscle volume	5.140	118.97	3	3.70	0.24	3.46	7.3e-03**	-0.24	3.71	2.7e-04*
mAMES volume	0.363	13.619	3	1.63	4.5e-03*	3.17	0.25	1.54	2.88	0.38
mAMEM volume	0.117	4.613	3	1.23	4.3e-02*	4.23	0.04*	3.00	2.87	0.71
mAMEP volume	0.234	2.064	3	1.31	2.0e-02*	3.35	0.17	2.04	2.60	7.7e-02
mAMP volume	0.543	19.663	3	2.03	4.7e-04*	3.00	0.99	0.97	2.89	0.45
mPSTs volume	0.087	4.330	3	0.97	1.2e-03*	3.41	0.35	2.44	2.56	7.8e-02
mPSTp volume	0.042	0.183	3	0.54	1.4e-02*	3.15	0.82	2.61	2.32	5.4e-02
mPTd volume	1.112	61.348	3	2.34	3.7e-02*	3.02	0.90	0.68	3.09	0.38
mPTv volume	1.940	90.91	3	2.83	0.62	3.80	1.2e-04**	0.97	3.35	4.7e-03*
mIRA volume	0.273	7.122	3	1.81	0.15	3.36	3.9e-03**	1.55	3.12	0.57
mIMA volume	0.563	6.937	3	2.32	0.35	3.19	0.20	0.87	2.95	0.82
mLB volume	0.049	0.357	3	0.96	4.6e-02*	2.32	4.1e-02**	1.36	2.12	1.1e-03*

*A significant p-value signifies a significant difference from isometric slope.

**Significant.

Table 3.3. Additional allometric relationships. Features with more rapid trajectories bolded.

Feature Y	Feature X	Slope	Overall isometric slope	p-value*
Total muscle volume (mm³)	Mandibular division diameter (mm)	3.86	3	1.84e-04**
Maxillomandibular ganglion volume (mm ³)	Total muscle volume (mm³)	0.514	1	2.8e-16**
Maxillomandibular ganglion volume (mm ³)	Skull length (mm)	1.94	3	5.8e-15**
Mandibular division diameter (mm)	Skull length (mm)	0.875	1	2.7e-03**
Total muscle volume (mm³)	Skull length (mm)	3.66	3	6.6e-05**
Maxillomandibular ganglion volume (mm³)	Mandibular surface area (mm ²)	0.810	2/3	1.1e-02**
Mandibular division diameter (mm)	Mandibular surface area (mm²)	0.359	1/2	1.5e-05**
Total muscle volume (mm³) + Mandibular surface are (mm²)	Maxillomandibular ganglion volume (mm ³)	3.10	5/3	5.6e-08**
Total muscle volume (mm³) + Mandibular surface are (mm²)	Mandibular division diameter (mm)	6.70	5	1.1e-04**
Maxillomandibular ganglion volume (mm ³)	Mandibular division diameter (mm)+ Maxillary division diameter (mm)	1.10	3/2	1.3e-12**
Ophthalmic ganglion volume (mm ³)	Ophthalmic division diameter (mm)	2.19	3	2.2e-08**
Total brain volume (mm ³)	Maxillomandibular ganglion volume (mm³)	0.816	1	4.1e-05**
Pons & medulla volume (mm ³)	Maxillomandibular ganglion volume (mm³)	0.815	1	4.2e-05**
Pons & medulla volume (mm ³)	Total brain volume (mm³)	0.989	1	0.45

*A significant p-value signifies a significant difference from isometric slope.

**Significant.

Table 3.4. Cranial nerve allometric relationships (all measurements were log-transformed for allometric slopes).

Metric	Isometric slope	Overall allometric slope	p-value*
Skull width	Body size proxy	-	-
CN V diameter	1	0.85715	2.844568e-05**
CN I diameter	1	0.4466	0.09886057
CN II diameter	1	0.60586	0.002656904**
CN III diameter	1	0.7459	0.04272081**
CN IV diameter	1	-0.0244	0.01763117**
CN VI diameter	1	-0.2443	0.004908724*
CN VII diameter	1	0.1858	0.03438247**
CN VIII diameter	1	0.6732	0.02524841**
CN IX diameter	1	0.76592	0.04270268**
CN X diameter	1	0.47227	4.773126e-05**
CN XII diameter	1	0.77811	0.03888058**

*A significant p-value signifies a significant difference from isometric slope.

**Significant.

Figure 3.1. Developing brain and trigeminal nerves of embryonic (a.) MUVc AL091 [F10d10-11], (b.) MUVc AL092 [F13d15], (c.) MUVc AL093 [F16d21], (d.) MUVc AL089 [F19d27-28], (e.) MUVc AL094 [F22d38], (f.) MUVc AL095 [F24d46-50], and (g.) MUVc AL096 [F25d51-60] and hatched (h.) MUVc AL031 [yearling] and (i.) juvenile 2 [juvenile]. All scale bars 1 mm.

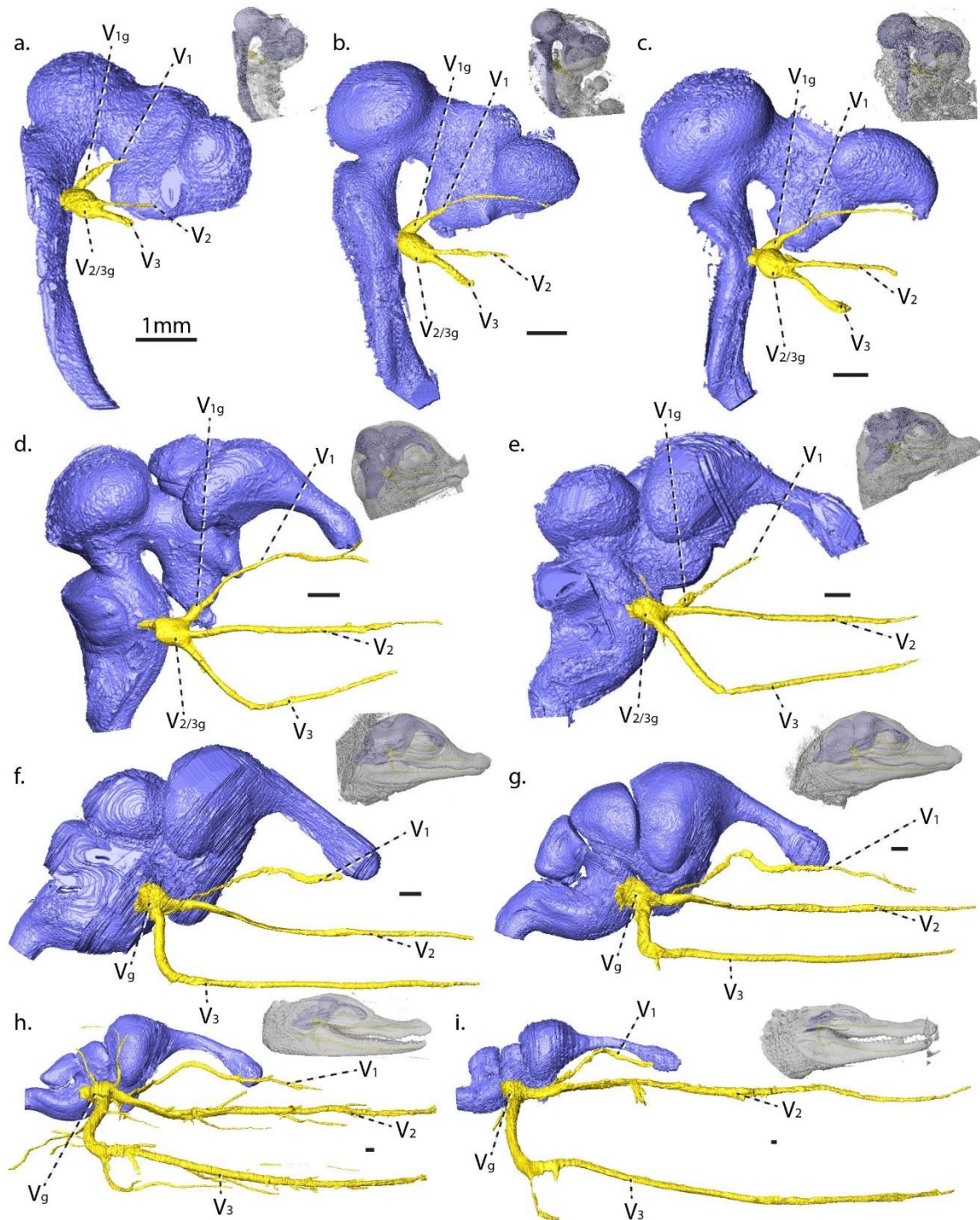


Figure 3.2. Developing musculature of embryonic (a.) MUVc AL092 [F13d15], (b.) MUVc AL093 [F16d21], (c.) MUVc AL089 [F19d27-28], (d.) MUVc AL094 [F22d38], (e.) MUVc AL095 [F24d46-50], and (f.) MUVc AL096 [F25d51-60] and hatched (g.) MUVc AL031 [yearling] and (h.) juvenile 2 [juvenile] with associated trigeminal nerves. All scale bars 1 mm.

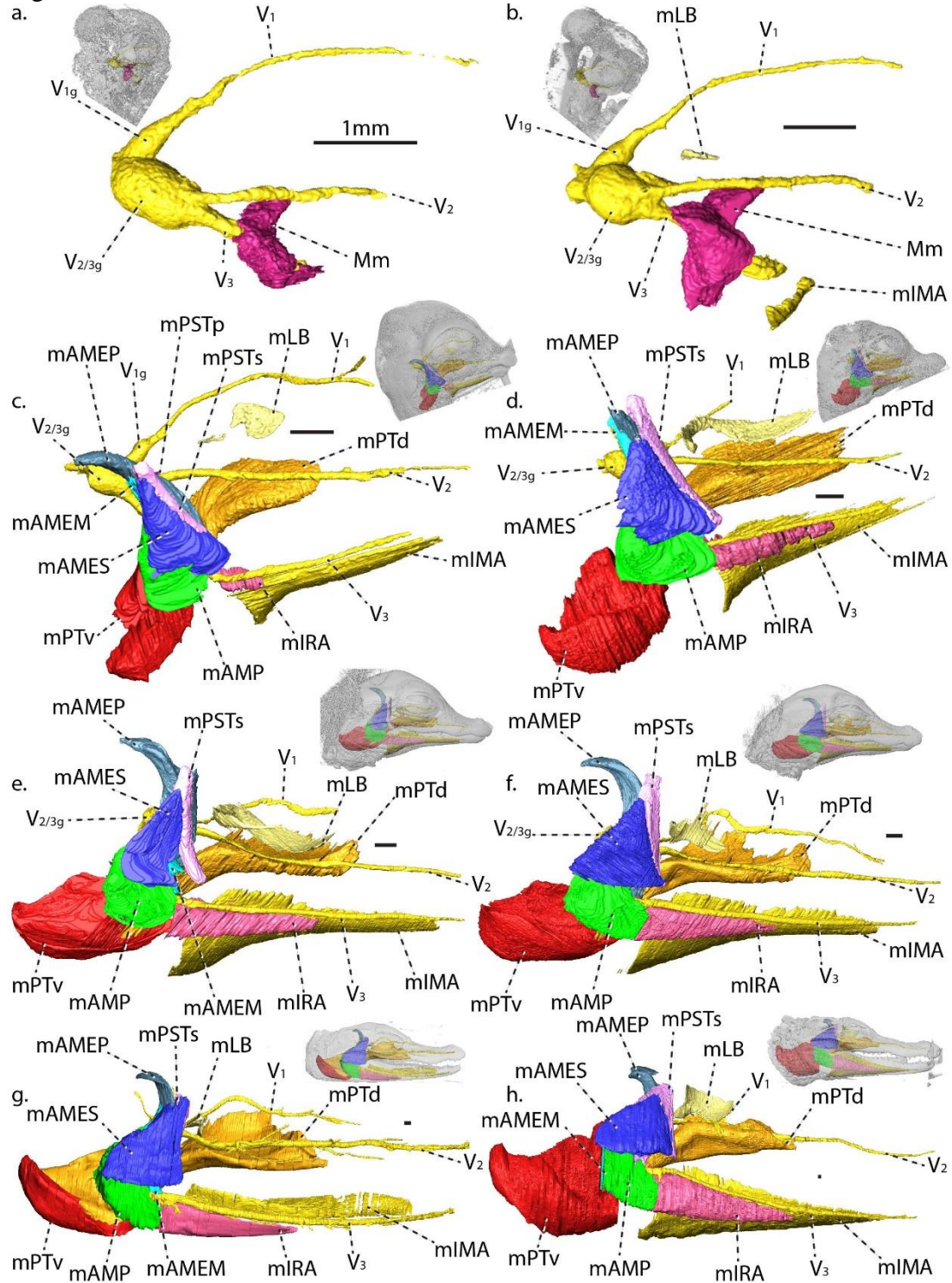


Figure 3.3. Developing epipterygoid region (columella prootica, ascending process of the palatoquadrate, pseudotemporalis profundus, and depressor palpebrae inferioris) of (a.) stage 17 [F17d22-23] and (b.) MUVc AL089 [F19d27-28] with comparisons from (c.) Edgeworth [1935] and (d.) Klembara [1991]. All scale bars 1 mm.

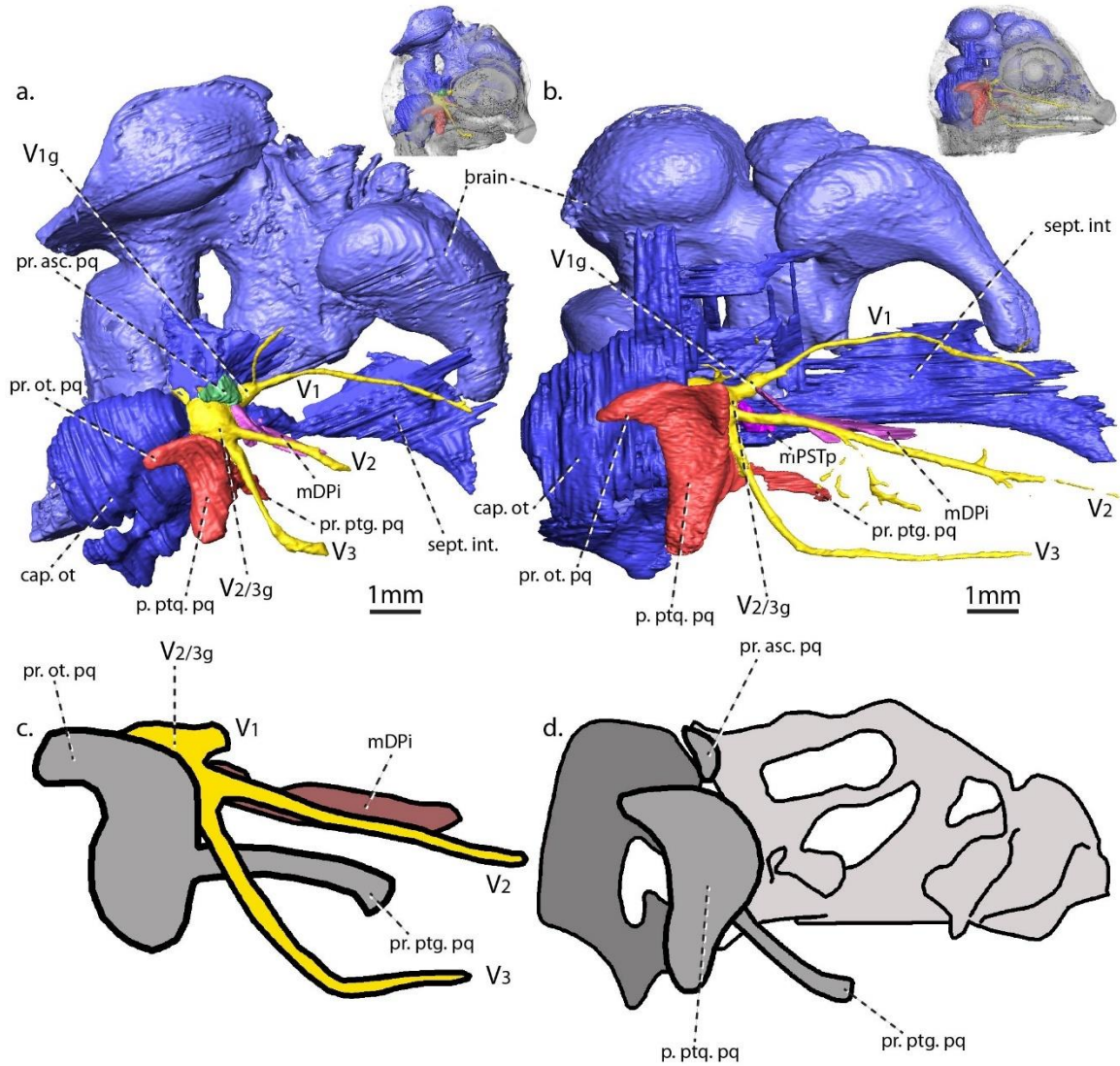


Figure 3.4. Developing cartilages of embryonic alligators (a.) MUVC AL093 [F16d21], (b.) MUVC AL089 [F19d27-28], (c.) MUVC AL094 [F22d38], (d.) MUVC AL095 [F24d46-50], and (e.) MUVC AL096 [F25d51-60] with associated trigeminal nerves. All scale bars 1 mm. * for unnamed process between maxillary and mandibular divisions in stage F22 only.

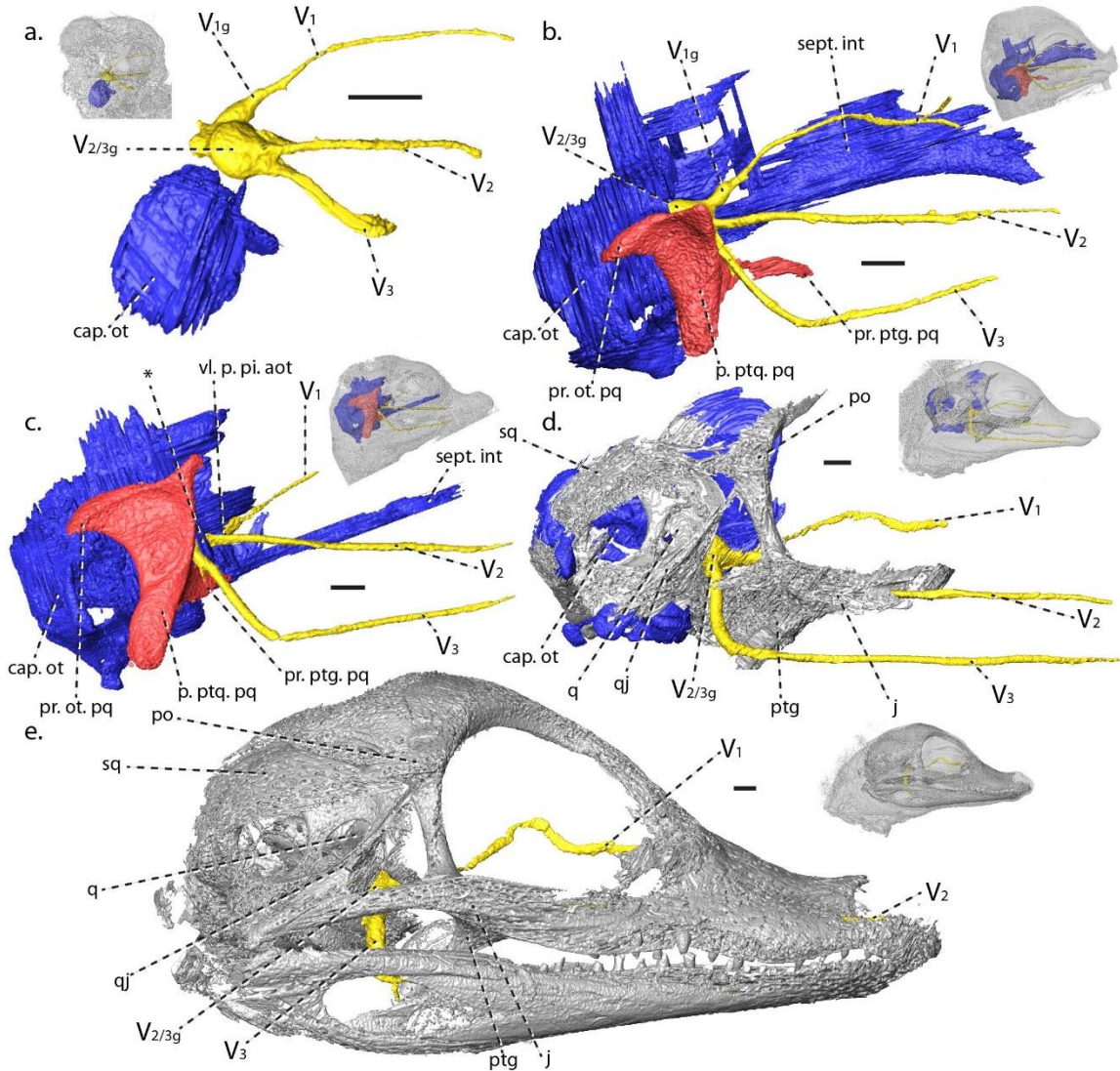


Figure 3.5. Plot of relative growth of cerebral regions by skull width. All values are \log_{10} transformed.

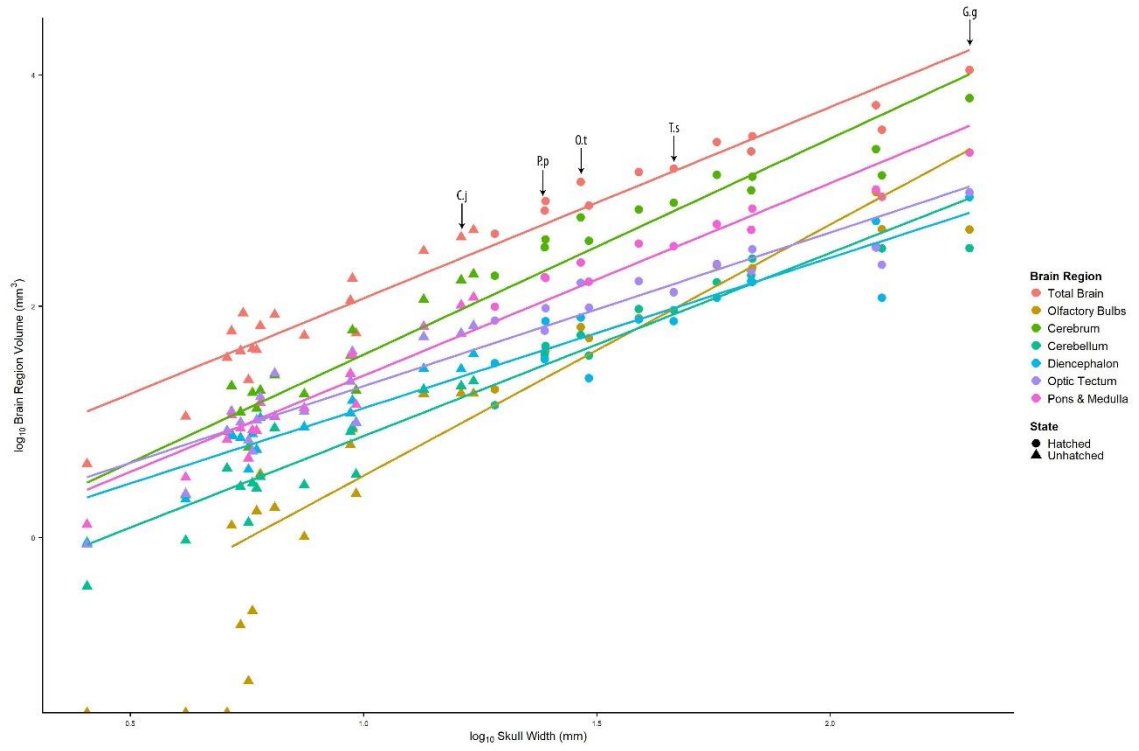


Figure 3.6. Plot of relative growth of trigeminal nerve ganglia and divisions by skull width (a.) across all developmental stages, (b.) across embryonic stages only, (c.) and across hatched stages only. All values are \log_{10} transformed.

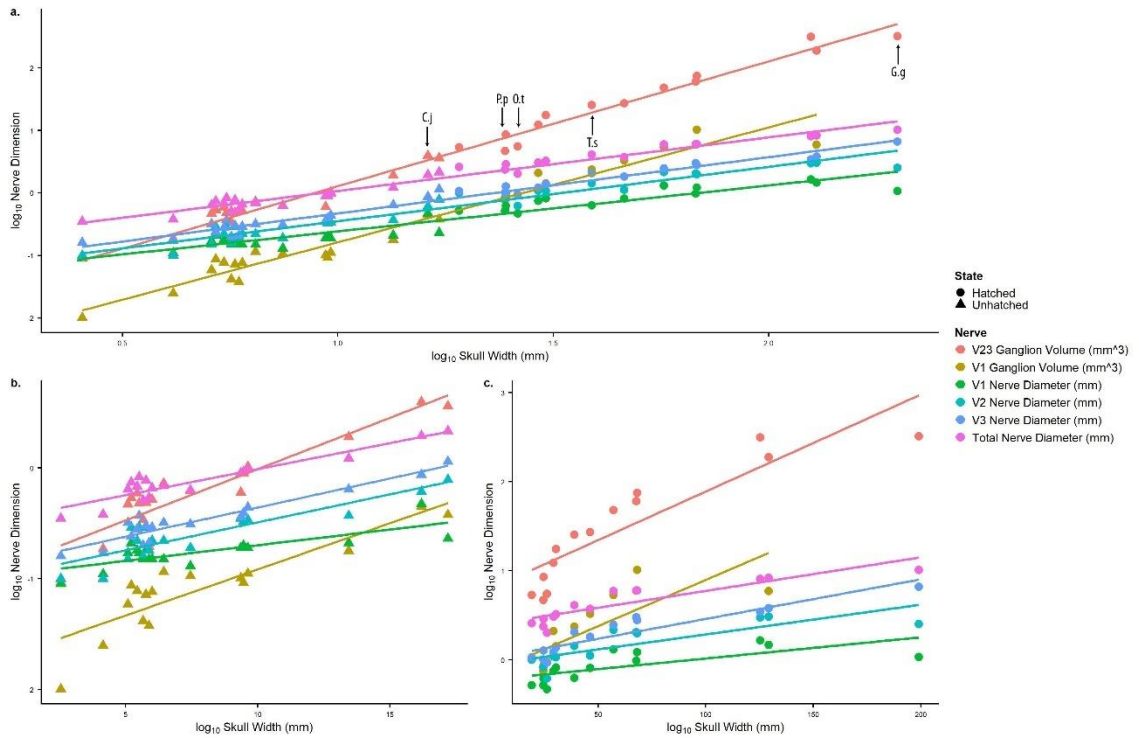


Figure 3.7. Plot of relative growth of muscles by skull width (a.) across all developmental stages, (b.) across embryonic stages only, (c.) and across hatched stages only. All values are \log_{10} transformed.

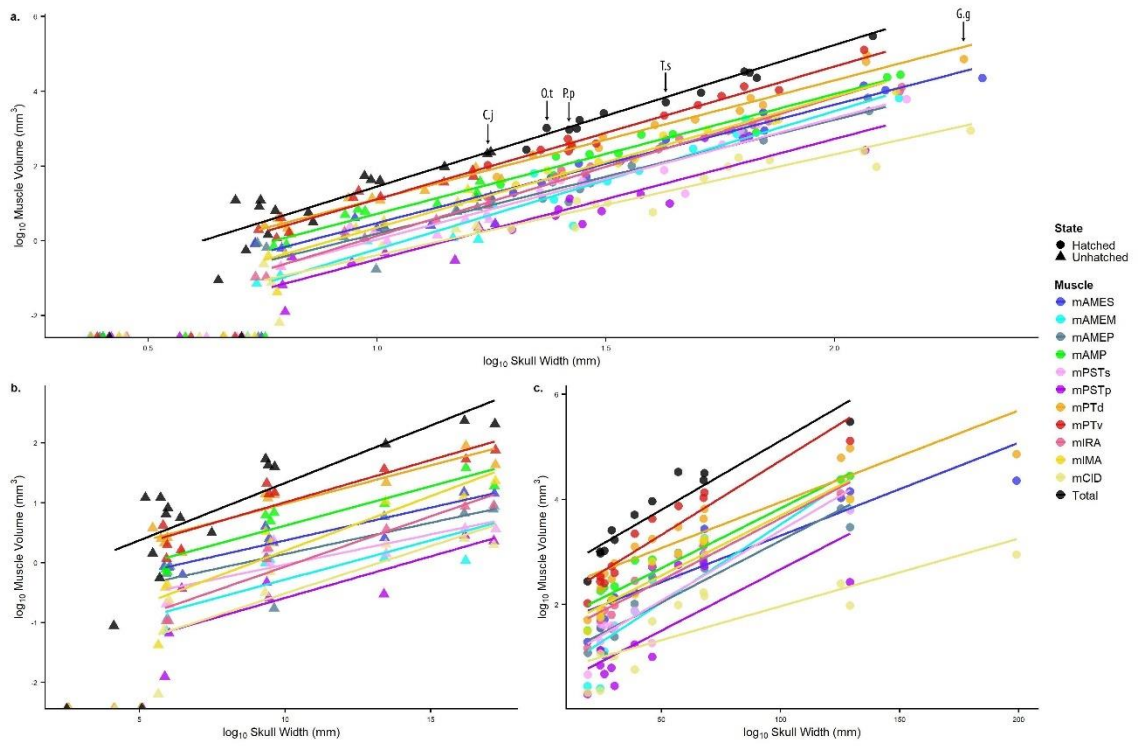


Figure 3.8. Plot of relative growth of cranial nerve diameters by skull width. All values are \log_{10} transformed.

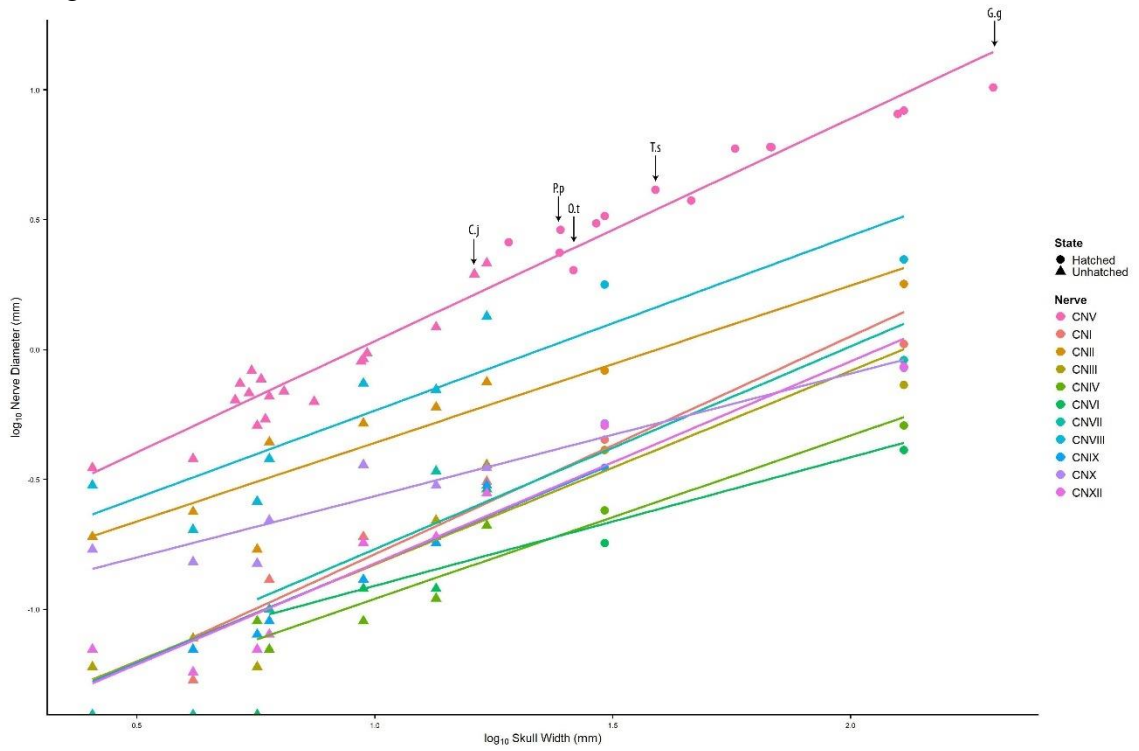


Figure 3.9. Plot of growth of structures over time using metrics (a.) skull width, (b.) skull length, (c.) spinal cord width, (d.) spinal cord height, (e.) maxillomandibular ganglion volume, (f.) ophthalmic ganglion volume, (g.) ophthalmic nerve volume, (h.) maxillary nerve volume, (i.) mandibular nerve volume, (j.) ophthalmic nerve diameter, (k.) maxillary nerve diameter, (l.) mandibular nerve diameter, (m.) total trigeminal nerve diameter, (n.) total brain volume, (o.) olfactory bulb volume, (p.) cerebrum volume, (q.) cerebellum volume, (r.) diencephalon volume, (s.) optic tectum volume, (t.) pons and medulla volume, (u.) mAMES volume, (v.) mAMEM volume, (w.) mAMEP volume, (x.) mAMP volume, (y.) mPSTs volume, (z.) mPSTp volume, (aa.) mPTd volume, (ab.) mPTv volume, (ac.) mIRA volume, (ad.) mIMA volume, (ae.) mLB volume, (af.) total muscle volume.

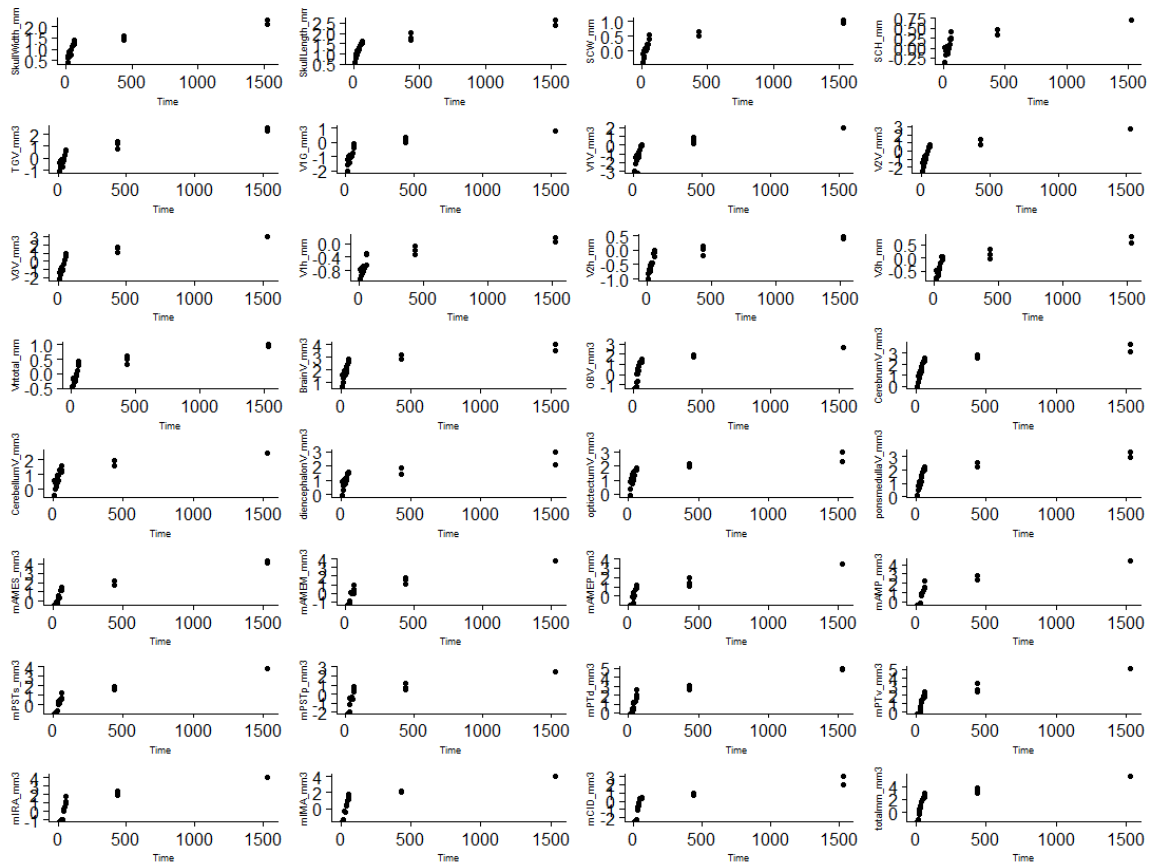


Figure 3.10. Plot of relative growth of structures by skull width using metrics (a.) skull width, (b.) skull length, (c.) spinal cord width, (d.) spinal cord height, (e.) maxillomandibular ganglion volume, (f.) ophthalmic ganglion volume, (g.) ophthalmic nerve volume, (h.) maxillary nerve volume, (i.) mandibular nerve volume, (j.) ophthalmic nerve diameter, (k.) maxillary nerve diameter, (l.) mandibular nerve diameter, (m.) total trigeminal nerve diameter, (n.) total brain volume, (o.) olfactory bulb volume, (p.) cerebrum volume, (q.) cerebellum volume, (r.) diencephalon volume, (s.) optic tectum volume, (t.) pons and medulla volume, (u.) mAMES volume, (v.) mMEM volume, (w.) mAMEP volume, (x.) mAMP volume, (y.) mPSTs volume, (z.) mPSTp volume, (aa.) mPTd volume, (ab.) mPTv volume, (ac.) mIRA volume, (ad.) mIMA volume, (ae.) mLB volume, (af.) total muscle volume. All values are \log_{10} transformed.

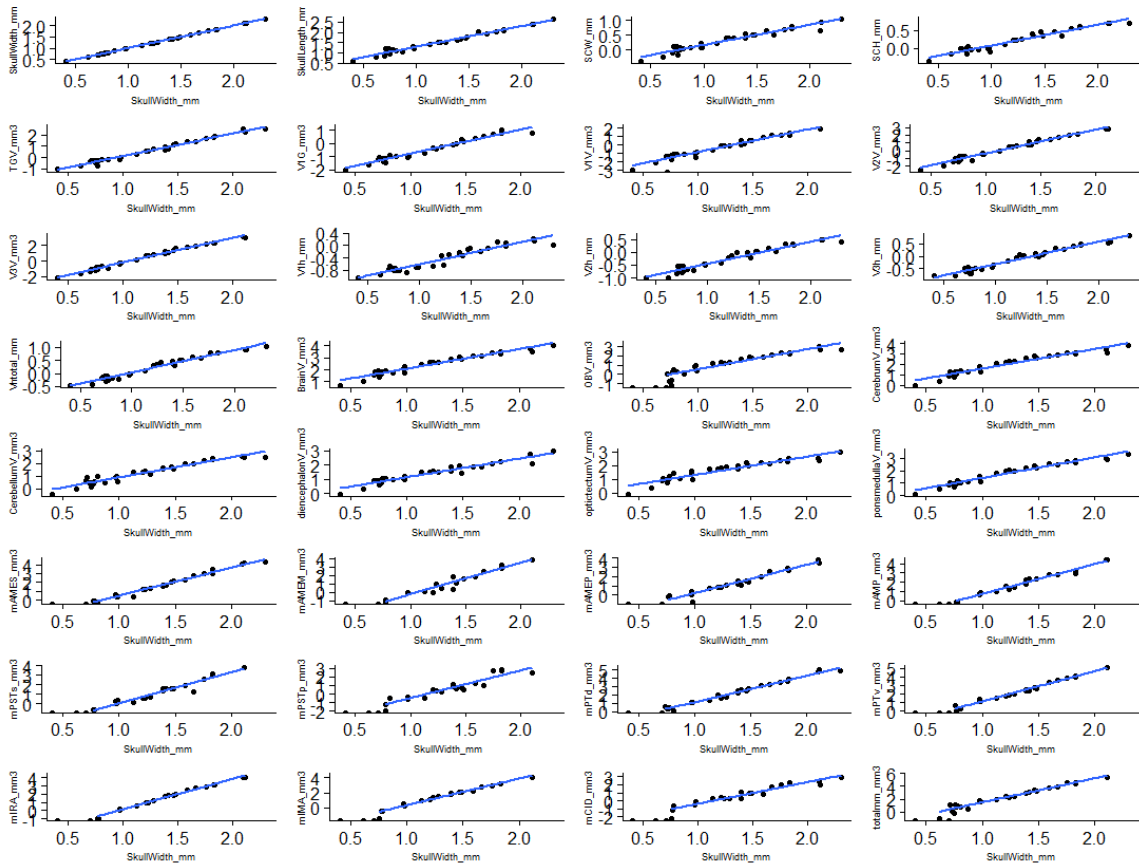
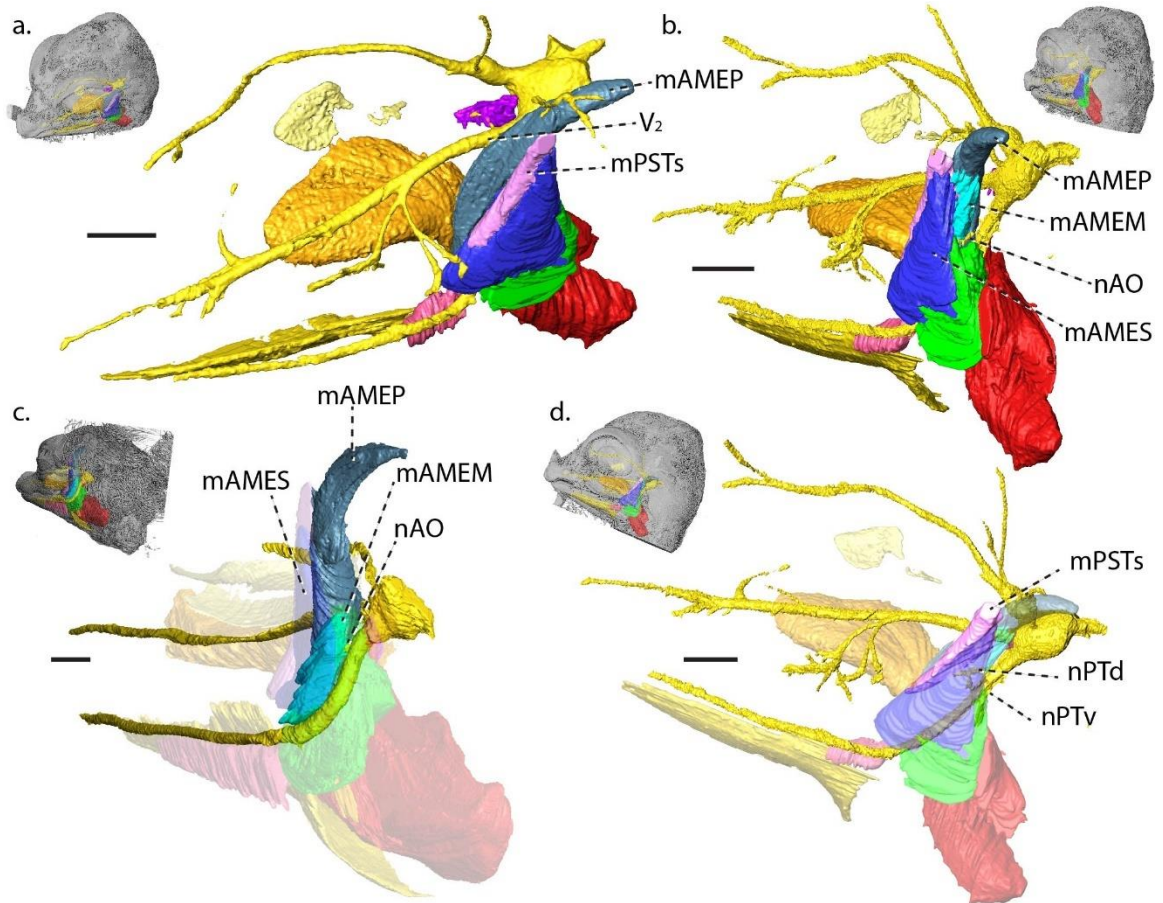


Figure 3.11. Development of topologically informative structures including the maxillary nerve and mAMEP and mPSTs in (a) MUVc AL089 [F19d27-28], the angulus oris and mAME musculature in (b) MUVc AL089 [F19d27-28] and (c) MUVc AL095 [F24d46-50], and the pterygoid nerve and mPSTs in (d) MUVc AL089 [F19d27-28].



Chapter 4 — Quantifying neurovascular canal branching patterns reveals a shared crocodylian arrangement

INTRODUCTION

In the natural world we see repetition of structural patterns including the highly-branched, dendritic form found in streams, plants, and numerous anatomical structures including neurovasculature. A variety of methods have been developed to quantify and analyze these patterns including assigning orders to streams (Horton, 1945; Scheidegger, 1965; Shreve, 1966; Strahler, 1957), assigning ramification matrices to and encoding ductal networks (Bakic, Albert, & Maidment, 2003; Megalooikonomou, Barnathan, Kontos, Bakic, & Maidment, 2009), calculating transit times and applying algorithms to bronchial trees (Fujii et al., 2020; Horsfield & Cumming, 1968; Sauret, Goatman, Fleming, & Bailey, 1999), building 3D structural models of trees (Lau et al., 2018), automating encoding of vessels (Martínez-Perez et al., 2002; Skoura, Bakic, & Megalooikonomou, 2013), assigning stream orders and applying algorithms to neurons (Berry & Bradley, 1976; Hollingworth & Berry, 1975; Kanari et al. 2018; Uylings, Smit, & Veltman, 1975; Uylings, Van Pelt, & Verwer, 1989; Verwer & VanPelt, 1986), and secondary fractal analysis of numerous structures (e.g., Beer & Borgas, 1993; Horton, 1945; Khanbabaei, Karam, & Rostamizad, 2013; LaBarbera & Rosso, 1989; Pelletier & Turcotte, 2000). Here I have adapted methods and quantities from these studies to investigate neurovascular canal branching patterns in the inferior alveolar canal of crocodylians, a clade of reptiles known for a derived sense of facial somatosensation mediated by the trigeminal nerve.

Utility in Comparative Morphology

Comparing branching patterns is a novel way to explore morphology of neurovascular canals across taxa. Variation in branching patterns reflects variation in

distribution of neurovasculature which leads to estimation of nerve and vessel density across an area. In the case of the inferior alveolar canal, the contents include the inferior alveolar branch of the mandibular division of the trigeminal nerve and the mandibular artery and vein.

In vertebrates, the trigeminal nerve is the primary somatosensory nerve of the head and courses a conserved pathway from its hindbrain origin to nerve endings across the face. The trigeminal nerve passes from the brain, through the trigeminal ganglion, and splits into three divisions. Of these, the mandibular division offers the clearest signal of integumentary innervation necessary for tactile sensation as the other divisions innervate the nasal cavity and orbit in addition to the skin of the jaws. The mandibular division originates from the trigeminal ganglion, housed alongside the braincase in crocodylians (Holliday & Witmer, 2009; Hopson, 1977). From there, the mandibular division passes through a bony foramen, passing between the jaw muscles into a bony canal in the mandible via the inferior alveolar foramen. After traversing canals and foramina perforating the mandibles, the mandibular nerves terminate in sensory receptors on the skin of the lower jaw. In crocodylians, these integumentary sensory organs (ISOs) are specialized for a semi-aquatic lifestyle, providing the rostrum the ability to sense minute changes in water pressure, temperature, and pH (Di-Poi & Milinkovitch, 2013). Consequently, all living crocodylians can discriminate between the range of stimuli experienced during behaviors such as navigating environments and capturing prey and engage in tactile-foraging. When this system and behavior appeared in the evolutionary history of this clade is unknown.

Extensive vascular networks in crocodilian oral, nasal, and orbital regions are associated with thermoregulation of neurosensory tissues (Porter, Sedlmayr, & Witmer, 2016). Although vascular networks play a thermoregulatory role elsewhere in the crocodilian head, this is likely not the case in the lower jaws as the inferior alveolar canal is located in the mandible, a region not suited or often used for thermoregulation. Also, neurovascular networks within the rostrum are more typically tied with nervous anatomy in extant taxa (e.g., Crole & Soley, 2016; Cunningham et al., 2010; George & Holliday, 2013) and the inferior alveolar canal in crocodylians is occupied by significantly more nervous than vascular tissue (Fig. 4.1). Therefore, results are interpreted strictly as indicators of nervous tissue and sensory ability.

The inferior alveolar canal is an osteological correlate for the mandibular vessels and inferior alveolar nerve and is preserved in fossils of extinct organisms. Evaluation and comparison of branching patterns provides insight into the evolution of both physiology and behavior of extinct taxa.

Ordering Strategies

The need to measure properties of river drainage basins in lieu of solely qualitative descriptions led Horton (1945), Hack (1957), and Strahler (1957) to develop methods of quantifying stream structures. Their methods use branching and bifurcation patterns to classify or order, streams centripetally (from the origins, towards the main channel) whereas the topological method classifies streams centrifugally (from the main channel, towards the origins) (Uylings et al., 1975) (Fig. 4.2). Like streams with numerous tributaries coming together at various nodes to eventually drain into a main

channel, neurovascular canals have main canals with numerous branches bifurcating from various nodes, so these methods are easily adapted to quantify neurovasculature.

Topological

Analyzing and comparing neurovascular branching patterns requires identification of a main canal. Topological order determines a main canal when one is not readily identifiable by variation in diameter of the canal (i.e., the main canal typically has the largest diameter) and thus is necessary before continuing with Horton and Hack ordering. In addition, topological ordering determines location of terminal segments (those connected to a single node [Fig. 4.2e]) along the main canal. Topological orders are designated by assigning an order of 1 to the origin segment (in this case the segment originating at the opening of the inferior alveolar canal [Fig. 4.2e]) (Fig. 4.2ai). Order increases by 1 at each node (Fig. 4.2aiv-vi). The main canal is then identified as the set of segments with the longest total length that start at the origin and end with the terminal segment of highest topological order.

Strahler

Strahler order determines the order of a main canal (see Topological for assigning a main canal) and thus is necessary before continuing with Horton ordering. Strahler orders are assigned by assigning an order of 1 to all terminal segments that are not the origin segment (Fig. 4.2bi). Order 2 is then assigned to all segments sharing nodes where two 1st order segments converge (Fig. 4.2bii). From there, when two segments of the same order share a node, the order of the other segment sharing that node is 1 higher than the other two segments (Fig. 4.2biii-v). If two segments of different orders converge, the order of the other segment sharing that node takes the higher order of the two segments.

Horton

Horton order distinguishes branch complexity. To assign Horton order, the highest Strahler order is assigned to every main canal segment (see Topological for main canal assignment) (Fig. 4.2ci). Then, terminal segments branching off the main canal are assigned order 1 (Fig. 4.2cii). For paired terminal segments, the shorter of the two are assigned order 1 (Fig. 4.2cii). A set of segments (segments sharing nodes end-to-end that are assigned the same order [Fig. 4.2e]) is assigned order 2 if it only shares nodes with 1st order segments (Fig. 4.2ciii). A set of segments is assigned order 3 if it only shares nodes with 2nd or 1st order segments (Fig. 4.2civ). This pattern continues until all segments are assigned orders.

Hack

Hack order is useful in comparing terminal segments. To assign Hack order, all main canal segments (see Topological for main canal assignment) are assigned order 1 (Fig. 4.2di). All longest (in number of segments first and total length second) segment sets branching off the main canal are assigned order 2 (Fig. 4.2dii). All longest segment sets branching off the 2nd order segment sets are assigned order 3 (Fig. 4.2diii). This pattern continues until all segments are assigned orders.

Here, the utility of applying river network quantification methods to comparably branched crocodylian inferior alveolar canals is assessed and similarity among crocodylians is evaluated. Further, the quantified bony morphology is considered and discussed in the context of neurovascular contents, their distribution, and sensory and behavioral implications.

MATERIALS AND METHODS

Computed Tomography Scanning and Segmentation

Thirteen crocodylian specimens and two birds were CT scanned at different resolutions (see Table 4.1) based on their availability and size, allowing for visualization of bone and neurovascular canals. The influence of scan resolution on the results was tested for and discounted by the absence of any significant correlation between voxel size and the derived quantities explored below (e.g., topological center of mass, dendritic density, first segment Horton order proportions). Contrast-enhanced scans (Gignac et al., 2016) of *Alligator* (MUVC AL031) were used to verify neurovascular canal contents, which themselves are too small to trace the length of dentary (Fig. 4.1). Scan data were imported as DICOM and TIFF files into Avizo v. 9.7 [Thermo Fisher Scientific; Waltham, MA] for segmentation. Anterior dentaries (the portion of the dentary anterior to the opening of the inferior alveolar canal) and neurovascular canals were segmented manually using both magic wand and paintbrush tools (Fig. 4.1).

3D Model Measurement and Processing

Measurements were taken in Avizo directly from the segmented CT data to explore relationships of the branching patterns with size. Linear measurements, including trans-quadratic skull width and dentary length, were measured from 3D volumes in Avizo using the 2D length tool. To measure dentary surface area, triangles of the lateral, integumentary, foraminiferous portion of the dentary were selected on the unsmoothed, generated surface using the surface editor. Area was calculated using the surface area statistics module.

Reconstructed neurovascular canals were simplified in Avizo to assign segment orders and collect segment lengths more easily. To do so, a spatial graph was generated from segmented neurovascular canals using the ‘Centerline Tree’ module with tube

parameters of slope = 1.5-2, zeroVal = 3-4, and a manual root set at the proximal origin of the neurovascular canal (Fig. 4.1). Parameters for each specimen were adjusted manually until the spatial graph appeared to best represent the reconstructed canal. Attribute graph tables containing the length of each segment were exported from Avizo as .xml files and converted to .xlsx files for analysis in R. 3D annotations were placed on the spatial graph to assign topological, Strahler, Horton, and Hack order to segments (Fig. 4.1). Columns for segment Strahler and Horton orders were added to the attribute graph .xlsx file by identifying segments using the spatial graph table.

Sensitivity analysis: Avizo parameters

The ‘Centerline Tree’ module used to create the spatial graph to which orders are assigned allows adjustment of tube parameters ‘slope’ and ‘zeroVal’. These parameters adjust module sensitivity (Thermo Fisher Scientific, 2019). In general, using manual adjustment, slope = 1.5-2 and zeroVal = 3-4, seemed to accurately represent the segmented data. To test the effect of these parameters on ordering results, the neurovascular canal from *C. johnstoni* (TMM M-6807) was analyzed across a range of parameters (slope = 1-3 by intervals of 0.5, and zeroVal = 2-5 by intervals of 1) and orders assigned by the Strahler and Horton methods. Strahler branch counts and Horton first segment counts and percentages were collected (as below) per parameter combination.

Derived Quantities

Derived quantities were collected using a combination of single measurements from the processes described above.

Total length

Total length of all segments was used to calculate relative lengths in derived quantities below. Total length of all segments was calculated as the sum of ‘Curved Length’ from the attribute graph table after all segments not assigned Horton orders were removed.

Topological center of mass

Topological center of mass (topological COM) describes the average distance in segments of terminal segments from the origin segment of the neurovascular canal. This single measure was calculated as described by Uylings et al. (1989). Calculation requires the sum of the topological orders of all segments (C) and the number of terminal segments (n) and is calculated as: $\bar{C} = C/(2n-1)$.

Density metrics

The following derived quantities describe distribution of neurovascular canals across the dentary.

Dendritic density: Dendritic density is a calculation of total length of all segments divided by the area they cover and is classically known in the stream literature as ‘drainage density’ (Hollingworth & Berry, 1975; Horton, 1945).

Segment frequency: Segment frequency is defined as number of segments (‘streams’ in the stream literature) per unit of area (Horton, 1945). This quantity was adapted for neurovascular canals as the number of neurovascular canal segments per unit area. Number of segments were tallied from Horton ordered neurovascular canals.

Tip frequency: Tip frequency is defined as number of terminal segments per unit of area. Number of terminal segments were tallied from Strahler ordered canals (all segments of Strahler order 1).

Segment counts

Number of segments per order were tallied per specimen for the Strahler, Horton, and Hack ordering methods to quantitatively describe branching patterns and log-transformed where applicable (i.e., Strahler). The segment counts quantify the overall structure of the neurovascular canal, with Strahler highlighting organization at the terminal segments and Horton and Hack the organization of first segments with respect to the main canal.

First segment Horton order proportions

Horton orders of the first segments to branch from the main inferior alveolar canal were tallied to quantify branch complexity or number and arrangement of segments and terminal tips of each branch from the main canal. Tallies of individual orders of first segments were compared to the total number of first segments to calculate percentage of first segments per order for each specimen (Fig. 4.3).

Relative mean Strahler segment lengths

Average segment lengths per Strahler order were calculated for each specimen using 'Curved Length' of the attribute graph tables to explore segment structure. These were divided by total length, creating a relative mean.

Analysis

The metrics and derived quantities above were used to quantify structure of crocodylian neurovascular canal and test for a shared neurovascular canal branching pattern within crocodylians. Density metrics were compared across taxa to determine whether the neurovascular canal is distributed across the dentary uniformly within crocodylians. Relationships of topological COM and size were compared across taxa.

Segment and first segment counts and lengths per order were compared across taxa or parameter combination. Phylogenetic linear models (Freckleton, Harvey, & Pagel, 2002) were fit using R packages [caper] (Orme et al., 2013) and [phytools] (Revell, 2012), both using an adapted phylogeny of Wilberg, Turner, and Brochu (2019). Blomberg's K (Blomberg, Garland, & Ives, 2003) and Mantel tests (Hardy & Pavoine, 2012) were used to calculate phylogenetic signal of traits using R packages [phytools] (Revell, 2012) and [vegan] (Oksanen et al., 2007), respectively. The phylogeny was adapted to account for multiple specimens per species by representing species as hard polytomies of individuals. Branch lengths follow those of Wilberg et al. (2019) and are based on geological ages. Significance was assessed at an alpha-level of $p = 0.05$.

RESULTS

Sensitivity analysis: Avizo parameters

Strahler segment counts were and plotted against order per combination of parameters (Fig. 4.4a). Horton proportions were plotted against order (Fig. 4.4b). Welch two sample t-tests were performed for the Strahler and Horton data and neither the default Avizo parameters, nor the parameters assigned when the centerline tree was fit manually to the segmented volume are significantly different from the crocodylian data below. Finally, *C. johnstoni* (TMM M-6807) counts (Order 1: 19, order 2: 11, order 3: 1) and percentages (Fig. 4.4c) (Order 1: 61.3%, order 2: 35.5%, order 3: 3.2%) fit within the range of all crocodylian and parameter values and compare favorably with the average of all crocodylians and parameters (Tables 4.2,4.4). Including slope and zeroVal as covariates in ANOVAs of the two metrics reveals that changing zeroVal has a larger effect than slope on the resulting centerline tree and Strahler and Horton order assignments.

Topological complexity

Topological terminal segment orders were tallied and orders scaled to the highest order per specimen (Fig. 4.5). This representation eliminates size and shape and allows for relative comparison of branching extent along the neurovascular canal. The neurovascular canals show branches all along the length of the canal with an increase in branches towards the rostral end. *C. johnstoni* canals show constant, lower branch counts across their length than other specimens, whereas *Alligator* canals show constant, higher branch counts across their length.

Phylogenetic signal of derived quantities

Blomberg's K was calculated, and a Mantel test was run for the following variables to estimate the magnitude of phylogenetic signal of the following variables before further analysis and interpretation of the data. The K statistic indicates degree of phylogenetic signal by comparing similarity among related taxa to the phylogeny and expectations based on a model of Brownian motion; $K = 1$ describes trait evolution that follows the pattern expected under Brownian motion, $K < 1$ describes that closely-related taxa are more different than expected under Brownian motion, and $K > 1$ describes that taxa are more similar (Blomberg et al. 2003). Blomberg's K is close to 1 for Horton first segment order proportions, Strahler, Hack, and Horton first segment counts, and mode relative segment lengths. Blomberg's K is close to 0.2 for topological COM, dendritic density, and segment frequency and close to 0.3 for tip frequency, Horton segment counts, relative mean segment lengths, and median relative segment lengths.

The Mantel test determines the extent of correlation between phylogenetic distance and trait distance between taxa; a value close to 0 describes no correlation, and

values close to -1 or 1 indicate strong negative and positive correlation, respectively (Hardy & Pavoine 2012). Mantel correlation statistics are close to 0.1 for all metrics except for dendritic density and Horton first segment counts, which are close to -0.1 and segment frequency and tip frequency, which are close to 0.3. Mantel correlation statistics close to 0 and Blomberg's K values close to 1 imply there is as much phylogenetic variation as is expected given the phylogeny of Wilberg et al. (2019). Thus, the following analyses use phylogenetic regression, in the form of phylogenetic generalized least squares (PGLS) and phylogenetic ANOVAs, to correct for phylogenetic dependence.

Topological center of mass

The relationship of \bar{C} to log-transformed total length of the neurovascular canal for each canal shows no significant relationship using a PGLS linear model (Fig. 4.6a) of topological COM regressed on size, whether total length (Fig. 4.6a; $p = 0.39$, $R^2 = 0.07$), area (Fig. 4.12a), or trans-quadratic skull width (Fig. 4.12b). The mean distance of crocodylian terminal segments from the origin of the neurovascular canal (measured in segments) ranges from 17.1 in *C. johnstoni* (TMM M-6807) to 34.3 in *Tomistoma* (FMNH 11085) (Table 4.3). Across the crocodylians evaluated, topological COM is 24.4 on average.

Density metrics

Log-transformed total length of all segments, number of segments and number of tips were plotted against log-transformed dentary surface area for each specimen to explore density of canals using PGLS linear models (Figs. 4.6b-d).

Dendritic density

There is a strong positive relationship between total canal length and dentary surface area (Fig. 4.6b; $p < 0.001$, $R^2 = 0.97$). Dendritic densities range from 0.28 to 1.84 mm of segment \cdot mm⁻² (Table 4.3).

Segment frequency

There is a no significant relationship between number of segments and dentary surface area (Fig. 4.6c; $p = 0.10$, $R^2 = 0.23$). Number of segments ranges from 119 in *C. johnstoni* (FMNH 16162) to 390 in *Osteolaemus* (FMNH 98936). Across the crocodylians evaluated, the average number of segments is 253 and is independent of dentary surface area. Segment frequencies range from 0.051 to 2.66 segments \cdot mm⁻² (Table 4.3).

Tip frequency

There is no significant relationship between number of tips and dentary surface area (Fig. 4.6d; $p = 0.60$, $R^2 = 0.03$). Number of tips ranges from 61 in *C. johnstoni* (TMM M-6807) to 194 in *Osteolaemus* (FMNH 98936). Across the crocodylians evaluated, the average number of tips is 128.5 and is independent of dentary surface area. Tip frequencies range from 0.016 to 2 tips \cdot mm⁻² (Table 4.3).

There is a weak positive relationship between number of segments and number of tips (Fig. 4.12c) and between number of segments and total canal length (Fig. 4.12d). There is no relationship between number of tips and total canal length (Fig. 4.12e).

First segment order proportions

Proportions were plotted against order (Fig. 4.3b). Group means were compared across specimens and orders using phylogenetic ANOVAs and post-hoc pairwise t-tests. Ranges in order counts, minimum counts, maximum counts, ranges in percentages,

minimum percentages, maximum percentages as well as average counts and percentages (Fig. 4.3a) are summarized per order in Table 4.4. There is no significant difference in specimen means ($p = 0.999$), but there is a significant difference between means of orders ($p = 0.001$). Post-hoc testing shows a significant difference between means of all orders ($p = 0.006$) except for between orders 3 and 4 ($p = 0.072$). In general, as order increases, proportion of first segments decreases.

Segment count vs. Order

Segment counts were plotted against order (Fig. 4.7). Group means were compared across specimens and orders using phylogenetic ANOVAs and post-hoc pairwise t-tests. There are no significant differences between specimen means across all comparisons ($p = 0.998 - 1$) and significant differences between means of orders ($p = 0.001$). Post-hoc testing shows means of orders 1 and 2 are significantly different across all comparisons ($p = 0.006 - 0.01$). Means of orders 3 to 5 are not significantly different when comparing Strahler and Horton segment counts ($p = 1$) but are when comparing Hack segment and Horton first segment counts ($p = 0.02 - 0.022$).

In general, for Strahler and Horton segment counts, in specimens with no 5th order segments, segment count decreases through orders 1 to 3 and increases to order 4. With specimens with 5th order segments, segment count decreases through orders 1 to 4 and increases to order 5. (Fig. 4.7a,b) For Hack segment counts, in specimens with no 5th order segments, segment count increases through orders 1 and 2 and decreases through orders 3 and 4. In specimens with 5th order segments, segment count increases through orders 1 to 3 and decreases through orders 4 and 5.

Relative mean segment lengths

Relative mean segment lengths were plotted against order (Fig. 4.8). Group means were compared across and orders using phylogenetic ANOVAs. Neither specimen nor order means are significantly different ($p = 0.217$, $p = 0.232$). In general, lowest (1st) and highest (4th or 5th) orders are the longest and the middle (2nd or 3rd) orders are the shortest.

Distributions of relative Strahler Order lengths

Lengths and corresponding Strahler orders were collected for each specimen. Distributions were plotted for each order and provided a visual comparison of segment lengths (Fig. 4.9). Size was accounted for by dividing each segment length by trans-quadratic skull width (a reliable proxy for body size in crocodylians; see O'Brien et al. 2019). Segment length modes were collected from the density peaks. The density maxima were log-transformed and plotted against order (Fig. 4.10b). From the same data, boxplots were created for each order and median values collected (Figs. 4.10a,c). Density peaks and boxplot medians were compared across specimens using phylogenetic ANOVAs and post-hoc pairwise t-tests. For density peaks, there is no significant difference in specimen means ($p = 0.831$) and order means show significant difference ($p = 0.007$). Post-hoc testing of density peak data show means of orders 1 and 2 are significantly different from each other ($p = 0.03$) and means of orders 3 to 5 are not significantly different from any order ($p = 0.072 - 1$). For boxplot medians, there is no significant difference between specimen means or order means ($p = 0.365$, $p = 0.054$).

For most specimens, short segments are the most frequent, and segment frequency decreases as segment length increases (Fig. 4.9). In general, most 1st order segments were longer than 2nd and 3rd order segments, though most 3rd order segments are longer than

2nd order segments (Fig. 4.10). Most 4th and 5th order segments are longer than 3rd order segments but shorter than 1st order segments.

DISCUSSION

Avizo parameter sensitivity analysis

The insignificant difference between the default and manual centerline trees and other parameter combinations indicates that it is acceptable to use default settings and adjust parameters manually until the centerline tree appears to fit the segmented neurovascular canal volume. Also, using the centerline tree is not necessary but makes neurovascular canals easier to visualize for order assignment. Without this simplification, overlapping and crossing may obscure branch arrangement and attachment in complex neurovascular canals as in crocodylians. Also, centerline trees may provide accurate neurovascular canal estimates when expanding this method to fossil specimens in which neurovascular canals may have internal damage, obscuring or eliminating the exact anatomy.

Shared branching pattern within crocodylians

This adaptation of methods (traditionally used for river drainage basin quantification) to crocodylian neurovascular canals provides a new method of analysis and comparison. Overall, crocodylian neurovascular canals demonstrate similar patterns both with respect to segment lengths, and branch location, arrangement, and complexity.

Size and ontogenetic independence

Number of segments, number of terminal segments, and topological COM are independent of size-related, osteological variables (i.e., area, trans-quadratic skull width, total length) indicating that the crocodylian inferior alveolar neurovascular canal pattern is independent of size (Figs. 4.6,4.12). Size independence is further supported by the

absence of the influence of size with respect to other analyses (e.g., segment count vs. order, relative mean segment length) and the large range in sizes sampled here (i.e., specimens across the 17.67 to 163.45 mm range in skull width show similar patterns). Also, in comparing the three density metrics above (dendritic density, segment frequency, tip frequency), total length of the neurovascular canal, number of segments, and number of tips, these are independent of one another (Table 4.3). These relationships (or lack of) imply the independence of a complex branching pattern from size, represented by total canal length or area.

Similarly, the results indicate the canal pattern is independent of ontogeny. No pattern is present when comparing the different-aged, same-species specimens. This is expected considering the presence of the inferior alveolar neurovasculature before the ossification of the mandibles (Sperber, 2001) and that the crocodylian trigeminal sensory system is fully formed by the time of hatching (Di-Poi & Milinkovitch, 2013). These results also indicate no further remodeling of the inferior alveolar canal occurs during growth to adulthood.

Shared patterns

Overall the crocodylians show the same trends in neurovascular canal arrangement, represented by segment locations, order counts, proportions, and lengths. There was minimal variation between taxa. Those with repeated significant differences of means in multiple tests include both *C. johnstoni* specimens (FMNH 16162, TMM M-6807) and *C. porosus* (OUVC 10899), but there is no indication why. Ranges of values in density metrics (Table 4.3) and lack of relationships between density metrics within specimens do suggest some variation in the branching patterns within crocodylians.

Elimination of size and shape reveals similarities in branching location (topological complexity) among the crocodylian inferior alveolar canal. Notably, though branches are present across the entirety of canal, there is an increase in the number of branches towards the rostral end. Topological COM, which summarizes average distance of terminal segments from the origin was similar across taxa as well (Table 4.3).

In addition to segment location, crocodylians exhibit similar patterns in types of branches off the main neurovascular canal as exhibited by the similar proportions of first segment orders (Fig. 4.3b) and Horton first segment counts (Fig. 4.7d). Organization and arrangement of segments were also similar as evidenced by the similarities between Strahler, Horton, and Hack segment counts. Similar patterns of Strahler orders indicate similarities in the orders of the main neurovascular canals (Fig. 4.7a). Crocodylians exhibit Strahler orders of 4-5, a useful single-term descriptor indicating the presence of distal branching and complexity. Strahler order provides a simplified manner of comparison that will be useful in future comparisons with non-crocodylian taxa. Shared patterns of Horton and Hack orders across crocodylians indicate similarities in the types of branches both from the main canal and other segments (Figs. 4.3,4.7b,d). Horton first segment orders simplify branches from the main canal into a single number describing the complexity and distribution of these branches. Shared patterns of Hack orders indicate similarities in the orders of terminal segments (Fig. 4.7c). In addition to providing a simplified manner of comparison across taxa, Horton first segment order and Hack ordering provide a manner of comparison between branches and terminal segments within a single specimen. Relative segment lengths of different ordered segments

followed similar trends as well and are yet another shared feature of crocodylian neurovascular canals (Figs. 4.9-10).

Biological implications of branching patterns

In the aquatic environment, the crocodylian trigeminal nerve mediates discrimination between very fine changes in wave frequency (i.e. 1.2 Hz) and distance estimation from a single wave (Grap, Matchts, Essert, & Bleckmann, 2020). This behavior requires high sensitivity, made possible by high receptor density (Dehnhardt & Kaminski, 1995; Nicoletis, Lin, & Chapin, 1997). For a region with high density of sensory receptors, more innervation is required (Kandel, Schwartz, & Jessel, 2000; Marino, 2007; Oelschlager & Oelschlager 2002). In this case, the innervation is transmitted through the inferior alveolar canal, which may be used as a proxy for mandibular sensation. Thus, the shared crocodylian morphology quantified here (e.g., an average of 253 segments, 128.5 tips, a topological COM of 24.4, 50% first order branches, 33% second, 15% third, and 2% fourth, a Strahler order of 4-5, high dendritic density, and overall topology) is adequate to provide innervation to the integumentary sensory organs responsible for the tactile-foraging behavior this clade engages in.

Preliminary comparisons with other taxa indicate that this dendritic morphology is unique to taxa with high sensitivity (Fig. 4.11, Lessner & Holliday, 2020b). Lower orders (indicating less complexity of nervous tissue), lower density metrics (indicating lower density of nervous tissue), and lower topological COM (indicating less distribution of nervous tissue) and therefore a simpler topology would not allow for the distribution of nervous tissue necessary for fine discrimination. For example, topological COM provides a single-term, size-independent descriptor of canal topology and other taxa engaging in

tactile foraging are expected to have similar values as the 24.4 of crocodylians, whereas non-tactile, less sensitive taxa are expected to have lower values (preliminary results confirm $\bar{C} = 23.4$ in *Anas* [a tactile forager, Schneider, Gracheva, & Bagriantsev, 2016] but only in 9.88 *Phasianus*).

Such observations should also hold true when comparing regions along a single canal. Increase in number of branches towards the rostral end of the crocodylian canal implies an increase in neurovascular complexity and density towards the rostral end of the face (Fig. 4.5). Similar, but unquantified, distributions of branches are found in the bill-tip organs in the rostral end of the beak of tactile-foraging birds (e.g., Avilova, 2018; Cunningham et al., 2010; Lessner & Holliday, 2020a). Therefore, there is likely an increase in trigeminal sensitivity at the end of the crocodylian rostrum. Additionally, lower branch counts across the length of the *C. johnstoni* canals (Fig. 4.5) may indicate lower sensitivity than other species, whereas higher branch counts across the length of the *Alligator* canals may indicate higher sensitivity than other species, but stimulus discrimination testing across species (e.g., Grap et al., 2020) would be necessary to confirm differences in performance.

CONCLUSIONS

Overall, the analyses presented provide a method of quantifying the morphology of organic dendritic structures. The structure of crocodylian neurovascular canals, branches, and terminal segments compare favorably in a quantitative sense, as does the distribution of these structures through the dentary. Assuming identical canal contents, the shared pattern facilitates distribution of nervous and vascular tissue similarly across crocodylians. This coincides with the shared semi-aquatic ecology and tactile-foraging behavior of the clade. Application of this method across extant reptiles, all with bony

inferior alveolar canals, allows for comparisons to be drawn between structures and inferences of behavior and ecology to be made in both extant and extinct species. Patterns in crocodylians reflect the high density of innervation across the crocodylian rostrum and are not expected to be shared by taxa with less innervation. Preliminary investigation into other clades shows this method is able to discriminate between taxa engaging in tactile-sensation (e.g., crocodylians and *Anas*) and non-tactile taxa (e.g., *Phasianus*) (Lessner & Holliday, 2020a) (Fig. 4.11). This research focused on the inferior alveolar canal as a proxy for the mandibular division of the trigeminal nerve, but there are many other branched anatomical structures that could be compared using these methods (e.g., nervous and vascular networks, trabecular architecture, etc.). At minimum, this method has potential to quantify osteological correlates and use them as support for answering questions of nervous and vascular, and therefore sensory and physiological evolution.

Table 4.1. Specimens used in this study.

Specimen	Taxon	Skull Width (mm)	Voxel Size (μm)
MUVC AL031	<i>Alligator mississippiensis</i> Daudin, 1802	30.42	83.4
MUVC AL712	<i>Alligator mississippiensis</i> Daudin, 1802	146.72	410
FMNH 73711	<i>Caiman crocodilus</i> Linnaeus, 1758	59.14	65.5
FMNH 16162	<i>Crocodylus johnstoni</i> Krefft, 1873	17.67	24.7
TMM M-6807	<i>Crocodylus johnstoni</i> Krefft, 1873	54.54	221
TMM M-4980	<i>Crocodylus moreletii</i> Duméril and Bibron, 1851	163.45	190
OUVC 10899	<i>Crocodylus porosus</i> Schneider, 1801	34.81	92.0
TMM M-3529	<i>Mecistops cataphractus</i> Cuvier, 1824	146.39	165
FMNH 53632	<i>Osteolaemus tetraspis</i> Cope, 1861	26.24	60.8
FMNH 98936	<i>Osteolaemus tetraspis</i> Cope, 1861	54.38	54.7
FMNH 22817	<i>Paleosuchus palpebrosus</i> Cuvier, 1807	23.87	58.9
FMNH 11085	<i>Tomistoma schlegelii</i>	38.12	99.3

	Muller, 1838		
TMM M-6342	<i>Tomistoma schlegelii</i> Muller, 1838	142.11	165
OUVC 10252	<i>Anas platyrhynchos</i> Linnaeus, 1758	36.73	92.0
MUVC AV263	<i>Phasianus colchicus</i> Linnaeus, 1758	30.51	22.2

Table 4.2. First segment order count and percentage summary for Avizo parameter test.

Order	Mean count	Count range	Count minimum	Count maximum	Average percent	Percent range	Percent minimum	Percent maximum
1	16.5	19	12	33	61.1%	27.3%	50.0%	77.3%
2	9.4	8	5	13	35.8%	23.5%	22.7%	46.2%
3	1.0	4	0	4	3.1%	10.5%	0%	10.5%

Table 4.3. Topological center of mass and density metrics.

Specimen	Taxon	\bar{C}	Total length (mm)	Dendritic density (mm/mm ²)	Segment count	Segment frequency (segments/mm ²)	Tip count	Tip frequency (tips/mm ²)	Area (mm ²)
MUVC AL031	<i>Alligator mississippiensis</i>	23.20	185.99	1.028	169	0.934	117	0.647	180.90
MUVC AL712	<i>Alligator mississippiensis</i>	27.41	1193.92	0.278	218	0.051	85	0.020	4279.33
FMNH 73711	<i>Caiman crocodilus</i>	19.78	320.49	0.840	340	0.472	109	0.151	720.38
FMNH 16162	<i>Crocodylus johnstoni</i>	17.13	605.03	1.597	158	2.660	111	1.869	59.39
TMM M- 6807	<i>Crocodylus johnstoni</i>	17.64	94.87	0.471	119	0.146	61	0.075	817.42
TMM M- 4980	<i>Crocodylus moreletii</i>	23.90	385.28	0.067	272	0.048	138	0.024	5724.77
OUVC 10899	<i>Crocodylus porosus</i>	29.68	1445.70	0.957	221	0.660	112	0.334	335.01
TMM M- 3529	<i>Mecistops cataphractus</i>	21.76	1518.58	0.304	326	0.065	79	0.016	5001.97
FMNH 53632	<i>Osteolaemus tetraspis</i>	23.73	187.41	1.234	215	1.415	142	0.935	151.93
FMNH 98936	<i>Osteolaemus tetraspis</i>	31.42	539.00	1.136	390	0.822	194	0.409	474.61
FMNH 22817	<i>Paleosuchus palpebrosus</i>	20.00	158.90	1.842	216	2.504	172	1.994	86.28
FMNH 11085	<i>Tomistoma schlegelii</i>	34.31	331.24	0.832	272	0.683	165	0.414	398.15
TMM M- 6342	<i>Tomistoma schlegelii</i>	26.82	1461.10	0.287	374	0.074	186	0.037	5086.81

Table 4.4. First segment order count and percentage summary

Order	Average count	Count range	Count minimum	Count maximum	Average percent	Percent range	Percent minimum	Percent maximum
1	20.3	23	10	33	50.1%	31.9%	29.4%	61.3%
2	13	13	9	22	32.8%	17.5%	23.7%	41.2%
3	5.3	7	1	8	14.8%	19.7%	3.2%	22.9%
4	0.84	4	0	4	2.2%	11.4%	0%	11.4%

Figure 4.1. Methods. Specimens are CT-scanned and neurovascular canals are segmented in Avizo then converted to spatial graphs. Ordering methods are applied to the spatial graphs.

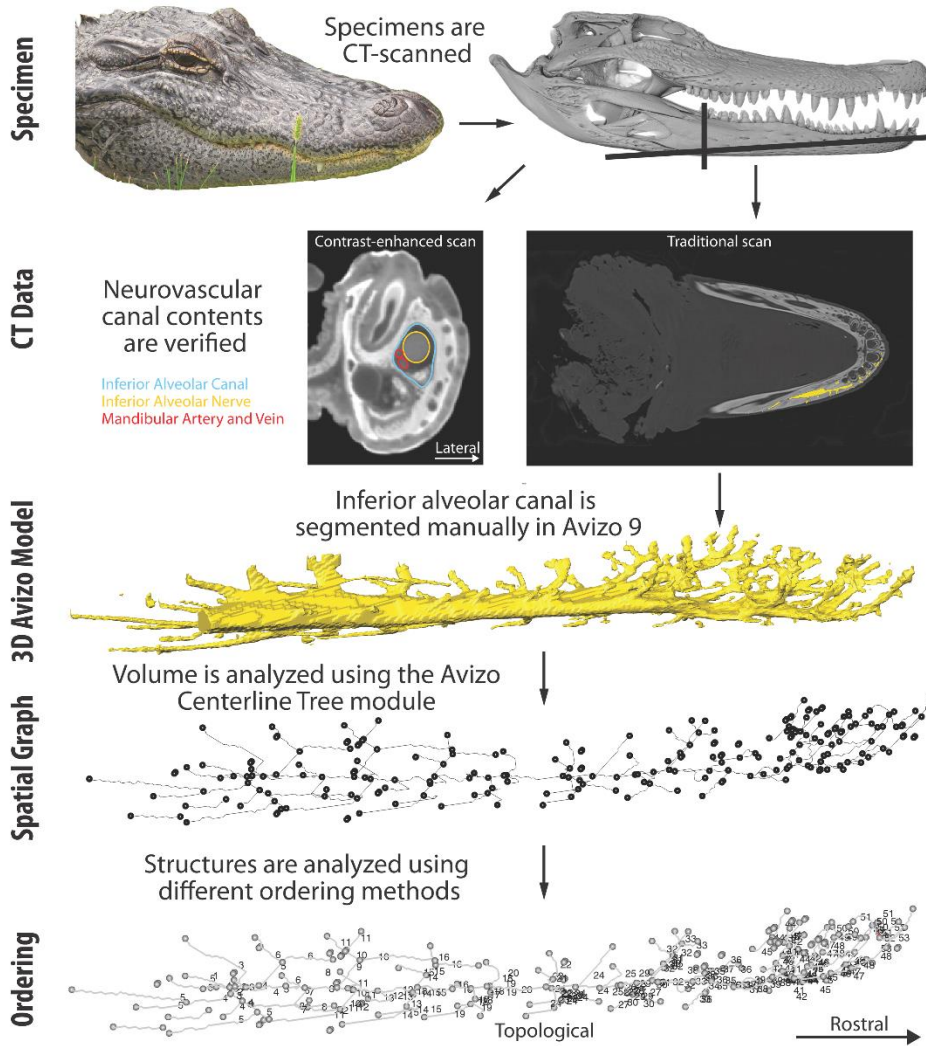


Figure 4.2. Ordering. Progressions of (a) Topological, (b) Strahler, (c) Horton, and (d) Hack ordering methods with (e) a visual explanation of terms.

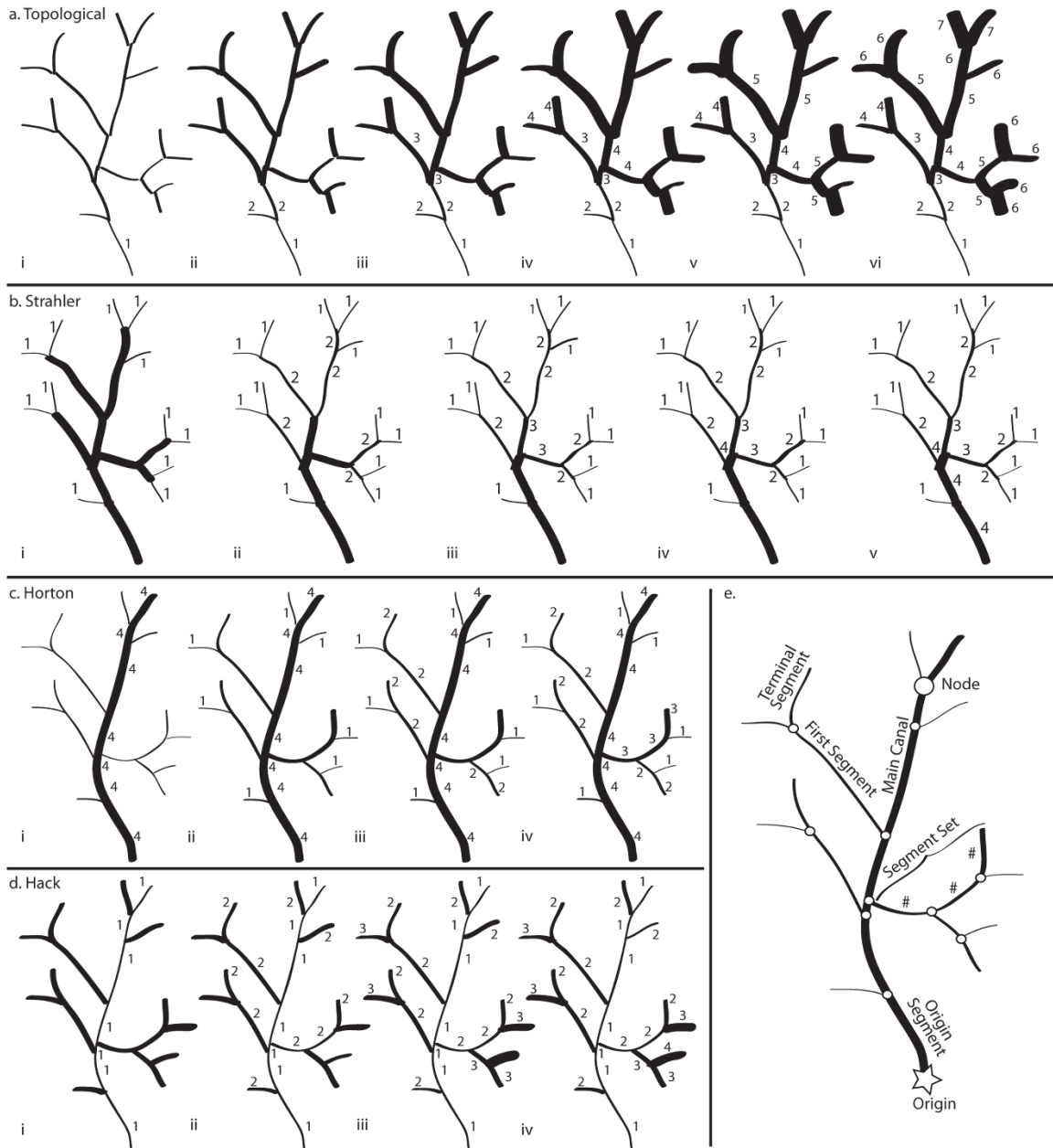


Figure 4.3. First segment order proportions. (a) Counts of Horton segments per order with segment counts (center) and percentages (top) and (b) Horton order count proportions vs. order.

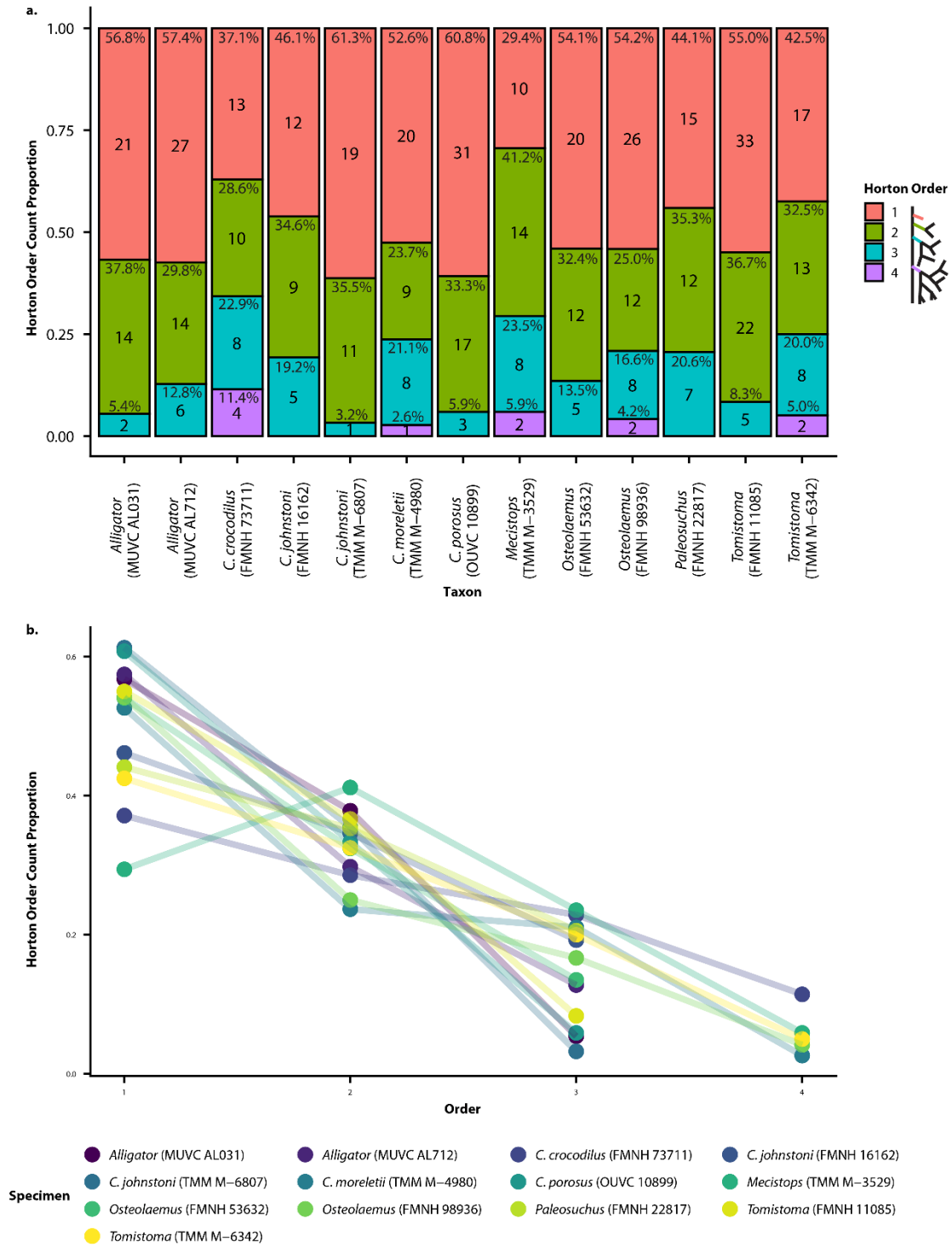


Figure 4.4. Avizo parameters. (a) Strahler segment counts vs. order per specimen. (b) Horton order count proportions vs. order per specimen. (c) Counts of Horton segments per order with segment counts (center) and percentages (top).

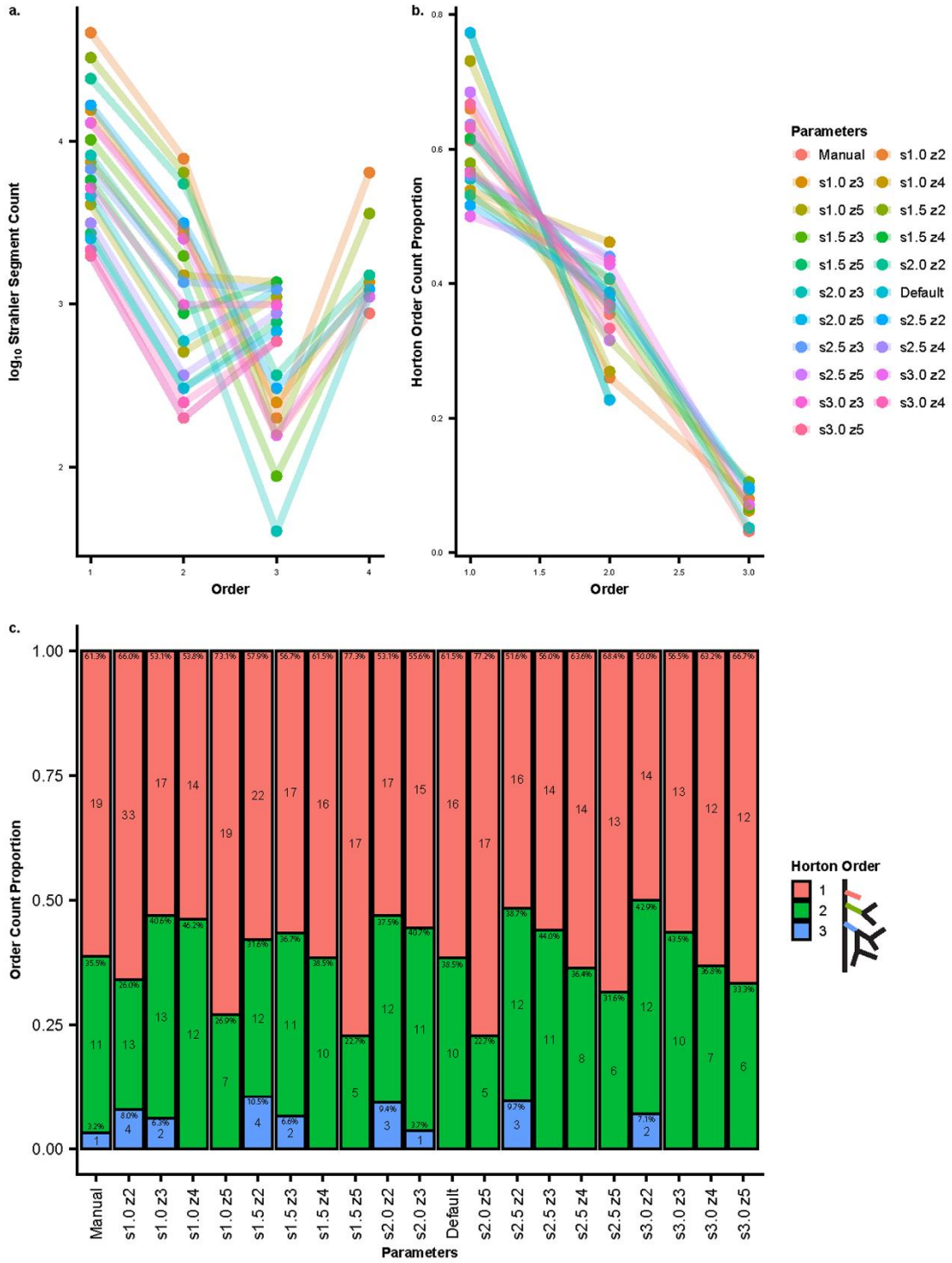


Figure 4.5. Topological complexity. Tally of terminal topological segments scaled to neurovascular canal length representing branch location along the neurovascular canal.

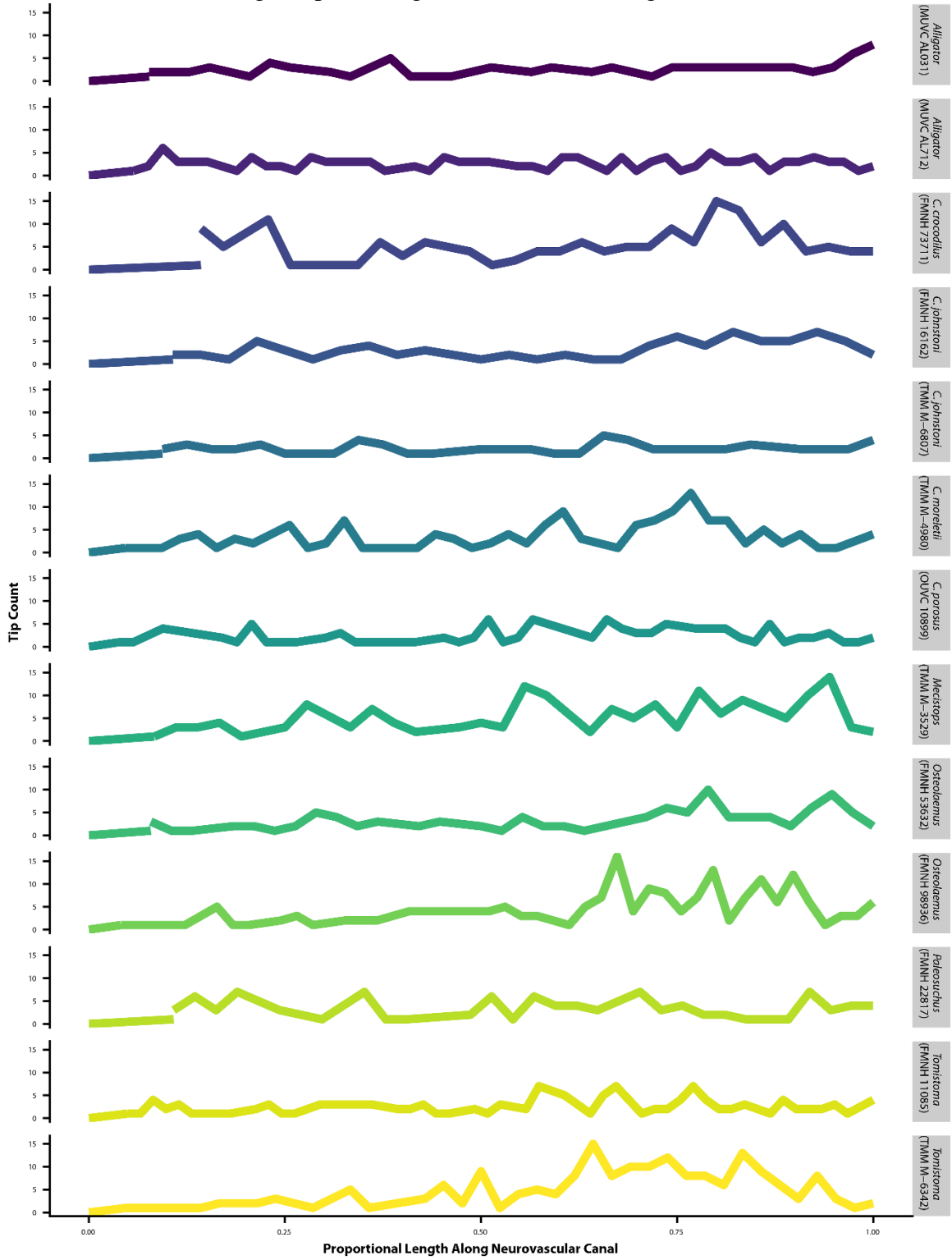


Figure 4.6. Topological center of mass and density metrics. (a) Topological center of mass vs. total length of the neurovascular canal. (b) Total neurovascular canal length vs. surface area of the dentary. (c) Number of segments vs. surface area of the dentary. (d) Number of tips vs. surface area of the dentary. Plots are fit with PGLS linear models.

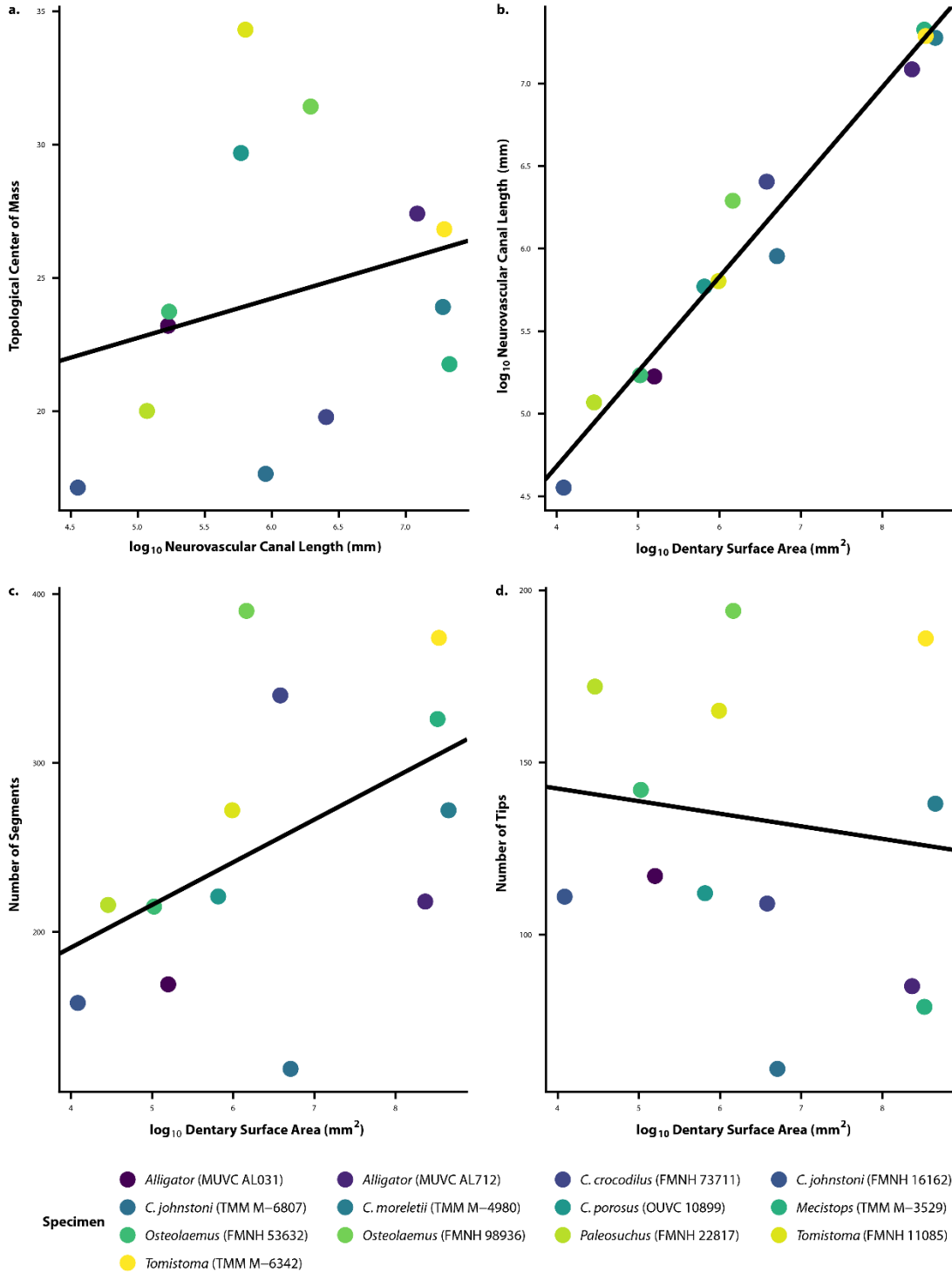


Figure 4.7. Segment count vs. order. (a) Horton, (b) Strahler, and (c) Hack segment counts vs. order and (d) Horton first branch counts vs. order.

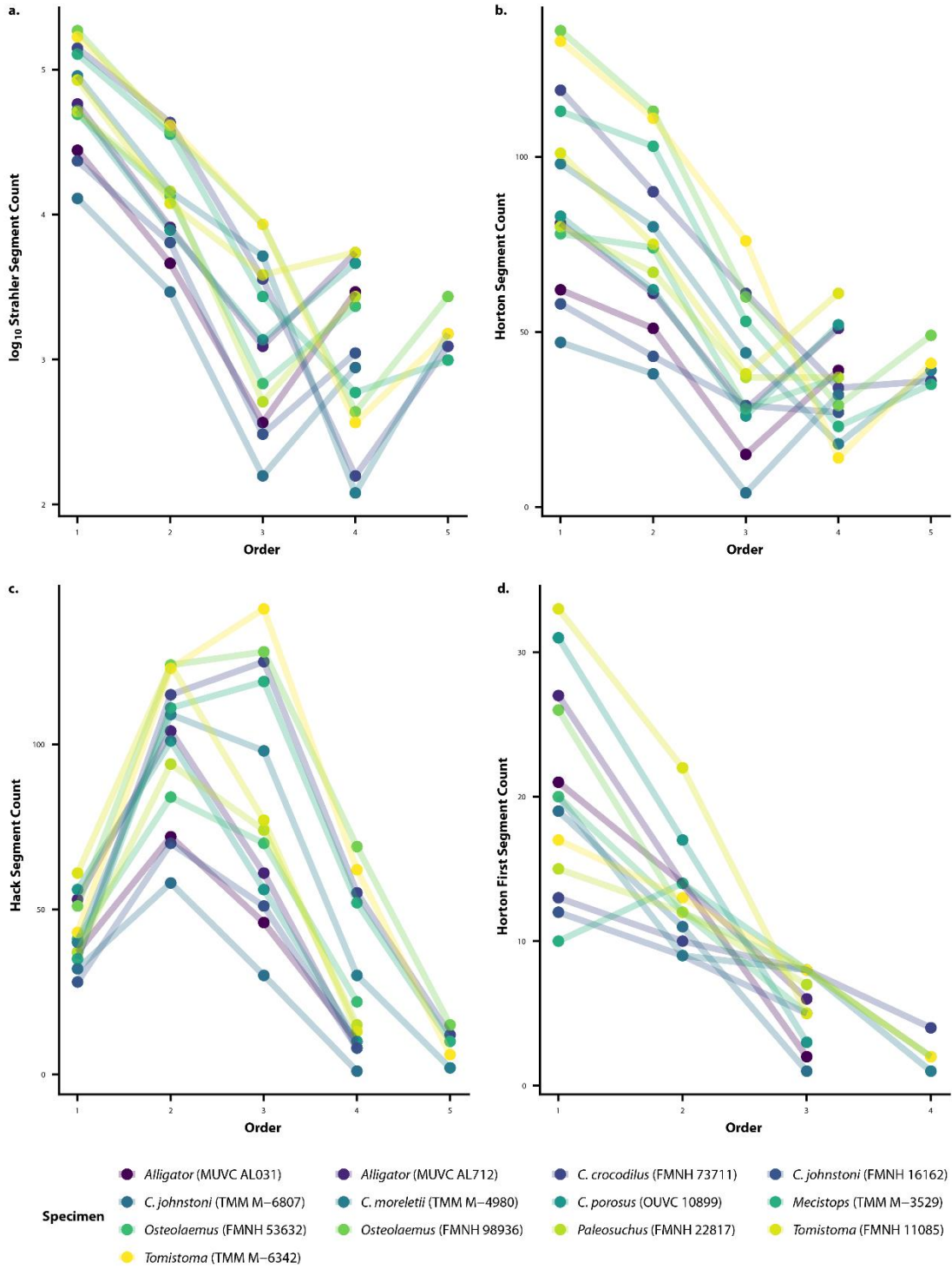


Figure 4.8. Mean segment lengths. Relative mean segment lengths vs. Strahler order per specimen.

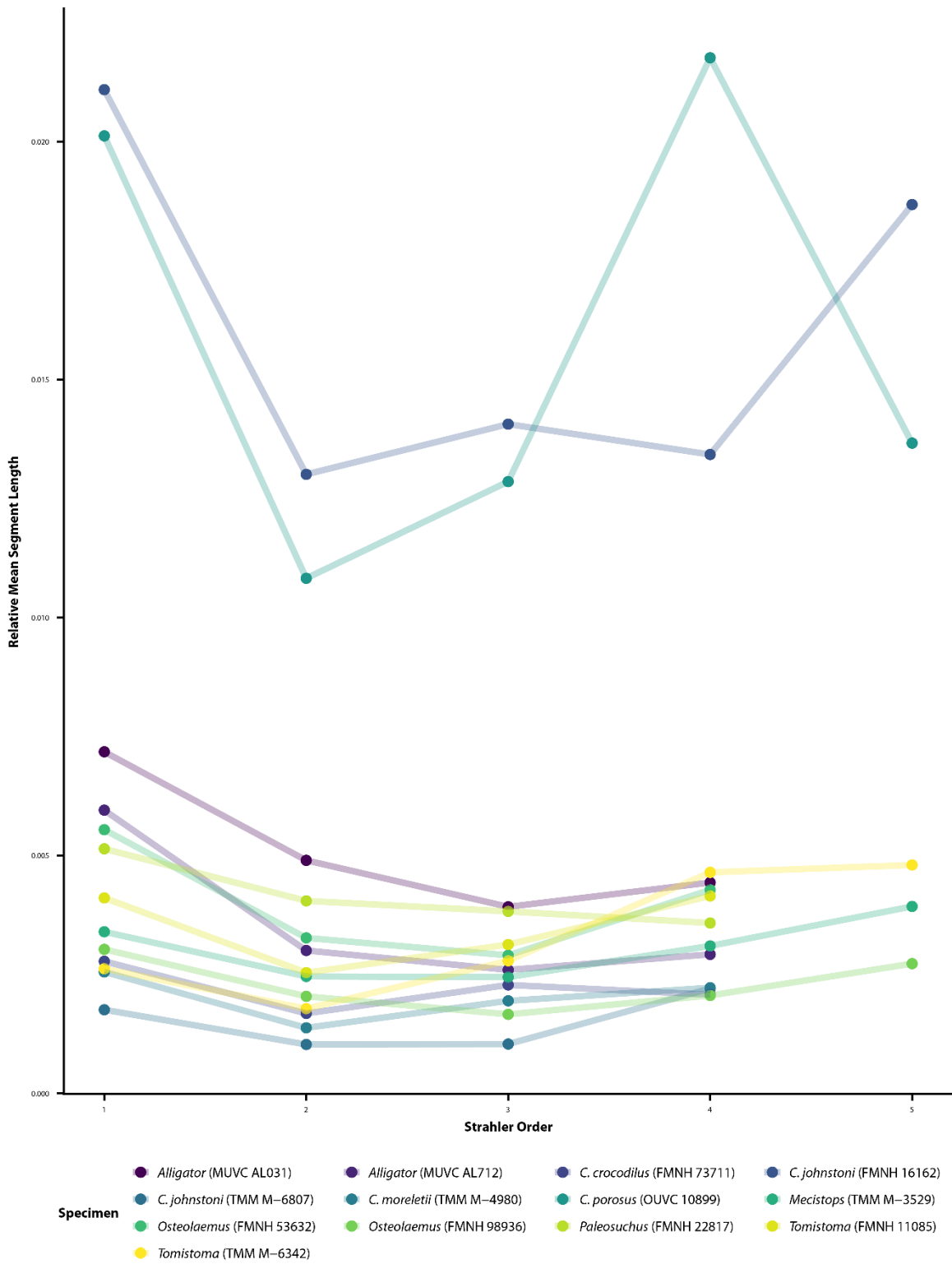


Figure 4.9. Density curves. Distribution of segment lengths (adjusted for body size) by Strahler order.

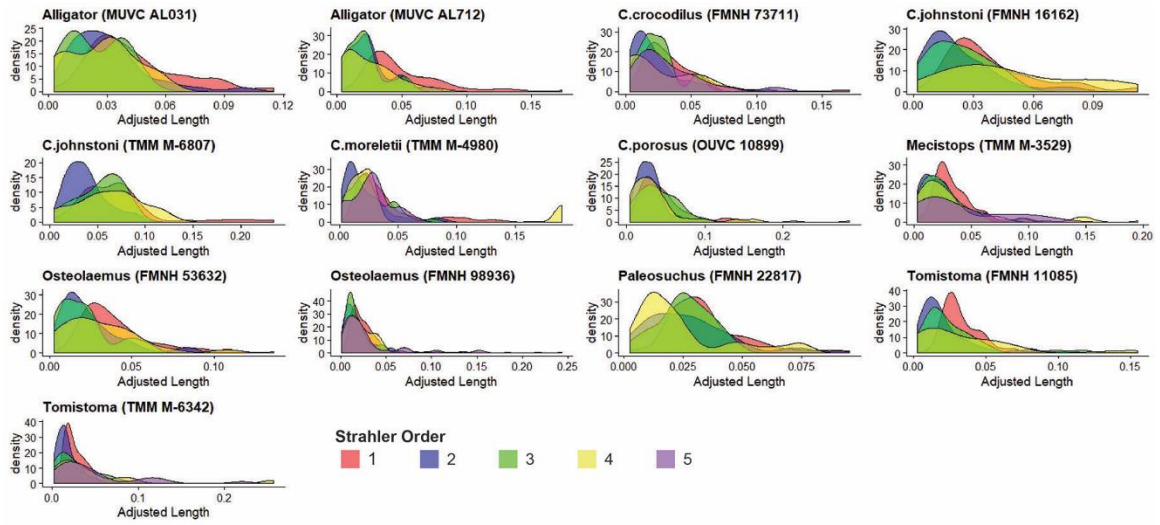


Fig. 4.10. Boxplots and density peaks. (a) Segment lengths (adjusted for body size) by Strahler order. (b) Peaks of density curves vs. Strahler order per specimen. (c) Median lengths (adjusted for body size) vs. Strahler order per specimen.

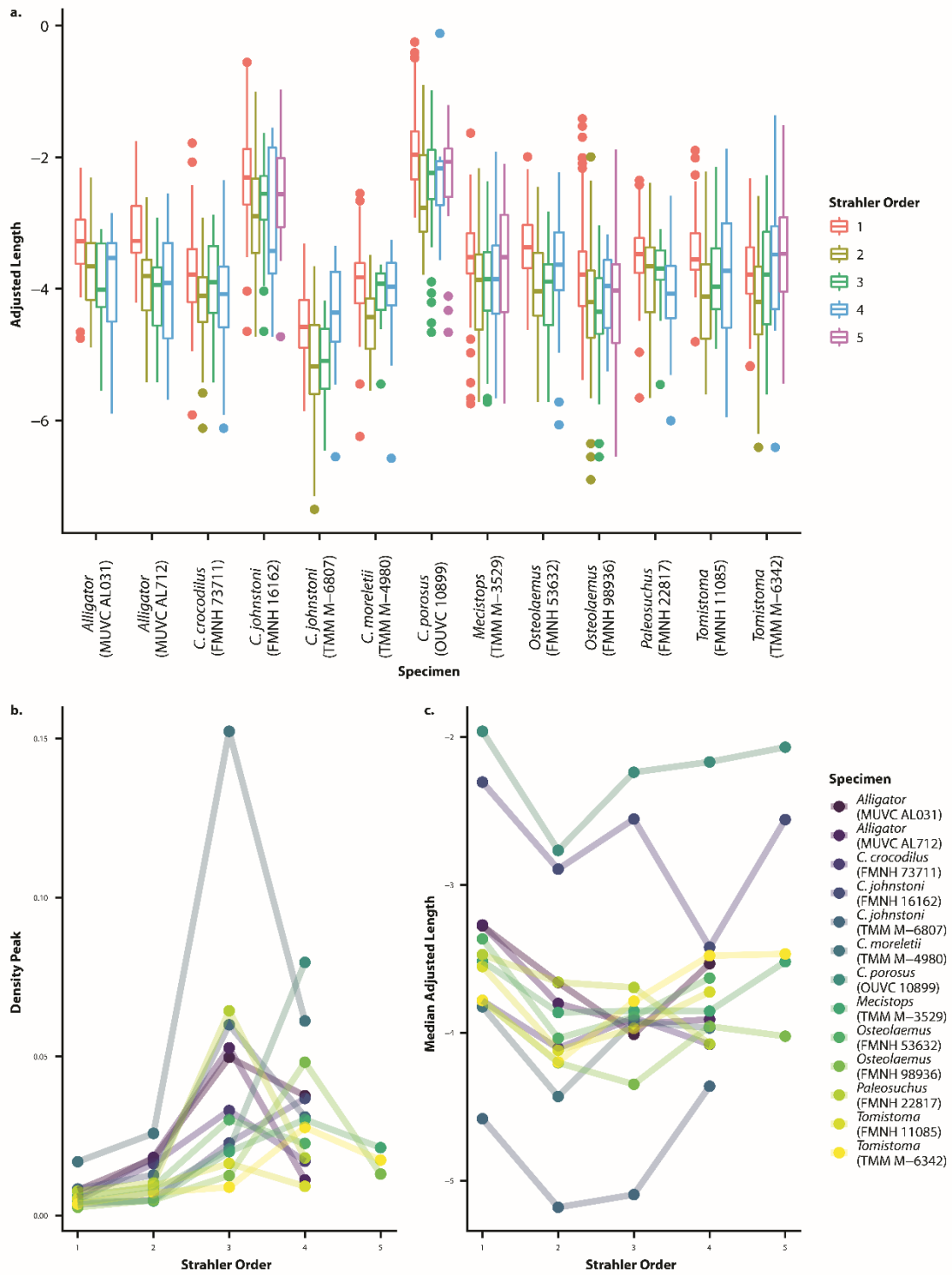


Fig. 4.11. Preliminary comparative data including all crocodylians and two avian taxa, *Anas* (grey) and *Phasianus* (black). (a) Counts of Horton segments per order with segment counts. (b) Total neurovascular canal length vs. surface area of the dentary. (c) Number of tips vs. surface area of the dentary. Previous plots (b and c) are fit with PGLS linear models for crocodylians only. (d) Strahler segment counts vs. order.

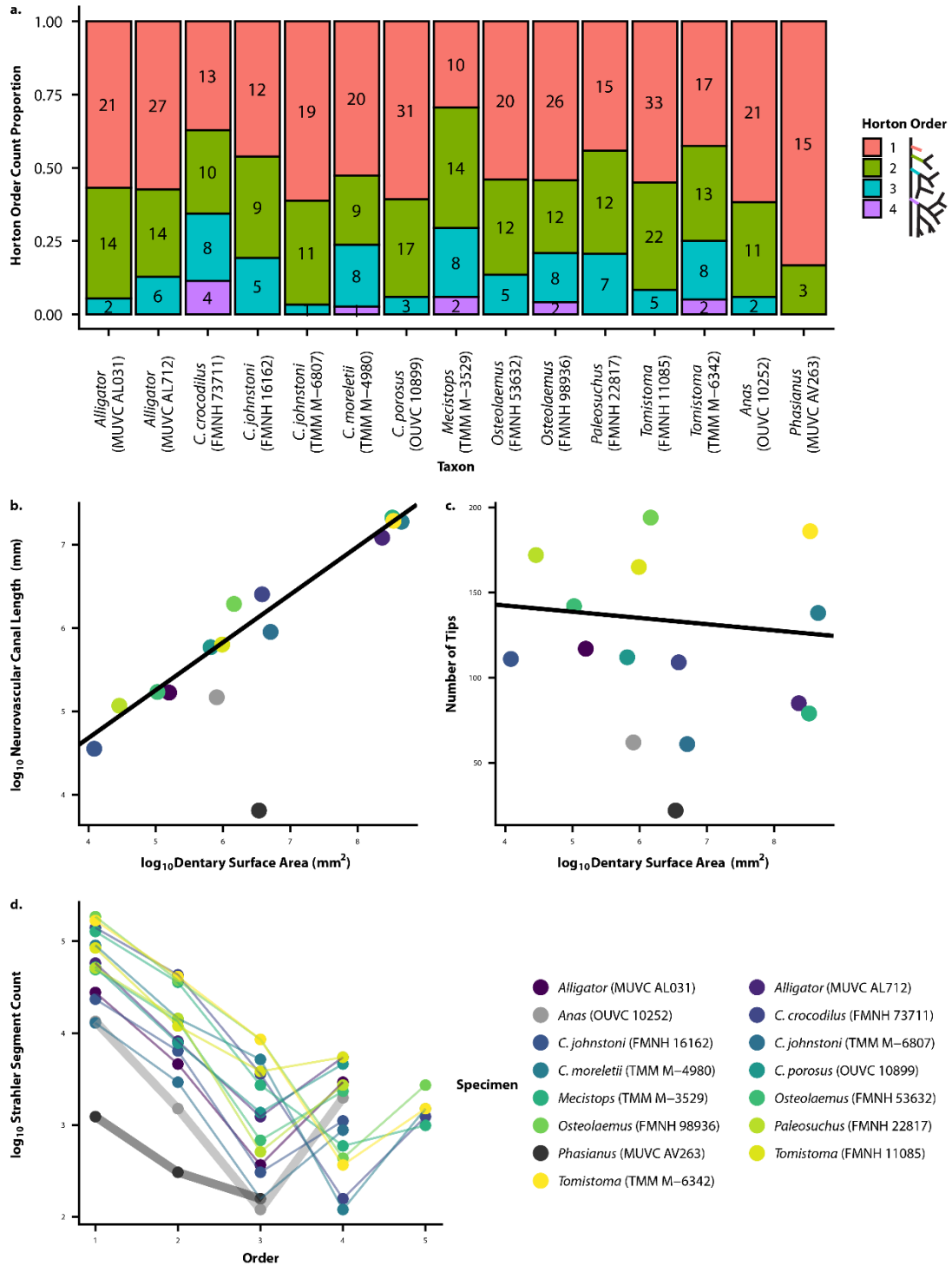
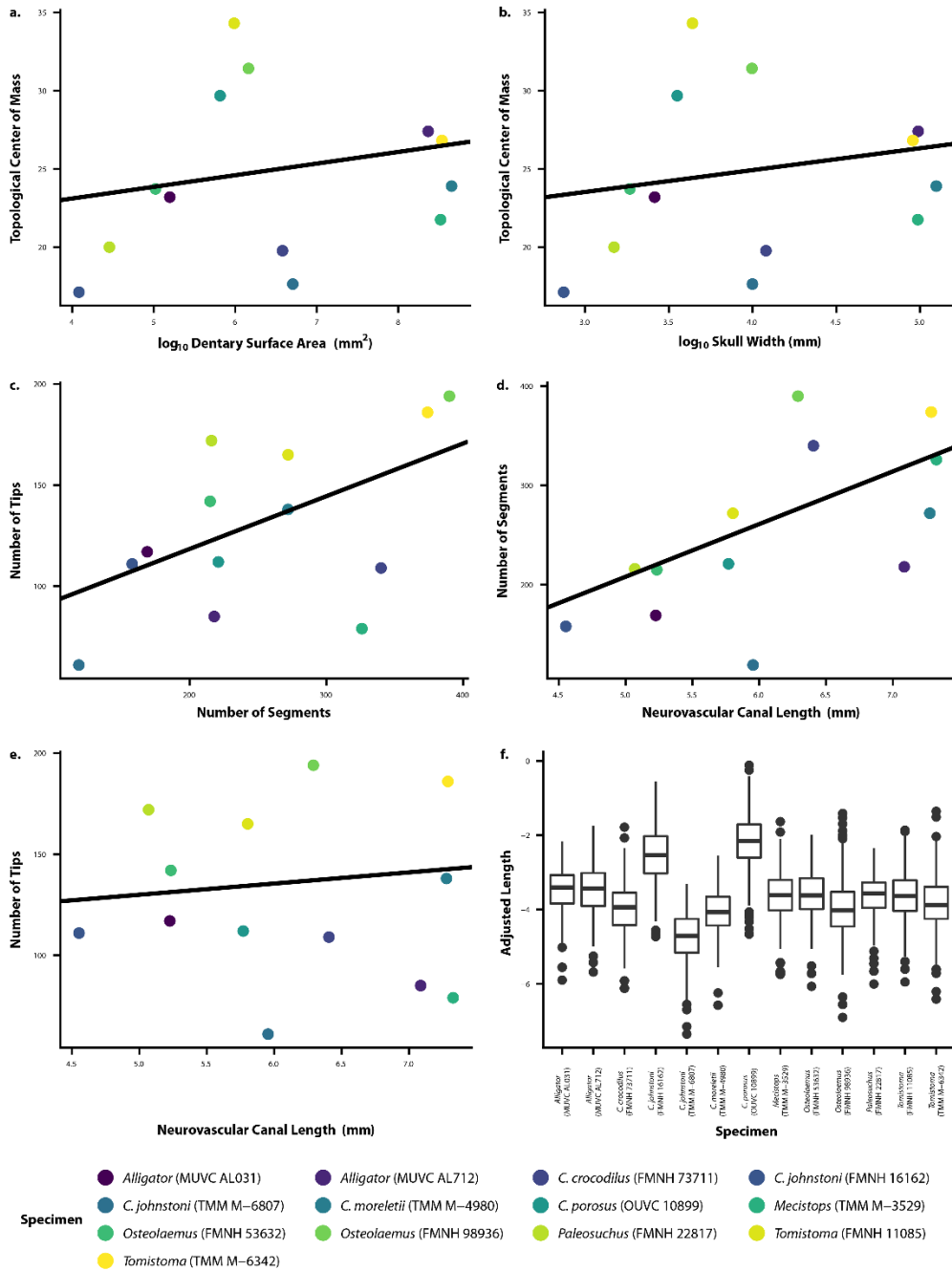


Fig. 4.12. Additional comparisons. (a) Topological center of mass vs. surface area of the dentary. (b) Topological center of mass vs. trans-quadratic skull width. (c) Number of tips vs. number of segments. (d) Number of segments vs. total length of the neurovascular canal fit with a linear model. (e) Number of tips vs. total length of the neurovascular canal. Plots (a-e) are fit with PGLS linear models. (f) All segment lengths (adjusted for body size); average of Fig. 4.10a



Chapter 5 — Ecomorphological patterns in trigeminal canal branching among sauropsids reveals suchian sensory shift

INTRODUCTION

The vertebrate trigeminal nerve is the primary mediator of somatosensory information from nerve endings across the face. The trigeminal nerve and associated neurovasculature leave osteological correlates in the form of foramina, depressions, grooves, and canals which can be traced along the pathway from hindbrain to integument through the skull. The trigeminal system, though conserved in general form, is diverse across vertebrates, particularly sauropsids, which have evolved extreme forms of cranial somatosensation as in probe-feeding birds, infrared-sensing pit vipers, and touch-sensitive crocodylians (Cunningham et al. 2010, Goris 2011, Leitch and Catania 2012). It remains to be understood how these adaptations for cranial sensation evolved among different clades of sauropsids, including specific lineages of lepidosaurs, crocodylians, and birds. Previous research has used osteological structures to predict nervous tissue anatomy in small ranges of extinct dinosaur and crocodylian species (e.g., Soares 2002, Rothschild and Naples 2017, Carr et al. 2017). However, these hypotheses require thorough testing using modern imaging, morphometrics, and phylogenetic comparative methods. Additionally, the osteological correlates of the peripheral trigeminal system have been little considered with respects to phylogeny (Benoit et al. 2021). Overall, we still lack consistent anatomical means of comparing relative sensation across lineages of reptiles, and the origins of extreme forms of sensation in the clade remain largely unexplored.

This research identifies patterns in form, function, and evolution of the sauropsid trigeminal system, focusing on tactile sensation of the lower jaws. Across lepidosaurs, integumentary sensory receptors are well known and their morphology and distribution

have been extensively studied. (e.g., Breyer 1929, Grace et al. 1999, Jackson and Doetsch 1977, Matveyeva and Ananjeva 1995). Tactile specialists remain unidentified (with the exception of the tentacled snake [Catania et al. 2010]) and function is less well known, but Hiller (1978) confirmed some receptors served a mechanosensitive function. Trigeminal-supplied bill-tip-organs are known from multiple families of probe- and tactile-foraging birds (e.g., Baumel and Witmer 1993, Berkhoudt 1980, Cunningham et al. 2010), and the presence of lower densities of beak tactile sensors have been noted in other clades of birds (e.g., Genbrugge et al. 2012, Van Hemert et al. 2012). Extant crocodylians are known for having highly-sensitive snouts covered with integumentary sensory organs (ISOs). In crocodylians, this sensory system is specialized for a semi-aquatic lifestyle, with the ability to sense minute changes in water pressure (Di-Poi and Milinkovitch 2013, Grap et al. 2020).

Wilberg et al. (2019) explored crocodylomorph morphological traits and depositional environments and established a sequence of habitat shifts within the clade. A notable transition within crocodylomorphs is the transition from a terrestrial to semiaquatic habitat at some point during the Early Jurassic (200-174 Ma) (Wilberg et al. 2019). The sensory system commonly changes in concert with habitat shifts (Thewissen and Nummela 2008). As such, all extant crocodylians are semiaquatic and have sensory systems specialized to this habitat including a highly-sensitive, trigeminal-innervated mechanosensory system (Soares 2002, Leitch and Catania 2012, Di-Poi and Milinkovitch 2013, Grap et al. 2020). It has been hypothesized this extant condition originated in the Early Jurassic based on the presence of rostral foramina (Soares 2002), and other trigeminal osteological correlates have been suggested as proxies for facial sensation

(e.g., George and Holliday 2013). However, these studies were limited in quantitative analysis and sample size.

Lessner (2020) introduced a method to quantify the complex branching patterns of mandibular neurovascular canals that terminate in tactile sensory receptors and hypothesized the method could discriminate between organisms of different sensory abilities. This project builds upon that work, using a sample of extant reptiles with known tactile sensory abilities to build predictive, statistical models for hypothesizing sensory ability across the fossil record and evolutionary transitions. The models use multiple variables, several of which are body size-independent, increasing predictive capacity. This allows ecological predictions to be drawn from isolated, and possibly even fragmentary, dentaries rather than requiring complete skulls.

MATERIALS AND METHODS

Whole-mount nerve staining

Whole mount nerve staining (Fig. 5.1) provides an alternative method of nerve visualization when high resolution, contrast-enhanced CT scanning is not possible. Specimens were fixed in 10% NBF, immersed in distilled water then hydrogen peroxide, and macerated in a sodium borate-trypsin solution as in Filipinski and Wilson (1986, see Lessner et al. 2019 for complete protocol). This was followed by immersion in water, ethanol, Sudan Black B stain, and glycerol. A Nikon Digital Sight U2/L2 camera and NIS-Elements F v 4.30.01 software were used to photograph specimens through a Nikon SMZ100 microscope.

CT scanning and segmentation

Thirty-five extant specimens (8 avians, 13 crocodylians, 14 lepidosaurs) and sixteen fossil specimens (1 archosauriform, 5 non-avian dinosaurs, 10 non-crocodylian

suchians) underwent computed tomography (CT) scanning at various resolutions allowing for visualization of bone and neurovascular canals (Fig. 5.2, Table 5.1). Neurovascular canal contents were verified and compared with canal size in representative extant taxa using contrast-enhanced (Gignac et al. 2016) CT scans (marked on Table 5.2, Fig. 5.3). These specimens were immersed in I₂KI (4.1-12.3% w/v) for varying durations. Scan data were imported as DICOM and TIFF files into Avizo v. 9 (Thermo Fisher Scientific; Waltham, MA) for segmentation and ImageJ (Schneider et al. 2012) for analysis. Magic wand and paint-brush tools with interpolation were used to segment rostral dentaries (the portion rostral to the complete enclosure of the mandibular canal by bone) and neurovascular canals within the rostral dentaries.

3D-model measurement and processing

Skull width was collected using the ‘Measure: 2D length’ tool, and cross sectional areas were collected in Avizo using the ‘Material Statistics: Area per slice’ module or in Image J. Dentary surface area was collected (of the lateral, integumentary, foraminiferous portion) using the surface editor and ‘Surface Area Statistics’ module. Neurovascular canals were reconstructed using the ‘Centerline Tree’ module, annotated with topological, Strahler, and Horton orders, and these values (segment lengths and orders) collected in attribute graph .xlsx files as described by Lessner (2020). Topological orders and Horton first segment orders were collected as well.

Derived quantities

The following quantities were calculated from combinations of the individual measurements described above:

Density metrics

Three derived quantities were used to quantify neurovascular canal distribution throughout and across the dentary. These include dendritic density (total neurovascular canal length vs. dentary surface area), segment frequency (number of neurovascular canal segments vs. dentary surface area), and tip frequency (number of terminal segments vs. dentary surface area) (Lessner 2020). Residuals from these comparisons were used in the analyses described below.

Topological center of mass (topological COM)

This quantity, describing the distance of terminal segments from the origin of the neurovascular canal, is collected as described by Lessner (2020) [$\bar{C} = C/(2n-1)$].

Topological tips

To compare branching extent along the neurovascular canal, terminal segment orders were tallied and orders scaled to canal length (in this case, the highest order per specimen). This resulted in each tip being designated a percentage representing its location along the canal. To explore morphological differences across individual sections of the neurovascular canal, each canal was also divided into 10 bins and number of tips per segment tallied and compared against the total number of tips. The resulting quantities were proportions of tips per bin of the neurovascular canal. These values were used in the analyses described below.

Quantities by order

Number of Strahler segments per order were tallied per specimen to quantify overall branching patterns. Number of Horton first segment orders were tallied to quantify complexity of branches from the main canal. Relative segment lengths were

collected (relative to rostrocaudal length of the dentary) and segment mean, median, and mode calculated per order to further quantify overall canal structure.

Analysis

The above variables were used to quantify structure of sauropsid neurovascular canals and test for shared morphological patterns within ecological groups. Density metric residuals were collected using phylogenetic linear models and R packages (caper) (Orme et al. 2013) and (phytools) (Revell 2012). Based upon observed behaviors from the literature, each extant specimen was assigned to one of two groups: those engaging in tactile-sensory behaviors and those in which tactile-sensory behaviors were absent (Table 5.2). Group differences were confirmed for all variables in R using the (phytools) (Revell 2012) package to run phylogenetic ANOVAs. Generalized linear models (i.e., logistic regression and discriminant analysis) were used to estimate probabilities to decide group membership for fossil specimens using R packages (stats) (R Core Team 2020), (mda) (Hastie and Tibshirani 2020), and (arm) (Gelman and Su 2020). The phylogeny used in analysis was an adapted phylogeny of Wilberg et al. (2019), Ruebenstahl (2019), Prum et al. (2015), Pyron et al. (2013), Carrano et al. (2012), and Makovicky et al. (2003). Multiple specimens per species were represented as hard polytomies and branch lengths were estimated using the R package (phytools) (Revell 2012) to calculate Pagel's lambda per variable (Pagel 1999). Significance was assessed at an alpha-level of $p=0.05$.

RESULTS

Gross anatomy

In general, the reptilian mandibular canal originates from the dorsolateral aspect of the Meckelian canal in the caudal dentary (discussion of name and homology below). From there it passes rostrally, extending branches dorsally to the alveoli and teeth and

laterally and rostrally to the integumentary surface of the dentary through foramina in the dentary. Here only branches to the integumentary surface of the dentary were quantified. Canal contents include the mandibular division of the trigeminal nerve and the mandibular artery and vein which occupy variable amounts of the canal space across taxa sampled (Table 5.3). Remarkable aspects of the mandibular canals and contents of the taxa investigated are detailed below.

The lepidosaur mandibular canal contains the mandibular nerve dorsally and the mandibular artery and vein ventrally and passes through the dentary ventral to the teeth. The lepidosaur mandibular canal has few accessory canals, and these begin branching from the mandibular canal just rostral to the complete enclosure of the neurovascular canal by the dentary and separation from the Meckelian canal. This separation occurs at the level of the 23rd (from rostral) dentary tooth in *Sphaerodactylus*, the 19th tooth in *Anolis*, the 17th tooth in *Crotaphytus* and *Pogona*, the 15th tooth in *Ctenosaura*, between the 11th and 12th tooth in *Uromastyx* and *Trioceros*, the 9th tooth in *Physignathus*, the 8th tooth in *Dracaena*, and caudal to the teeth in *Varanus* and *Sphenodon*. Though rostrally, the mandibular canal becomes distinct from the lepidosaur Meckelian canal and groove, the mandibular canal remains large, dwarfing its contents in *Uromastyx*, *Trioceros*, and *Physignathus*. *Eremias*, *Crotaphytus*, *Brookesia*, and *Varanus* display a different condition in which the mandibular canal becomes distinct from Meckel's cartilage at the complete enclosure of the neurovascular canal as in crocodylians (see below; also the rostral extent of the intramandibularis muscle in *Eremias*) and the canal has little extra space around the neurovasculature. *Dracaena*, *Sphaerodactylus*, *Anolis*, *Pogona*, *Sphenodon*, and *Ctenosaura* fall in between the above conditions, with a smaller

mandibular canal with some space around the contents. Generally, the mandibular canal is occupied by large vessels and the smaller mandibular nerve (Fig. 5.3). Sensory organs were visible in *Sphaerodactylus* (216) and *V. salvator* (600) and with 6 and 5 foramina, respectively each foramen distributes to 36 and 120 receptors. The foramina are arranged linearly, parallel and ventral to the tooth row (Fig. 5.4).

The canal in *Trilophosaurus* follows the expected pathway from Meckelian canal to rostral dentary and has an intermediate number of terminal segments (19), when compared to the lepidosaurs (4-7) and archosaurs (suchians 22-194); avemetatarsalians 14-268). The foramina associated with the terminal segments are arranged linearly, with few segments that do not parallel the tooth row.

The avian mandibular canal takes a number of forms depending on the taxon. Generally, the canal contains the mandibular artery and vein and similarly sized mandibular nerve with little room for other tissues (Fig. 5.3). The mandibular nerve enters the mandible near the rostral attachment of the pseudotemporalis profundus muscle (Holliday and Witmer 2007) first passing along the medial surface of the mandible before entering the dentary, sometimes dorsal to Meckel's cartilage (Crole and Soley 2016). The vessels are located either dorsal or ventral to the nerve. Because of the thinness of the dentary the distance from the canal to the keratinous beak are short and therefore branches are short. Branches typically do not occur in the caudal half of the dentary and are extremely concentrated at the tip in taxa engaging in tactile-sensory behaviors (e.g., *Scolopax*, *Anas*, *Arenaria*). In some taxa (e.g., *Alle*), the canal passes through the caudal dentary before the contents exit laterally, extending forward within a deep groove on the lateral surface of the dentary before reentering the dentary at the rostral tip. In many taxa,

including *Alle*, *Fulica*, *Phasianus*, and *Pandion*, the canal expands at the rostral tip of the dentary, terminating in a single, large foramen. The terminal foramina are generally clustered at the rostral tip in all avians but are not arranged in any particular pattern (Fig. 5.4). In *Anas* and *Scolopax*, the nerve is very large, occupying all of the mandibular canal and the canal occupying most of the dentary. In *Anas* the canal extends branches to the tomium as well as the lateral and ventral surface of the beak (these were not quantified) and terminates in an extreme density of branches at the bill tip organ (Fig. 5.1). This extreme density of branches is present across the rostral two-thirds of the *Scolopax* dentary and in both *Anas* and *Scolopax*, this density of nerve branches is reflected by a high density of foramina across the surface of the dentary. In *Psittacus* additional branching of the nerve occurs in the keratin after the neurovasculature exits the rostral tip of the dentary (these branches were not included in quantitative analysis).

Across the extinct dinosaurs sampled, the mandibular canal extends rostrally from the Meckelian canal to become a unique canal. In *Majungasaurus*, *Dilophosaurus*, and *Allosaurus* the mandibular canal extends from the dorsolateral aspect of the Meckelian groove and remains lateral to the alveoli for several teeth before moving ventral to the alveoli (Fig. 5.5). In *Tyrannosaurus* the canal extends rostrally from the lateral aspect of the Meckelian groove and passes ventromedial to the alveoli (Fig. 5.5). In *Dilophosaurus* the mandibular canal merges with the Meckelian canal at the level of the 8th dentary tooth (from rostral) then separates from the Meckelian canal at the level of the 4th tooth. In all non-avian dinosaurs sampled, branching occurs incrementally, generally with two branches to the lateral dentary surface per tooth until the rostral third of the dentary where more branches are present. This results in a line of foramina on the lateral surface

of the dentary ventral to the teeth and a scattering of foramina at the rostral aspect of the lateral surface of the dentary (Fig. 5.4).

The crocodylian mandibular canal contains the mandibular nerve laterally and the mandibular artery and vein medially and passes through the dentary ventrolateral to the alveoli and teeth. Accessory canals begin branching from the mandibular canal to the lateral surface of the dentary at the level of the rostral termination of the intramandibularis muscle and complete enclosure of the neurovascular canal by the dentary and separation from the Meckelian canal. Small vessels accompany larger nerves laterally through these numerous canals in the dentary to integumentary sensory organs (Fig. 5.3; Leitch and Catania 2012). The neurovasculature passing through an individual accessory canal supplies 2 to 4 sensory receptors (a range of 269 to 514 receptors and 85 to 172 foramina). Some of the foramina associated with the terminal segments are arranged in a line ventral to and paralleling the teeth, and the rest are arranged randomly, increasing in density towards the rostral tip (Fig. 5.4). In *A. mississippiensis*, *C. johnstoni*, *O. tetraspis*, and *P. palpebrosus* branch density notably increases near the level of the 8th and 9th dentary teeth (counted from rostral). In *T. schlegelii* a similar increase in density occurs near the level of the 15th (from rostral) dentary teeth, which seems to be a similar distance caudal from the symphysis (about 4 teeth) as the taxa listed above.

Across the extinct suchians sampled, it was only impossible to reconstruct the complete canal in *Pelagosaurus* because of poor contrast between bone and matrix. However, only the caudal origination from the mandibular canal was absent, a region lacking branches in many pseudosuchians. Otherwise, branch numbers increase rostrally in *Pelagosaurus*. The shortened and curved shape of the dentary of *Simosuchus* results in

a similarly blunted mandibular canal (Fig. 5.2). In *Simosuchus*, the canal originates as a small invagination dorsal to the large space for Meckel's cartilage, ventrolateral to the alveoli and teeth before continuing rostrally (Fig. 5.6). The *Araripesuchus* mandibular canal is larger than that of *Simosuchus*, occupying more of the dentary, but smaller than that of *Nominosuchus*. Both *Araripesuchus* and *Nominosuchus* were damaged at the rostral extent, but little of the mandibular canal was missing. In *Macelognathus* the mandibular canal originates on the lateral aspect of the Meckelian canal rather than the dorsal and the canal increases in diameter in the edentulous aspect of the dentary (Fig. 5.6). The *Junggarsuchus* mandibular canal increases in diameter rostrally as well between the 5th and 6th teeth (from rostral) and then quickly decreases in diameter rostrally. In *Junggarsuchus* at the level of the 8th tooth (from rostral) the Meckelian groove extends a canal laterally into the dentary, to which the mandibular canal extends a branch at the level of the 5th tooth (from rostral). Rostral to the 5th tooth in *Junggarsuchus*, this accessory Meckelian canal extends the branches to the rostromedial dentary surface, whereas the proper mandibular canal extends branches to the rostromedial dentary surface. A similar communication between the Meckelian canal and the mandibular canal occurs between the 7th and 8th tooth from rostral in *Litargosuchus* and just caudal to the 1st tooth in *Longosuchus* (though there is an edentulous, rostral portion of the *Longosuchus* dentary). Though the dentary of *Litargosuchus* is slenderer than the other suchians investigated, the mandibular canal does not appear to have decreased in diameter and therefore occupies a large cross section of the dentary. Both *Orthosuchus* and *Protosuchus* have a noticeable increase in branches at the level of the 3rd tooth (from rostral). all taxa except for *Junggarsuchus* and *Protosuchus*, the foramina

associated with the terminal segments are arranged randomly; in *Junggarsuchus* and *Protosuchus* there is a linear arrangement ventral to the tooth row and a small rostral scattering.

Canal contents

In lepidosaurs, nervous tissue in the caudal dentary ranges from occupying 34.3% to 5.5% of the canal, vascular tissue from 14.3% to 3% and all other contents from 91.5% to 51.4% (Table 5.3, Fig. 5.7). In the rostral lepidosaur dentary, near the symphysis, nervous tissue ranges from occupying 34.2% to 4.3%, vascular from 26.7% to 1% and all other contents from 90.7% to 40%. In birds, nervous tissue in the caudal dentary ranges from occupying 89.8% to 7.6% of the canal, vascular tissue from 20.7% to 3% and all other contents from 87.5% to 7.2%. In the rostral avian dentary, near the symphysis, nervous tissue ranges from occupying 68.9% to 14.8%, vascular from 40.1% to 8.5% and all other contents from 61.8% to 22.3%. In crocodylians, nervous tissue in the caudal dentary ranges from occupying 63.5% to 26.7% of the canal, vascular tissue from 19.7% to 4.6% and all other contents from 66.9% to 16.7%. In the rostral crocodylian dentary, near the symphysis, nervous tissue ranges from occupying 41.6% to 19.7%, vascular from 26.3% to 6.8% and all other contents from 69.7% to 37.1%. Taxa engaging in tactile sensory behaviors have higher percentages of nervous tissue occupying canals than those that do not engage in these behaviors (Table 5.3).

Canal cross sectional areas (CSAs) at the origin of the mandibular canal and symphyseal region were compared with skull width (a proxy for body size validated within crocodylomorphs by O'Brien [et al. 2019]). Though there is a significant, positive relationship between proximal canal CSA and skull width by pGLS ($p = 0.000$, $R^2 =$

0.501), phylogenetic ANOVA shows no significant differences between means of residuals between clades ($p = 0.952$) nor between tactile and non-tactile taxa ($p = 0.722$). There is also a significant, positive relationship between symphyseal canal CSA and skull width by pGLS ($p = 0.000$, $R^2 = 0.844$), and phylogenetic ANOVA of means of residuals between clades shows no significant differences between clades ($p = 0.856$) nor between tactile and non-tactile taxa ($p = 0.595$). Though relationships are insignificant it does appear that taxa engaging in tactile sensory behaviors exhibit larger CSAs (Fig. 5.7). Pearson correlations coefficients between canal and nerve contents are 0.565 for the proximal canal ($p = 0.004$) and 0.922 for the symphyseal canal ($p < 0.001$). Correlations coefficients between canal and vessel contents are 0.819 for the proximal canal ($p < 0.001$) and 0.726 for the symphyseal canal ($p < 0.001$).

Topological Tips

Crocodylians show a high density of tips along entire length of the canal with an increase in density at the rostral end of the dentary (Figs. 5.8-9). Lepidosaurs have few tips, but these are evenly spaced across the canal. *Trilophosaurus* shares a similar pattern. Some birds follow a similar pattern as lepidosaurs, but birds with tactile ecologies (e.g., *Anas*, *Scolopax*) have higher densities of tips across the length of the canal and highest tip densities at the rostral end of the dentary. Fossil dinosaurs and suchians show similar tip distributions to avians. Within extinct avemetatarsalians, the dentary has few tips spread uniformly across the dentary in most taxa examined (Fig. 5.9). *Majungasaurus* and *Tyrannosaurus* have a slight increase in tips at their rostral extent, whereas *Allosaurus* has a rostral radiation of tips. Within extinct pseudosuchians, the dentary has tips spread

uniformly across the dentary with most taxa (except for *Longosuchus*, *Nominosuchus*, and *Araripesuchus*) also exhibiting an increase in tips at the rostral end.

Phylogenetic ANOVA of numbers of tips across 10 bins representing the length of the canal (Fig. 5.9) shows no significant difference in tips across the length by clade ($p = 0.319$). However, tactile and non-tactile taxa do have near-significant differences in tip distribution across the length of the canal ($p = 0.043$).

Binned tips were compared using linear discriminate analysis across the extant taxa. The resulting model predicted extant ecology with 91% accuracy (only *Arenaria* and *Psittacus* with nearly incorrect predictions), with few posterior probabilities within 20% of one another. The resulting model was used to predict ecology in the fossil taxa and bin predictions of all taxa were compiled into a ‘percent tactile’ (Table 5.2) (empty bins were scored as 0% tactile on the basis that tactile sensation requires innervation). The fossil posterior probabilities were also largely not within a 20% margin. Excluding just *C. johnstoni* (TMM M-6807) at 70%, all crocodylian taxa were 80-100% tactile. Tactile-avian taxa were between 50-100% tactile and non-tactile avian taxa between 10-60% tactile. Lepidosaurs were between 0-10% tactile. All dinosaurs were between 30-80% tactile, suchians between 20-80% tactile, and *Trilophosaurus* was 20% tactile.

Density Metrics and Topological COM

Dendritic density

By pGLS, there is a significant, positive relationship between rostral dentary surface area and total canal length ($p = 0.000$, $R^2 = 0.8502$) across all taxa (Fig. 5.10). Residuals of this relationship were collected to represent a single metric for dendritic density. In extant taxa, clade means are not significantly different ($p = 0.332$) but

differences between tactile and non-tactile taxa are significant ($p = 0.063$) as revealed by phylogenetic ANOVA.

Segment frequency

By pGLS, there is a significant, positive relationship between rostral dentary surface area and number of canal segments ($p = 0.000$) (Fig. 5.10). However, there is high variability across the data ($R^2 = 0.5067$). Residuals of this relationship were collected to represent a single metric for segment frequency. In extant taxa, clade means are not significantly different ($p = 0.274$), but differences between tactile and non-tactile taxa are significant ($p = 0.019$) as revealed by phylogenetic ANOVA.

Tip frequency

By pGLS, there is a significant, positive relationship between rostral dentary surface area and number of terminal segments ($p = 0.000$) (Fig. 5.10). However, there is high variability across the data ($R^2 = 0.3304$). Residuals of this relationship were collected to represent a single metric for tip frequency. In extant taxa, clade means are not significantly different ($p = 0.445$), but differences between tactile and non-tactile taxa are significant ($p = 0.073$) as revealed by phylogenetic ANOVA.

Topological COM

By pGLS, there is a significant, positive relationship between rostral dentary surface area and topological center of mass ($p = 0.0000$) (Fig. 5.10). However, there is high variability across the data ($R^2 = 0.3630$). Residuals of this relationship were collected to represent a single metric for topological center of mass. In extant taxa, clade means are not significantly different ($p = 0.472$), but differences between tactile and non-tactile taxa are significant ($p = 0.100$) as revealed by phylogenetic ANOVA.

Residuals of the above density metrics and topological center of mass against rostral dentary surface area were collected and compared using linear discriminant analysis across the extant taxa. The resulting model predicted extant ecology with 97% accuracy (only *Fulica* being predicted incorrectly), with few posterior probabilities within 70% of one another. The resulting model was used to predict ecology in the fossil taxa (Table 5.2). The fossil posterior probabilities were also largely not within a 30% margin.

Quantities by order

Strahler segment counts

Crocodylians and *Scolopax* have the most segments and lepidosaurs the fewest, with all other avian and fossil taxa falling in between (Fig. 5.11). Two patterns are evident. The first, seen in lepidosaurs, some avians, and some fossil taxa, segment count decreases as order decreases. The second forms a ‘check-mark’, seen in crocodylians, some avians, and some fossil taxa, where count order decreases to the second to last order present and then increases to the final order. In extant taxa, phylogenetic ANOVA shows clade means are significantly different ($p = 0.001$), with significant differences between avians, lepidosaurs, and crocodylians. Differences between tactile and non-tactile taxa are significant ($p = 0.001$).

Segment counts per order were compared to extant ecology with multiple regression and only first order segment counts were found to be significant ($p = 0.02835$). Logistic regression using only extant, first order segment counts predicts extant ecology with 97% accuracy (only *Arenaria* being predicted incorrectly) and with a 60% margin

between posterior probabilities. Probabilities from prediction of fossil ecology by first order segment counts (Table 5.2) are not within a 20% margin.

Horton first segment counts

Across most taxa (all but *Scolopax*, *Mecistops*, and *Araripesuchus*), there are fewer first segments as order increases (Fig. 5.11). Crocodylians and *Protosuchus* had first segments up to Horton order 4, whereas lepidosaurs only had first segments of Horton order 1. All other taxa fell in between. Phylogenetic ANOVA of extant taxa shows clade means are nearly significantly different ($p = 0.074$), but differences between tactile and non-tactile taxa are significant ($p = 0.015$).

Horton first segment counts per order were compared to extant ecology with multiple regression and only first and second order first segment counts were found to be significant ($p = 0.00585$, $p = 0.00302$). Logistic regression using only extant, first and second order first segment counts predicts extant ecology with 95% accuracy (only *Arenaria* and *Phasianus* are predicted incorrectly and only for first order first segments) with a 20% margin between posterior probabilities. Probabilities from prediction of fossil ecology by first and second first segment counts (Table 5.2) are not within an 18% margin.

Mean relative segment lengths

Exploring mean segment lengths per Strahler order relative to rostrocaudal dentary length, lepidosaur segments are the longest and crocodylian and *Scolopax* segments the shortest, with all other taxa falling between (Fig. 5.12). In lepidosaurs and *Alle*, second order relative segment means are higher than first order, whereas second order relative segment means are lower than first order in other taxa. Phylogenetic

ANOVA of extant taxa shows clade means are significantly different ($p = 0.003$), with a significant difference between lepidosaurs and crocodylians and a nearly significant difference between lepidosaurs and avians. Differences between tactile and non-tactile taxa are significant ($p = 0.001$).

Mean segment lengths per order were compared to extant ecology with multiple regression and only first, second, and third order segments were found to be significant ($p = 0.0258$, $p = 0.0294$, $p = 0.0301$). Logistic regression using only extant, first, second, and third order segment means predicts extant ecology with 98% accuracy (only *Arenaria* and *Phasianus* predicted incorrectly for order 3) with a 20% margin between most posterior probabilities. Probabilities from predictions of fossil ecology by first, second, and third relative mean segment lengths are mostly not within a 25% margin and predictions are reported as a percentage (Table 5.2).

Median relative segment lengths

Exploring median segment lengths per Strahler order relative to total canal length, results follow that described for mean relative segment lengths above with clade means significantly differing ($p = 0.027$) and pairwise corrected p-values indicating near significant differences between crocodylians and lepidosaurs and avians and lepidosaurs. Ecological means differ significantly ($p = 0.001$) (Fig. 5.12). As above, first, second, and third order segments were found to be significant with multiple regression ($p = 0.0001$, $p = 0.00008$, $p = 0.00008$), and logistic regression using extant first, second, and third segment medians predicts extant ecology with 91% accuracy (only *Paleosuchus*, *Pandion* and *Psittacus* are predicted incorrectly for second order segments and *Fulica*, *Sphaerodactylus*, and *Trioceros* for first) with a 20% margin between most posterior

probabilities. Probabilities from predictions of fossil ecology by first, second, and third relative median segment lengths are mostly not within a 20% margin, and predictions are reported as a percentage (Table 5.2).

Mode relative segment lengths

Exploring mode segment lengths per Strahler order relative to rostrocaudal dentary lengths, lepidosaur segments are longest and crocodylians shortest with all other taxa falling between (Fig. 5.12). For all lepidosaurian taxa, most second order segments are longer than first order segments, though for all other taxa, this is the opposite (Fig X). Phylogenetic ANOVA of extant taxa shows clade means are significantly different ($p = 0.006$) but pairwise corrected p -values show significant differences between lepidosaurs and crocodylians only. Differences between tactile and non-tactile taxa are significant ($p = 0.004$). As above, first, second, and third order segments were found to be significant with multiple regression ($p = 0.00006$, $p = 0.001$, $p = 0.001$), and logistic regression using extant first, second, and third segment modes predicts extant ecology with 93% accuracy (only *Anas*, *C. johnstoni* [TMM M-6807], *Fulica*, and *Paleosuchus* first order and *Pandion* second and third orders are predicted incorrectly), with few posterior probabilities within a 40% margin. Probabilities from predictions of fossil ecology by first, second, and third relative mode segment lengths are mostly not within a 20% margin, and predictions are reported as a percentage (Table 5.2).

DISCUSSION

The mandibular canal, morphology and homology

The caudal, or proximal, extent of the canal quantified in this project is marked by the complete enclosure of the mandibular nerve and vasculature by the bony dentary. Location and homology of this canal (i.e., mandibular canal, inferior alveolar canal)

across reptiles has received little attention in the literature, and here is termed the ‘mandibular canal’ in order to include edentulous taxa. Romer (1956) describes its origination in the reptilian Meckelian fossa and calls it the ‘Meckelian canal,’ but the neurovasculature and Meckel’s cartilage do not share the same pathway through the dentary in all taxa.

Across non-avian reptiles, Meckel’s cartilage and the mandibular neurovasculature typically pass through the Meckelian fossa together but are enclosed by distinct canals further rostrally (Oelrich 1956). This rostral division appears to occur just rostral to the medially branching oral intermandibular nerve (sometimes the lingual nerve, anterior mylohyoid nerve; Poglayen-Neuwall 1953, Abdel-Kader et al. 2010, Watkinson 1906, Oelrich 1956) and thus is obscured by the splenial in intact skulls (Fig. 5.4). This division of canals is also near the rostral extent of the intramandibularis muscle in crocodylians, lacertid lepidosaurs (e.g., *Eremias*), and charadriiform (e.g., *Alle*) and procellariiform birds though this muscle is not homologous across reptiles (Iordansky 2008, Daza et al. 2011).

In birds there is also a ‘Meckelian fossa,’ termed the *fossa aditus canalis mandibulae* (fossa leading to the opening of the mandibular canal; Baumel & Witmer 1993) but Meckel’s cartilage does not always persist in adult forms. In *Struthio* and *Dromaius* Meckel’s cartilage and the neurovasculature share a single canal through the mandible (Crole & Soley 2018), and in *Phasianus* Meckel’s cartilage departs the mandibular canal quite rostrally. In birds lacking Meckel’s cartilage, there is a single mandibular canal.

Even less discussion exists in the fossil literature. A foramen within the Meckelian canal is noted in the archosauriform *Osmolskina* and hypothesized to house the mandibular nerve (Borsuk-Bialynicka & Evans 2008). A neurovascular foramen is also described within the Meckelian canal in a hylaeochampsid suchian (Yi et al. 2017). With respect to theropod dinosaurs, the Meckelian groove in *Poekilopleuron?*, *Allosaurus*, and *Sinraptor* contains dorsal and ventral foramina, and the dorsal canal is hypothesized to have housed the mandibular neurovasculature (Allain 2002). In the context of edentulism, Wang et al. (2017) details an additional alveolar canal dorsal to the mandibular canal in *Limusaurus*, Caenagnathidae, and *Sapeornis* that is likely homologous to the alveoli of toothed archosaurs.

Comparative CT data allow for some clarification, helping distinguish canals, their distribution, and contents (in the case of contrast-enhanced data). A canal may be identified as transmitting the mandibular neurovasculature by its communication with alveoli or the tomial surface as well as the lateral integumentary surface. Across the reptiles investigated in this study, the percentage of canal contents vary both rostrocaudally within an individual and across individuals (Fig. 5.7). The only evident trend is that the taxa engaging in tactile sensory behaviors dedicate more canal space to nervous tissue than taxa not engaging in tactile sensory behaviors. Exploring the cross sectional area of the mandibular canal as an osteological correlate for nervous or vascular contents reveals that the proximal CSA is not well correlated with nervous CSA and is somewhat correlated with vascular CSA. The canal at the symphysis is well correlated with nerve CSA and somewhat correlated with vascular CSA. However, since there is no significant relationship between mandibular canal CSA and ecology in extant taxa, in

combination with the observation that canal contents are highly variable, mandibular canal CSA cannot be used to predict sensory ability in fossil taxa. Similarly, volume of the mandibular canal is not a reliable proxy for sensory ability, especially because of the varied overlap with Meckel's cartilage and distribution to differing numbers of teeth.

Quantification of canal morphology and comparison

Exploring the tips by the topological ordering method reveals high distributions of tips across the dentary (independent of size) in extant taxa engaging in tactile sensory behaviors in contrast to few tips across the dentary in non-tactile taxa. In addition, extant tactile taxa have an increase of tips at the rostral end of the mandible (Figs. 5.8-9). This finding is in agreement with the presence of bill tip organs in ducks and probing birds (Cunningham et al. 2013, Berkhoudt 1976, Avilova 2018, Hoerschelmann 1972) and supports the hypothesis that the rostral end of crocodylian mandibles functions similarly, with smaller receptive fields and increased discriminatory abilities in comparison with the rest of the mandible (Leitch and Catania 2012). From the condition in the lepidosaurian taxa and the archosauriform *Trilophosaurus*, it appears the basal archosaurian condition is a mandibular canal with few tips, evenly distributed across the dentary (Figs. 5.8, 5.13, 5.14a). Though there is little evidence of a pattern within the avemetatarsalians, perhaps because of a smaller sample size, the rostral increase in tips within the extinct pseudosuchians suggests origins of the derived, extant crocodylian condition within more basal members of the clade. Terminal segment distribution may be visualized by observation of foramina on the dentary surface (Figs. 5.14-15). Across reptiles there tends to be a line of terminal segments just ventral to and paralleling the alveoli. In archosaurs, another line of terminal segments parallels the ventral border of

the dentary. Among basal pseudosuchians and avemetatarsalian taxa, there are few randomly distributed foramina across the rostralmost dentary (Fig. 5.14b-i, 5.15), whereas among derived pseudosuchians, there are far more foramina distributed densely across much of the dentary (Fig. 5.14j-w).

Density metrics (i.e., residuals of dendritic density, segment frequency, tip frequency) are all larger in taxa engaging in tactile sensory behaviors than non-tactile taxa. Large density metrics indicate increased distribution of nervous tissue to the integument covering the dentary and therefore increased discrimination and decreased receptive field size (Fig. 5.10). Similarly, the large topological center of mass in taxa engaging in tactile-sensory behavior indicates a larger distance (in segments) between the origin of the canal to terminal segments. As such, a larger topological center of mass suggests more accessory branching and topological complexity regardless of size within the dentaries of taxa engaging in tactile sensory behaviors. The predictive model developed from this set of values was the most accurate (at 97%). The categorization of *Fulica* as tactile rather than the non-tactile status it was assigned may signal morphological and sensory convergence with ducks. In fact, feeding convergence has been noted between coots, dabbling ducks, and other waterfowl (Allouche and Tamisier 1984), and similar feeding styles may necessitate similar sensory requirements.

Strahler segment counts are in agreement with topological center of mass values. Larger Strahler segment counts are present in taxa engaging in tactile sensory behaviors and smaller counts are present in non-tactile taxa (Fig. 5.11). Additionally, in non-tactile taxa, segment count tends to decrease as order increases, which is the case for tactile taxa until the final order, in which there is an increase in segment counts. The highest ordered

segments in the Strahler ordering method are the segments along the caudal portion of the main canal. More of these segments means that complicated branches (i.e. with third or fourth order first segments) are present immediately at the rostral end of the canal. Fewer high order segments means that such complicated branches are absent, or they occur further caudally. Exploration of Horton branches confirms this. Non-tactile taxa have few Horton branches larger than the second Horton order. Accessory canals in tactile taxa are not only more complex than those in non-tactile taxa, but there are also more accessory canals, thus distributing a higher density of tips across the density in these taxa.

The three metrics used to quantify relative Strahler segment length (i.e., mean, median, and mode) generally provide the same results (Fig. 5.12). Segment length results again indicate *Fulica*'s categorization as non-tactile taxon may be incorrect (see above). The longer length of lepidosaur segments relative to tactile taxa seems to be because the lack of branches fail to break the neurovascular canal into segments. When taxa have high segment counts, frequency of short segments is often higher (Fig. 5.12). Longer second order segments in lepidosaurs than in other taxa reflect the lack of interruption of second order segments by additional branches. This trend continues in other taxa in which the higher order segments tend to be longest because their terminal nature means they are uninterrupted.

Assumptions, limitations, and constraints

Before exploring the predictions derived from the metrics and models described above there are assumptions made that are important to take into consideration. These predictions are based on an osteological correlate (i.e., the mandibular canal) of a soft tissue feature (i.e., mandibular nerve). This study has been able to quantify the bony

morphology necessary to distribute nerves and enable trigeminal-innervated tactile sensation in extant taxa and assessed the same bony morphology in extinct taxa. Most extant taxa have had contents verified (Fig. 5.3) and nerves are present. However, nerve and vessel development are tightly connected, sharing molecular mechanisms for pattern formation and guiding one another via molecular expression (Mukoyama et al. 2002, Carmeliet and Tessier-Lavigne 2005) so it cannot be certain that one has more influence than another. Canal contents are quite variable (Fig. 5.7), and therefore canal contents remain uncertain and predictions tentative. Though across the extant taxa explored, dendritic branching does not occur in taxa exhibiting tactile sensory behaviors regardless of canal contents. Additionally, across reptiles not all nerve distribution and branching occur within bone (Fig. 5.1e). It is possible that additional branching once nerves have exited canals within the dentary allows for widespread distribution of nervous tissue.

Because dentary length was used as a size proxy in metrics relying on size (i.e., mean, median, and mode relative segment lengths), predictions based on these metrics may not be completely accurate in the cases of taxa with elongated or truncated dentaries (e.g., *Litargosuchus*, *Simosuchus*). Initial exploration of segment length relative to the total length of the canal (Lessner 2020) largely reflected the number of segments present rather than providing comparative data on segment lengths across taxa. Dentary length was used instead in the absence of complete skulls for all taxa, in which case skull width might be a useful replacement proxy for body size (O'Brien et al. 2019). It is expected this method would work for fragmentary specimens as well (i.e., *Pelagosaurus*) because an incomplete dentary means an equal reduction of the canal. Skull width was tested for mean segment lengths but differences were not significant between ecologies ($p = 0.509$).

However, predictions of tactile ability decreased in many extant taxa and increased in many lepidosaurs and extinct taxa (Table 5.2).

It is necessary to note that predictions based on Strahler segment counts are only made using first order (i.e., terminal) segments. It is expected that there is a minimum number of terminal segments per surface area necessary for even non-tactile taxa to innervate integument at minimal sensitivity. It is likely the case that larger non-tactile organisms simply require more terminal segments to distribute even minimal nervous tissue to the integument. However, nerve distribution and size appear to be limited in larger organisms, constraining sensory abilities (More et al. 2010). Large body size poses an issue in that the time a nerve takes to conduct a signal along the length of its axons to the central nervous system (responsiveness) is dependent on axon diameter. More et al. (2010) demonstrated that it was not possible for an elephant to increase nerve cross sectional area to maintain the signal speed and/or receptive field size (resolution) present in a shrew. Though axon numbers and diameters do increase, responsiveness and resolutions are still lower. As such, signal delays are up to 17 times longer in large mammals than small mammals (More and Donelan 2018). However, it has also been shown that signal speed is slowed by branching in axons (Manor et al. 1991) and therefore larger animals may be able to maintain comparative signal speeds by having fewer terminal receptors. Though receptive fields would shrink as a result.

Terminal segment (i.e., foramina) distribution has been quantified in the past in the context of reptilian extra-oral tissues (Morhardt 2009), but is often observed qualitatively with simply the presence of foramina cited as evidence for crocodylian level sensitivity in fossil reptiles (Ibrahim et al. 2014, Barker et al. 2017, Carr et al. 2017,

Rothschild and Naples 2017, Cerroni et al. 2020, Cau et al. 2017, Martill et al. 2021, Álvarez-Herrera et al. 2020). Our data suggest that an increase in terminal segments (i.e., foramina) is not enough to distribute the neurovasculature for tactile-sensory morphology. In addition to increasing tips, the branching itself must complexify and tip density must increase. This is reflected in the trend from a non-tactile rating in all lepidosaurian taxa, to neutral in *Trilophosaurus* and some pseudosuchians, to tactile in more derived pseudosuchian taxa (Table 5.2) and the data for tip frequency (Fig. 5.10c). It is also reflected in qualitative observation of foramina across the dentaries of numerous archosaurian taxa (Figs. 5.14-15). Therefore, I strongly advise against use of foramina alone as proxies for trigeminal-innervated sensation. Instead, I suggest taking internal morphology and distribution into account as well.

A comment on non-avian, theropod dinosaurs

The above discussion most specifically applies to hypotheses of behavior and ecology in non-avian, theropod dinosaurs. The presence of neurovascular foramina and canals has often been cited within Dinosauria, usually Theropoda, as a proxy for trigeminal nerve-innervated sensitivity (e.g., Ibrahim et al. 2014, Barker et al. 2017, Carr et al. 2017, Rothschild and Naples 2017, Cerroni et al. 2020, Cau et al. 2017). However, these hypotheses remain qualitative, merely based on presence or absence of osteological correlates, and are not supported by quantitative analyses or extensive comparison of these trigeminal features.

This investigation included analysis of five theropod taxa: *Dilophosaurus*, *Majungasaurus*, *Allosaurus*, *Tyrannosaurus*, and *Byronosaurus*. The early diverging *Dilophosaurus* and *Majungasaurus* both have few, non-complex branches (about 1 per

tooth dorsally, and few ventrally) resulting in an overall non-tactile assessment (Table 5.2). *Allosaurus* has more, and more complex branches (about 2 per tooth dorsally, and several ventrally) resulting in an overall assessment indicating it has potential for high tactile-sensitivity (Fig. 5.2). Quantitative assessment of the morphologies of *Tyrannosaurus* and *Byronosaurus* indicate the potential for intermediate tactile sensitivity. Overall, there is no obvious trend within the clade, and these data do not support the presence of the unique sensory structures, abilities, or behavioral adaptations suggested in the literature (Carr et al. 2017, Cerroni et al. 2020, Rothschild and Naples 2017, Barker et al. 2017). However, a more detailed theropod investigation may reveal trends in phylogeny or ecology especially towards the diversity of extant conditions.

Paleoecological implications in pseudosuchian transitions

Pseudosuchia proves a useful group in which to evaluate hypotheses of changing trigeminal tissues with shifting ecology. Osteological correlates in pseudosuchians are robust and habitat shifts are well known. Basal pseudosuchians occupied terrestrial habitats from their origins in the Early Triassic (+245 Ma) (Fig. 5.13; Nesbitt 2011). Two habitat shifts by non-surviving clades include the transition from a terrestrial to marine habitat by the thalattosuchians tentatively in the Early Jurassic (~195 Ma) and a transition from a terrestrial to freshwater habitat by some notosuchian crocodyliforms in the Early Cretaceous (~130 Ma) (Wilberg et al. 2019). Along the neosuchian line to modern crocodylians, a transition from a terrestrial to semiaquatic habitat occurred in the Middle Jurassic (~174.1 Ma) (Fig. 5.13; Wilberg et al. 2019). These ecological shifts are tied with morphological shifts (Brusatte et al. 2016, Schwab et al. 2020, Gearty and Payne 2020) and this data demonstrates that these were accompanied by changes in sensory

systems towards the extant condition. Specifically, the integumentary sensory organs dispersed across the rostrum allow for fine discrimination between small water movements in the semi-aquatic habitat occupied by all extant crocodylians (Soares 2002, Leitch and Catania 2012, Di-Poï and Milinkovitch 2013, Grap et al. 2020).

Assuming the extinct taxa had the soft tissue means necessary, the predictive models verified the necessary morphology to facilitate trigeminal-innervated tactile sensation in reptiles and resulted in the following paleoecological inferences (see Table 5.2 for a summary). Results from this study (i.e., low segment/branch counts, small topological COM, low density metrics, few topological tips) suggest the basal archosaurian condition was one lacking the necessary morphology for tactile sensation. This is indicated by the lepidosaurian morphology as well as that of the terrestrial archosauromorph *Trilophosaurus*, which was present during the early Late Triassic (~230mya) (Fig. 5.13; Spielmann et al. 2008). Quantification of the neurovascular canals of basal, terrestrial pseudosuchians *Longosuchus* (Late Triassic ~225mya; Parrish 1994) and *Litargosuchus* (Early Jurassic ~195mya; Clark and Sues 2002) reveals an intermediate morphology (i.e., intermediate segment/branch counts, topological center of mass, and density metrics, some topological tips) between completely non-tactile taxa and crocodylians (Table 5.2). The terrestrial, non-crocodyliform crocodylomorph *Junggarsuchus* (Middle Jurassic ~165mya; Clark et al. 2004) lacks the morphology necessary for tactile sensation, whereas the later diverging terrestrial, crocodylomorph *Macelognathus* (Late Jurassic ~152mya; Marsh 1884) is quantified as intermediate. Within crocodyliformes, terrestrial protosuchids *Protosuchus* (~190mya; Busbey and Gow 1984) and *Orthosuchus* (Early Jurassic ~195mya; Dollman et al. 2019) are

quantified with slightly more potential for tactile sensory abilities. *Orthosuchus* and *Protosuchus* are slightly more tactile than *Litargosuchus*, *Longosuchus*, and *Macelognathus* (i.e., 50% and 80% topological tips, respectively; tactile for density metrics/topological COM and Strahler segments; neutral for Horton branches). The Late Jurassic (~150mya; Efimov 1996), terrestrial *Nominosuchus* demonstrates the intermediate morphology. The terrestrial, notosuchians *Araripesuchus* (late Early Cretaceous ~107mya; Price 1959) and *Simosuchus* (Late Cretaceous ~70mya;) both have morphologies quantified as tactile. The marine (Early Jurassic ~180mya; Pierce and Benton 2006) *Pelagosaurus* demonstrates the intermediate morphology. These morphologies confirm a trend towards tactile sensory abilities and suggest the necessary morphology may have been present in most early terrestrial crocodylomorphs by the Jurassic (Fig. 5.13). If this is the case, and the potential for tactile sensation appeared before the mesoeucrocodylian radiation and before neosuchians entered aquatic habitats in the Middle Jurassic (Wilberg et al. 2019). Divergence dates for the first taxa rated as having the morphology for tactile sensory behaviors (i.e., *Macelognathus* and the protosuchids) are in the Late Triassic (Fig. 5.13; Leardi et al. 2017, Turner et al. 2017) meaning the tactile-sensing morphology was present within pseudosuchians by this point. The increase in trigeminal sensory abilities suggested by this data indicates the sensory transition preceded the terrestrial to semiaquatic transition in the Middle Jurassic (Wilberg et al. 2019). It is possible that the potential for more tactile sensory input was a key innovation allowing for successful pseudosuchian occupation of semi-aquatic habitats.

An Early Jurassic hypothesis for crocodylian integumentary sensory organs was proposed by Soares (2002) on the qualitative basis of foramina patterns on the rostral cranial elements. Though my timeline only slightly precedes this hypothesis, I find the suggestion that *Protosuchus* and other terrestrial crocodylians do not compare with the extant condition to be untrue. George and Holliday (2013) do not come to a conclusion on timing of origins of the extant condition because of a small sample size, but demonstrate the utility of other aspects of the trigeminal system (i.e., ganglion) in sensory ability prediction. They also discuss a possible secondary reduction of the trigeminal sensory system in the marine tethysuchian *Rhabdognathus* (George and Holliday 2013). Our data for the marine thalattosuchian *Pelagosaurus* also suggest minimal trigeminal sensory abilities, which may be convergent or a character of the clade depending on the phylogenetic position of thalattosuchians (Wilberg 2015, Ruebenstahl 2019).

CONCLUSIONS

The indication that the pseudosuchian tactile trigeminal morphology preceded their terrestrial-semiaquatic transition is yet another example of sensory innovations preceding species diversification (Carlson and Arnegard 2011, Parker 2008). Exploring similar trigeminal sensory transitions in other clades (e.g., evolution of whiskers in mammals, bill tip organs in birds) may reveal morphological and ecological trends. These methods may also be useful in fragmentary materials where only portions of the dentary are available as demonstrated by the presence of significant differences between ecological groups across regions of the dentary (Fig. 5.9). Isolation of dentary regions may also lead to easier detection of regions of increased sensitivity (i.e., bill tip organs). Finally, combination of branching analysis with other trigeminal-related metrics (e.g., trigeminal ganglion volume) and their associated osteological correlates (e.g., trigeminal

foramen diameter) will strengthen ecomorphological groups and hypotheses of sensory abilities in extinct animals.

Table 5.1. CT scan data.

Specimen	Specimen Number	Scan Resolution(s)	CT Scanner	Scan Source	Stain (I ₂ KI) concentration by % (w/v)	Stain duration
<i>Alle alle</i>	OUVc 10752	0.090, 0.025	General Electric eXplore Locus	Morphosource*	X	X
<i>Alligator mississippiensis</i>	MUVC AL031	0.083, 0.041	Zeiss Xradia Versa 510	In house ^o	12.3	5 weeks
<i>Alligator mississippiensis</i>	MUVC AL712	0.410	Siemens Inveon	In house ^o	N/A	N/A
<i>Allosaurus fragilis</i>	DINO 2560	0.793x0.793x0.625	Lightspeed VCT XT	In house	N/A	N/A
<i>Anas platyrhynchos</i>	OUVc 10252	0.092	X	In house	N/A	N/A
<i>Anolis sagrei</i>	MUVC LI089	0.029, 0.032	Zeiss Xradia Versa 510	In house		
<i>Araripesuchus wegneri</i>	AMNH 24450	0.105	X	Colleague	N/A	N/A
<i>Arenaria melanocephala</i>	USNM 612977	0.034	Bruker SkyScan 1173	Morphosource**	N/A	N/A
<i>Brookesia</i>	UADBA HERP 15550	0.012	General electric phoenix v tome x m 240	Morphosource		10 days
<i>Byronosaurus</i>	IGM100/983	0.11x0.125x0.26	UTCT 1997	Digimorph	N/A	N/A
<i>Crocodylus johnstoni</i>	FMNH 16162	0.023, 0.025	NSI scanner	In house ^o	8	9 months
<i>Crocodylus johnstoni</i>	TMM M-6807	0.221x0.221x0.228	UTCT 1995?	Digimorph	N/A	N/A
<i>Crocodylus moreletii</i>	TMM M-4980	0.190	UTCT 2003	Digimorph	N/A	N/A
<i>Crocodylus porosus</i>	OUVc 10899	0.092, 0.047	General Electric eXplore Locus	Morphosource*	X	X
<i>Caiman crocodilus</i>	FMNH 73711	0.065	UTCT 2002	Digimorph	N/A	N/A
<i>Crotaphytus collaris</i>	TMM M-16243	0.013	NSI scanner	In house	5	11 months
<i>Ctenosaura pectinata</i>	MUVC LI084	0.035	Zeiss Xradia Versa 510	In house	5	X
<i>Dilophosaurus wetherilli</i>	TMM 43646	0.134	NSI scanner	In house	N/A	N/A
<i>Dracaena guianensis</i>	TMM M-16152	0.013	NSI scanner	In house	5	11 months
<i>Eremias arguta</i>	TMM M-16147	0.010	NSI scanner	In house	5	11 months
<i>Fulica americana</i>	MUVC AV285	0.033	NSI scanner	In house	4.1	2 months
<i>Junggarsuchus sloani</i>	IVPP V14010	0.046	X	Colleague	N/A	N/A
<i>Litargosuchus leptorhynchus</i>	BP-5237	0.042	X	Colleague	N/A	N/A
<i>Longosuchus meadi</i>	TMM 31185-84	0.114	NSI scanner	In house	N/A	N/A
<i>Macelognathus vagans</i>	LACM 150148	0.017	X	In house	N/A	N/A
<i>Majungasaurus crenatissimus</i>	FMNH PR2100	0.254,x0.254x0.2	X	Colleague	N/A	N/A
<i>Mecistops cataphractus</i>	TMM M-3529	0.165x0.165x0.449	UTCT 2005	Digimorph	N/A	N/A
<i>Nominosuchus</i>	IVPP 14392	0.046	X	Colleague	N/A	N/A
<i>Orthosuchus stormbergi</i>	SAM PK-K409	0.066	X	Colleague	N/A	N/A
<i>Osteolaemus tetraspis</i>	FMNH 53632	0.046, 0.061	NSI scanner	In house ^o	8	9 months
<i>Osteolaemus tetraspis</i>	FMNH 98936	0.055	UTCT 2005	Digimorph	N/A	N/A
<i>Paleosuchus palpebrosus</i>	FMNH 22817	0.035, 0.059	NSI scanner	In house ^o	8	9 months
<i>Pandion haliaetus</i>	MUVC AV335	0.035	NSI scanner	In house	4.1	2 months
<i>Pelagosaurus typus</i>	BRSLI M1413	0.072x0.072x0.156	UTCT	Digimorph	N/A	N/A
<i>Phasianus colchicus</i>	MUVC AV263	0.022	NSI scanner	In house	4.1	2 months
<i>Physignathus cocincinus</i>	TMM M-16082	0.012	NSI scanner	In house	5	11 months
<i>Pogona vitticeps</i>	SAMA R52521	0.012	X	Colleague	X	X
<i>Protosuchus haughtoni</i>	BP-1-4770	0.054	X	Colleague	N/A	N/A
<i>Psittacus erithacus</i>	MUVC AV092	0.051	NSI scanner	In house	X	X
<i>Scolopax rusticola</i>	USNM 292760	0.034	Bruker SkyScan 1173	Morphosource**	N/A	N/A
<i>Simosuchus clarki</i>	UA8679	0.131		Colleague	N/A	N/A
<i>Sphaerodactylus caicosensis</i>	UF HERP 95971	0.011	General Electric phoenix v tome x m 240	Morphosource	X	X
<i>Sphenodon punctatus</i>	SAMA 70524	0.032, 0.025		Colleague	X	X
<i>Tomistoma schlegelii</i>	FMNH 11085	0.099, 0.056	NSI scanner	In house ^o	8	9 months
<i>Tomistoma schlegelii</i>	TMM M-6342	0.165x0.165x0.46	UTCT 2005	Digimorph	N/A	N/A
<i>Trilophosaurus buettneri</i>	TMM 31025-233	0.032	NSI scanner	In house	N/A	N/A
<i>Trioceros bitaeniatius</i>	TMM M-16233	0.011	NSI scanner	In house	5	11 months
<i>Tyrannosaurus rex</i>	MOR 1125	0.566x0.566x8	X	Colleague	N/A	N/A

<i>Uromastyx geyri</i>	TMM M-16221	0.012	NSI scanner	In house	5	11 months
<i>Varanus exanthematicus</i>	OUVV 10417	0.009	X	In house	X	X
<i>Varanus salvator</i>	MUVV LI074	0.053	NSI scanner	In house	8	10 months

*WitmerLab at Ohio University provided access to these data, the collection of which was funded by NSF. The files were downloaded from www.MorphoSource.org, Duke University.

**The Smithsonian National Museum of Natural History provided access to these data, the collection of which was funded by oVert TCN (NSF DBI-1701714, NSF DBI-1701665), an NSF Graduate Research Fellowship to Catherine M. Early (DGE-1060934, DGE-1645419), and an American Museum of Natural History Chapman Ornithology Grant to Catherine M. Early. The files were downloaded from www.MorphoSource.org, Duke University.

^oAvailable from Open Science Framework, CrocNet (<https://osf.io/jmpck/>). Research sponsored by NSF IOS 1457319, NSF EAR 1636753, and University of Missouri.

Table 5.2. Specimens and prediction results (fossil specimens shaded).

Specimen	Specimen Number	State	Clade	Ecology (literature citations below)	% Tactile: Topological Tips	Density COM and Orders	Strahler Segments	Horton first segments	% Tactile: Mean Segment Length	% Tactile: Median Segment Lengths	% Tactile: Mode Segment Lengths
<i>Alle alle</i>	OUVC 10752	Extant*	Avian	Non-tactile	10	Non-tactile	Non-tactile	Non-tactile	0	0	0
<i>Alligator mississippiensis</i>	MUVC AL031	Extant*	Crocodylian	Tactile (1)	80	Tactile	Tactile	Tactile	100 (67) ^a	100	100
<i>Alligator mississippiensis</i>	MUVC AL712	Extant**	Crocodylian	Tactile (1)	100	Tactile	Tactile	Tactile	100 (67)	100	100
<i>Allosaurus fragilis</i>	DINO 2560	Fossil	Theropod	Unknown	80	Non-tactile	Tactile	Tactile	100 (33)	0	67
<i>Anas platyrhynchos</i>	OUVC 10252	Extant**	Avian	Tactile (2)	80	Tactile	Tactile	Tactile	100 (67)	100	67
<i>Anolis sagrei</i>	MUVC LI089	Extant*	Lepidosaur	Non-tactile	0	Non-tactile	Non-tactile	Non-tactile	0(0)	0	0
<i>Araripesuchus gomesii</i>	AMNH 24450	Fossil	Crocodyliform	Unknown	50	Tactile	Tactile	Tactile	67 (67)	33	33
<i>Arenaria melanocephala</i>	USNM 612977	Extant	Avian	Tactile (2)	50	Tactile	Non-tactile	Neutral	67 (67)	100	100
<i>Brookesia</i>	UADBA HERP 15550	Extant*	Lepidosaur	Non-tactile	0	Non-tactile	Non-tactile	Tactile	0 (0)	0	0
<i>Byronosaurus</i>	IGM100/983	Fossil	Theropod	Unknown	50	Tactile	Non-tactile	Neutral	33	67	67
<i>Crocodylus johnstoni</i>	FMNH 16162	Extant*	Crocodylian	Tactile (1)	90	Tactile	Tactile	Tactile	100 (67)	100	100
<i>Crocodylus johnstoni</i>	TMM M-6807	Extant**	Crocodylian	Tactile (1)	70	Tactile	Tactile	Tactile	100 (67)	100	67
<i>Crocodylus moreletii</i>	TMM M-4980	Extant	Crocodylian	Tactile (1)	90	Tactile	Tactile	Tactile	100 (67)	100	100
<i>Crocodylus porosus</i>	OUVC 10899	Extant*	Crocodylian	Tactile (1)	100	Tactile	Tactile	Tactile	100 (67)	100	100
<i>Caiman crocodilus</i>	FMNH 73711	Extant	Crocodylian	Tactile (1)	100	Tactile	Tactile	Tactile	100 (100)	100	100
<i>Crotaphytus collaris</i>	TMM M-16243	Extant*	Lepidosaur	Non-tactile	0	Non-tactile	Non-tactile	Non-tactile	0 (0)	0	0
<i>Ctenosaura pectinata</i>	MUVC LI084	Extant*	Lepidosaur	Non-tactile	0	Non-tactile	Non-tactile	Non-tactile	0 (0)	0	0
<i>Dilophosaurus wetherilli</i>	TMM 43646	Fossil	Theropod	Unknown	30	Non-tactile	Non-tactile	Neutral	0	0	0
<i>Dracaena guianensis</i>	TMM M-16152	Extant*	Lepidosaur	Non-tactile	0	Non-tactile	Non-tactile	Non-tactile	0 (0)	0	0
<i>Eremias arguta</i>	TMM M-16147	Extant*	Lepidosaur	Non-tactile	10	Non-tactile	Non-tactile	Non-tactile	0 (0)	0	0
<i>Fulica americana</i>	MUVC AV285	Extant*	Avian	Non-tactile	40	Tactile	Tactile	Non-tactile	0 (33)	33	33
<i>Junggarsuchus sloani</i>	IVPP V14010	Fossil	Crocodylomorph	Unknown	30	Non-tactile	Non-tactile	Non-tactile	33 (33)	0	33
<i>Litargosuchus leptorhynchus</i>	BP-5237	Fossil	Crocodylomorph	Unknown	50	Tactile	Non-tactile	Neutral	33 (67)	67	100
<i>Longosuchus meadi</i>	TMM 31185-84	Fossil	Suchian	Unknown	50	Non-tactile	Tactile	Neutral	33	67	67
<i>Macelognathus vagans</i>	LACM 150148	Fossil	Crocodylomorph	Unknown	60	Tactile	Tactile	Neutral	33	0	33
<i>Majungasaurus crenatissimus</i>	FMNH PR2100	Fossil	Theropod	Unknown	40	Non-tactile	Non-tactile	Neutral	33	67	33
<i>Mecistops cataphractus</i>	TMM M-3529	Extant	Crocodylian	Tactile (1)	100	Tactile	Tactile	Tactile	100 (100)	100	100
<i>Nominosuchus</i>	IVPP 14392	Fossil	Crocodyliform	Unknown	40	Tactile	Non-tactile	Neutral	33 (67)	0	0
<i>Orthosuchus stormbergi</i>	SAM PK-K409	Fossil	Crocodyliform	Unknown	60	Tactile	Tactile	Neutral	100 (100)	67	67
<i>Osteolaemus tetraspis</i>	FMNH 53632	Extant*	Crocodylian	Tactile (1)	100	Tactile	Tactile	Tactile	100 (67)	100	100
<i>Osteolaemus tetraspis</i>	FMNH 98936	Extant**	Crocodylian	Tactile (1)	100	Tactile	Tactile	Tactile	100 (100)	100	100
<i>Paleosuchus palpebrosus</i>	FMNH 22817	Extant*	Crocodylian	Tactile (1)	80	Tactile	Tactile	Tactile	100 (100)	67	67
<i>Pandion haliaetus</i>	MUVC AV335	Extant*	Avian	Non-tactile	20	Non-tactile	Non-tactile	Non-tactile	0 (67)	33	67
<i>Pelagosaurus typus</i>	BRS LI M1413	Fossil	Crocodyliform	Unknown	30	Non-tactile	Tactile	Neutral	100	100	100
<i>Phasianus colchicus</i>	MUVC AV263	Extant*	Avian	Non-tactile	40	Non-tactile	Non-tactile	Non-tactile	33 (67)	0	33
<i>Physignathus cocincinus</i>	TMM M-16082	Extant*	Lepidosaur	Non-tactile	0	Non-tactile	Non-tactile	Non-tactile	0 (50)	0	0
<i>Pogona vitticeps</i>	SAMA R52521	Extant*	Lepidosaur	Non-tactile	0	Non-tactile	Non-tactile	Non-tactile	0 (50)	0	0
<i>Protosuchus haughtoni</i>	BP-1-4770	Fossil	Crocodyliform	Unknown	80	Tactile	Tactile	Neutral	33 (100)	33	33
<i>Psittacus erithacus</i>	MUVC AV092	Extant*	Avian	Tactile (2)	50	Tactile	Tactile	Tactile	100 (100)	67	100

<i>Scolopax rusticola</i>	USNM 292760	Extant*	Avian	Tactile (2)	100	Tactile	Tactile	Tactile	100 (100)	100	100
<i>Simosuchus clarki</i>	UA8679	Fossil	Crocodyliform	Unknown	60	Tactile	Tactile	Tactile	100 (67)	0	33
<i>Sphaerodactylus caicosensis</i>	UF HERP 95971	Extant*	Lepidosaur	Non-tactile	0	Non-tactile	Non-tactile	Non-tactile	0 (0)	50	0
<i>Sphenodon punctatus</i>	SAMA 70524	Extant*	Lepidosaur	Non-tactile	10	Non-tactile	Non-tactile	Non-tactile	0 (0)	0	0
<i>Tomistoma schlegelii</i>	FMNH 11085	Extant*	Crocodylian	Tactile (1)	100	Tactile	Tactile	Tactile	100 (100)	100	100
<i>Tomistoma schlegelii</i>	TMM M-6342	Extant*	Crocodylian	Tactile (1)	100	Tactile	Tactile	Tactile	100 (100)	100	100
<i>Trilophosaurus buettneri</i>	TMM 31025-233	Fossil	Archosauromorph	Unknown	20	Non-tactile	Non-tactile	Neutral	33	33	33
<i>Trioceros bitaeniatus</i>	TMM M-16233	Extant*	Lepidosaur	Non-tactile	0	Non-tactile	Non-tactile	Non-tactile	0 (50)	50	0
<i>Tyrannosaurus rex</i>	MOR 1125	Fossil	Theropod	Unknown	60	Non-tactile	Tactile	Non-tactile	0	0	0
<i>Uromastyx gevyi</i>	TMM M-16221	Extant*	Lepidosaur	Non-tactile	0	Non-tactile	Non-tactile	Non-tactile	0 (0)	0	0
<i>Varanus exanthematicus</i>	OUV 10417	Extant*	Lepidosaur	Non-tactile	10	Non-tactile	Non-tactile	Non-tactile	0 (50)	0	0
<i>Varanus salvator</i>	MUVC LI074	Extant*	Lepidosaur	Non-tactile	0	Non-tactile	Non-tactile	Non-tactile	0 (0)	0	0

(1) Leitch and Catania 2012, Di-Poï and Milinkovitch 2013, Grap et al. 2020

(2) Cunningham et al. 2013

(*) Contrast-enhanced scan for soft-tissue verification

(**) Soft-tissue verified in contrast-enhanced scan of alternate specimen

(a) Values when skull width is used as a proxy for size

Table 5.3. Neurovascular canal contents by clade (tactile taxa shaded).

Specimen	Proximal canal CSA residual	% Nerve Proximal	% Vessel Proximal	% Other Proximal	Symphyseal canal CSA residual	% Nerve Symphysis	% Vessel Symphysis	% Other Symphysis
<i>Alle alle</i>	-0.257	23.1	17.9	59.1	-0.517	29.3	39.7	31
<i>Anas platyrhynchos</i>	0.988	89.8	3	7.2	0.124	61.1	11.8	27.1
<i>Fulica americana</i>	0.685	7.6	4.9	87.5	0.332	25.9	12.4	61.8
<i>Pandion haliaetus</i>	-0.995	28.1	15.3	56.6	-0.577	68.9	8.8	22.3
<i>Phasianus colchicus</i>	-1.337	33.8	12.7	53.5	0.133	14.8	8.5	76.7
<i>Psittacus erithacus</i>	-1.1545	61.5	20.7	17.9	0.172	40.3	23.5	36.3
<i>Scolopax rusticola</i>	0.659	63.3	13.5	23.2	0.329	36.1	40.1	23.8
<i>Anolis sagrei</i>	1.355	17.9	9.8	72.3	0.949	23.7	19.7	56.6
<i>Crotaphytus collaris</i>	-1.169	25	13	62	-0.746	22.8	22.8	54.4
<i>Dracaena guianensis</i>	0.349	15.5	6.2	78.3	0.138	10	7.4	82.6
<i>Eremias arguta</i>	0.279	15.7	3.2	81	-1.074	33.3	26.7	40
<i>Physignathus cocincinus</i>	-1.032	11.2	7.5	81.2	0.736	4.3	5	90.7
<i>Pogona vitticeps</i>	-0.883	6.2	3.1	90.8	-1.476	8.3	8.3	83.3
<i>Sphaerodactylus caicosensis</i>	0.124	34.3	14.3	51.4	-0.177	22.5	1	76.4
<i>Trioceros bitaeniatus</i>	0.424	5.5	3	91.5	0.170	14.6	10.4	75
<i>Uromastix geyri</i>	-1.078	14.3	14.3	71.4	-0.785	15.7	7.8	76.5
<i>Varanus exanthematicus</i>	0.042	19.2	8.8	72	0.077	25.6	8.5	65.9
<i>Varanus salvator</i>	0.816	7.7	4.9	87.4	-1.102	34.2	22.8	43
<i>Alligator mississippiensis</i>	0.602	35.2	8.3	56.5	0.599	36.6	26.3	37.1
<i>Crocodylus johnstoni</i>	0.027	56.6	4.9	38.5	0.955	41.6	16.9	41.6
<i>Crocodylus porosus</i>	0.146	63.5	19.7	16.7	0.099	30.4	16.3	53.3
<i>Osteolaemus tetraspis</i>	-0.067	37.6	4.6	57.8	0.566	19.7	10.7	69.7
<i>Paleosuchus palpebrosus</i>	0.578	26.7	6.4	66.9	0.282	34.7	17.5	47.8
<i>Tomistoma schlegelii</i>	0.901	33.3	5.3	61.5	0.793	36.4	6.8	56.8
<i>Allosaurus fragilis</i>	2.836	-	-	-	-1.103	-	-	-
<i>Araripesuchus wegneri</i>	-0.212	-	-	-	0.745	-	-	-
<i>Junggarsuchus sloani</i>	-0.316	-	-	-	0.054	-	-	-
<i>Litargosuchus leptorhynchus</i>	-1.192	-	-	-	-0.435	-	-	-
<i>Nominosuchus</i>	1.101	-	-	-	0.888	-	-	-
<i>Orthosuchus stormbergi</i>	-1.152	-	-	-	-0.157	-	-	-
<i>Protosuchus haughtoni</i>	-3.039	-	-	-	-0.181	-	-	-
<i>Simosuchus clarki</i>	-0.580	-	-	-	1.133	-	-	-

Figure 5.1. Sudan Black B staining of myelinated nerve branches in (a) *Spinus tristis* (MUVC AV287), (b) *Toxostoma rufum* (MUVC AV107), (c) *Anas platyrhynchos* (MUVC AV098), (d) *Iguana iguana* (MUVC LI036), (e) *Pantherophis* (MUVC SE002), and (f) *Alligator mississippiensis* (MUVC AL809). Hemimandibles are in left lateral view (a, d, reversed), right lateral view (b), and ventral view of the left side (c, e, f). All stained nerves are within bone with the exception of small branches in d and all branches in e.

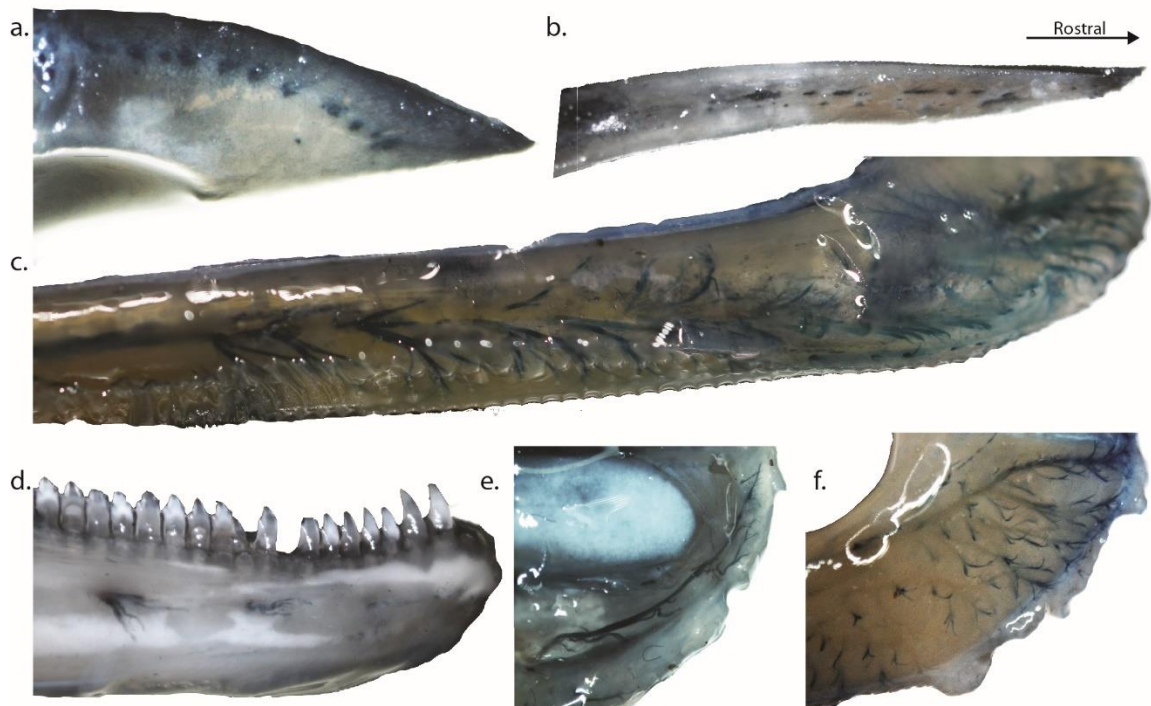


Figure 5.2. Phylogenetic representation of study taxa including 3D reconstructions of select (bolded) specimens (gray) and neurovascular canals (yellow) accompanied by simplified canal models (right).

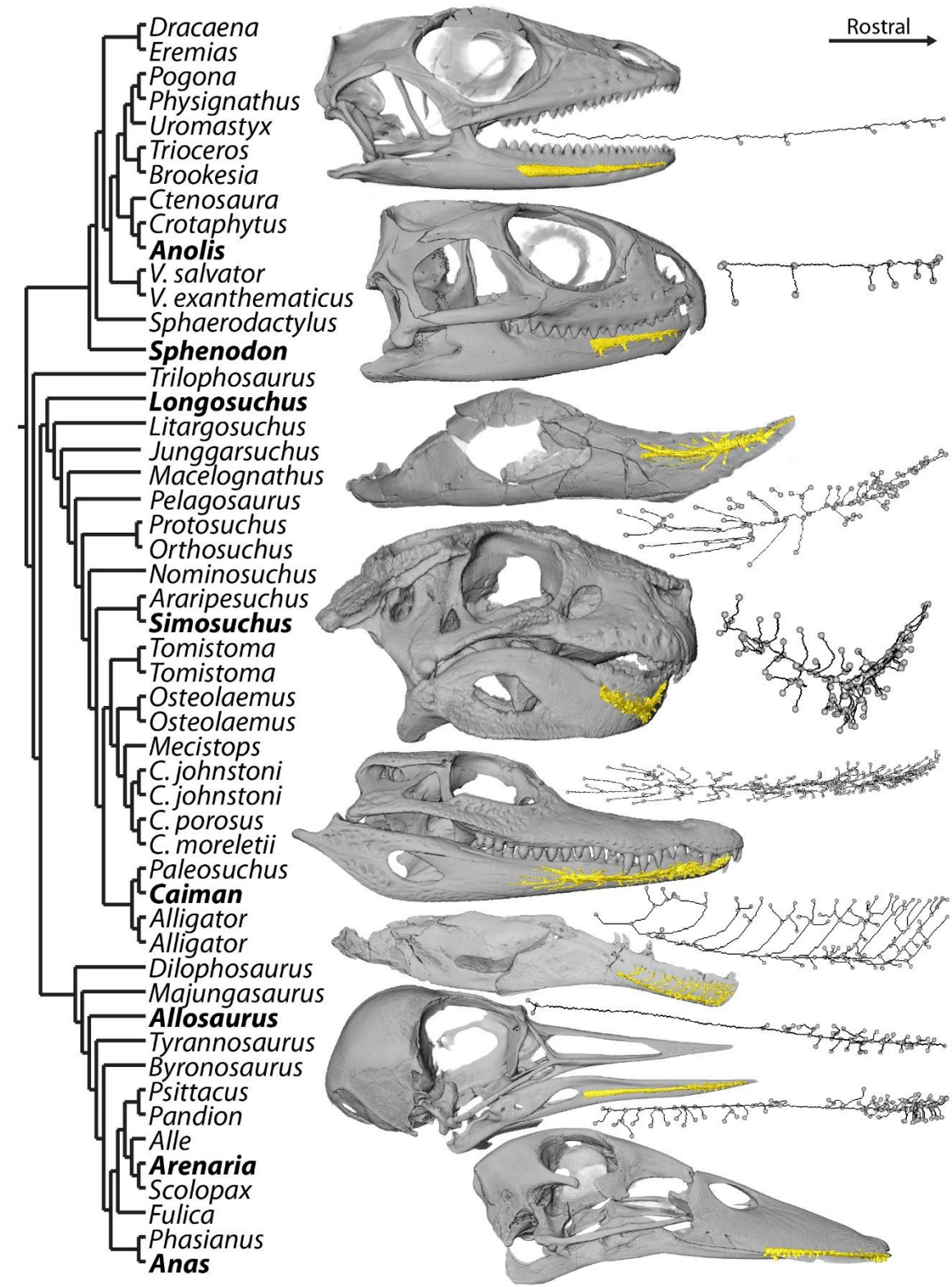


Figure 5.3. Coronal CT scan slices of representative mandibles from contrast-enhanced, extant taxa and extinct taxa displaying neurovascular canal (c), nerve (n), and vasculature (v) at the caudal origin of the mandibular canal of (a, f) *Alligator mississippiensis* (MUVc AL031), (b) *Protosuchus haughtoni* (BP-1-4770), (c, g) *Psittacus erithacus* (MUVc AV092), (d) *Dilophosaurus wetherilli* (TMM 43646), (e) *Eremias arguta* (TMM M-16147), and (h) *Anolis carolinensis* (MUVc LI089) and location in the neurovascular canal (cNv) of diversion of the lingual nerve (nL) from the mandibular nerve (nM), vasculature (v) and Meckel's cartilage (Mc).

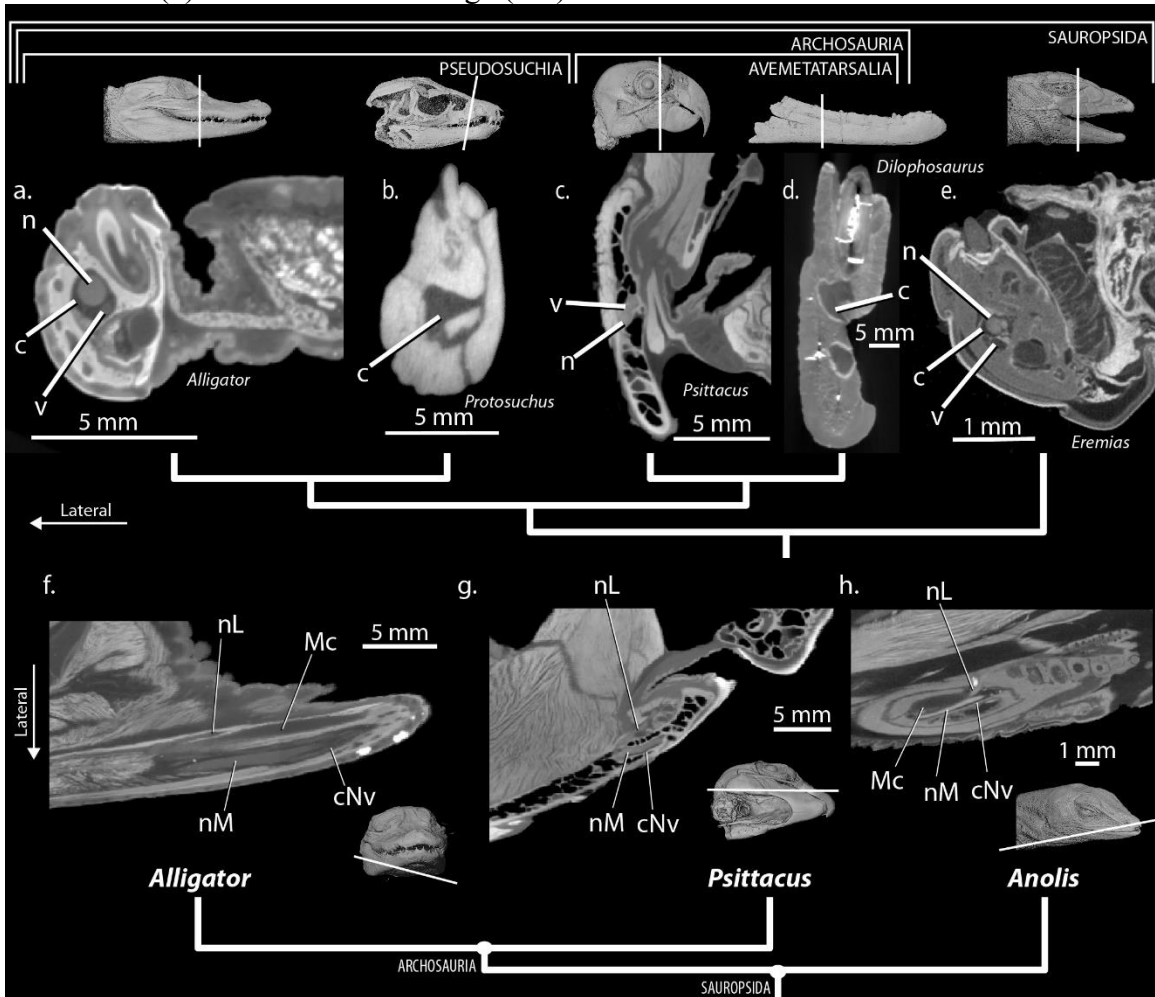


Figure 5.4. Dentaries of (a) *Anolis* (MUVCL1089), (b) *Majungasaurus* (FMNH PR2100), (c) *Psittacus* (MUVCLAV092), (d) *Macelognathus* (LACM 150148), and (e) *Alligator* (MUVCLAL623) in caudal (left), left lateral (top), and left medial (bottom) views. Nerve canal (c) and Meckelian groove (Mc) labelled.

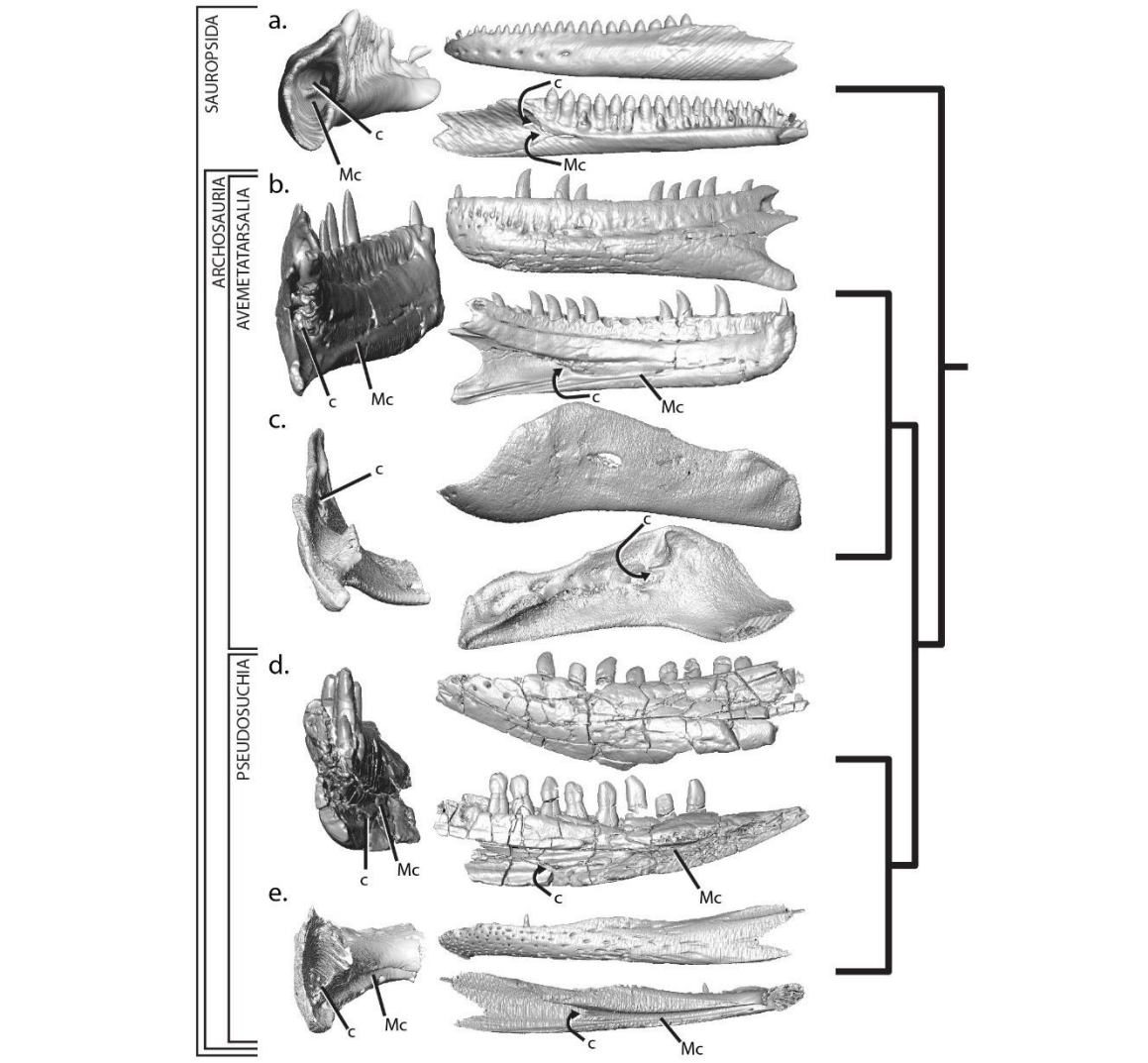


Figure 5.5. Location of mandibular canal (star) within the Meckelian fossa in fossil specimens (a-d, above) and CT scan data (e-h, below) of non-avian dinosaur taxa (a,e) *Dilophosaurus wetherilli* (TMM 43646, reflected), (b,f) *Majungasaurus* (FMNH PR2100), (c,g) *Allosaurus* (fossil: UMNH VP6477, CT data: DINO 2560), and (d,h) *Tyrannosaurus* (MOR 1125, reflected). Inset of *Majungasaurus* dentary shows where slices were taken.

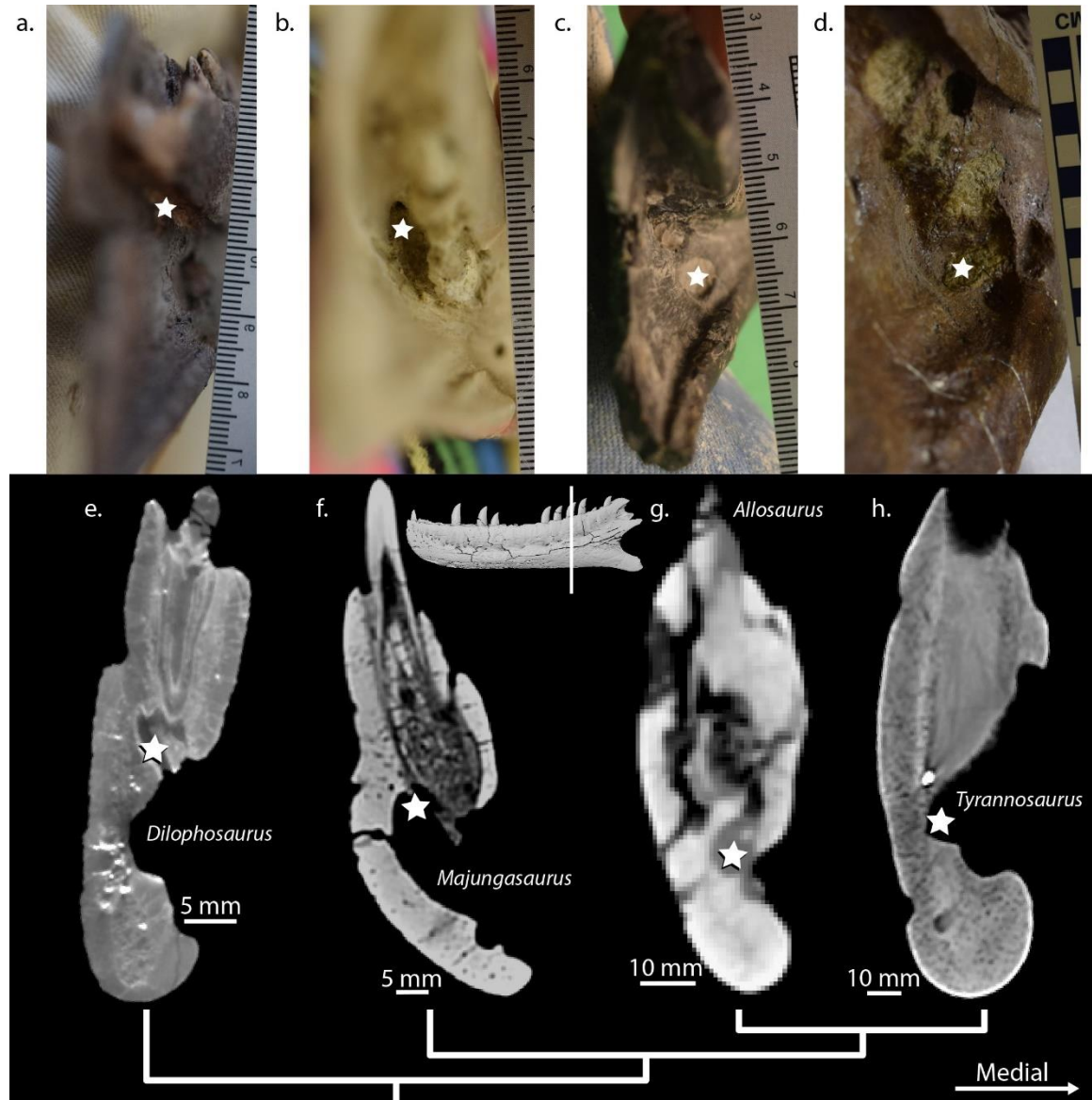


Figure 5.6. Location of mandibular canal (star) within the Meckelian fossa in non-crocodylian suchian taxa (a) *Longosuchus meadi* (TMM M-31185-84), (b) *Litargosuchus leptorhynchus* (BP-5237, reversed), (c) *Protosuchus haughtoni* (BP-1-4770, reversed), (d) *Orthosuchus stormbergi* (SAM PK-K409), (e) *Junggarsuchus sloani* (IVPP V14010), (f) *Macelognathus vagans* (LACM 150148), (g) *Nominosuchus* (IVPP 14392), (h) *Araripesuchus wegeneri* (AMNH 24450), and (i) *Simosuchus clarki* (UA 8679, reversed).

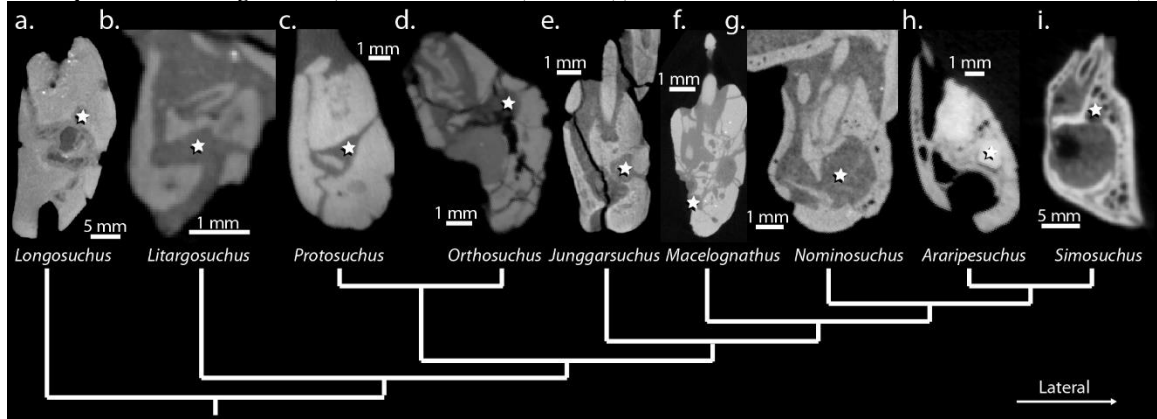


Figure 5.7. Proximal and symphyseal canal contents of extant taxa by percentage (a), and cross sectional area of mandibular canal at the proximal end (b) and symphysis (c) vs. skull width by clade and ecology of extant and select extinct (see Table 5.3) taxa.

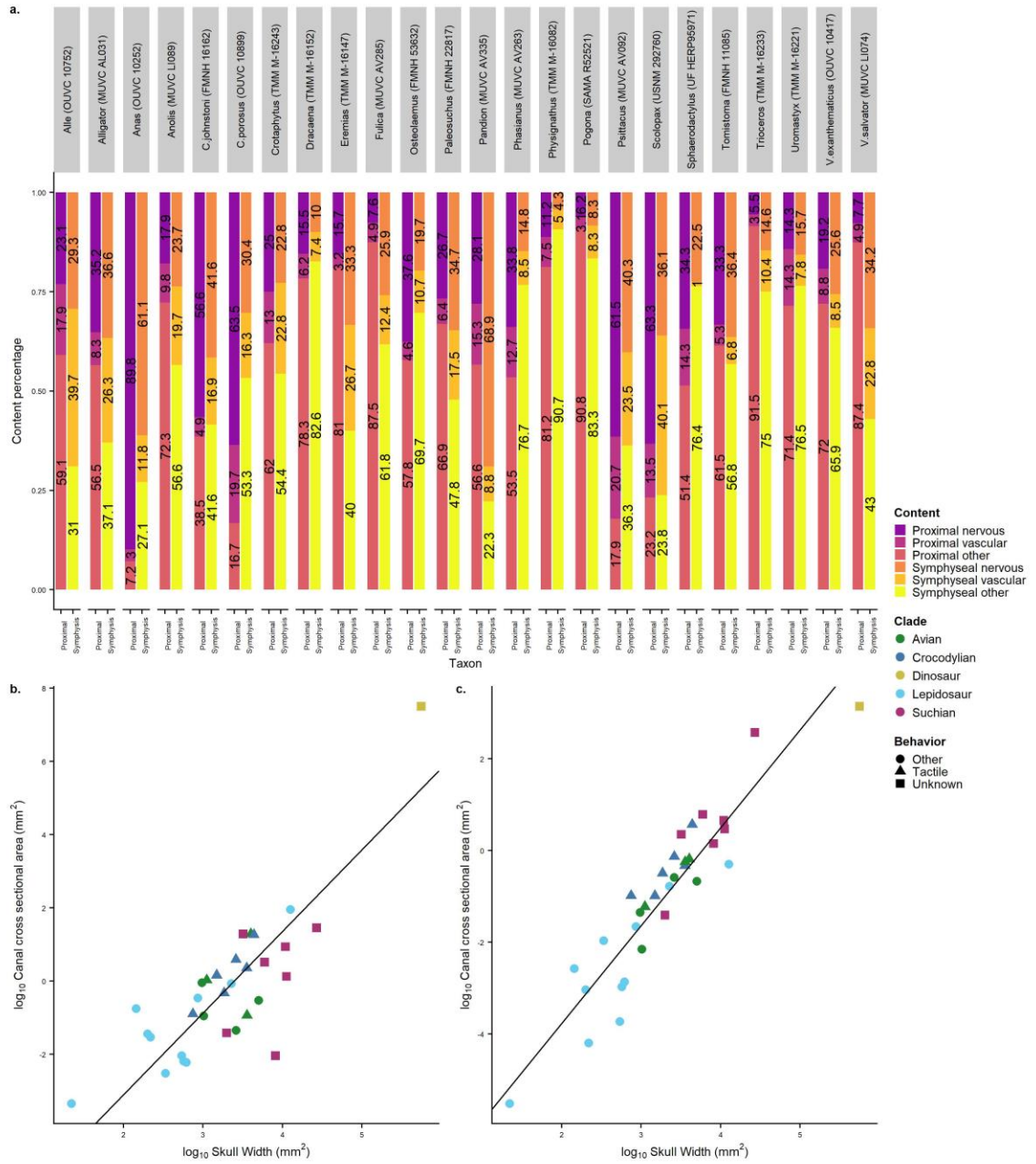


Figure 5.8. Canal topology represented by counts of terminal topological segments along the scaled neurovascular canal by clade of all taxa (a) and by ecology of extant taxa (b).

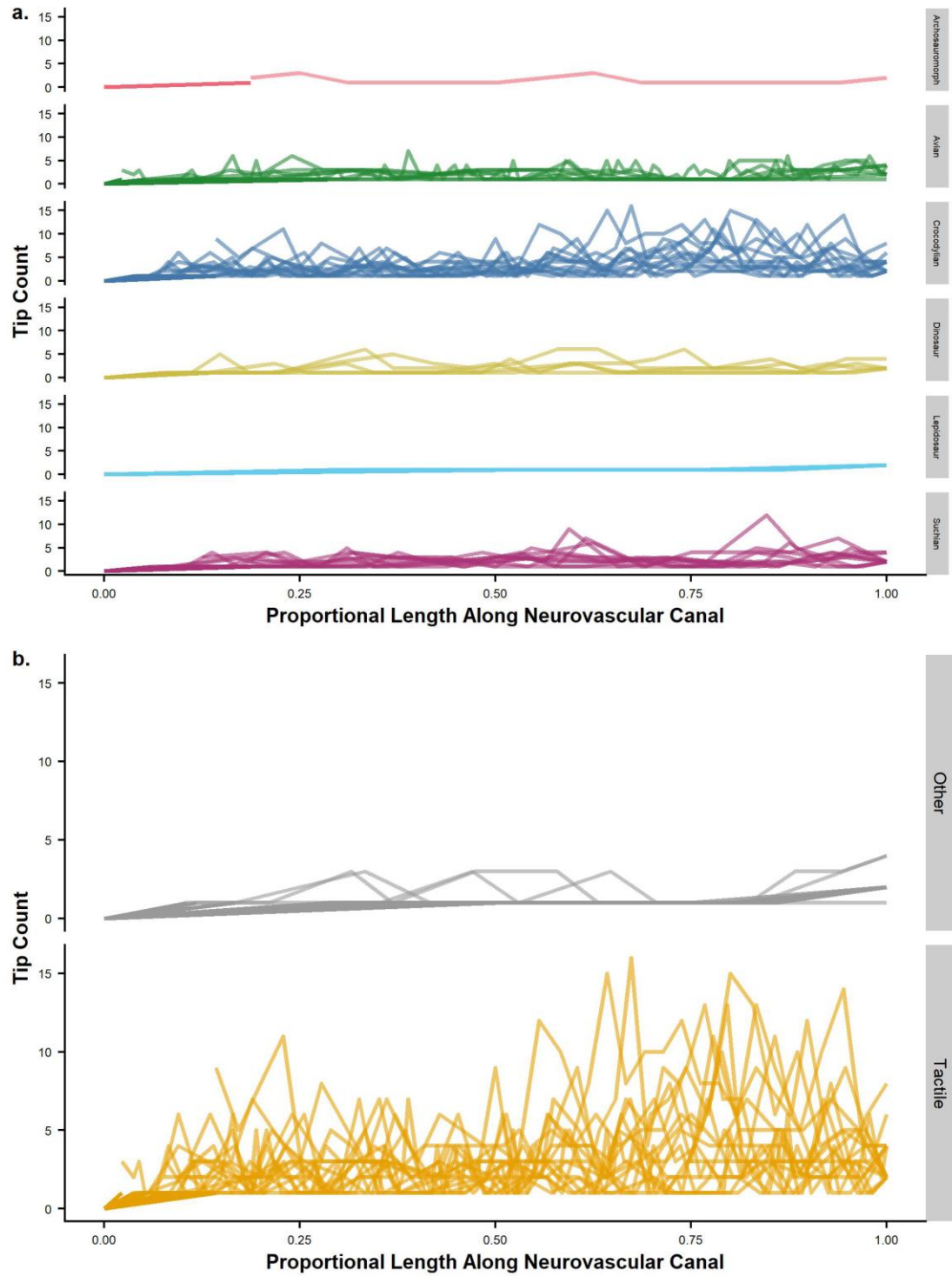


Figure 5.9. Number of topological tips by dentary region by clade and ecology.

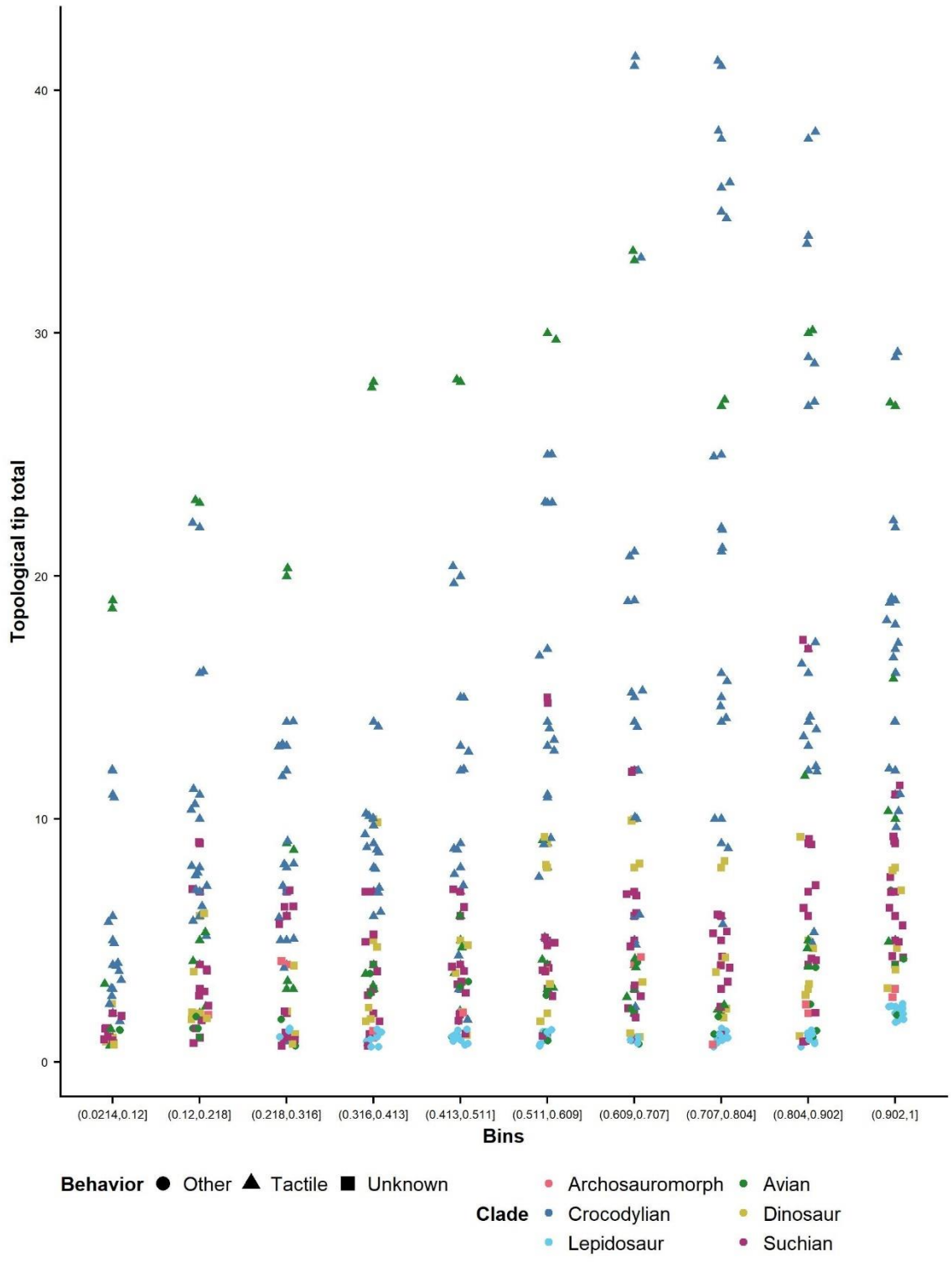


Figure 5.10. Density metrics, including dendritic density, represented by neurovascular canal length vs. dentary surface area (a), segment frequency, represented by number of segments vs. dentary surface area (b), and tip frequency, represented by number of tips vs. dentary surface area (c) and topological center of mass compared vs. dentary surface area (d) by clade and ecology of all taxa.

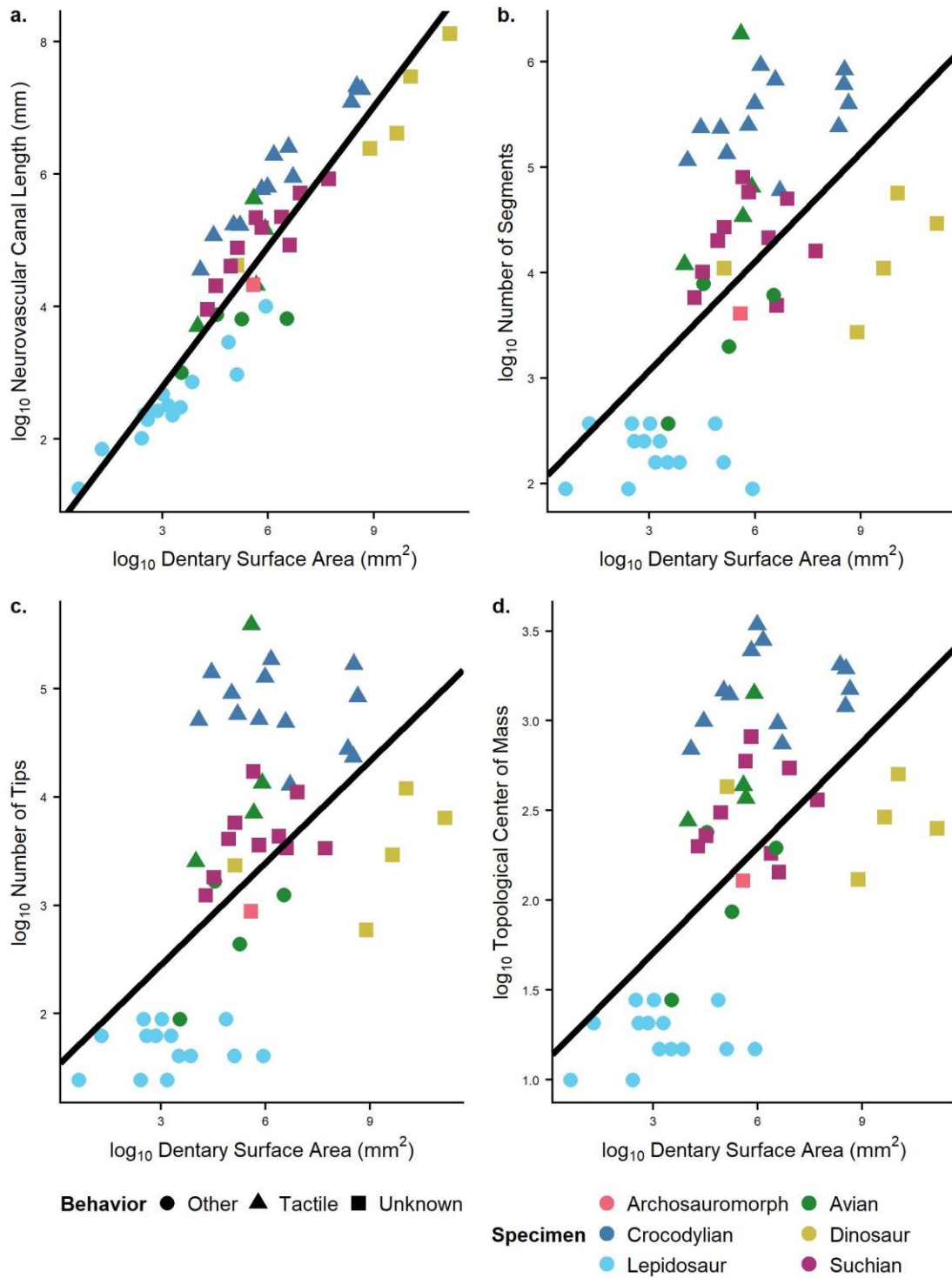


Figure 5.11 Strahler segment (a) and Horton first segment counts (b) by clade and ecology of all taxa..

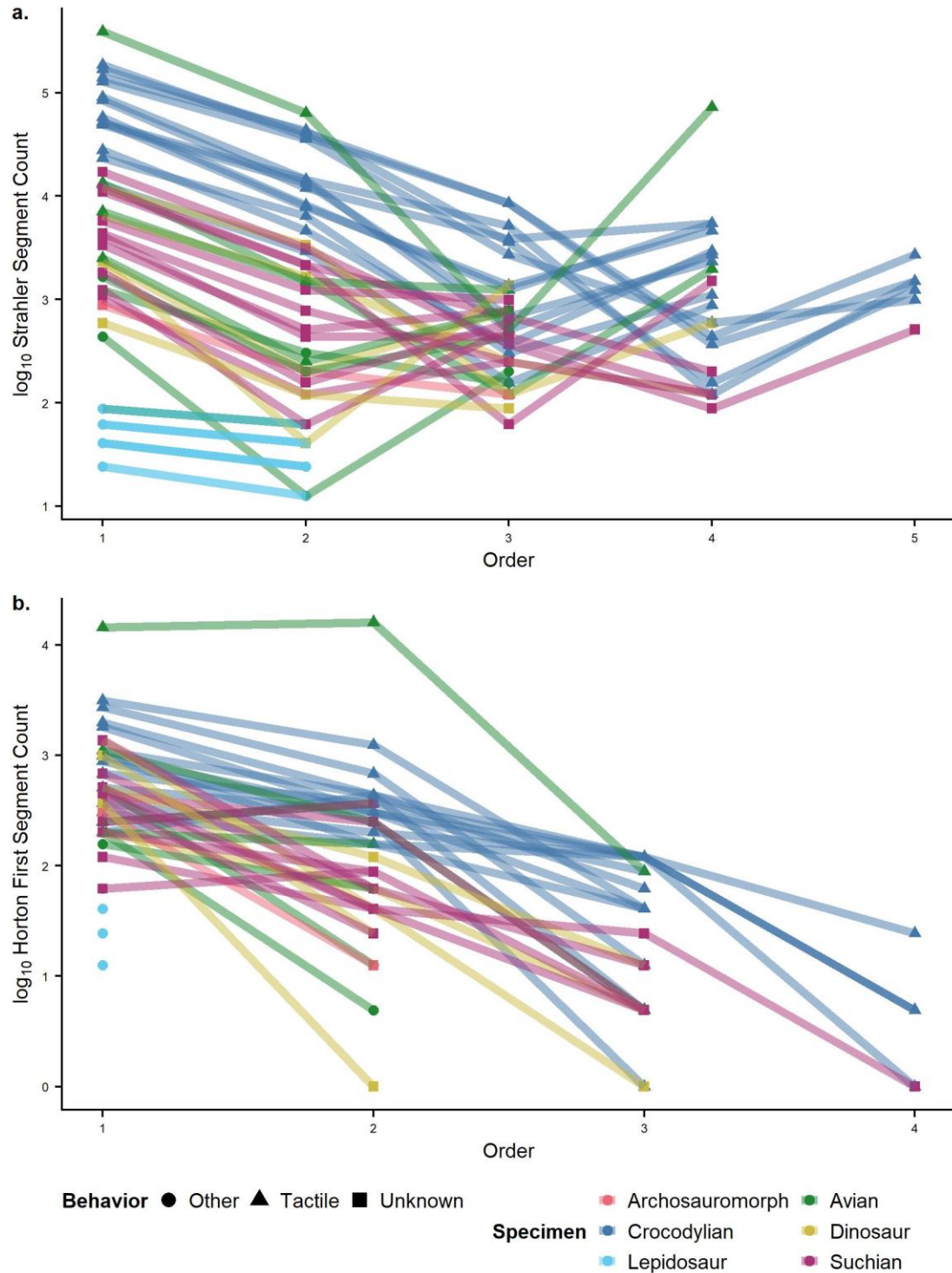


Figure 5.12. Segment lengths represented by segment mean (a), medians from boxplots (b), and modes from density plots (c) by clade and ecology.

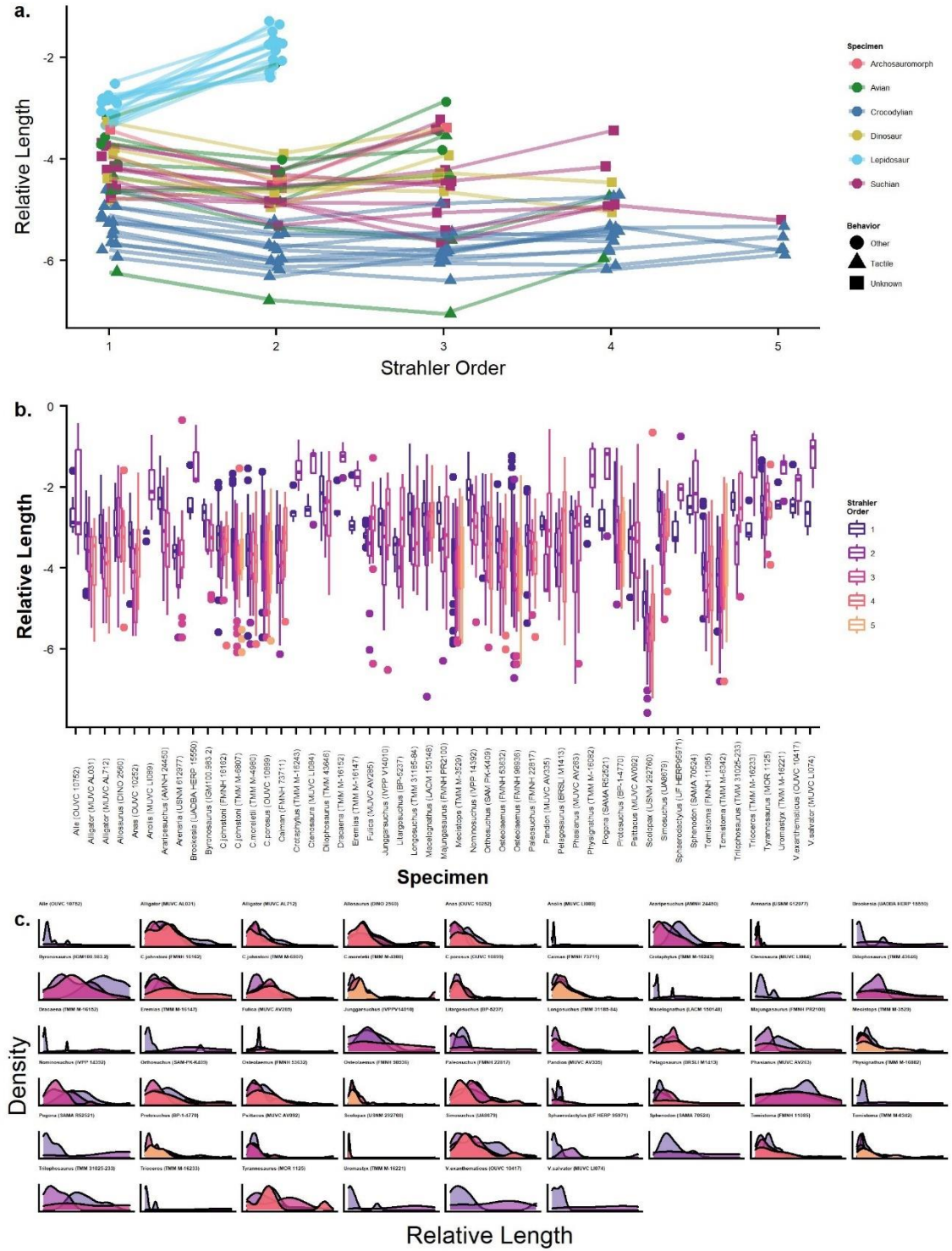


Figure 5.13. (a) Chronogram of non-crocodylian suchian study taxa and outgroup (*Trilophosaurus*) including simplified canal models with predicted ecologies (dates from Turner et al. 2017, Leardi et al. 2017, and The Paleobiology Database), and (b) phylogeny of extant, crocodylian study taxa including simplified canal models with known ecologies

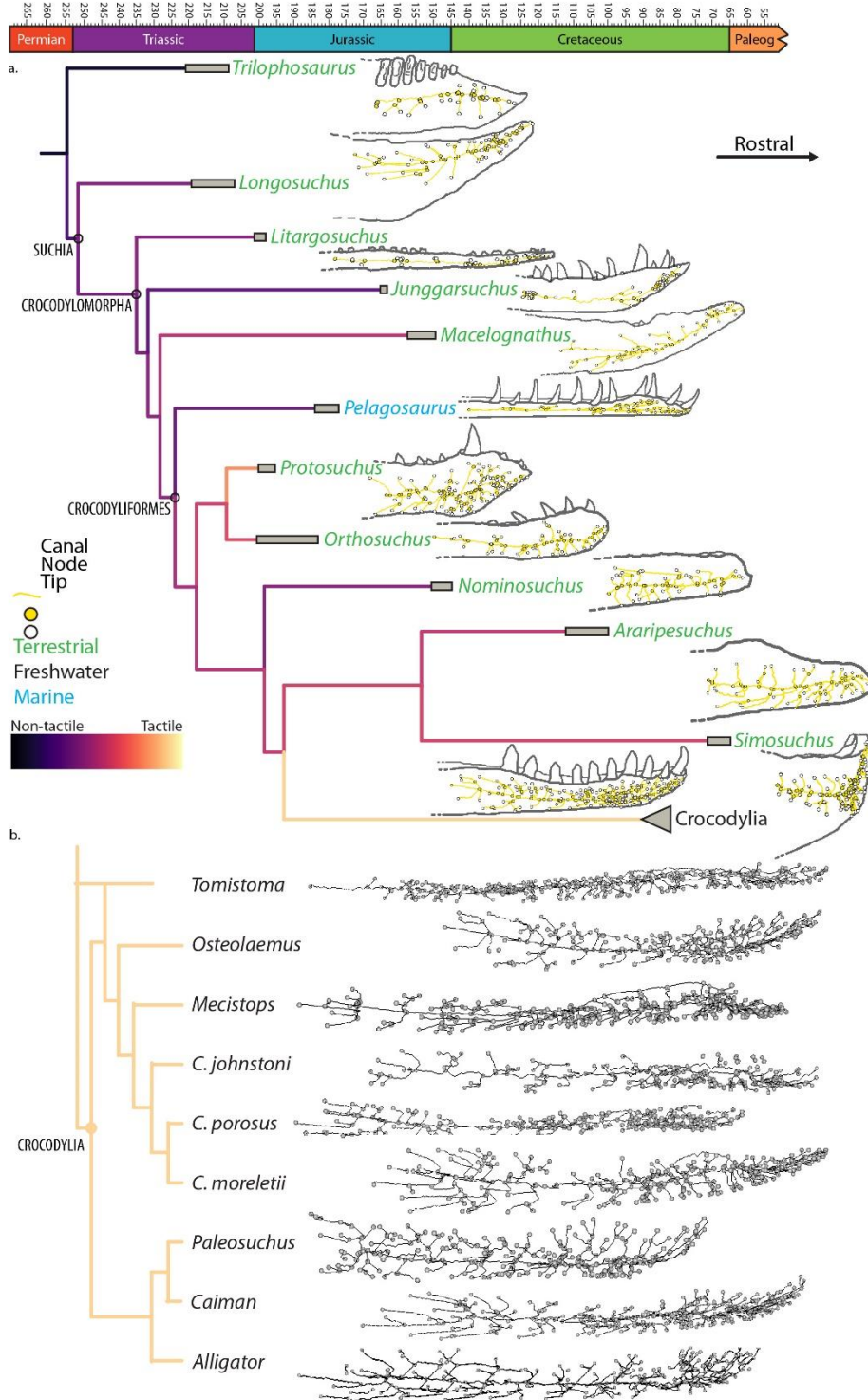


Figure 5.14. Photographs of dentaries with neurovascular foramina of fossil pseudosuchians including (a) *Trilophosaurus* (TMM 31025-125), (b) *Phytosaur* (MNA V3601), (c) *Revueltosaurus* (PEFO 34561), (d) *Longosuchus* (TMM 31100-1338), (e) *Batrachotomus* (SMNS 80260), (f) *Hesperosuchus* (cast, AMNH 6758), (g) *Sphenosuchus* (SAM PK-3104), (h) *Dromicosuchus* (UNC 15574), (i) *Junggarsuchus* (IVPP V14010), (j) *Macelognathus* (LACM 150148), (k) *Orthosuchus* (SAM PK-K409), (l) *Gomphosuchus* (UCMP 97638), (m) *Protosuchus* (MCZ 6727), (n) *Anatosuchus* (MNN GAD17), (o) *Hamadasuchus* (BSPG 2005 I 83), (p) *Kaprosuchus* (MNN IGU12), (q) *Araripesuchus* (BSPG 2008 I 41), (r) *Malawisuchus* (Mal-49), (s) *Simosuchus* (UA 8679), (t) *Dakosaurus* (SMNS 8203), (u) *Steneosaurus* (UC 402), (v) *Rhamphosuchus* (BMNH R5936), and (w) *Allognathosuchus* (FMNH P12141).



Figure 5.15. Photographs of dentaries with neurovascular foramina of fossil avemetatarsalians including (a) *Silesaurus* (ZPAL Ab III/437/1), (b) *Dilophosaurus* (TMM 43646-1), (c) *Ceratosaurus* (UMNH VP5278), (d) *Masiakasaurus* (FMNH PR2471), (e) *Majungasaurus* (FMNH PR2100), (f) *Tyrannosaurus* (MOR 1125), (g) *Allosaurus* (DINO 2560), and (h) *Marshosaurus* (UMNH VP6368).



Chapter 6 — Quantitative analysis of trigeminal osteological correlates among reptiles

INTRODUCTION

Gross anatomy and qualitative variation in the trigeminal nervous system and osteological correlates are well known among sauropsids (see Chapter 1 for a thorough discussion). However, minimal quantitative assessment of the relevant features has been performed the few assessments have explored only small clades of reptiles or single cranial features (e.g., George and Holliday 2013, Iwaniuk et al. 2009). This project (along with Chapters 4 and 5) aims to expand our knowledge of trigeminal features and increase predictive power of osteological correlates in predicting somatosensory behaviors in extinct organisms. Particularly, rarely have ecological categorizations of taxa been used in quantitative comparison of trigeminal osteological features (e.g., Wylie et al. 2015).

Taxa exhibiting enhanced trigeminal somatosensitive abilities or specializations are generally known, having been observed engaging in distinct behaviors. Among sauropsids, these include extant crocodylians, known for their abilities to discriminate between fine stimuli in the semi-aquatic environment (e.g., Di-Poï and Milinkovitch 2013, Leitch and Catania 2012, Grap 2020). Other specialized somatosensitive taxa are probing and dabbling birds, which make use of tactile cues to acquire food particles and prey (e.g., Cunningham et al. 2010, Cunningham et al. 2013, Gottschaldt and Lausmann 1974). Generally, with the exception of some snakes (e.g., Catania 2010, Goris 2011), lepidosaurs are assumed to engage in minimal trigeminal-innervated somatosensory behaviors, though their specific ecologies remain unknown.

Here I assess the strength of trigeminal osteological correlates, use what knowledge exists in the literature to determine whether there is a relationship between correlate size and ecology, and make predictions in fossil taxa based on these results. The

resulting predictions are used to inform evolutionary trends in trigeminal-innervated somatosensory behaviors.

MATERIALS AND METHODS

Specimens

Both osteological and digital specimens were investigated for this project. Some extant specimens underwent iodine contrast-enhanced microCT scanning (Gignac et al. 2016) in order to allow for contrast between hard and soft tissue structures. Other extant and all fossil specimens underwent traditional micro- and medical CT scanning to differentiate bone from surrounding tissue, matrix, or air.

Measurements

From extant, contrast-enhanced CT-scanned specimens volume of the trigeminal ganglion and cross sectional area and height of the mandibular division of the trigeminal nerve at the opening of the proximal opening of the mandibular canal were collected. Osteological features (i.e., skull width, foramen magnum width, trigeminal fossa volume, maxillomandibular foramen diameter, mandibular nerve foramen cross sectional area and height, rostral dentary foramen count, rostral dentary length, rostral dentary surface area) were collected from all extant contrast-enhanced specimens, from additional extant specimens, and from various fossil specimens. The trigeminal fossa was measured as the space bounded by the laterosphenoid, prootic, and quadrate. Both the maximum and the minimum distance across the foramen through which the maxillary and mandibular (and sometimes ophthalmic) division pass were collected.

I focused on the mandibular division of the trigeminal nerve because its sensory targets are largely integumentary, providing the best signal for inferences of sensory behaviors from osteological correlates. The cross-sectional area and height of the

mandibular nerve were collected at the proximal-most extent of the mandibular canal, at the first instance where the canal exhibited complete enclosure. This point is rostral to the separation of the lingual branch of the trigeminal nerve and thus measurements are not in conflict with any influence of tongue innervation requirements (see Chapter 5, figure 5.3f-h). The dentary measurements (i.e., foramen count, length, surface area) were taken rostral to the proximal opening of the mandibular canal. The dentary surface area only included the lateral, integumentary surface of the dentary. Additional features, (i.e., skull width, foramen magnum width) were collected for use in normalizing for body-size.

Soft tissue features were measured digitally using 3D-imaging software, Avizo (Thermo Fisher Scientific; Waltham, MA). Linear measurements were collected using the ‘Measure: 2D length’ tool, and cross-sectional areas collected using the ‘Material Statistics: Area per slice’ module. Surface areas were collected using the surface editor and ‘Surface Area Statistics’ module. Trigeminal ganglia, trigeminal fossae, and mandibular canals were manually segmented using magic wand and paint-brush tools with interpolation. Volumes were collected using the ‘Material Statistics’ module.

Analysis

The above measurements were compared to determine statistical significance of osteological correlates and to test for shared morphological patterns within ecological groups. Correlation was assessed while accounting for phylogeny using the R package ‘phytools’ (Revell 2012). Proxies for size were determined based on evidence by O’Brien (et al. 2019) that skull width is a statistically supported proxy for body size in crocodylomorphs. Because of the fragmentary or partial nature of many specimens, I determined the utility of foramen magnum width and anterior dentary surface area using

phylogenetic linear modeling (Revell 2012) and the R packages ‘ape’ (Paradis and Schliep 2019) and ‘nlme’ (Pinheiro et al. 2013), and ‘phytools’ (Revell 2012). Based upon observed behaviors from the literature (Cunningham et al. 2013, Di-Poi and Milinkovitch 2013, Grap et al. 2020, Leitch and Catania 2012), each extant specimen was assigned to one of two groups: those engaging in tactile-sensory behaviors and those in which tactile-sensory behaviors were absent. Group differences were tested for all variables in R using the ‘evomap’ (Smaers and Mongle 2014) package to run phylogenetic ANCOVAs. Generalized linear models (i.e., discriminant analysis) were used to estimate probabilities to decide group membership for fossil specimens using R packages ‘stats’ (R Core Team 2021) and ‘MASS’ (Venables and Ripley 2002). The R package ‘mice’ (van Buuren and Groothuis-Oudshoorn 2011) was used for imputing data. The phylogeny used in analysis was an adapted from those listed in Supplemental File 2. Multiple specimens per species were represented as hard polytomies and branch lengths were estimated using the R packages (phytools) (Revell 2012) and ‘geiger’ (Pennell et al. 2014) to calculate and assign Pagel’s lambda per variable (Pagel 1999). Significance was assessed at an alpha-level of $p = 0.05$.

RESULTS

Gross anatomy

This section details the morphology of the lateral braincase wall of the specimens investigated and expands on the description of the osteological correlates of the mandibular nerve provided in Chapter 5 by adding description of turtles and additional fossil specimens.

Lateral braincase wall

As described in Chapter 1 and among the lepidosaurs investigated most taxa (e.g., *Anolis* [MUVC LI089, 090, 091, 092], *Crotaphytus* [TMM M16243], *Eremias* [TMM M16147], *Pogona* [SAMA R52521], *Dracaena* [TMM M16152], *Physignathus* [TMM M16082], *Uromastyx* [TMM M16221], *Trioceros* [TMM M16233], *Ctenosaura* [MUVC LI084], *Varanus* [OUVC 10417, MUVC LI074], *Sphenodon* [SAMA 70524], *Gekko*) have two distinct trigeminal ganglia that are located within the trigeminal notch of the prootic bone (Fig 6.1a). The small gecko *Sphaerodactylus* [UF HERP95971] has a single ganglion within a completely enclosed trigeminal foramen as described by Daza et al. (2013). The snakes investigated (e.g., *Morelia* [MUVC LI004], *Agkistrodon* [MUVC LI085], *Python* [MUVC LI073]) also have distinct trigeminal ganglia, but have three foramina for the trigeminal nerve divisions. *Agkistrodon* has a large maxillary division, innervating infrared-sensing pit organs (Goris 2011).

The archosauromorph *Trilophosaurus* (YPM 4187; TMM 31025-140) exhibits a single trigeminal opening in the prootic at the rostral border of a round fossa.

Among the ornithischian dinosaurs sampled, the thyreophorans (e.g., *Gastonia* [BYU 15466, 15656, 14659; DMNH 53033, 50169, 50168], *Gargoyleosaurus* [DMNH 27726], *Mymoorapelta* [MWC 5435], ankylosaurid [UMNH 21000], *Kenturosauros* endocranial cast [MCZ 4115], *Stegosaurus* [UMNH 5731; DMNH 2818; YPM 1853], nodosaurid [BYU 16409], *Sauropelta* [YPM 5529]) have one large, single trigeminal opening. Thyreophoran trigeminal foramina are marked by anterodorsal notches for the middle cerebral vein (e.g., *Sauropelta* [YPM 5529]) and grooves for the three trigeminal nerve divisions (e.g., *Stegosaurus* [UMNH 5731], *Gastonia* [DMNH 50168]) (Averianov 2007, Kuzmin et al. 2020).

The small orodromines *Oryctodromeus* (MOR 1636), *Orodromeus* (MOR 403), and *Zephyrosaurus* (MCZ 4392) only preserve posterior braincases and thus lack the expected osteological correlates for the ophthalmic division of the trigeminal nerve. However, there is a foramen for the trigeminal nerve on the anteroventral border of the prootic (Scheetz 1999, Krumenacker 2017) that is large in *Zephyrosaurus* (MCZ 4392). Other ornithopods possess large trigeminal openings and follow the hypothesis of morphological change through ontogeny (e.g., progressive enclosure of the ophthalmic groove [Holliday 2006]). In the smallest specimen observed (*Tenontosaurus* [MCZ 4205]) the trigeminal opening is a large foramen surrounded by a slight fossa. In the next largest specimen (*Brachylophosaurus* [MOR 1071-7-13-99-87-I]) the fossa has a narrow bony ridge on the posterodorsal border resulting in the presence of a fossa only rostroventrally and a rostral groove for the ophthalmic division. In the larger *Parasaurolophus* (DMNH 132300), hadrosaurid (UMNH 30162), iguanodontid (BYU 22080), *Bactrosaurus* (YPM 2549), ‘*Camptosaurus*’ (YPM 1856), and *Acristavus* (MOR 1155, UMNH 16007) the fossa is deeper, the ridge more robust, and the ophthalmic groove deeper. In the largest specimens (*Edmontosaurus* [YPM 618] and *Brachylophosaurus* [MOR 1071-7-7-98-86]) the fossa is even deeper and the ophthalmic groove deep and nearly enclosed into a true canal.

The ceratopsid morphologies observed (e.g., *Triceratops* [MOR 3027, MCZ 1102]) are identical to the literature (e.g., Holliday 2006, Kirkland and DeBlieux 2010, Lehman 1989, Bullar 2021) in that there is a large opening for the maxillary and mandibular divisions of the trigeminal nerve and a separate rostral foramen for the opening of the ophthalmic division. The only smaller specimen investigated was

incomplete (*Einosaurus* [MOR 456]) and thus it is unclear whether the separation of the ophthalmic division is an ontogenetic feature (Holliday 2006).

The sauropods investigated all follow the known morphology of a single trigeminal opening (Witmer et al. 2008). Three non-phylogenetic morphologies are present: the subcircular opening (e.g., *Abdyosaurus* [DINO 39727, 17849], *Camarasaurus* [UMNH 9062, 5665, 5952 right side], *Mierasaurus* [UMNH 26004], *Moabosaurus* [BYU 14359, 11614, 14877 left side]); the dorsoventrally tall and mediolaterally compressed opening (e.g., *Apatosaurus* [YPM 1860], *Camarasaurus* [BYU 9199, 9048; DINO 4825], *Moabosaurus* [BYU 14670], *Pleurocoelus* [TMM 40435]), and the trilobate opening (e.g., *Camarasaurus* [UMNH 5952 left side], *Moabosaurus* [BYU 14877 right side]).

The non-avian theropods investigated also follow the morphology described in the literature (Holliday 2006, Sampson and Witmer 2007) with a single trigeminal foramen present in *Majungasaurus* (FMNH PR 2100), *Acrocanthosaurus* (MUO-8-0-59), *Ceratosaurus* (BYU 12893), *Suchomimus* (MNN GDF214), and *Irritator* (SMNS 58022), whereas *Falcarius* (UMNH 15000), *Tyrannosaurus* (MOR 1125), and *Allosaurus* (YPM 14554; DINO 11541, 2560; BYU 13679, 5287; UVP 910; UMNH 5472, 16605, 23132/21117) have two separate foramina for the maxillomandibular and ophthalmic divisions (Fig. 6.1b). *Majungasaurus* (FMNH PR 2100), *Suchomimus* (MNN GDF214), *Irritator* (SMNS 58022), and potentially *Ceratosaurus* (BYU 12893) have a rostral groove for the ophthalmic division of the trigeminal nerve. Similar to other megalosaurid theropods, *Marshosaurus* (DMNH 3178) exhibits a bilobate trigeminal opening (Allain 2002) and a separate ophthalmic foramen (Knoll et al. 1999).

As noted above, the avian trigeminal ganglia are typically located within the large braincase, resulting in bony foramina for the exit of the ophthalmic and maxillomandibular divisions of the trigeminal nerve (Baumel and Witmer 1993; Fig. 6.1c). In most taxa observed (e.g., *Scolopax* [MUVC AV194], *Anas* [MUVC AV097, 222, 226], *Psittacus* [MUVC AV092], *Megascops* [MUVC AV073], *Fulica* [MUVC AV285], *Mareca* [MUVC AV245], *Phasianus* [MUVC AV263], *Meleagris* [OUVC 10624], *Alle* [OUVC 10752], *Amazona* [MUVC AV076], *Cynoramphys* [MUVC AV079], *Phoebastria* [OUVC 10905], *Phalacrocorax* [OUVC 10847], *Columba* [NHMUK PAL001] the trigeminal ganglia are distinct and separate. In *Pandion* (MUVC AV335), *Megaceryle* (MUVC AV333), *Buteo* (MUVC AV351), and *Struthio* (MUVC AV348) the ganglia are not distinct, though contrast-enhanced CT data indicates that the ganglia are distinguishable histologically. The presence of this feature in *Pandion* and *Buteo*, both accipitriformes indicates that there may be some phylogenetic significance to this arrangement. The maxillomandibular ganglion sometimes leaves a slight impression (as in *Pandion* [MUVC AV335], *Amazona* [MUVC AV076], *Struthio* [MUVC AV348], *Phoebastria* [OUVC 10905]) and in other instances, (as in *Scolopax* [MUVC AV194], *Anas* [MUVC AV097, 222, 226], *Mareca* [MUVC AV245]) a deep fossa. The cases in which the enlarged maxillomandibular ganglion leaves a deep fossa are shared by anseriformes and charadriiformes, both clades known for highly sensitive, trigeminal-innervated bill-tip-organs (Cunningham et al. 2010). These taxa also exhibit very large trigeminal nerve divisions. Of all taxa investigated, only *Meleagris* (OUVC 10624) exhibits three separate foramina for the ophthalmic, maxillary, and mandibular divisions of the trigeminal nerve and only on one side. Baumel and Witmer (1993) note three

foramina in additional taxa, some of which were examined here, indicating that the presence of three foramina is highly variable. All other taxa have two foramina, one for the maxillary and mandibular divisions between the prootic and laterosphenoid, and one for the ophthalmic division between the laterosphenoid and basisphenoid, parasphenoid, interorbital septum complex (Baumel and Witmer 1993). In some taxa the maxillomandibular foramen is a canal rather than just a hole (e.g., *Columba* [NHMUK PAL001], *Phalacrocorax* [OUVC 10847], *Alle* [OUVC 10752], *Pandion* [MUVC AV335]).

Among the basal pseudosuchians investigated, phytosaurs (GR H3-410, GR H2-2010-06-26, UMNH 24306, TMM 3110-1337, *Nicrosaurus* [SMNS 4378, 13007]), aetosaurs (*Longosuchus* [TMM 31100-531], *Desmatosuchus* [UCMP 27410], *Neoaetosauroides* [PVL 5698], *Scutarx* [PEFO 34616], *Coahomasuchus* [TMM 31100-437]), and *Batrachotomus* (SMNS 80260) all exhibit a single trigeminal opening accompanied by the deep trigeminal fossa. The crocodylomorphs *Litargosuchus* (BP 5237), *Dibothrosuchus* (IVPP V7907), and *Junggarsuchus* (IVPP V14010) possess a single opening and fossa as well (Fig. 6.1d,e). In *Litargosuchus* (BP 5237) the fossa is bounded by a thin bony ridge. The teleosaurids *Steneosaurus* (SMNS 1.4.13), *Pelagosaurus* (NHMUK PV OR32599), and *Metriorhynchus* also have a single trigeminal foramen and fossa and exhibit a groove in the laterosphenoid for the passage of the ophthalmic division. The crocodyliform *Protosuchus* (BP I 4770) exhibits a single foramen in the laterosphenoid (Dollman 2020), whereas *Orthosuchus* (SAM PK K409) and *Nominosuchus* (IVPP 14392) do exhibit trigeminal foramina but are too fragmentary in nature to provide details (Fig. 6.1g,h). Among notosuchids (e.g., *Araripesuchus*

[AMNH 24450; MNN GAD19], *Hamadasuchus* [ROM 52620], *Mahajangasuchus* [FMNH PR 2448], *Simosuchus* [UA 8679]), there is a separate foramen for the maxillary and mandibular divisions and the ophthalmic division because of the presence of a laterosphenoid bridge and varying contribution by the epipterygoid (detailed by Holliday and Witmer 2009; Fig. 6.1i). In *Simosuchus* (UA 8679), this foramen is not completely enclosed and is more notch-like (Fig. 6.1j). A groove for the ophthalmic division is also present in *Rhabdognathus* (CNRST SNY190) and *Aegisuchus* (ROM 54530) but a foramen bounded by the laterosphenoid lateral bridge and pterygoid is present in *Eutretauranosuchus* (AMNH 570). In all other extinct suchians (e.g., *Leidyosuchus* [ROM 1903], *C. robustus* [MCZ 1006], *T. cairensis* [SMNS 50740], *T. gavialoidea* [SMNS 11785], *C. megarhinus* [SMNS 1122412], *Crocodylus* [SMNS 12649], *T. africanum* [SMNS 112417], *Allognathosuchus* [UMNH 28395]) the laterosphenoid lateral bridge contributes to a separate foramen for the ophthalmic and maxillomandibular divisions.

The crocodylians observed (e.g., *Alligator* [MUVC AL031], *Crocodylus* [FMNH 16162], *Osteolaemus* [FMNH 53632], *Paleosuchus* [FMNH 22817], *Tomistoma* [FMNH 11085], *Gavialis* [TNHC 110000]) do not deviate from the known morphologies described above, the variation in laterosphenoid lateral bridge morphologies described in Holliday and Witmer (2009), and all other description by Kuzmin (2021) (Fig. 6.11).

Dentary

Turtles are unique. *Caretta* (TMM M-7143) and *Chelydra* (TMM M-2337) possess highly perforated dentaries, *Trachemys* (TMM M-858, 7159) slightly less perforated dentaries, and *Gopherus* (TMM M-4934) and *Trionyx* (TMM M-3132) even

less perforated dentaries. All have a distinctive row of foramina along the tomial edge of the dentary. *Gopherus* (TMM M-4934) possesses a rostral concentration of foramina and the pattern in *Caretta* (TMM M-7143) is radiate, resembling that of aetosaurs.

Descriptions of osteological correlates of trigeminal tissues in the dentary (e.g., mandibular canal, lateral foramina) made from direct observation of fossil material are detailed here. Several observations apply to all taxa including: foramina on the caudal portion of the dentary are often groove-like, and the groove is directed caudally; if the specimen possesses a rostral mandible that is mediolaterally wide rather than dorsoventrally tall there is a concentration of rostral foramina; and there is a row of foramina paralleling the dorsal dentary margin. In the descriptions below, few describes foramina counts typically less than 30, but density is based on mandible surface area, which was not quantified for all taxa (see Chapter 5 for density metrics).

The neodiapsid *Champsosaurus* (YPM 16239) has few foramina (~8) on the dentary; most of those present are located along the alveolar margin and are elongate and groove-like in shape. This is similar to the condition with in lepidosaurs (see Chapter 5 for more description) in which there tend to be 5 to 6 foramina distributed in a line paralleling the tooth row. The allokotosaurid archosauromorph *Trilophosaurus* (TMM 31025-125, 116, 223) has a similar arrangement in which there are few foramina present (~19), with most falling in a row parallel to the alveolar margin (Fig 6.2b). The mandibular canal in *Trilophosaurus* (TMM 31025-233) becomes distinct from the Meckelian fossa at the level of the 7th tooth (from rostral) and is located ventromedial to the teeth. The archosauriform *Proterochampsia* (MCZ 3408) possesses a higher density of foramina, which are elongate in shape.

Among crocodylian-line archosaurs, phytosaurs *Mystriosuchus* (SMNS 9134), *Rutiodon* (YPM 7899), and phytosaur (MNA V3601) have a higher density of foramina than the non-archosaur diapsids and a row of foramina paralleling the tooth row. Phytosaurs typically possess a rostral concentration of foramina on the dentary tip. The mandibular canal in phytosaurs (MNA V3601) is located lateral to the alveoli rostrally. Aetosaurs *Paratypoyhorax* (SMNS 19003), *Stenomyti* (DMNH 60708), *Aetosaurus* (SMNS 5770), and *Longosuchus* (TMM 31100-1338, TMM 31185-84) have a low density of foramina (~8-34) that are accompanied by grooves arranged in a stellate pattern, radiating from a point on the rostrolateral surface of the mandible (Fig 6.2c). They also possess a row of foramina on the edentulous portions of the mandible and paralleling the alveolar margin. A foramen is present at the rostral tip of the mandible. The mandibular canal in *Longosuchus* (TMM 31185-84) becomes distinct from the dorsal aspect of the Meckelian fossa at the level of the 4th tooth (from rostral) and continues rostrally lateral to the alveoli. The non-paracrocodylomorph suchian *Gracilisuchus* (MCZ 4117), as well as the unnamed suchian SMNS 1977, and the non-crocodylomorph loricatans *Saurosuchus* (MCZ 4687, 4690) and *Batrachotomus* (SMNS 52970, 80260) all have few foramina (~4-27). In *Batrachotomus* (SMNS 52970, 80260), there is a distinct line of foramina within a groove paralleling the alveolar margin caudally and the alveolar margin rostrally. SMNS 80260 also has a distinct row of foramina long the ventral margin of the dentary, and the opening for the mandibular canal is present at the rostral narrowing of the Meckelian fossa. In the non-crocodyliform crocodylomorphs *Litargosuchus* (BP 5237), *Junggarsuchus* (IVPP V14010), and the unnamed YPM 57103, there is a low density of foramina with a row of foramina paralleling the alveolar and

ventral dentary margins (~26-34) (Fig 6.2 d, f). In the non-crocodyliform crocodylomorph *Macelognathus* (LACM 150148) there is a higher density of foramina especially at the rostral edentulous portion of the jaw (~30) (Fig. 6.2e). In *Litargosuchus* (BP 5237), *Junggarsuchus* (IVPP V14010), and *Macelognathus*, (LACM 150148), the mandibular canal is located ventrolateral to the alveoli. The protosuchian crocodylomorph *Platyognathus* (CUP 2083) has a large opening for the mandibular canal. Several thalattosuchians were investigated including *Steneosaurus* (SMNS 53661, 20218, 10114; P 14541), *Machimosaurus* (SMNS 81608, 91415), *Pelagosaurus* (SMNS 50374; BRSLI M1413), *Metriorhynchus* (SMNS 10115), and *Dakosaurus* (SMNS 8203), all of which possessed a low density of foramina (~38). The foramina of the thalattosuchians were elongate and groove-like. In *Dakosaurus* (SMNS 8203), the foramina paralleled the tooth row and the ventral dentary margin, and in *Machimosaurus* (SMNS 91415), there was a rostral concentration of foramina. The non-neosuchian crocodyliforms *Protosuchus* (BP 1 4770; MCZ 6727), *Orthosuchus* (SAM PK K409), and *Nominosuchus* (IVPP 14392) have a higher density of foramina (~26-69), and *Protosuchus* (BP 1 4770; MCZ 6727) a notable rostral concentration (Fig 6.2f, g, i). The mandibular canal in these taxa is located ventrolateral to the alveoli and is large in *Nominosuchus* (IVPP 14392). Among notosuchians, the more basal *Mahajangasuchus* (FMNH PR 2721) and *Kaprosuchus* (MNN IGU 12) have a low density of foramina, but exhibit high rugosity of the mandible. In *Kaprosuchus* (MNN IGU 12), the foramina are present largely along the alveolar margin. Other notosuchians, *Simosuchus* (UA 8679), *Anatosuchus* (MNN GAD17), and *Araripesuchus* (MNN GAD20, 27; UCRCPV 3; AMNH 24450) possess more foramina (~35-40), exhibiting

high rostral densities, and lower densities elsewhere across the dentary (Fig. 6.2h, j). In *Simosuchus* (UA 8679) and *Araripesuchus* (AMNH 24450), the mandibular canal is located ventrolateral to the alveoli. The tethysuchid *Elosuchus* (UCRCPV G4-7) exhibits a low density of foramina. The unnamed non-crocodylian eusuchian MCZ 4453 has a high density of foramina and the basal non-crocodylian eusuchian *Laganosuchus* (UCRCPV 2) a low density of foramina. The crocodylians *Allognathosuchus* (FMNH P 12141), *Gavialosuchus* (UC 610), *A. mcgrewi* (FMNH P 26242), and *A. olseni* (MCZ 4703) all exhibit density on the scale of extant crocodylians, whereas *Diplocynodon* (SMNS 59595) has fewer foramina along with a higher rugosity and elongate, narrow foramina. Extant crocodylians all share a high density of foramina with a rostral concentration (Fig 6.2k).

Among avemetatarsalians, ornithischians tend to have low densities of foramina. *Stegosaurus* (DMNH 2818; UMNH VP5490, 165490) have few foramina (~7-16), with large rostral foramina, and rows paralleling the alveolar and ventral dentary margin. The nodosaurids *Gargoyelosaurus* (DMNH 27726) and *Sauropelta* (YPM 5502) have few foramina as well (~11-14), with a row along the alveolar margin, and large rostral foramina. The mandibular canal in *Sauropelta* (YPM 5502) originates in a deep fossa. The ceratopsids *Triceratops* (YPM 1823, 3220; MOR 3027), *Utahceratops* (UMNH VP16697), and *Einosaurus* (MOR 456) have large, but few foramina (~14-21) often paralleling the alveolar margin (in a groove in [MOR 3027]) and all possess large rostral foramina. In *Triceratops* (MOR 3027), the mandibular canal originates in a deep fossa. The pachycephalosaurid *Stegoceras* (YPM 57176; UALVP 1) has few foramina (~6) and those present largely parallel the alveolar margin. The parksosaurids *Orodromeus* (MOR

294, 1141) and *Zephyrosaurus* (MCZ 4392) possess few foramina (~5) and a row of large foramina along the alveolar margin. The ornithopods *Dryosaurus* (DMNH 9001; SMNS 52361; YPM 1876), *Eolambia* (FMNH PR 4378), hadrosaurid (FMNH PR 2249; MCZ 2771), *Lambeosaurus* (UC 1479), *Maiasaura* (FMNH PR 2538), *Acristavus* (MOR 1155), *Brachylophosaurus* (MOR 1071), *Camptosaurus* (UMNH VP16452, 16455; YPM 1888, 7421, 1886), and *Gryposaurus* (UMNH VP12265) all have few foramina (~4-13), and many possess a row of foramina within a depression along the alveolar margin and large rostral foramina. The mandibular canal is large, ventrally placed, and present in a deep fossa in the parasaurolophine (DMNH 132300), *Acristavus* (MOR 1155), *Brachylophosaurus* (MOR 1071), and *Dryosaurus* (SMNS 52358). The sauropodomorphs *Sarhsaurus* (MCZ 8893), *Plateosaurus* (SMNS 54935, 91297; YPM 8161), and *Anchisaurus* (YPM 1883) have few foramina (~12-13), and most are along the alveolar margin. *Sarhsaurus* (MCZ 8893) has some foramina long the ventral margin of the dentary, and *Plateosaurus* (SMNS 91297) has large rostral foramina. The sauropods *Abdyosaurus* (DINO 16488, 17848, 39727) and *Mierasaurus* (UMNH VP26010) have few (~10) but large foramina, whereas *Camarasaurus* (DINO 2580; UMNH VP1162, 5539; YPM 1905) has notably more foramina (~45-63). The mandibular canal is ventrally placed in *Abdyosaurus* (DINO 17848) and *Camarasaurus* (YPM 1905) and has a notch extend dorsally from it in *Camarsaurus*. Among the non-avian theropods, the herrerasaurid *Staurikosaurus* (MCZ 1669) has few foramina (~10) and a row of foramina along the alveolar margin. The basal theropod *Dilophosaurus* (TMM 43646-1.80) has very few foramina (~16), some are in a groove paralleling the alveolar margin, others along the ventral dentary margin, and the mandibular canal is located ventral to the

alveoli (Fig. 6.2l). The ceratosaurids *Masiakasaurus* (FMNH PR 2178, 2471; UA 8680) and *Ceratosaurus* (UMNH 5278) have few foramina (~23), most located along the alveolar and ventral dentary margin and have a ventrally located mandibular canal. The abelisaurid *Majungasaurus* (FMNH PR 2100) has a row of foramina in a groove paralleling the alveolar margin and a similar density of foramina as the megalosaurid *Marshosaurus* (UMNH VP6367, 6368) (~35-45) (Fig. 6.2m). The megalosaurid *Torvosaurus* (BYU 2003) has a lower density of foramina (~10). *Allosaurus* (BYU 2028; DINO 2560; MWC 5440; UMNH VP6477, 9348; YPM 14554) has more foramina than other theropods (~23-59), and caudally, these are located in a groove paralleling the alveolar margin, whereas rostrally, the foramina are directly along the alveolar and ventral dentary margin (Fig. 6.2o). The mandibular foramen in *Allosaurus* is present ventral to the alveoli. In the tyrannosaurids *Teratophoneus* (BYU 9398), tyrannosaurid (FMNH PR 1196), and *Gorgosaurus* (YPM 21843) the few foramina (~27) are present in a groove paralleling the alveolar margin and along the ventral margin of the dentary. In *Tyrannosaurus* (MOR 1125), the foramina are more dense (~73) though arranged similarly, and the mandibular canal is located ventral to the alveoli (Fig. 6.2n). In the dromaeosaurid *Deinonychus* (MCZ 4142) and troodontid *Byronosaurus* (IGM 100.983), the foramina (~29-39) are mostly along the alveolar margin (Fig. 6.2p). On the dentary of the extinct avians *Amdalgalornis* (FMNH P 14357) and *Andrewsornis* (FMNH P 13417) there is a large rostral foramen. The dentary of the extinct avian *Dinornis* (FMNH PA35) is highly foraminiferous. Avian mandibles (e.g., Fig. 6.2q) are variable and foramen distribution tied with ecology (see Chapter 5 for details).

Confirming osteological correlates

Trigeminal ganglion volume was compared with the maximum and minimum diameters of the maxillomandibular foramen (or prootic notch in lepidosaurs) in extant reptiles while accounting for phylogeny (Table 6.1, Fig. 6.3a-b). Among all reptiles, these features are highly correlated ($c = 0.94$). Maxillomandibular foramen diameter is even more highly correlated with trigeminal ganglion volume within crocodylians and lepidosaurs individually, though less so in birds ($c = 0.95, 0.98, c = 0.96, c = 0.59, 0.61$, respectively).

Cross sectional area of the mandibular division of the trigeminal nerve as it passes into the dentary was also compared to cross sectional area of the mandibular canal at the same location in extant reptiles while accounting for phylogeny (Table 6.1, Fig. 6.3). Among all reptiles, these features are well correlated ($c=0.911$). Correlation is stronger when assessed within crocodylians ($c = 0.985$) but less so when assessed just within lepidosaurs and birds ($c = 0.882, 0.853$, respectively).

Height of the mandibular division of the trigeminal nerve as it passes into the dentary was also compared to height of the mandibular canal at the same location in extant reptiles while accounting for phylogeny (Table 6.1, Fig. 6.3). Among all reptiles, these features are well correlated ($c = 0.868$). Correlation is stronger when assessed within just lepidosaurs and birds ($c = 0.977, 0.875$, respectively) but less so when assessed within crocodylians ($c = 0.815$).

The same correlations above were assessed for extant members of the non-tactile and tactile groups and are still strong (Table 6.1).

Trigeminal ganglion volume and mandibular nerve cross sectional area and height were also compared in extant reptiles to the number of foramina on the dentary rostral to

the point where the mandibular nerve enters the dentary (typically excludes few foramina; Table 6.1, Fig. 6.3). Correlations are very weak among sauropsids ($c = 0.453, 0.329, 0.352$, respectively) and thus were not explored further.

Establishing a size proxy

Because of the limited availability of complete skeletons or skulls, to make the most from the collected data, I explored foramen magnum width as a proxy for size in addition to skull width (O'Brien et al. 2019) using 102 extant sauropsids with both metrics measurable. Phylogenetic Reduced Major Axis (RMA) regression of skull width vs. foramen magnum width reveals a significant relationship between the two metrics ($R^2 = 0.87$, p -value = 0.000; Fig. 6.4a). A 95% CI captures all but 18 specimens. Because of the strength of this relationship, we use foramen magnum width as a covariate for size in future linear models involving features of the neurocranium (e.g., maxillomandibular foramen size).

I also explored anterior (to the complete enclosure of the mandibular canal) surface area of the dentary as a proxy for size to be used when only dentaries are available for measurement. This was tested using phylogenetic RMA regression of skull width vs. anterior surface area in extant and extinct specimens. I find a significant relationship between the two metrics ($R^2 = 0.84$, p -value = 0.000; Fig. 6.4b) using 57 extant sauropsids, and a 95% CI captures all specimens. I use anterior surface area of the dentary as a covariate for size in future linear models involving mandibular features (e.g., mandibular canal size).

Because of the uncertainty surrounding these variables, when necessary phylogenetic RMA regression was used to explore and illustrate (Fig. 6.5) relationships

between the proxies and other variables of interest. In this case, the size proxies are uncertain, likely covarying with unknown and unaccounted for variables, and phylogenetic RMA adjusts for this and phylogeny by assuming both the x and y variables have associated error rather than just the y variable.

Differences among ecologies

With osteological correlates confirmed (see ‘Confirming osteological correlates’, above) and a proxy for size established (see ‘Establishing a size proxy’, above) I performed phylogenetic ANCOVAs to test for size and phylogeny-controlled differences in osteological correlates among ecologies.

Comparisons between minimum and maximum diameters of the maxillomandibular foramen, cross sectional area and height of the mandibular canal, and foramen count were made between tactile and non-tactile sauropsids with size proxies included as covariates. Relative maxillomandibular foramen diameters (i.e., minimum and maximum) are not significantly different between groups (Fig. 6.5a-b; $p = 0.65, 0.90$, respectively; n tactile = 53, n non-tactile = 40). Relative canal dimensions (i.e., cross sectional area and height) are not significantly different between groups either (Fig. 6.5c-d; $p = 0.33, 0.43$; n tactile = 26, 26, n non-tactile = 30, 21, respectively). Relative foramen counts are significantly different between groups (Fig. 6.5e; $p \leq 0.0001$; n tactile = 27, n non-tactile = 32).

Since most features showed no significant differences among Sauropsida, differences were investigated within Archosauria, though this greatly reduced the sample size of non-tactile taxa. Relative maxillomandibular foramen diameters (i.e., minimum and maximum) are significantly different between groups (Fig. 6.5f-g; $p = 0.0083$,

0.0023, respectively; n tactile = 53, n non-tactile = 7). Relative canal dimensions (i.e., cross sectional area and height) and foramen counts are also significantly different between groups (Fig. 6.5h-j; $p \leq 0.001$; n tactile = 26, 26, 27, n non-tactile = 4, 5, 6, respectively).

Predictions

With significant differences in ecologies present among features within Archosauria, linear discriminant analysis was used to predict affinity of fossil specimens after removing all lepidosaurs from the dataset. Of the archosaurs sampled only 28 extant and 8 fossil specimens had all metrics present (i.e., maxillomandibular foramen metrics, mandibular canal metrics, foramen count, size proxies). A model including all metrics predicts extant ecology with 96% accuracy, with only *Psittacus* (MUV C AV092) being predicted opposite as classified, as a non-tactile taxon (Fig. 6.6a). Using the rostral metrics only, the model predicted extant ecology with 97% accuracy, with only *Psittacus* (MUV C AV092) being predicted opposite as classified, as a non-tactile taxon (Fig. 6.6b). Using the maximum diameter of the maxillomandibular foramen and foramen magnum width as a covariate, the model predicted extant ecology with 92% accuracy, with only *Psittacus* (MUV C AV092), *Fulica* (MUV C AV285), *Phasianus* (MUV C AV263), *Phoebastria* (OUVC 10905), and *Scolopax* (USNM 292760) predicted opposite as classified (Fig. 6.6c). For the minimum diameter of the maxillomandibular foramen and foramen magnum width as a covariate, the model predicted extant ecology with 90% accuracy, with only *Psittacus* (MUV C AV092), *Pandion* (MUV C AV335), *Fulica* (MUV C AV285), *Phoebastria* (OUVC 10905), *Scolopax* (USNM 292760), and *Arenaria* (USNM 612977) predicted opposite as classified (Fig. 6.6d). The model of the cross-

sectional area of the mandibular canal with dentary surface area as a covariate predicted extant ecology with 93% accuracy, with only *Psittacus* (MUVC AV092) and *Fulica* (MUVC AV285) predicted opposite as classified (Fig. 6.6e). A model using height of the mandibular canal and dentary surface area predicted extant ecology with 94% accuracy, with only *Megascops* (MUVC AV073) and *Fulica* (MUVC AV285) predicted opposite as classified (Fig. 6.6f). A final model using foramen count and dentary surface area as a covariate predicted extant ecology with 94% accuracy, with only *Psittacus* (MUVC AV092) and *Arenaria* (USNM 612977) predicted opposite as classified (Fig.6.6g). All predictions for fossil specimens are listed in Table 6.2 (Fig. 6.6).

Missing data was imputed and the dataset re-evaluated using the model including all metrics broadening the sample to 64 extant and 124 fossil specimens. The model predicted extant ecology with 98% accuracy, with only *Psittacus* (MUVC AV092) predicted opposite as classified (Fig. 6.6h). All predictions for fossil specimens are listed in Table 6.2 (Fig. 6.6h).

Among the extinct archosaurs, the imputed data is consistent in predicting the stem archosaur *Trilophosaurus* as non-tactile. Members of Phytosauria and Aetosauria were predicted as tactile. Non crocodyliform-crocodylomorphs were largely predicted as tactile in all models except for *Litargosuchus*, *Junggarsuchus*, *Macelognathus*. Among the non-crocodylian crocodyliforms sampled *Protosuchus*, and *Nominosuchus* are the only taxa in which models result in non-tactile predictions. Among the avemetatarsalians, each clade (except ankylosaurids, n=1) contained both non-tactile and tactile predictions with little pattern (Table 6.2).

Relative size of osteological correlates

Means of relative osteological correlates (e.g., minimum and maximum maxillomandibular foramen diameter vs. foramen magnum width, and foramen count, mandibular foramen height, and mandibular foramen cross sectional area vs. dentary surface area) among phylogenetically grouped taxa (e.g., lepidosaurs, non-archosaurian archosauromorphs phytosaurs, aetosaurs, non-crocodylomorph suchians, non-crocodyliform crocodylomorphs, non-crocodylian crocodyliforms, nodosaurids, ankylosaurids, pachycephalosaurids, stegosaurids, ornithopods, parksosaurids, ceratopsids, non-sauropod sauropodomorphs, sauropods, non-avian theropods, and avians) were compared using phylogenetic ANOVAs with size proxies included as covariates. Though there was no significant difference between group means, some patterns were evident in the data (Fig. 6.7-8).

Relative maxillomandibular foramen size is largest in extant crocodylians. Ornithopods, lepidosaurs, ceratopsids, parksosaurids, and suchians excluding non-crocodyliform crocodylomorphs share a similar mean, and are just larger than sauropods, theropods, ankylosaurids, and nodosaurids. Crocodylomorphs, stegosaurids, and avians share the smallest means. Relative mandibular canal cross sectional area is largest in theropods, smallest in avians, and all other taxa fall in between. Relative mandibular canal height is largest in crocodyliforms and avians have some of the smallest canals. Relative foramen counts increase along the pseudosuchian line to extant crocodylians. Avian relative foramen counts are intermediate, and theropod and lepidosaur taxa have the lowest relative foramen counts. Tactile taxa have greater means than non-tactile taxa for all metrics.

DISCUSSION

Morphology

Lateral braincase wall

The specimens observed here do not vary significantly from discussions of lateral braincase wall evolution detailed elsewhere (e.g., Holliday 2006, Holliday and Witmer 2009) and therefore, there is no further discussion here.

Dentary

In general, foramina or trigeminal neurovasculature distribution in dorsoventrally tall mandibles tends to occur along the alveolar margin (sometimes in a groove) and along the ventral dentary margin. When mandibles are dorsoventrally compressed and more spatulate in shape, (e.g., phytosaurs, crocodylians) there is often a rostral concentration of foramina. In the theropod taxa with mediolaterally compressed mandibles, the mandibular canal is located ventral to the alveoli rather than ventrolateral as in the pseudosuchian taxa and neurovascular morphology may differ as a result of alveolar depth (Bouabdellah et al. 2022). Additionally, in taxa with narrow, elongate mandibles (e.g., *Laganosuchus*, thalattosuchians, *Elosuchus*), there is a reduction in foramina numbers. These taxa are secondarily aquatic and I hypothesize this reduction occurs as a result of morphological constraint. Whereas a reduction in foramina is present in some taxa, notosuchian crocodyliforms have an increase in foramina. Whether this is an independent origin of foraminiferous mandibles from the condition in extant crocodylians, or marks their phylogenetic origin of foraminiferous mandibles among suchians is unknown. The latter would be the case if the presence of few foramina in *Elosuchus* is a secondary reduction.

There are some similarities in osteological correlates between taxa believed or known to have keratinous structures in addition to the bony mandible (e.g., Knutsen

2007, Holliday & Nesbitt 2013). Distinct foramina accompany the keratinous rhamphotheca on the dentary of birds and turtles, notably the large rostral foramina in many birds, and the row of foramina along the tomial edge in turtles. In extant birds, many of these rostral neurovascular foramina are present at oblique angles (Hieronymus et al. 2009). In extinct suchian taxa with edentulous portions of the dentary (e.g., aetosaurs, *Macelognathus*), the edentulous portion is often accompanied by more, larger, and groove-like foramina. This rostral portion of the aetosaur mandible has been hypothesized to have a keratinous covering and the foramina passages for vasculature to supply keratin (Demir & Özsemir 2021, Parrish 1994). Some dinosaurian taxa reviewed here demonstrate a similar morphology of large rostral foramina (e.g., *Stegosaurus*, *Saruopelta*, hadrosaurs, ceratopsids). I hypothesize the especially large rostral foramina in these taxa allow for neurovasculature to pass into predentaries and/or keratinous rhamphotheca and nourish and supply innervation to rostral rhamphotheca. This hypothesis is also supported by the presence of highly foraminiferous predentaries in many taxa (e.g., ceratopsid *Einosaurus* [MOR 456]). Such keratinous coverings might form specialized feeding structures (Lind and Poulsen 1963, Louyran et al. 2021) or dissipate stress during feeding (Lautenschlager et al. 2013).

I propose the use of foramen density as a phylogenetic character in future analysis. Though the taxonomic status of the suchian MCZ 4453 is unknown, the high density of foramina supports its postulated position within Eusuchia (Turner & Pritchard 2015). The unique high foramen counts in dinosaurs such as *Camarasaurus*, *Allosaurus*, and *Tyrannosaurus* have been hypothesized to indicate special sensory structures (Ibrahim et al. 2014, Barker et al. 2017, Carr et al. 2017, Rothschild and Naples 2017,

Cerroni et al. 2020, Kawabe and Hattori 2021) though these studies ignore distribution of foramina and specimen size. It must be noted that these specimens are typically large-bodied, so foramen count does not necessarily provide the increased density of neurovasculature across the mandible that is present in extant crocodylians and necessary for unique tactile behaviors (Leitch & Catania 2012, Lessner 2020, Chapter 5).

Osteological correlates

The strength of the correlations indicates that most of the trigeminal osteological features (i.e., trigeminal foramen diameter, mandibular canal cross sectional area, mandibular canal height) are suitable correlates for their soft-tissue counterparts (i.e., trigeminal ganglion volume, mandibular nerve cross sectional area, mandibular nerve height). The exception is the count of foramina on the dentary, which does not correlate well with any measured soft tissue feature. The strength of correlations among clades and ecological categories indicates these patterns occur independent of phylogeny and ecology. Therefore, all osteological features noted, except for foramen counts, may be used for direct predictions of soft tissues in bony and fossil taxa.

Size proxy and other limitations

One drawback of the fragmentary nature of fossil material is that we often lack a good size proxy, which is necessary for comparing relative sizes, and therefore implications of the data are often obscured. It is unclear whether the proxies for size used here (i.e., foramen magnum width, dentary surface area) are suitable for such a large sample. There is a general trend of increasing skull size with increasing foramen magnum size and dentary surface area and using these features did allow for an increased sample size and use of fragmentary specimens. Because many fossil specimens are fragmentary,

I felt it useful to use commonly present features as proxies for size. However, foramen magnum width likely varies widely based on numerous neural and biomechanical constraints and dentary surface area similarly varies with head shape and other features. For this reason, conservative statistical approaches (e.g., phylogenetic RMA regression) were used when relying on these features was necessary. Further assessment of foramen magnum dimensions and dentary morphologies among vertebrates may discount or support the use of these measurements.

Also, the braincase wall is variable in structure among sauropsids and thus osteological correlates vary in soft tissue contents. We measured the maxillomandibular foramen in taxa as a proxy for trigeminal ganglion size. Among sauropsids the ophthalmic division is variable in its exit from the braincase (see Chapter 1 for a summary) and therefore, its contribution was included in some taxa measured here and ignored in others. Because trigeminal ganglion volume and the diameter of the prootic notch (lepidosaurs) and maxillomandibular foramen (archosaurs) were well correlated with trigeminal ganglion size, I was confident in excluding ophthalmic measurements. This feature is often small, unprepared, and difficult to measure in fossil specimens as well.

Differences among ecologies

Though no significant differences were found among ecologies when including lepidosaurs in the sample (Fig 6.5a-e), differences were significant among archosaurs (Fig 6.5f-j). This is likely a result of weaknesses introduced by the size proxy used or the limited understanding of lepidosaurian ecologies. Regardless, means of all trigeminal osteological correlates were larger in taxa engaging in tactile sensory behaviors. Since

these osteological features correlate well with their soft-tissue counterparts, it is apparent that trigeminal-innervated tactile sensation is dependent on more trigeminal tissues and increased size of morphologically-related bony structures.

Though no trigeminal soft tissue features were found to correlate with foramen counts, here I note a distinct difference in foramen distribution between taxa engaging in tactile behavior and those not. Rostral foramen counts are commonly and irresponsibly used to predict sensory abilities in fossil taxa (e.g., Ibrahim et al. 2014, Barker et al. 2017, Carr et al. 2017, Rothschild and Naples 2017, Cerroni et al. 2020, Kawabe and Hattori 2021). I demonstrate that using this feature to predict sensory ecology is only appropriate when size is controlled and density of foramina is assessed (Fig. 6.5j).

Predictions

Of the extant archosaurs, crocodylians were consistently predicted to have the trigeminal tissues for tactile sensation, and only a few avian species were predicted opposite as categorized. Though parrots have been noted to possess a highly innervated rostral bill tip (Goujon 1869, Menzel and Lüdiche 1974), and thus I categorized them as tactile, models consistently indicate that their morphology was more representative of the non-tactile ecology. I posit this prediction results from the presence of a high concentration of innervation solely on the rostral tomia, rather than a widely distributed bill-tip-organ as in probe- and tactile-foraging birds (Cunningham et al. 2010). Similarly, *Fulica* is consistently predicted as tactile despite non-tactile classification. The non-tactile classification was chosen because there is little indication in the literature of specialized tactile-sensory behaviors in coots. This is an interesting case because feeding convergence is present between coots, dabbling ducks, and other waterfowl (Allouche

and tamisier 1984). Ducks and geese exhibit a highly-innervated rostral bill tip organ used for tactile discrimination of food (Gottschaldt & Lausmann 1974, Berkhoudt 1980), and this data indicates that there is a sensory system convergence between ducks and *Fulica* in addition to the known feeding convergence.

The non-tactile prediction for the stem-archosaur indicates the basal archosaurian condition was one lacking enhanced trigeminal sensory abilities. Among pseudosuchians, the tactile prediction for phytosaurs is in line with their occupation of semi-aquatic habitats and predictions of enhanced trigeminal sensation in the clade (Lessner & Stocker 2017). The non-crocodylomorph suchians largely included aetosaurs, which were predicted as tactile. Aetosaurs exhibit relatively larger trigeminal foramina than other suchians (personal communication, W. Reyes). As discussed above, the rostral, edentulous portion of the aetosaur mandible may have had a keratinous covering and therefore, the enlarged rostral trigeminal features may be a result of the need to extend more vasculature to nourish the growing keratin, rather than providing nervous tissue to the jaws (Demir & Özsemir 2021). These data reveal a trend of increasing tactile sensory ability along the line to extant crocodylians similar to that described in Chapter 5. The non-tactile predictions among the non-crocodyliform crocodylomorphs *Litargosuchus*, *Junggarsuchus*, and *Macelognathus* and the non-crocodylian crocodyliforms *Nominosuchus* and *Protosuchus* indicate that the transition occurred amongst early branching crocodyliforms, diverging in the Late Triassic, and preceding the Neosuchian transition to a semi-aquatic ecology (see Chapter 5 for divergence dates and other details). Among the non-avian dinosaurs investigated, no trends emerge. maxillomandibular foramen diameters resulted in predictions of tactile ecologies for most

taxa, with the exception of *Saraksaurus* and *Falcarius* and therefore are not as informative as hoped. Non-avian taxa with a range of cranial measurements include theropods *Dilophosaurus*, *Tyrannosaurus*, *Allosaurus*, and *Byronosaurus*. Ecologies of these taxa are mostly predicted as tactile, but based on foramen density in *Byronosaurus* and foramen density, rostral characters, and imputed data in *Dilophosaurus* those taxa have some non-tactile affinities.

Relative size of osteological correlates

Though not statistically-significantly different, the trends appearing upon comparison of relative sizes of osteological correlates generally match the model predictions. The models indicate an increase in tactile sensory abilities present along the crocodylian line, and maxillomandibular foramen diameter, mandibular canal cross-sectional area, and foramen count all increase from non-crocodyliform crocodylomorphs to extant crocodylians (Fig. 6.7). There is some variation among basal pseudosuchians, which may be because of potential semi-aquatic specialization of the phytosaur trigeminal system and beak innervation in aetosaurs.

Trends among non-avian dinosaurs are less clear. However, though the sample was not adequate to assess allometry among all sauropsids, I believe there are some ontogenetic differences as well. Among the ornithopods measured, the specimen with the largest relative trigeminal features (*Brachylophosaurus* [MOR 1071-7-13-99-87-I]) had the smallest skull (Fig. 6.7). Therefore, it is possible that during early growth, the rates of trigeminal tissue growth are more rapid than other features, impacting the growth of their osteological correlates. As neural growth slows, relative correlate size would then decrease.

Lepidosaurs are expected to have small relative features, but generally do not (Fig. 6.7-8). Both the degree of variation and high average in lepidosaur maxillomandibular foramen diameters (Fig. 6.7) indicates foramen magnum width may not be a suitable size proxy. These measurements may also be artificially inflated because of the lack of complete bony bounds for the trigeminal ganglion and divisions. Therefore, measuring the prootic notch in the absence of soft tissue may be an overestimate of trigeminal tissue size. Additionally, little is known about relative sensitivity among lepidosaurs, therefore it is possible that non-tactile designations assigned in analysis are not accurate and lepidosaurs retain large trigeminal nervous tissues for increased tactile abilities.

The degree of variation and inconsistent averages in avians indicates similar issues. Beak shape is highly variable and thus may confound surface area measurements (Fig. 6.7). Regardless, tactile taxa consistently exhibit larger osteological correlates with respect to the mandible (Fig. 6.7) but not with respect to the braincase (Fig. 6.7). The avian braincase is relatively large and takes up most of the skull (Balanoff et al. 2013) leaving little room for other tissues. Therefore, foramina and canals are often exactly the size of their contents and direct osteological correlates for neurovasculature. For this reason, I suspect that maxillomandibular foramen size in avians may underestimate trigeminal ganglion size as the intracranial ganglion can be substantially larger than the nerve divisions. Often, trigeminal ganglia leave an impression in the avian braincase, and this feature may be more useful for comparison. In contrast, non-avian dinosaurs do not have relatively large brains and may have had more space for tissues intra- and extra-cranially.

CONCLUSIONS

Overall, the osteology associated with the trigeminal sensory system is quite variable among sauropsids. In spite of this variation, statistically-supported predictions of somatosensory abilities are still possible and this data, in addition to data from Chapter 5 supports evolutionary trends within pseudosuchians. Though other conclusions are limited, this reveals a number of interesting avenues worth pursuing, including broad proxies for body size, relative sensitivities and ecologies of lepidosaurs, and use of osteological correlates as phylogenetic characters. Further quantification of additional osteological correlates among clades and ecologies will help inform inferences of behavior in extinct animals and contribute to a complete picture of vertebrate sensory evolution.

Table 6.1. Correlations of soft tissue features and their osteological correlates.

Soft Tissue Feature	Osteological Correlate	Sauropsids	Lepidosaurs	Crocodylians	Avians	Non-tactile	Tactile
Ganglion volume (mm ³)	Foramen min diameter (mm)	0.935	0.958	0.950	0.591	0.877	0.953
Ganglion volume (mm ³)	Foramen max diameter (mm)	0.943	0.960	0.985	0.609	0.827	0.975
V ₃ CSA (mm ²)	Canal CSA (mm ²)	0.911	0.882	0.985	0.853	0.920	0.817
V ₃ height (mm)	Canal Height (mm)	0.868	0.977	0.815	0.875	0.882	0.920
Ganglion volume (mm ³)	Foramen count	0.453	-	-	-	-	-
V ₃ CSA (mm ²)	Foramen count	0.329	-	-	-	-	-
V ₃ Height (mm)	Foramen count	0.352	-	-	-	-	-

Table 6.2. Ecological predictions from linear discriminant analysis.

Specimen	Taxon	Comb- ined	Comb- ined Imput- ed	Rostral Only	V23 Max Diam.	V23 Min Diam.	Cross Sect. Canal Area	Canal Height	Foramen Count
Ankylosaur_UMNH21000	Ankylosaurid		Tactile		Tactile	Tactile			
A.platyrhynchos_MUVC_AV097	Avian	Tactile	Tactile	Tactile	Tactile	Tactile	Tactile	Tactile	Tactile
Psittacus_MUVC_AV092	Avian	Other	Other	Other	Other	Other	Other	Tactile	Other
Megascops_MUVC_AV073	Avian	Other	Other	Other	Other	Other	Other	Tactile	Other
Pandion_MUVC_AV335	Avian	Other	Other	Other	Other	Tactile	Other	Other	Other
Fulica_MUVC_AV285	Avian	Other	Other	Other	Tactile	Tactile	Tactile	Tactile	Other
A.carolinensis_MUVC_AV222	Avian	Tactile	Tactile	Tactile	Tactile	Tactile	Tactile	Tactile	Tactile
Megaceryle_MUVC_AV333	Avian		Other		Other	Other		Other	Other
Anas_OUVC_10252	Avian		Tactile						Tactile
Phasianus_MUVC_AV263	Avian	Other	Other	Other	Tactile	Other	Other	Other	Other
Alle_OUVC_10752	Avian		Other						Other
Amazona_MUVC_AV076	Avian		Tactile		Tactile	Tactile			
Cyanoramphus_MUVC_AV076	Avian		Tactile		Tactile	Tactile			
Deroptylus_MUVC_AV074	Avian		Tactile		Tactile	Tactile			
Phoebastris_OUVC_10905	Avian		Other		Tactile	Tactile			
Scolopax_USNM_292760	Avian	Tactile	Tactile	Tactile	Other	Other	Tactile	Tactile	Tactile
Arenaria_USNM_612977	Avian	Tactile	Tactile	Tactile	Tactile	Other	Tactile	Tactile	Other
Columba_NHMUK_PAL001	Avian		Other						
Colaptes_MUVC_AV050	Avian		Other		Other	Other			
Einosaurus_MOR456	Ceratopsid		Tactile		Tactile	Tactile			
Triceratops_MOR3027	Ceratopsid		Other		Tactile	Tactile			
Triceratops_YPM1820	Ceratopsid		Other		Tactile	Tactile			
Triceratops_YPM1821	Ceratopsid		Other		Tactile	Tactile			
Alligator_MUVC_AL002	Crocodylian	Tactile	Tactile	Tactile	Tactile	Tactile	Tactile	Tactile	Tactile
Alligator_MUVC_AL004	Crocodylian		Tactile	Tactile					Tactile
Alligator_MUVC_AL008	Crocodylian	Tactile	Tactile	Tactile	Tactile	Tactile	Tactile	Tactile	Tactile
Alligator_MUVC_AL015	Crocodylian	Tactile	Tactile	Tactile	Tactile	Tactile	Tactile	Tactile	Tactile
Alligator_MUVC_AL016	Crocodylian	Tactile	Tactile	Tactile	Tactile	Tactile	Tactile	Tactile	Tactile
Alligator_MUVC_AL022	Crocodylian	Tactile	Tactile	Tactile	Tactile	Tactile	Tactile	Tactile	Tactile
C.johnstoni_OUVC_10425	Crocodylian	Tactile	Tactile	Tactile	Tactile	Tactile	Tactile	Tactile	Tactile
C.johnstoni_TMM_M6807	Crocodylian	Tactile	Tactile	Tactile	Tactile	Tactile	Tactile	Tactile	Tactile
Tomistoma_TMM_M6342	Crocodylian	Tactile	Tactile	Tactile	Tactile	Tactile	Tactile	Tactile	Tactile
Osteolaemus_FMNH_98936	Crocodylian	Tactile	Tactile	Tactile	Tactile	Tactile	Tactile	Tactile	Tactile
Caiman_FMNH_73711	Crocodylian	Tactile	Tactile	Tactile	Tactile	Tactile	Tactile	Tactile	Tactile
C.moreletii_TMM_M4980	Crocodylian	Tactile	Tactile	Tactile	Tactile	Tactile	Tactile	Tactile	Tactile
Melanosuchus_niger	Crocodylian	Tactile	Tactile	Tactile	Tactile	Tactile	Tactile	Tactile	Tactile
Gavialis_TMM_M5490	Crocodylian		Tactile		Tactile	Tactile	Tactile	Tactile	
Mecistops_TMM_M3529	Crocodylian	Tactile	Tactile	Tactile	Tactile	Tactile	Tactile	Tactile	Tactile

Leidyosuchus_ROM1903	Crocodylian		Tactile	Tactile			Tactile	Tactile	Tactile
Alligator_MUVC_AL031	Crocodylian	Tactile	Tactile	Tactile	Tactile	Tactile	Tactile	Tactile	Tactile
Alligator_MUVC_AL606	Crocodylian		Tactile		Tactile	Tactile			
Gavialis_gangeticus	Crocodylian		Tactile		Tactile	Tactile			
C.porosus_OUVC_10899	Crocodylian	Tactile	Tactile	Tactile	Tactile	Tactile	Tactile	Tactile	Tactile
Paleosuchus_FMNH_22817	Crocodylian	Tactile	Tactile	Tactile	Tactile	Tactile	Tactile	Tactile	Tactile
Osteolaemus_FMNH_53632	Crocodylian	Tactile	Tactile	Tactile	Tactile	Tactile	Tactile	Tactile	Tactile
Tomistoma_FMNH_11085	Crocodylian	Tactile	Tactile	Tactile	Tactile	Tactile	Tactile	Tactile	Tactile
C.johnstoni_FMNH_16162	Crocodylian	Tactile	Tactile	Tactile	Tactile	Tactile	Tactile	Tactile	Tactile
Alligator_MUVC_AL003	Crocodylian		Tactile		Tactile	Tactile			
Alligator_MUVC_AL007	Crocodylian		Tactile		Tactile	Tactile			
Alligator_MUVC_AL024	Crocodylian		Tactile		Tactile	Tactile			
Alligator_MUVC_AL062	Crocodylian		Tactile		Tactile	Tactile			
Alligator_MUVC_AL075	Crocodylian		Tactile		Tactile	Tactile			
Alligator_MUVC_AL079	Crocodylian		Tactile		Tactile	Tactile			
Alligator_MUVC_AL114	Crocodylian		Tactile		Tactile	Tactile			
Alligator_MUVC_AL600	Crocodylian		Tactile		Tactile	Tactile			
Alligator_MUVC_AL605	Crocodylian		Tactile		Tactile	Tactile			
Alligator_MUVC_AL607	Crocodylian		Tactile		Tactile	Tactile			
Alligator_MUVC_AL608	Crocodylian		Tactile		Tactile	Tactile			
Alligator_MUVC_AL612	Crocodylian		Tactile		Tactile	Tactile			
Alligator_MUVC_AL622	Crocodylian		Tactile		Tactile	Tactile			
Alligator_MUVC_AL626	Crocodylian		Tactile		Tactile	Tactile			
Alligator_MUVC_AL700	Crocodylian		Tactile		Tactile	Tactile			
Alligator_MUVC_AL701	Crocodylian		Tactile		Tactile	Tactile			
Alligator_MUVC_AL703	Crocodylian		Tactile		Tactile	Tactile			
Alligator_MUVC_AL709	Crocodylian		Tactile		Tactile	Tactile			
Alligator_MUVC_AL710	Crocodylian		Tactile		Tactile	Tactile			
Alligator_MUVC_AL711	Crocodylian		Tactile		Tactile	Tactile			
Alligator_MUVC_AL712	Crocodylian		Tactile		Tactile	Tactile			Tactile
Alligator_MUVC_AL721	Crocodylian		Tactile		Tactile	Tactile			
Crocodylus_niloticus	Crocodylian		Tactile		Tactile	Tactile			
Allognathosuchus_UMNH28395_1	Crocodylian		Tactile		Tactile	Tactile			
T.africanum_SMNS112417	Crocodylian		Tactile		Tactile	Tactile			
Crocodylus_SMNS12649	Crocodylian		Tactile		Tactile	Tactile			
T.africanum_SMNS1122412	Crocodylian		Tactile		Tactile	Tactile			
C.megarhinus_SMNS12650	Crocodylian		Tactile		Tactile	Tactile			
T.cairensis_SMNS50740	Crocodylian		Tactile		Tactile	Tactile			
MCZ4452	Crocodylian		Tactile		Tactile	Tactile			
C.robustus_MCZ1006	Crocodylian		Tactile		Tactile	Tactile			
Crocodylus_MCZ3390	Crocodylian				Tactile	Tactile			
Nominosuchus_IVPP_14392	Crocodylomorph	Tactile	Tactile	Tactile	Tactile	Tactile	Tactile	Tactile	Other
Orthosuchus_SAM_PKK409	Crocodyliform	Tactile	Tactile	Tactile	Tactile	Tactile	Tactile	Tactile	Tactile

Protosuchus_BP14770	Crocodyliform	Tactile	Tactile	Tactile	Tactile	Tactile	Other	Tactile	Tactile
Mahajangasuchus_PR2448	Crocodyliform		Tactile		Tactile	Tactile			
Eutretauranosuchus_AMNH570	Crocodyliform		Tactile		Tactile	Tactile			
Simosuchus_UA8679	Crocodyliform	Tactile	Tactile	Tactile	Tactile	Tactile	Tactile	Tactile	Tactile
Araripesuchus_AMNH_24450	Crocodyliform		Tactile	Tactile			Tactile	Tactile	Tactile
Araripesuchus_MNN_GAD19	Crocodyliform		Tactile		Tactile	Tactile			
Junggarsuchus_IVPP_V14010	Crocodylomorph	Other	Other	Tactile	Tactile	Tactile	Tactile	Tactile	Tactile
Dibothrosuchus_IVPP_V7907	Crocodylomorph		Tactile		Tactile	Tactile	Tactile		Other
Macelognathus_LACM_150148	Crocodylomorph		Tactile				Tactile		Other
Rhabdognathus_CNRST_SNY190	Crocodylomorph		Tactile		Tactile	Tactile			
Pelagosaurus_PV_OR32599	Crocodylomorph		Tactile		Tactile	Tactile			
Metriorhynchus_?	Crocodylomorph		Tactile		Tactile	Tactile			
Leidyosuchus_?	Crocodylian		Tactile		Tactile	Tactile			
Hamadasuchus_ROM_52620	Crocodyliform		Tactile		Tactile	Tactile			
Aegisuchus_ROM_54530	Crocodyliform		Tactile		Tactile	Tactile			
Litargosuchus_BP5237	Crocodylomorph	Tactile	Other	Other	Other	Other	Tactile	Other	Other
Nodosaurid_BYU16409	Nodosaurid		Other		Tactile	Tactile			
Gastonia_BYU15466	Nodosaurid		Tactile		Tactile	Tactile			
Gastonia_BYU15656	Nodosaurid		Other		Tactile	Tactile			
Gastonia_BYU14659	Nodosaurid		Other		Tactile	Tactile			
Mymoorapelta_MWC5435	Nodosaurid		Other		Tactile	Tactile			
Gargoyleosaurus_DMNH27726	Nodosaurid		Tactile		Tactile	Tactile			
Gastonia_DMNH53033	Nodosaurid		Other		Tactile	Tactile			
Gastonia_DMNH50169	Nodosaurid		Tactile		Tactile	Tactile			
Gastonia_DMNH50168	Nodosaurid		Tactile		Tactile	Tactile			
Sauropelta_YPM5529	Nodosaurid		Tactile		Tactile	Tactile			
Tyrannosaurus_BMRP_2002.4.1	Theropod		Tactile				Tactile		Tactile
Majungasaurus_FMNH_PR2100	Theropod		Tactile				Tactile		Tactile
Tyrannosaurus_MOR1125	Theropod		Tactile						
Allosaurus_UMNH5472	Theropod		Tactile		Tactile	Tactile			
Allosaurus_UMNH16605	Theropod d		Tactile		Tactile	Tactile			
Allosaurus_UMNH23132_21117	Theropod		Tactile		Tactile	Tactile			
Theropod_?	Theropod		Tactile		Tactile	Tactile			
Falcarius_UMNH15000	Theropod		Other		Other	Tactile			
Allosaurus_BYU13679	Theropod		Tactile		Tactile	Tactile			
Allosaurus_BYU5287	Theropod		Tactile		Tactile	Tactile			
Allosaurus_UUVP910	Theropod		Tactile		Tactile	Tactile			
Ceratosaurus_BYU12893	Theropod		Tactile		Tactile	Tactile			
Allosaurus_DINO11541	Theropod		Tactile		Tactile	Tactile			
Allosaurus_DINO_2560	Theropod	Tactile	Tactile	Tactile	Tactile	Tactile	Tactile	Tactile	Tactile
Byronosaurus_IGM100.983	Theropod		Tactile	Tactile			Tactile	Tactile	Other
Acrocanthosaurus_DINO13706	Theropod		Other		Tactile	Tactile			
Piatnitzkysaur_DMNH3178	Theropod		Tactile		Tactile	Tactile			

Masiakasaurus_FMNHPR2457	Theropod		Other		Tactile	Tactile			
Majungasaurus_FMNH_PR2100_nondigital	Theropod		Other		Tactile	Tactile			
Dilophosaurus_TMM43646.1	Theropod		Other	Other			Tactile	Tactile	Other
Suchomimus_MNNGDF214	Theropod		Tactile		Tactile	Tactile			
Allosaurus_YPM14554	Theropod		Tactile		Tactile	Tactile			
Brachylophosaurus_MOR1071_7_7_98_86	Ornithopod		Other		Tactile	Tactile			
Brachylophosaurus_MOR1071_7_13_99_87_I	Ornithopod		Tactile		Tactile	Tactile			
Acristavus_MOR1155	Ornithopod		Other		Tactile	Tactile			
Hadrosaurid_UMNH30162	Ornithopod		Tactile		Tactile	Tactile			
Acristavus_UMNH16607	Ornithopod		Tactile		Tactile	Tactile			
Camptosaurus_WPLcast	Ornithopod		Tactile		Tactile	Tactile			
Dryosaurus_cast	Ornithopod		Tactile		Tactile	Tactile			
Iguanodontid_BYU22086	Ornithopod		Tactile						
Iguanodontid_BYU22080	Ornithopod		Other		Tactile	Tactile			
Parasaurolophus_DMNH132300	Ornithopod		Tactile		Tactile	Tactile			
Hypsilophodontidae_MCZ4389	Ornithopod		Tactile		Tactile	Tactile			
Tenontosaurus_MCZ4205	Ornithopod		Tactile		Tactile	Tactile			
Bactrosaurus_YPM2549.1	Ornithopod		Tactile		Tactile	Tactile			
Anatosaurus_YPM618	Ornithopod		Other		Tactile	Tactile			
Tenontosaurus_YPM5472	Ornithopod		Tactile		Tactile	Tactile			
Camptosaurus_YPM1856a	Ornithopod		Other		Tactile	Tactile			
Orodromeus_MOR403	Parksosaurid		Other		Tactile	Tactile			
Oryctodromeus_MOR1636	Parksosaurid		Tactile		Tactile	Tactile			
Zephyrosaurus_MCZ4392	Parksosaurid		Other		Tactile	Tactile			
Camarasaurus_UMNH5665	Sauropod		Tactile		Tactile	Tactile			
Camarasaurus_UMNH5952	Sauropod		Other		Tactile	Tactile			
Mierasaurus_UMNH26004_1	Sauropod		Tactile		Tactile	Tactile			
Abdyosaurus_DINO17849	Sauropod		Tactile		Tactile	Tactile			
Abdyosaurus_DINO39727	Sauropod		Other		Tactile	Tactile			
Camarasaurus_BYU9199	Sauropod		Other		Tactile	Tactile			
Camarasaurus_BYU9048	Sauropod		Other		Tactile	Tactile			
Moabosaurus_BYU14760	Sauropod		Tactile		Tactile	Tactile			
Moabosaurus_BYU14877	Sauropod		Tactile		Tactile	Tactile			
Moabosaurus_BYU14359	Sauropod		Other		Tactile	Tactile			
Moabosaurus_BYU11614	Sauropod		Other		Tactile	Tactile			
Rapetosaurus_FMNHPR2197_2184	Sauropod		Tactile		Tactile	Tactile			
Apatosaurus_YPM1860	Sauropod		Tactile		Tactile	Tactile			
Sarhsaurus_TMM43646.2	Sauropodomorph		Other		Other	Tactile			
Plateosaurus_YPM8161	Sauropodomorph		Other		Tactile	Tactile			
Camarasaurus_BYU9062	Sauropod		Other		Tactile	Tactile			
Stegosaurus_UMNH5731	Stegosaurid		Tactile		Tactile	Tactile			
Stegosaurus_DMNH2818	Stegosaurid		Tactile		Tactile	Tactile			
Kentrosaurus_MCZ4115	Stegosaurid		Tactile		Tactile	Tactile			

Stegosaurus_YPM57171	Stegosaurid		Other		Tactile	Tactile			
Phytosaur	Suchian		Tactile				Tactile		Tactile
Phytosaur_GRH3410	Suchian		Tactile		Tactile	Tactile			
Phytosaur_GRH220100626	Suchian		Tactile		Tactile	Tactile			
Phytosaur_UMNH24306	Suchian		Tactile		Tactile	Tactile			
Phytosaur_TMM31100.1337	Suchian		Tactile		Tactile	Tactile			
Trilophosaurus_TMM_31025233	Archosauromorph		Other	Other			Tactile	Tactile	Other
Trilophosaurus_TMM31025.140	Archosauromorph		Other		Other	Tactile			
Nicrosaurus_?	Suchian		Tactile		Tactile	Tactile			
Nicrosaurus_??	Suchian		Tactile		Tactile	Tactile			
Trilophosaurus_YPM4820	Archosauromorph		Other		Tactile	Tactile			
Trilophosaurus_YPM4187	Archosauromorph		Other		Tactile	Tactile			
Longosuchus_TMM_3118584	Suchian	Tactile	Tactile	Tactile	Tactile	Tactile	Tactile	Tactile	Tactile
Desmatosuchus_UCMP_27410	Suchian		Tactile		Tactile	Tactile			
Typothorax_GRH4591110803	Suchian		Tactile		Tactile	Tactile			
Simosuchus_UA8679_nondigital	Crocodyliform		Tactile		Tactile	Tactile			
Longosuchus_TMM_31100.531	Suchian		Tactile		Tactile	Tactile			
Batrachotomus_SMNS80260	Suchian		Tactile		Tactile	Tactile			
Prestosuchid_MCZ9115	Suchian		Tactile		Other	Tactile			
Neoaetosauroides_PVL5698	Suchian		Tactile		Tactile	Tactile			
Scutarx_PFO34616	Suchian		Other		Tactile	Tactile			
Coahomasuchus_TMM_31100.437	Suchian		Other		Tactile	Tactile			

Figure 6.1. Lateral braincases of selected CT scanned taxa with reconstructed endocasts (blue) and trigeminal ganglia and nerves (yellow) in (a) *Anolis* (MUVCL I089; reflected), (b) *Allosaurus* (DINO 2560), (c) *Anas* (OUVC 10252; reflected), (d) *Litargosuchus* (BP 5237; reflected), (e) *Junggarsuchus* (IVPP V14010), (f) *Pelagosaurus* (BRLSI M1413), (g) *Protosuchus* (BP I 4770; reflected), (h) *Orthosuchus* (SAM PK K409; reflected), (i) *Hamadasuchus* (ROM 54513), (j) *Simosuchus* (UA 8679), (k) *Leidyosuchus* (ROM 1903), (l) *Alligator* (MUVCL AL606, reflected), and (m) phylogeny of figured taxa.

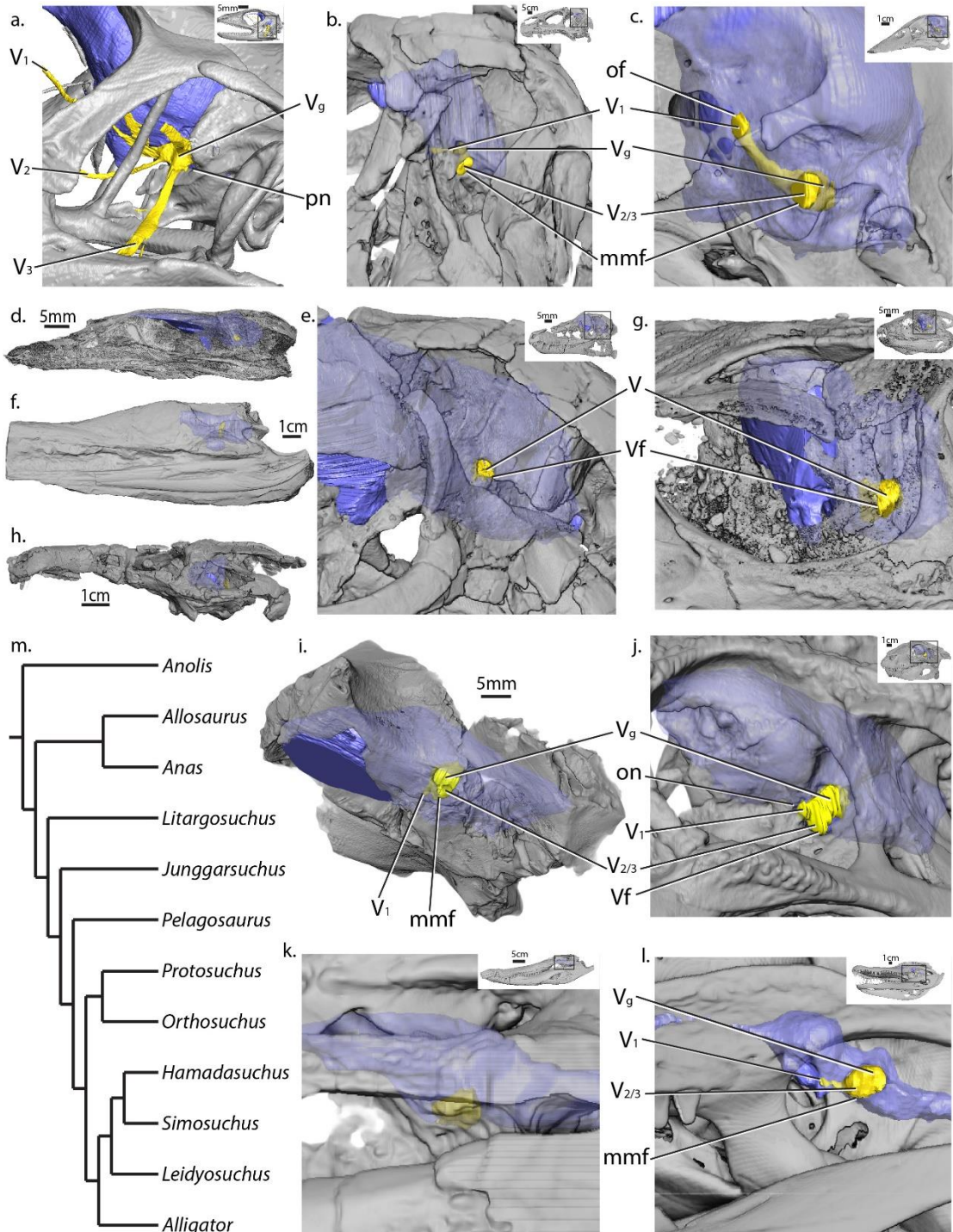


Figure 6.2. Dentaries of selected CT scanned taxa with reconstructed mandibular neurovascular canals (yellow) in (a) *Anolis* (MUVCL I089, reflected), (b) *Trilophosaurus* (TMM 31025-233, reflected), (c) *Longosuchus* (TMM 31185-84), (d) *Junggarsuchus* (IVPP V14010), (e) *Macelognathus* (LACM 150148), (f) *Nominosuchus* (IVPP 14392), (g) *Orthosuchus* (SAMPK K409, reflected), (h) *Araripesuchus* (AMNH 24450), (i) *Protosuchus* (BP I 4770), (j) *Simosuchus* (UA 8679, reflected), (k) *Caiman* (FMNH 73711, reflected), (l) *Dilophosaurus* (TMM 43646, reflected), (m) *Majungasaurus* (FMNH PR 2100), (n) *Tyrannosaurus* (MOR 1125, reflected), (o) *Allosaurus* (DINO 2560), (p) *Byronosaurus* (IGM 100/983), and (q) *Arenaria* (USNM 612977).

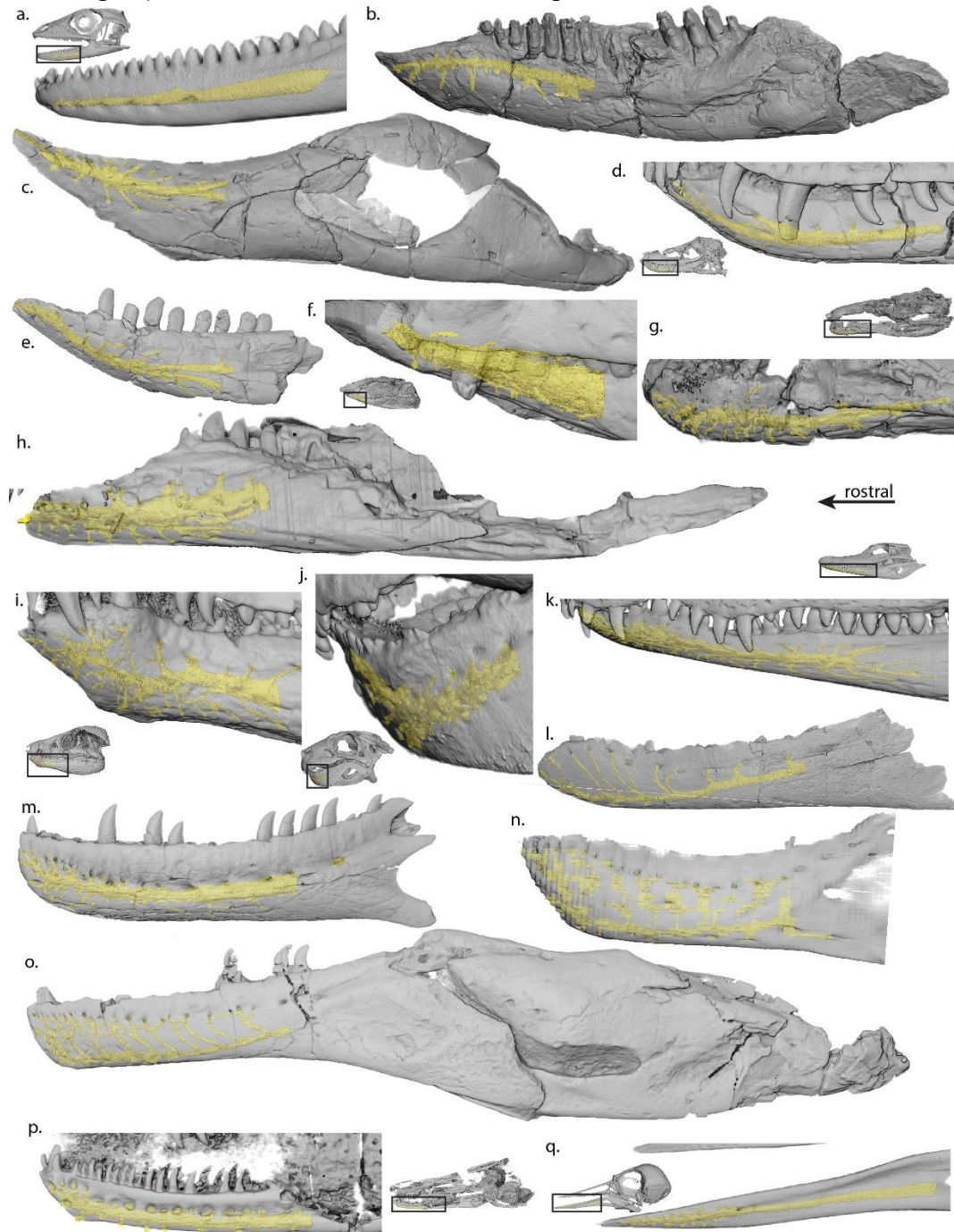


Figure 6.3. Relationships between soft tissue features and their osteological correlates featuring (a) trigeminal ganglion volume and minimum diameter of the maxillomandibular foramen, (b) trigeminal ganglion volume and maximum diameter of the maxillomandibular foramen, (c) cross sectional area of the mandibular nerve and cross sectional area of the mandibular canal, (d) diameter of the mandibular nerve and height of the mandibular canal, and (e) trigeminal ganglion volume and foramen count.

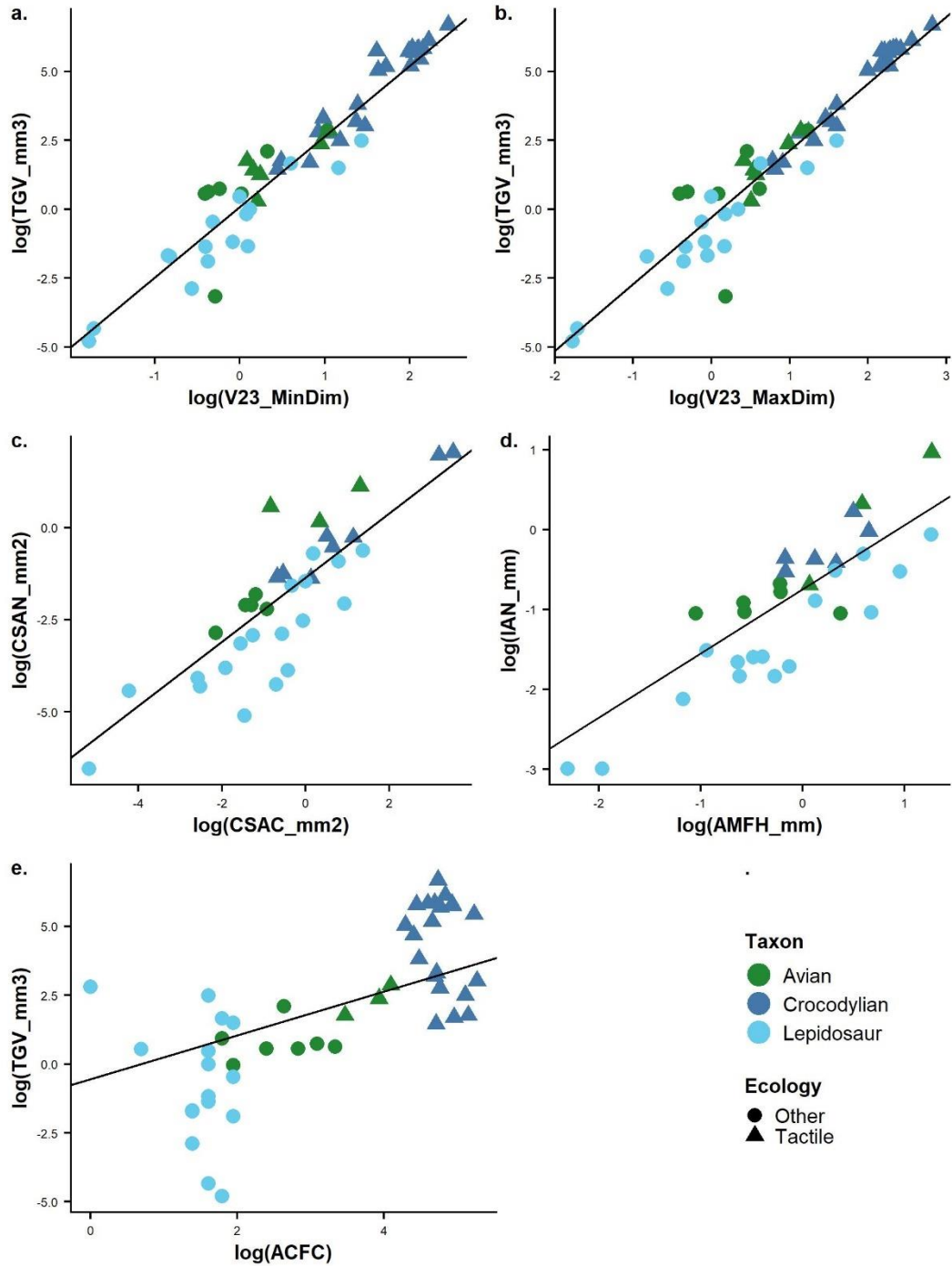


Figure 6.4. Phylogenetic RMA regression plots evaluating of foramen magnum width (a) and anterior dentary surface area (b) as proxies for body size by comparing to skull width. Thin lines represent 95% CI.

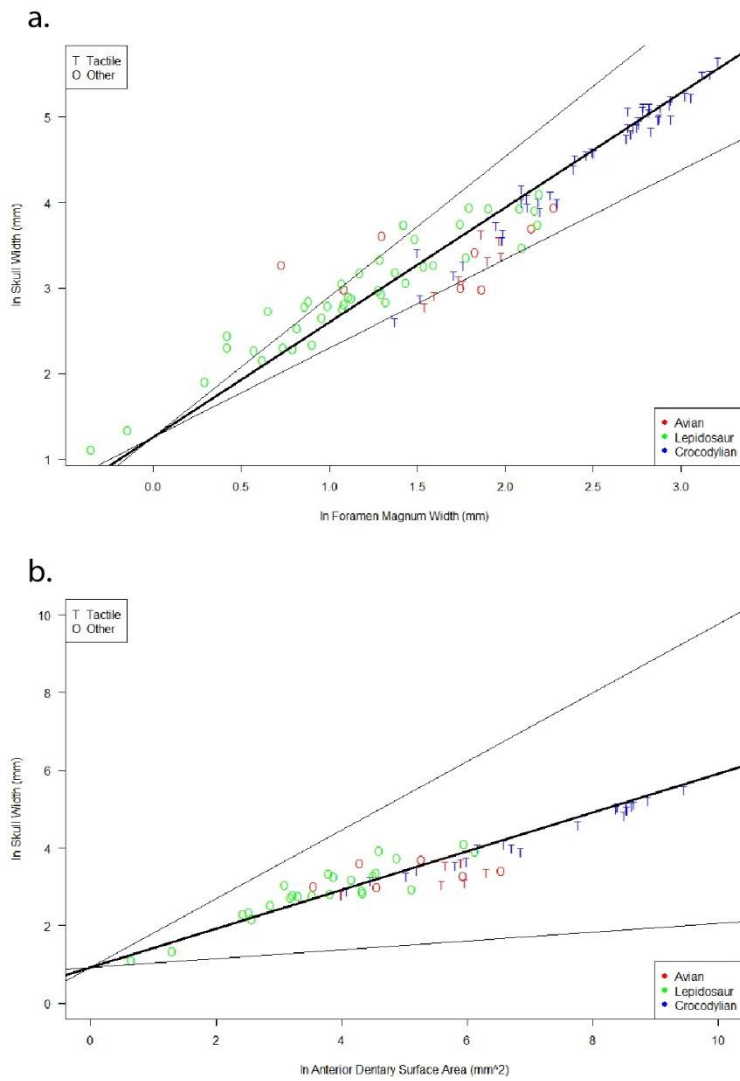


Figure 6.5. Ecological differences in relative osteological correlates including (a,f) maximum and (b,g) minimum diameter of the maxillomandibular foramen, (c,h) cross sectional area and (d,i) height of the mandibular canal, and (e,j) foramen count. Plots include (a-e) and exclude (f-j) lepidosaurs. Black line is regression line calculated by phylogenetic RMA regression, red line models the average of tactile taxa, and blue line models the average of non-tactile taxa.

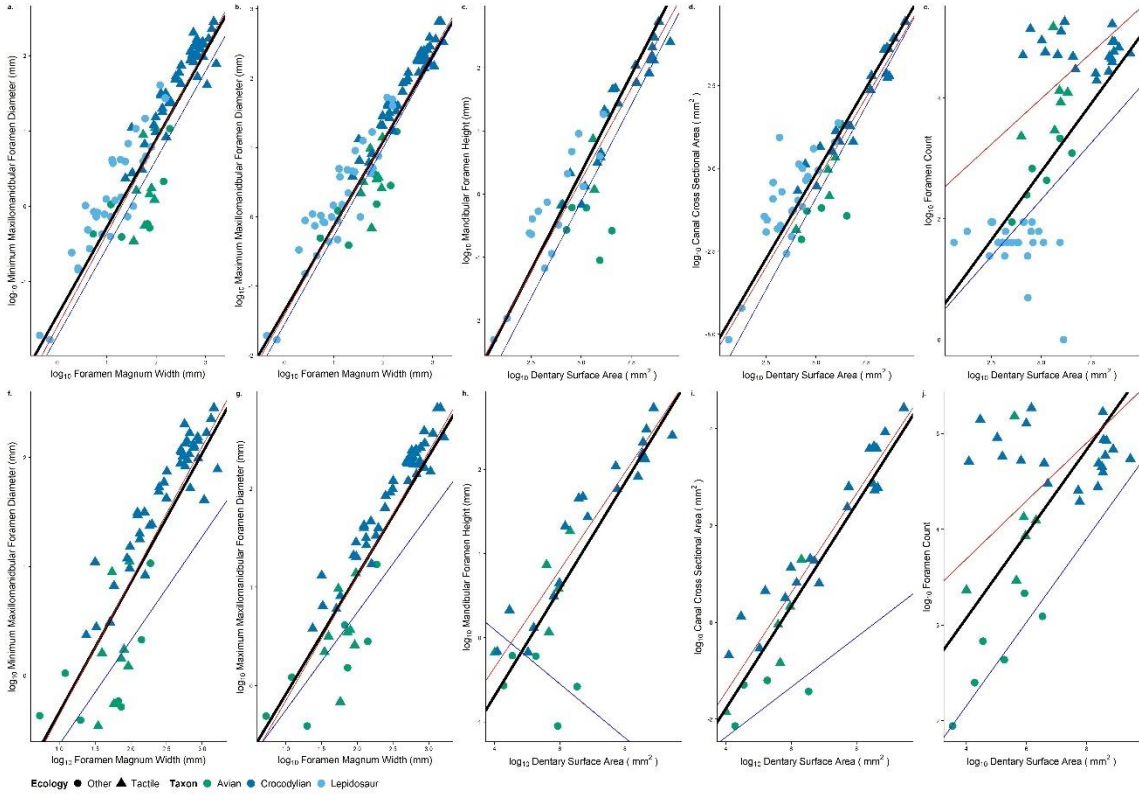
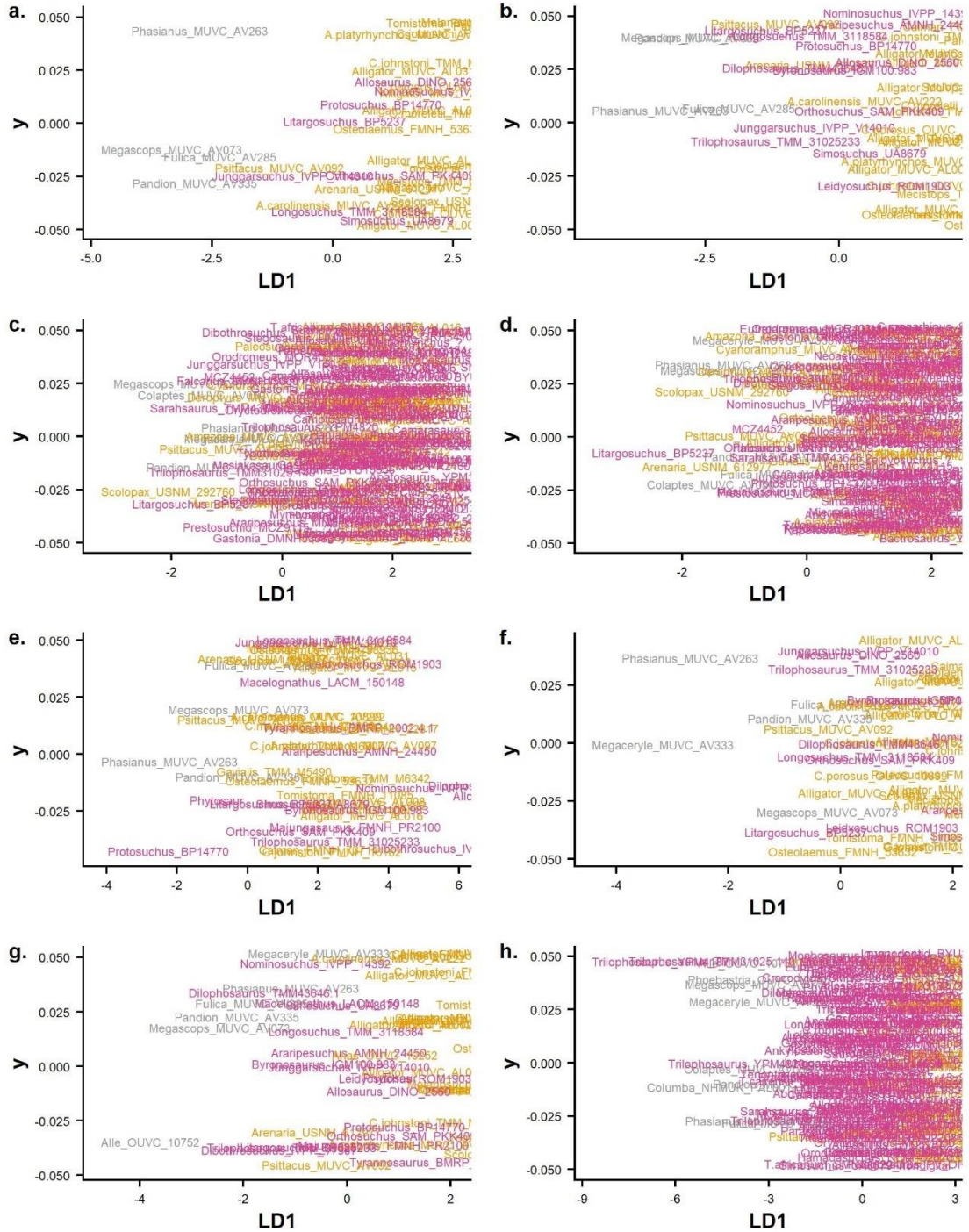
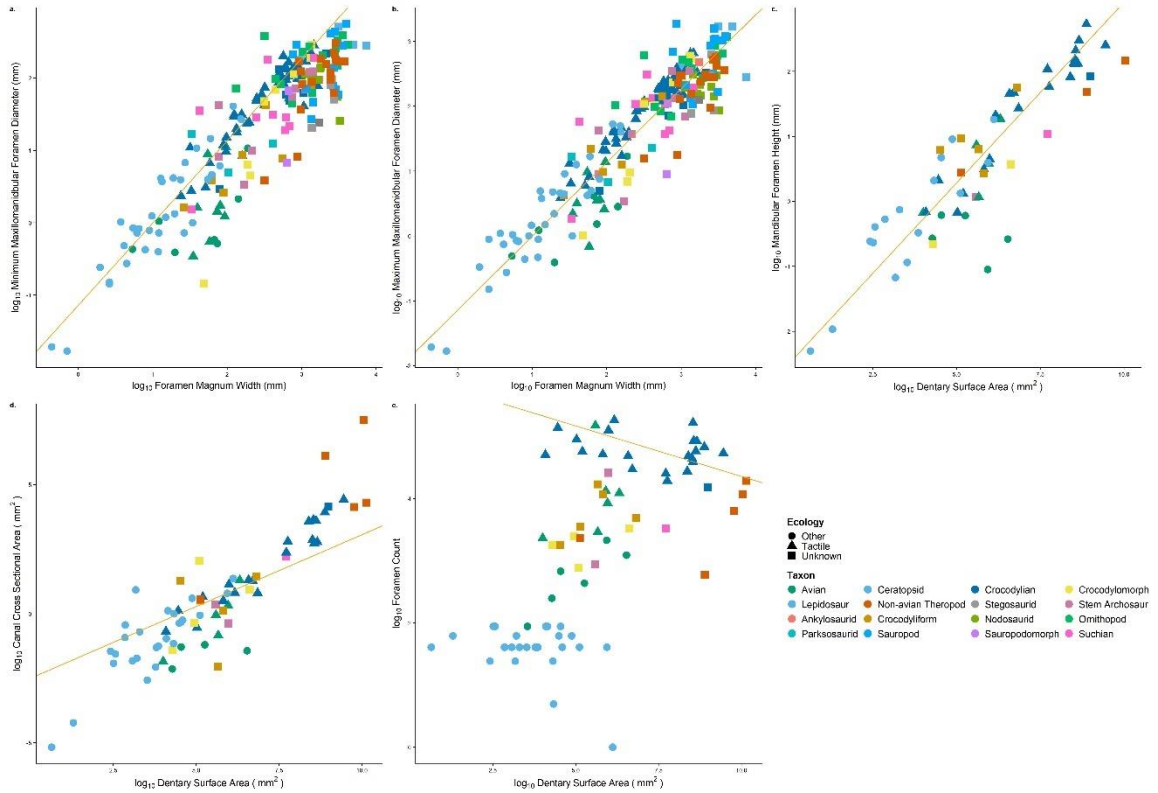


Figure 6.6. Linear discriminant analysis used for ecological predictions for fossil taxa based on (a) all metrics, (b) rostral metrics, (c) maximum diameter of the maxillomandibular foramen, (d) minimum diameter of the maxillomandibular foramen, (e) cross-sectional area of the mandibular canal, (f) height of the mandibular canal, (g) foramen count, and (h) imputed data.



species a Other a Tactile a Unknown

Figure 6.7. Relative sizes of cranial osteological correlates including (a) minimum and (b) maximum diameter of the maxillomandibular foramen, mandibular canal (c) cross sectional area and (d) height, and (e) foramen count. Orange regression in line is calculated by phylogenetic RMA regression and models the average of extant crocodylians.



Chapter 7 — Conclusions

This research is both a continuation and just the beginning of lifetimes of work investigating sensory ecomorphology. Together, through compilation of morphological and ecological data, I have scratched the surface of the evolution of sensory system and behavior among vertebrates. As a whole, using a robust extant phylogenetic bracket of birds, lizards, snakes and crocodylians, I have demonstrated that trigeminal osteological correlates hold significance in predicting soft tissue contents and ecologies. Thus, these features in fossil organism are useful in hypotheses of behavior and attempts to quantify similar features should be made in the future. I have shown that quantifying distribution of tissues across a space is an informative addition to traditional anatomic description, developing a method that may be applied more broadly.

Though this research was focused broadly among sauropsids, the nature of the materials and expertise resulted in a complete picture of the evolution of the pseudosuchian trigeminal sensory system. Linear and derived measurements and analyses of trigeminal osteological correlates revealed an increase in size, density, and hypothesized sensory ability along the line to modern crocodylians. Statistical models in Chapters 5 and 6 indicate that a transition occurred among early-diverging crocodyliforms in the Late Triassic, prior to the Neosuchian transition to a semiaquatic habitat (Leari et al. 2017, Wilberg et al. 2019). Developmental data from Chapters 2 and 3 indicate the sensory domination by the trigeminal system is well established among extant crocodylians early in ontogeny and maintained throughout. Overall, extant crocodylians represent a unique instance of trigeminal sensory specialization with a rich evolutionary and developmental history that allows for domination of the semi-aquatic habitat.

Future directions abound. This projects' exploration of gross trigeminal anatomy excluded several key anatomical regions and ignored other sources of variation that could prove valuable sources of information. Particularly, when explored, processing regions within the brain (e.g., nuclei, tracts), axon density, axon size, extent of myelination, vasculature distribution, speed of signal propagation, receptor sensitivity, receptor modality, receptive field size, behavior, among others, can provide a fully integrated view of the trigeminal system (Gutiérrez-Ibáñez et al. 2009, Kandel et al. 2000). Also of interest are the developmental origins and morphological convergence of other enhanced sensory systems (e.g., bill tip organs in birds, infrared receptors in snakes, electroreceptive platypus bills etc.; Cunningham et al. 2013, Goris 2011; Gregory et al. 1987). In general, receptor homology, relative sensitivity, ecological significance and many other aspects of sensory biology are unknown among reptiles, vertebrates, and animals as a whole. Comparative electrophysiological testing, analysis of gene expression, and ontogenetic studies are expected to disentangle much of this information (e.g., Di-Poï and Milinkovitch 2013, Leitch and Catania 2012). Additionally, such studies will provide data towards exploring potential tradeoffs between sensory systems from the gross morphological to the neuroanatomical levels. Detailing morphology of systems crucial to survival in extant organisms will prove useful in explaining evolutionary trends of sensory systems inferred from fossil specimens.

Comparative neurosensory ontogeny

This research also reveals that there is more to understanding sensory ecology than studying individual systems in static organisms. Since neural tissue is metabolically expensive, an organism's sensory profile is a result of tradeoffs between numerous

systems, and growth and development provide clues to the origins and ontogenetic progressions of variation (Stevens 2013). The crocodylian trigeminal sensory system develops rapidly and is initially large, as shown in Chapters 2 and 3. Without comparative data, it is impossible to determine whether this is just an artifact of typical cranial growth. However, it is expected that in taxa with other dominant sensory or muscular systems, patterns of growth and development in the cranial nerve supply to the system will reflect this dominance. For example, visual feeders (e.g., chameleons, galliform birds) are expected to show more rapid increases in optic nerve size than taxa that use somatosensory cues while feeding (e.g., crocodylians, anseriform birds).

Nerve diameter reflects more than just axon counts and is also inclusive of axon myelin thickness (Kandel et al. 2000). Since myelin plays a role in speed of signal propagation, exploration of developing myelin among reptile cranial nerves should provide another glimpse into comparative sensory abilities among reptiles. As myelin is also metabolically expensive, I expect its allocation to reflect dominant sensory systems. Similar trends (e.g., early and fast growth, increased myelination) are expected in neural processing regions of dominant sensory systems.

Receptor diversity and homology

The integument serves as the primary somatosensory contact with the environment on the reptilian cranium and understanding its structure and innervation is integral to understanding the integrated reptile sensory system. Though crocodylians are known for their densely packed integumentary sensory organs (ISOs), all reptiles have integument richly supplied with nervous tissues to engage in somatosensation and are marked by unique concentrations of nerve endings within their ISOs (e.g., Leitch and

Catania 2012, Di-Poï and Milinkovitch 2013, Ananjeva et al. 1991). The distribution of ISOs among reptiles has received previous attention, but comparative function, sensitivity, and development, evolution of these sensory systems, and relationship with ecology are unknown. In addition to identifying major transitions in vertebrate sensory patterns, comparing ISOs using a multi-level, integrative approach should provide an exceptional framework to address complex evolutionary relationships between organ specialization, ecological diversification, and environmental adaptations in vertebrates.

Methods including gross and histological morphology, patterns of gene expression and electrical activity, and ontogenetic investigation will be useful tools in describing developmental processes and determine which modalities and intensities trigger receptors. Comparing receptor density and structure in combination with morphometrics of the nerves supplying them will provide physiological information on means for transporting, processing, and interpreting stimuli mediate by integumentary receptors. Subjecting live specimens to various stimuli (e.g., mechanical, thermal, chemical, electric) and observing response can be complemented by measurement of receptor response and thresholds (e.g., frequency, amplitude). Both electric activity of individual receptors and receptive field somatotopy and size can be detected and used to determine regions of increased sensitivity and ecological importance (Di-Poï and Milinkovitch 2013, Leitch and Catania 2012). The genes known to encode ion channels related to different sensory modalities are known and so gene expression profiling can also be used to determine receptor function (Di-Poï and Milinkovitch 2013). It is expected that application of these methods across a comparative dataset will lead to

hypotheses of receptor homology or convergence among ecologies and an understanding of receptor evolution.

Development and evolution of dental neurovasculature

The teeth and alveoli were one area of trigeminal innervation ignored by this project. Investigations into neurovascular morphology as it associates with the cranial integument hold a wealth of useful information in understanding the evolution of the variety of dental strategies among vertebrates (Bertin et al. 2018). Dental morphology has been well explored across vertebrates and exhibits substantial variation, in development, implantation, attachment, etc. Despite extensive studies of dental strategies, associated variation in neurovascular supply has not been explored, ignoring mechanisms by which morphological transitions occur and an abundance of phylogenetically informative features. Amniotes are an ideal group in which to study this variation because of morphological diversity and numerous examples of convergence. The amniote plesiomorphic, socketed tooth gave rise to many diverse morphologies. Within sauropsids, the plesiomorphic condition was retained until divergence of lepidosaurs (teeth attached to the labial jaw surface; though many exhibit jaw margin tooth attachment). Crocodylian-line archosaurs evolved ligamentous, innervated tooth attachments similar to mammals, whereas extant avian-line archosaurs have no teeth, a transition that has occurred independently in several archosaurian clades. I am interested in characterizing variation in neurovascular requirements associated with dental features and the evolution of neurovasculature during the appearance of novel dental adaptations especially across evolutionary trends and adaptations (e.g., repeated replacement of archosaur teeth with a keratinous beak, appearance of ligamentous attachment in

archosaurs, and appearance and cooccurrence of implantation strategies in lepidosaurs). Overall, a complete understanding of dental strategies and neurovascular requirements will reveal the constraints and processes necessary to transition between morphologies. Additionally, evaluating relationships of these soft tissues to their osteological correlates will provide a validated method of testing hypotheses of systematic affinity of fossil specimens.

References

- Abdel-Kader, T. G., Ali, R. S., & Ibrahim, N. M. (2011). The Cranial Nerves of *Mabuya quinquetaeniata* III: Nervus Trigemini. *Life Sciences Journal*, 8, 650-669.
- Al-Hassawi, A. M. A. (2004). The osteology and myology of the craniocervical region in squamate reptiles: a comparative study. Phd Dissertation, University College London.
- Allain, R., & Chure, D. J. (2002). *Poekilopleuron bucklandii*, the theropod dinosaur from the Middle Jurassic (Bathonian) of Normandy. *Palaeontology*, 45(6), 1107-1121.
- Allen, V., Elsey, R. M., Jones, N., Wright, J., & Hutchinson, J. R. (2010). Functional specialization and ontogenetic scaling of limb anatomy in *Alligator mississippiensis*. *Journal of Anatomy*, 216, 423-445.
- Allouche, L., & Tamišier, A. (1984). Feeding convergence of Gadwall, Coot and the other herbivorous waterfowl species wintering in the Camargue: a preliminary approach. *Wildfowl*, 35, 135-142.
- Alonso, P. D., Milner, A. C., Ketcham, R. A., Cookson, M. J., & Rowe, T. B. (2004). The avian nature of the brain and inner ear of Archaeopteryx. *Nature*, 430(7000), 666.
- Álvarez-Herrera, G., Agnolin, F., & Novas, F. (2020). A rostral neurovascular system in the mosasaur *Taniwhasaurus antarcticus*. *The Science of Nature*, 107(3), 1-5.
- Ananjeva, N. B., Dilmuchamedov, M. E., & Matveyeva, T. N. (1991). The skin sense organs of some iguanian lizards. *Journal of Herpetology*, 25(2), 186-199.
- Arcilla, C. K., & Tadi, P. (2020). Neuroanatomy, Unmyelinated Nerve Fibers.
- Armstrong, E. (1990). Brains, bodies and metabolism. *Brain, Behavior and Evolution*, 36(2-3), 166-176.

- Averianov, A. O., Leshchinskiy, S. V., & Kudryavtsev, V. I. (2007). Braincase of a Late Jurassic stegosaurian dinosaur from Tuva, Russia (Central Asia). *Journal of Vertebrate Paleontology*, 27(3), 727-733.
- Avilova, K. V. (2018). Spatial organization of the epithelial structures in the bill tip organ of waterfowl (Anseriformes, Aves). *Biology Bulletin Reviews*, 8, 234-244. doi: 10.1134/S2079086418030027
- Bakic, P. R., Albert, M., & Maidment, A. D. (2003). Classification of galactograms with ramification matrices: preliminary results. *Academic Radiology*, 10, 198-204. doi: 10.1016/S1076-6332(03)80045-4
- Balanoff, A. M., Bever, G. S., & Ikejiri, T. (2010). The braincase of *Apatosaurus* (Dinosauria: Sauropoda) based on computed tomography of a new specimen with comments on variation and evolution in sauropod neuroanatomy. *American Museum Novitates*, 2010(3677), 1-32.
- Balanoff, A. M., Bever, G. S., Rowe, T. B., & Norell, M. A. (2013). Evolutionary origins of the avian brain. *Nature*, 501(7465), 93-96.
- Barbas-Henry, H. A., & Lohman, A. H. (1986). The motor complex and primary projections of the trigeminal nerve in the monitor lizard, *Varanus exanthematicus*. *Journal of Comparative Neurology*, 254(3), 314-329.
- Barker, C. T., Naish, D., Newham, E., Katsamenis, O. L., & Dyke, G. (2017). Complex neuroanatomy in the rostrum of the Isle of Wight theropod *Neovenator salerii*. *Scientific reports*, 7(1), 3749.
- Barlow, L. A. (2002). Cranial nerve development: Placodal neurons ride the crest. *Current Biology*, 12(5), 171-173.

- Baumel, J., & Witmer, L. (1993). Osteologia. *Handbook of Avian Anatomy: Nomina Anatomica Avium, 2nd Edition*, (23), 45–131.
- Beer, T., & Borgas, M. (1993). Horton's laws and the fractal nature of streams. *Water Resources Research*, 29, 1475-1487. doi: 10.1029/92WR02731
- Bellairs, A. A., & Kamal, A. M. (1981). The chondrocranium and the development of the skull in recent reptiles. *Biology of the Reptilia*, 11F, 1-263.
- Bellairs, A. A., & Shute, C. C. D. (1953). Observations on the narial musculature of Crocodilia and its innervation from the sympathetic system. *Journal of Anatomy*, 87, 367-378.
- Benninger, B., & McNeil, J. (2010). Transitional nerve: a new and original classification of a peripheral nerve supported by the nature of the accessory nerve (CN XI). *Neurol Res Int*, 2010.
- Benoit, J., Ford, D. P., Miyamae, J. A., & Ruf, I. (2021). Can maxillary canal morphology inform varanopid phylogenetic affinities? *Acta Palaeontologica Polonica*, 66, 1-5.
- Berkhoudt, H. (1972). The epidermal structure of the bill tip organ in ducks. *Netherlands Journal of Zoology*, 26(4), 561-566.
- Berkhoudt, H. (1980). The morphology and distribution of cutaneous mechanoreceptors (Herbst and Grandy corpuscles) in bill and tongue of the mallard (*Anas platyrhynchos*). *Netherlands Journal of Zoology*, 30, 1-34.
- Berkhoudt, H., Dubbeldam, J. L., & Zeilstra, S. (1981). Studies on the somatotopy of the trigeminal system in the mallard, *Anas platyrhynchos* L. IV. Tactile

- representation in the nucleus basalis. *Journal of Comparative Neurology*, 196(3), 407-420.
- Berry, M., & Bradley, P. M. (1976). The application of network analysis to the study of branching patterns of large dendritic fields. *Brain Research*, 109, 111-132. doi: 10.1016/0006-8993(76)90383-8
- Bertin, T. J., Thivichon-Prince, B., LeBlanc, A. R., Caldwell, M. W., & Viriot, L. (2018). Current perspectives on tooth implantation, attachment, and replacement in Amniota. *Frontiers in physiology*, 9, 1630.
- Bird, D. J., Amirkhanian, A., & Pang, B. (2014). Quantifying the cribriform plate: influences of allometry, function, and phylogeny in Carnivora, 2092(June), 2080–2092.
- Bird, D. J., Murphy, W. J., Fox-Rosales, L., Hamid, I., Eagle, R. A., & Van Valkenburgh, B. (2018). Olfaction written in bone: Cribriform plate size parallels olfactory receptor gene repertoires in Mammalia. *Proceedings of the Royal Society B: Biological Sciences*, 285(1874).
- Blomberg, S. P., Garland Jr, T., & Ives, A. R. (2003). Testing for phylogenetic signal in comparative data: behavioral traits are more labile. *Evolution*, 57, 717-745. doi: 10.1111/j.0014-3820.2003.tb00285.x
- Borsuk–Białynicka, M. and Evans, S.E. 2009. Cranial and mandibular osteology of the Early Triassic archosauriform *Osmolskina czatkowicensis* from Poland. *Palaeontologia Polonica* 65, 235–281.
- Bouabdellah, F., Lessner, E. J., & Benoit, J. The rostral neurovascular system of *Tyrannosaurus rex*. *Palaeontologia Electronica*, 25.

- Breyer, H. (1929). Über Hautsinnesorgane und Hautung bei der Lacertilien. *Zoologische Jarbücher (Anatomie) 51*, 549-581.
- Brochu, C. A. (1999). Phylogenetics, taxonomy, and historical biogeography of Alligatoroidea. *Journal of Vertebrate Paleontology*, *19*, 9-100.
- Buchtová, M., Páč, L., Knotek, Z., & Tichý, F. (2009). Complex sensory corpuscles in the upper jaw of Horsfield's Tortoise (*Testudo horsfieldii*). *Acta Veterinaria Brno*, *78*(2), 193-197.
- Brusatte, S. L., Muir, A., Young, M. T., Walsh, S., Steel, L., & Witmer, L. M. (2016). The braincase and neurosensory anatomy of an Early Jurassic marine crocodylomorph: implications for crocodylian sinus evolution and sensory transitions. *The Anatomical Record*, *299*(11), 1511-1530.
- Bullar, C. M. The braincase of ceratopsian dinosaurs. PhD Dissertation. University of Bristol.
- Busbey III, A. B. (1989). Form and function of the feeding apparatus of *Alligator mississippiensis*. *Journal of Morphology*, *202*, 99-127.
- Carlson, B. A., & Arnegard, M. E. (2011). Neural innovations and the diversification of African weakly electric fishes. *Communicative & Integrative Biology*, *4*(6), 720-725.
- Carmeliet, P., & Tessier-Lavigne, M. (2005). Common mechanisms of nerve and blood vessel wiring. *Nature*, *436*(7048), 193-200.
- Carlisle, A., & Weisbecker, V. (2016). A modified STABILITY protocol for accurate retrieval of soft-tissue data from micro-CT scans of IKI-stained specimens. Published online at <https://dicect.com/2016/08/09/stability/>, August 09, 2016.

- Carr, T. D., Varricchio, D. J., Sedlmayr, J. C., Roberts, E. M., & Moore, J. R. (2017). A new tyrannosaur with evidence for anagenesis and crocodile-like facial sensory system. *Scientific Reports*, 7(1), 1-11.
- Carrano, M. T., Benson, R. B., & Sampson, S. D. (2012). The phylogeny of Tetanurae (Dinosauria: Theropoda). *Journal of Systematic Palaeontology*, 10(2), 211-300.
- Cau, A., Beyrand, V., Voeten, D. F., Fernandez, V., Tafforeau, P., Stein, K., ... & Godefroit, P. (2017). Synchrotron scanning reveals amphibious ecomorphology in a new clade of bird-like dinosaurs. *Nature*, 552(7685), 395-399.
- Catania, K. C., Leitch, D. B., & Gauthier, D. (2010). Function of the appendages in tentacled snakes (*Erpeton tentaculatus*). *Journal of Experimental Biology*, 213(3), 359-367.
- Cerroni, M. A., Canale, J. I., Novas, F. E., & Paulina-Carabajal, A. (2020). An exceptional neurovascular system in abelisaurid theropod skull: New evidence from *Skorpiovenator bustingorryi*. *Journal of Anatomy*.
- Champoux, K. L., Miller, K. E., & Perkel, D. J. (2021). Differential development of myelin in zebra finch song nuclei. *Journal of Comparative Neurology*, 529(6), 1255-1265.
- Clark, J. M., & Sues, H. D. (2002). Two new basal crocodylomorph archosaurs from the Lower Jurassic and the monophyly of the Sphenosuchia. *Zoological Journal of the Linnean Society*, 136(1), 77-95.
- Clark, J. M., Xu, X., Forster, C. A., & Wang, Y. (2004). A Middle Jurassic 'sphenosuchian' from China and the origin of the crocodylian skull. *Nature*, 430(7003), 1021-1024.

- Colbert, E. H., Cowles, R. B., & Bogert, C. M. (1946). Temperature tolerances in the American alligator and their bearing on the habits, evolution, and extinction of the dinosaurs. *Bulletin of the AMNH*, 86.
- Cope, E. D. (1861). List of the Recent species of emydosaurian reptiles in the Museum of the Academy of Natural Sciences. *Proceedings of the Academy of Natural Sciences of Philadelphia*, 12, 549–550.
- Covell Jr, D. A., & Noden, D. M. (1989). Embryonic development of the chick primary trigeminal sensory-motor complex. *Journal of Comparative Neurology*, 286(4), 488-503.
- Crole, M. R., & Soley, J. T. (2016). Comparative morphology, morphometry and distribution pattern of the trigeminal nerve branches supplying the bill tip in the ostrich (*Struthio camelus*) and emu (*Dromaius novaehollandiae*). *Acta Zoologica*, 97, 49-59. doi: 10.1111/azo.12104
- Crole, M. R., & Soley, J. T. (2018). Persistence of Meckel's cartilage in sub-adult *Struthio camelus* and *Dromaius novaehollandiae*. *Acta Zoologica*, 101, 97-205.
- Crosby, E. C. (1917). The forebrain of *Alligator mississippiensis*. *Journal of Comparative Neurology*, 27, 325-402.
- Cull, G., Cioffi, G. A., Dong, J., Homer, L., & Wang, L. (2003). Estimating normal optic nerve axon numbers in non-human primate eyes. *Journal of glaucoma*, 12(4), 301-306.
- Cunningham, S. J., Alley, M. R., Castro, I., Potter, M. A., Cunningham, M., & Pyne, M. J. (2010). Bill morphology of ibises suggests a remote-tactile sensory system for prey detection. *The Auk*, 127, 308-316. doi: 10.1525/auk.2009.09117

- Cunningham, S. J., Castro, I., & Alley, M. R. (2007). A new prey-detection mechanism for kiwi (*Apteryx spp.*) suggests convergent evolution between paleognathous and neognathous birds. *Journal of Anatomy*, 211, 493-502.
- Cuvier, G. (1807). Sur les différentes espèces de crocodiles vivans et sur leurs caractères distinctifs. *Annales du Muséum d'Histoire Naturelle de Paris*, 10, 8–66.
- Cuvier, G. (1824). Résumé de M.le Baron Cuvier des observations sur les espèces de crocodiles fossiles. *Bulletin Universel des Sciences et de l'Industrie*, 1, 93–96.
- D'amico-Martel, A., & Noden, D. M. (1983). Contributions of placodal and neural crest cells to avian cranial peripheral ganglia. *American Journal of Anatomy*, 166(4), 445-468.
- Daudin, F. M. (1802). Histoire naturelle, générale et particulière des reptiles. Volume 2. Dufart, Paris.
- Daza, J. D., Bauer, A. M., & Snively, E. (2013). *Gobekko cretacicus* (Reptilia: Squamata) and its bearing on the interpretation of gekkotan affinities. *Zoological Journal of the Linnean Society*, 167(3), 430-448.
- Daza, J. D., Diogo, R., Johnston, P., & Abdala, V. (2011). Jaw adductor muscles across lepidosaurs: a reappraisal. *The Anatomical Record*, 294(10), 1765-1782.
- DeBeer, G. R. (1937). The development of the vertebrate skull. *Proceedings of the Zoological Society*, 289, 61.
- DeGusta, D., Gilbert, W. H., & Turner, S. P. (1999). Hypoglossal canal size and hominid speech. *Proceedings of the National Academy of Sciences*, 96(4), 1800-1804.

- Dehnhardt, G., & Kaminski, A. (1995). Sensitivity of the mystacial vibrissae of harbour seals (*Phoca vitulina*) for size differences of actively touched objects. *Journal of Experimental Biology*, *198*, 2317–2323.
- Demir, A., & Özsemir, K. G. (2021) Retrospective Study of Beak Deformities in Birds. *Turkish Veterinary Journal*, *3*(1), 13-20.
- Di-Poi, N., & Milinkovitch, M. C. (2013). Crocodylians evolved scattered multi-sensory micro-organs. *EvoDevo*, *4*, 19. doi: 10.1186/2041-9139-4-19
- Dodson, P. (1975). Functional and ecological significance of relative growth in *Alligator*. *Journal of Zoology London*, *175*, 315-355.
- Dollman, K. N. (2020). Biostratigraphy, systematics, taxonomy and palate evolution in early branching southern African crocodylomorphs. PhD dissertation. University of the Witwatersrand.
- Dollman, K. N., Viglietti, P. A., & Choiniere, J. N. (2019). A new specimen of *Orthosuchus stormbergi* (Nash 1968) and a review of the distribution of South African Lower Jurassic crocodylomorphs. *Historical Biology*, *31*(5), 653-664.
- Dufeu, D.L., & Witmer, L. M. (2015). Ontogeny of the middle-ear air-sinus system in *Alligator mississippiensis* (Archosauria: Crocodylia). *PLoS ONE*, *10*, 1-25.
- Dulac, C., Cameron-Curry, P., Ziller, C., & Le Douarin, N. M. (1988). A surface protein expressed by avian myelinating and nonmyelinating Schwann cells but not by satellite or enteric glial cells. *Neuron*, *1*(3), 211-220.
- Duméril, A.M.C., & Duméril, A. H. A. (1851). Catalogue méthodique de la collection des reptiles du Muséum d'Histoire Naturelle de Paris. Gide et Baudry/Roret, Paris, 224 pp.

- Edgeworth, F. H. (1907). Memoirs: The Development of the Head-muscles in *Gallus domesticus*, and the Morphology of the Head-muscles in the Sauropsida. *Journal of Cell Science*, 2(204), 511-556.
- Edgeworth, F. H. (1935). The cranial muscles of vertebrates. Cambridge: Cambridge University Press, pp 1-493.
- Efimov, M. B. (1996). The Jurassic crocodylomorphs of inner Asia. *The continental Jurassic. Museum of Northern Arizona Bulletin*, 60, 305-309.
- Erickson, G. M., Lappin, A. K., & Vliet, K. A. (2003). The ontogeny of bite-force performance in American alligator (*Alligator mississippiensis*). *Journal of Zoology*, 260, 317–327.
- Evans, S. E. (2008). The skull of lizards and tuatara. *Biology of the Reptilia*, 20, 1-347.
- Fabbri, M., Koch, N. M., Pritchard, A. C., Hoffman, E., Bever, G. S., Balanoff, A. M., Morris, Z. S., Field, D. J., Camacho, J., & Rowe, T. B. (2017). The skull roof tracks the brain during the evolution and development of reptiles including birds. *Nature Ecology and Evolution*, 1, 1543-1550.
- Ferguson, M. W. J. (1984). Craniofacial development in *Alligator mississippiensis*. The Structure, Development and Evolution of Reptiles. Orlando: Academic Press. p 223-273.
- Ferguson, M. W. J. (1985). Reproductive biology and embryology of the crocodylians. In: Gans C, Billet F, Maderson PFA, editors. *Biology of the Reptilia* vol 14. New York: Wiley. p 329-491.
- Ferguson, M. W. J. (1987). Post-laying stages of embryonic development in crocodylians. In: Webb GJW, Manolis SC, Whitehead PJ, editors. *Wildlife management:*

Crocodiles and alligators. Chipping Norton, NSW: Surrey Beatty & Sons. pp 427–444.

Filipski, G. T., & Wilson, M. V. H. (1986). Nerve staining using Sudan Black B and its potential use in comparative anatomy. In: Wadding J., Rudkin, D. M. (eds.) *Proceedings of the 1985 workshop on care and maintenance of natural history collections*. Toronto: Royal Ontario Museum Life Sciences Miscellaneous Publication, 33-36.

Freckleton, R. P., Harvey, P. H., & Pagel, M. (2002). Phylogenetic analysis and comparative data: a test and review of evidence. *The American Naturalist*, 160, 712-726. doi: 10.1086/343873

Fry, B. G., Vidal, N., Norman, J. A., Vonk, F. J., Scheib, H., Ramjan, S. R., Kuruppu, S., Fung, K., Hedges, S. B., Richardson, M. K., & Hodgson, W. C. (2006). Early evolution of the venom system in lizards and snakes. *Nature*, 439, 584-588.

Fry, B. G., Casewell, N. R., Wüster, W., Vidal, N., Young, B., & Jackson, T. N. (2012). The structural and functional diversification of the Toxicofera reptile venom system. *Toxicon*, 60, 434-448.

Fujii, S., Muranaka, T., Matsubayashi, J., Yamada, S., Yoneyama, A., & Takakuwa, T. (2020). The bronchial tree of the human embryo: an analysis of variations in the bronchial segments. *Journal of Anatomy*, 237, 311-322. doi: 10.1111/joa.13199

Gans, C. (1975). Tetrapod limblessness: evolution and functional corollaries. *American Zoologist*, 15(2), 455-467.

- Gauthier, J., Kearney, M., & Bezy, R. L. (2008). Homology of cephalic scales in xantusiid lizards, with comments on night lizard phylogeny and morphological evolution. *Journal of Herpetology*, 42(4), 708-723.
- Gearty, W., & Payne, J. L. (2020). Physiological constraints on body size distributions in Crocodyliformes. *Evolution*, 74(2), 245-255.
- Gelman, A., & Su, Y. (2020). arm: Data Analysis Using Regression and Multilevel/Hierarchical Models. R package version 1.11-2. <https://CRAN.R-project.org/package=arm>
- Genbrugge, A., Adriaens, D., De Kegel, B., Brabant, L., Van Hoorebeke, L., Podos, J., ... & Herrel, A. (2012). Structural tissue organization in the beak of Java and Darwin's finches. *Journal of Anatomy*, 221(5), 383-393.
- George, I. D., & Holliday, C. M. (2013). Trigeminal nerve morphology in *Alligator mississippiensis* and its significance for crocodyliform facial sensation and evolution. *The Anatomical Record*, 296, 670-680.
- Gignac, P. M., & Erickson, G. M. (2010). Ontogenetic bite-force modeling of *Alligator mississippiensis*: implications for dietary transitions in a large-bodied vertebrate and the evolution of crocodylian feeding. *Journal of Zoology*, 299, 229-238.
- Gignac, P. M., Kley, N. J., Clarke, J. A., Colbert, M. W., Morhardt, A. C., Cerio, D., ... & Echols, M. S. (2016). Diffusible iodine-based contrast-enhanced computed tomography (diceCT): an emerging tool for rapid, high-resolution, 3-D imaging of metazoan soft tissues. *Journal of Anatomy*, 228(6), 889-909.
- Goldby, F. (1925). The development of the columella auris in the Crocodylia. *Journal of Anatomy*, 59(Pt 3), 301.

- Goodrich, E. S. (1915). Memoirs: The chorda tympani and middle ear in reptiles, birds, and mammals. *Journal of Cell Science*, 2, 137-160.
- Goris, R. C. (2011). Infrared organs of snakes: an integral part of vision. *Journal of Herpetology*, 45(1), 2-15.
- Goswami, A. (2006). Cranial modularity shifts during mammalian evolution. *Am Nat*, 168, 270-280.
- Gottschaldt, K. M., & Lausmann, S. (1974). The peripheral morphological basis of tactile sensibility in the beak of geese. *Cell and tissue research*, 153(4), 477-496.
- Goujon, D. (1869). Sur un appareil de corpuscules tactiles situe dans le bec des perroquets. *J. de L'Anat. et de La Physiol.*, 6, 449-455
- Gould, S. J. (1966). Allometry and size in ontogeny and phylogeny. *Biological Reviews*, 41(4), 587-638.
- Grace, M. S., Church, D. R., Kelly, C. T., Lynn, W. F., & Cooper, T. M. (1999). The Python pit organ: imaging and immunocytochemical analysis of an extremely sensitive natural infrared detector. *Biosensors and Bioelectronics*, 14(1), 53-59.
- Graham, A. (2003). Development of the pharyngeal arches. *American Journal of Medical Genetics Part A*, 119(3), 251-256.
- Grap, N. J., Matchts, T., Essert, S., & Bleckmann, H. (2020). Stimulus discrimination and surface wave localization in Crocodylians. *Zoology*, 139, 125743. doi: 10.1016/j.zool.2020.125743
- Gregory, J. E., Iggo, A., McIntyre, A. K., & Proske, U. (1987). Electoreceptors in the platypus. *Nature*, 326(6111), 386-387.

- Gutiérrez-Ibáñez, C., Iwaniuk, A. N., & Wylie, D. R. (2009). The independent evolution of the enlargement of the principal sensory nucleus of the trigeminal nerve in three different groups of birds. *Brain, behavior and evolution*, 74(4), 280-294.
- Haas, G. (1973). Muscles of the jaws and associated structures in the Rynchocephalia and Squamata. In: Gans, C., Parsons, T. S., editors. *Biology of the Reptilia*, 4(D), 285-490.
- Hack, J. T. (1957). Studies of longitudinal stream profiles in Virginia and Maryland. U.S. *Geological Survey Professional Paper*, 294, 45-95. doi: 10.3133/pp294b
- Hamburger, V., & Hamilton, H. L. (1951). A series of normal stages in the development of the chick embryo. *Journal of morphology*, 88(1), 49-92.
- Hansen, A. (2007). Olfactory and solitary chemosensory cells: two different chemosensory systems in the nasal cavity of the American alligator, *Alligator mississippiensis*. *BMC Neurosci*, 8, 1-10.
- Hardy, O. J., & Pavoine, S. (2012). Assessing phylogenetic signal with measurement error: a comparison of Mantel tests, Blomberg et al.'s K, and phylogenetic distograms. *Evolution: International Journal of Organic Evolution*, 66, 2614-2621. doi: 10.1111/j.1558-5646.2012.01623.x
- Hartman, B. K., Agrawal, H. C., Kalmbach, S., & Shearer, W. T. (1979). A comparative study of the immunohistochemical localization of basic protein to myelin and oligodendrocytes in rat and chicken brain. *Journal of Comparative Neurology*, 188(2), 273-290.
- Hastie, T., & Tibshirani, R. (2020). mda: Mixture and Flexible Discriminant Analysis. R package version 0.5.2. Retrieved from <http://CRAN.R-project.org/package=mda>

- Hieronimus, T. L., & Witmer, L. M. (2010). Homology and evolution of avian compound rhamphothecae. *The Auk*, 127, 590-604.
- Hieronimus, T. L., Witmer, L. M., Tanke, D. H., & Currie, P. J. (2009). The facial integument of centrosaurine ceratopsids: morphological and histological correlates of novel skin structures. *The Anatomical Record: Advances in Integrative Anatomy and Evolutionary Biology*, 292(9), 1370-1396.
- Hiller, U. (1968). Untersuchungen zum Feinbau und zur Funktion der Haftborsten von Reptilien. *Zeitschrift für Morphologie und Ökologie der Tiere*, 62, 307-362.
- Hiller, U. (1978). Morphology and electrophysiological properties of cutaneous sensilla in agamid lizards. *Pflügers archiv*, 377(2), 189-191.
- Hoerschelmann, H. (1972). Strukturen der Schnabelkammer bei Schnepfenvögeln (Charadriidae und Scolopacidae). *Zeitschrift für wissenschaftliche Zoologie Journal*, 185, 105-121.
- Holliday, C. M. (2006). Evolution and function of the jaw musculature and adductor chamber of archosaurs (crocodilians, dinosaurs, and birds). PhD dissertation. Ohio University.
- Holliday, C. M. (2009). New insights into dinosaur jaw muscle anatomy. *The Anatomical Record: Advances in Integrative Anatomy and Evolutionary Biology*, 292(9), 1246-1265
- Holliday, C. M., & Nesbitt, S. J. (2013). Morphology and diversity of the mandibular symphysis of archosauriforms. *Geological Society, London, Special Publications*, 379(1), 555-571.

- Holliday, C. M., & Witmer, L. M. (2007). Archosaur adductor chamber evolution: integration of musculoskeletal and topological criteria in jaw muscle homology. *Journal of Morphology*, 268, 457-484.
- Holliday, C. M., & Witmer, L. M. (2009). The epipterygoid of crocodyliforms and its significance for the evolution of the orbitotemporal region of eusuchians. *Journal of Vertebrate Paleontology*, 29, 715-733.
- Holliday, C. M., Tsai, H. P., Skiljan, R. J., George, I. D., & Pathan, S. (2013). A 3D interactive model and atlas of the jaw musculature of *Alligator mississippiensis*. *PLoS ONE*, 8.
- Hollingworth, T., & Berry, M. (1975). Network analysis of dendritic fields of pyramidal cells in neocortex and Purkinje cells in the cerebellum of the rat. *Philosophical Transactions of the Royal Society of London. B, Biological Sciences*, 270, 227-264. doi: 10.1098/rstb.1975.0008
- Hopson, J. A. (1977). Relative brain size and behavior in archosaurian reptiles. *Annual Review of Ecology and Systematics*, 8, 429-448. doi: 10.1146/annurev.es.08.110177.002241
- Hopson, J. A. (1979). Paleoneurology. *Biology of the Reptilia*, 9(2), 39-148.
- Horton, R. E. (1945). Erosional development of streams and their drainage basis: hydrophysical approach to quantitative morphology. *Geological Society of America Bulletin*, 56, 275-370. doi: 10.1130/0016-7606(1945)56[275:EDOSAT]2.0.CO;2
- Horsfield, K., & Cumming, G. (1968). Morphology of the bronchial tree in man. *Journal of Applied Physiology*, 24, 373-383. doi: 10.1152/jappl.1968.24.3.373

- Hotton, N. (1960). The chorda tympani and middle ear as guides to origin and divergence of reptiles. *Evolution*, 14, 194-211.
- Ibrahim, N., Sereno, P. C., Dal Sasso, C., Maganuco, S., Fabbri, M., Martill, D. M., ... & Iurino, D. A. (2014). Semiaquatic adaptations in a giant predatory dinosaur. *Science*, 345(6204), 1613-1616.
- Iordansky, N. N. (1964). The jaw muscles of the crocodiles and some relating structures of the crocodylian skull. *Antomischer Anzeiger*, 115, 256-280.
- Iordansky, N. N. (1973). The skull of the Crocodylia. In: Gans C, editor. *Biology of the Reptilia*, Vol. 4: Morphology D. New York: Academic Press. p 201–262.
- Iordansky, N. N. (2000). Jaw muscle of the crocodiles: structure, synonymy, and some implications on homology and functions. *Russian Journal of Herpetology*, 7, 1-50.
- Iungman, J., Piña, C. I., & Siroski, P. (2008). Embryological development of *Caiman latirostris* (Crocodylia: Alligatoridae). *Genesis*, 46(8), 401-417.
- Iwaniuk, A. N., Olson, S. L., & James, H. F. (2009). Extraordinary cranial specialization in a new genus of extinct duck (Aves: Anseriformes) from Kauai, Hawaiian Islands. *Zootaxa*.
- Jackson, M. K., & Doetsch, G. S. (1977). Response properties of mechanosensitive nerve fibers innervating cephalic skin of the Texas rat snake. *Experimental Neurology*, 56(1), 78–90.
- Jarrar, B. M., & Taib, N. T. (1987). The Histochemistry of the labial Salivary Glands of the Spiny-Tailed Lizard *Uromastix microlepis* (Blandford). *Amphibia-Reptilia*, 8, 59-67.

- Jerison, H. J. (1969). Brain evolution and dinosaur brains. *The American Naturalist*, 103(934), 575-588.
- Jerison, H. J. (1973). *Evolution of the brain and intelligence*. New York: Academic Press.
- Jollie, M. T. (1960). The head skeleton of the lizard. *Acta Zoologica*, 41(1-2), 1-64.
- Jollie, M. T. (1962). *Chordate Morphology*. New York: Reinhold Publishing Co.
- Jonas, J. B., Schmidt, A. M., Müller-Bergh, J. A., Schlötzer-Schrehardt, U. M., & Naumann, G. O. (1992). Human optic nerve fiber count and optic disc size. *Investigative ophthalmology & visual science*, 33(6), 2012-2018.
- Jungers, W. L., Pokempner, A. A., Kay, R. F., & Cartmill, M. (2003). Hypoglossal canal size in living hominoids and the evolution of human speech. *Human Biology*, 75(4), 473-484.
- Kanari, L., Dłotko, P., Scolamiero, M., Levi, R., Shillcock, J., Hess, K., & Markram, H. (2018). A topological representation of branching neuronal morphologies. *Neuroinformatics*, 16, 3-13. doi: 10.1007/s12021-017-9341-1
- Kandel, E., Schwartz, J., & Jessell, T. (2000). *Principals of neural science*. 4th ed. New York: McGraw-Hill.
- Kardong, K. V., Weinstein, S. A., Smith, T. L. (2009). Reptile venom glands: form, function, and future. *Handbook of venoms and toxins of reptiles*, 65-91.
- Kawabe, S., & Hattori, S. (2021). Complex neurovascular system in the dentary of *Tyrannosaurus*. *Historical Biology*, 1-9.
- Kay, R. F., Cartmill, M., & Balow, M. (1998). The hypoglossal canal and the origin of human vocal behavior. *Proceedings of the National Academy of Sciences*, 95, 5417-5419.

- Khanbabaei, Z., Karam, A., & Rostamizad, G. (2013). Studying relationships between the fractal dimension of the drainage basins and some of their geomorphological characteristics. *International Journal of Geosciences*, 4, 636-642. doi: 10.4236/ijg.2013.43058
- Kirkland, J. I., & DeBlieux, D. D. (2010). New basal centrosaurine ceratopsian skulls from the Wahweap formation (middle campanian), grand staircase-escalante national monument, southern Utah. In *New Perspectives on Horned Dinosaurs: The Royal Tyrrell Museum Ceratopsian Symposium* (pp. 117-140). Bloomington: Indiana University Press.
- Klembara, J. (1991). The cranial anatomy of early ontogenetic stages of *Alligator mississippiensis* (Daudin, 1802) and the significance of some of its cranial structures for the evolution of tetrapods. *Palaeontographica. Abteilung A, Paläozoologie, Stratigraphie*, 215, 103-171.
- Klembara, J. (2001). Postparietal and prehatching ontogeny of the supraoccipital in *Alligator mississippiensis* (Archosauria, Crocodylia). *Journal of Morphology*, 249, 147-153.
- Klembara, J. (2004). Ontogeny of the palatoquadrate and adjacent lateral cranial wall of the endocranium in prehatching *Alligator mississippiensis* (Archosauria: Crocodylia). *Journal of morphology*, 262(2), 644-658.
- Knoll, F., Buffetaut, E., & Buelow, M. (1999). A theropod braincase from the Jurassic of the Vaches Noires cliffs (Normandy, France); osteology and palaeoneurology. *Bulletin de la Société géologique de France*, 170(1), 103-109.

- Knutsen, E. M. (2007). Beak morphology in extant birds with implications on beak morphology in ornithomimids (Master's thesis).
- Kreff, G. (1873). Remarks on Australian crocodiles and description of a new species. *Proceedings of the Zoological Society of London*, 334- 335.
- Krumenacker, L. J. (2017). Osteology, phylogeny, taphonomy, and ontogenetic histology of *Oryctodromeus cubicularis*, from the Middle Cretaceous (Albian-Cenomanian) of Montana and Idaho (Doctoral dissertation, Montana State University).
- Kuratani, S., & Tanaka, S. (1990). Peripheral development of the avian vagus nerve with special reference to the morphological innervation of heart and lung. *Anatomy and embryology*, 182(5), 435-445.
- Kuzmin, I. T. (2021). Anatomy and evolution of the braincase of crocodylians (Archosauria: Crocodylia). PhD Dissertation. St. Petersburg State University.
- Kuzmin, I., Petrov, I., Averianov, A., Boitsova, E., Skutschas, P., & Sues, H. D. (2020). The braincase of *Bissektipelta archibaldi*—new insights into endocranial osteology, vasculature, and paleoneurobiology of ankylosaurian dinosaurs. *Biological Communications*, 65(2), 85-156.
- LaBarbera, P., & Rosso, R. (1989). On the fractal dimension of stream networks. *Water Resources Research*, 25, 735-741. doi: 10.1029/WR025i004p00735
- Lakjer, T. (1926). Studien über die Trigeminus-versorgte Kaumuskulatur der Sauropsiden. Copenhagen, Denmark: CA Reitzel,.
- Landmann, L. (1975). The sense organs in the skin of the head of Squamata (Reptilia). *Israel Journal of Ecology and Evolution*, 24(3-4), 99-135.

- Lau, A., Bentley, L. P., Martius, C., Shenkin, A., Bartholomeus, H., Raumonon, P., Malhi, Y., Jackson, T., & Herold, M. (2018). Quantifying branch architecture of tropical trees using terrestrial LiDAR and 3D modelling. *Trees*, 32, 1219-1231. doi: 10.1007/s00468-018-1704-1
- Lautenschlager, S., Witmer, L. M., Altangerel, P., & Rayfield, E. J. (2013). Edentulism, beaks, and biomechanical innovations in the evolution of theropod dinosaurs. *Proceedings of the National Academy of Sciences*, 110(51), 20657-20662.
- Leardi, J. M., Pol, D., & Clark, J. M. (2017). Detailed anatomy of the braincase of *Macelognathus vagans* Marsh, 1884 (Archosauria, Crocodylomorpha) using high resolution tomography and new insights on basal crocodylomorph phylogeny. *PeerJ*, 5, e2801.
- Lehman, T. M. (1989). *Chasmosaurus mariscalensis*, sp. nov., a new ceratopsian dinosaur from Texas. *Journal of Vertebrate Paleontology*, 9(2), 137-162.
- Leitch, D. B., & Catania, K. C. (2012). Structure, innervation and response properties of integumentary sensory organs in crocodylians. *Journal of Experimental Biology*, 215, 4217-4230.
- Lessner, E. J. (2020). Quantifying neurovascular canal branching patterns reveals a shared crocodylian arrangement. *Journal of Morphology*, 282(2), 185-204.
- Lessner, E. J., & Holliday, C. M. (2020). Diversity and evolution of trigeminal branching patterns in sauropsids. *Society for Integrative and Comparative Biology, Annual Meeting Abstracts 2020*, P2-55.5.

- Lessner, E. J., & Holliday, C. M. (2020). A 3D ontogenetic atlas of *Alligator mississippiensis* cranial nerves and their significance for comparative neurology of reptiles. *The Anatomical Record*.
- Lessner, E. J., & Holliday, C. M. (2020). Trigeminal nerve branching patterns reveal diversity and evolution of facial sensitivity among archosaurs. *Journal of Vertebrate Paleontology Program and Abstracts*.
- Lessner, E. J., & Stocker, M. R. (2017). Archosauriform endocranial morphology and osteological evidence for semiaquatic sensory adaptations in phytosaurs. *Journal of Anatomy*, 231(5), 655-664.
- Lessner, E. J., Gant, C. A., Hieronymus, T. L., Vickaryous, M. K., & Holliday, C. M. (2019). Anatomy and ontogeny of the mandibular symphysis in *Alligator mississippiensis*. *The Anatomical Record*, 302(10), 1696-1708.
- Li, Z., & Clarke, J. A. (2015). New insight into the anatomy of the hyolingual apparatus of *Alligator mississippiensis* and implications for reconstructing feeding in extinct archosaurs. *Journal of Anatomy*, 227, 45-61.
- Lind, H., & Poulsen, H. (1963). On the morphology and behaviour of a hybrid between Goosander and Shelduck (*Mergus merganser* L. x *Tadorna tadorna* L.). *Zeitschrift für Tierpsychologie*, 20(5), 558-569.
- Linnaeus, C. (1758). *Systema naturæ per regna tria naturæ, secundum classes, ordines, genera, species, cum characteribus, differentiis, synonymis, locis. Tomus I. Editio decima, reformata*. Laurentii Salvii, Holmiæ. 10th Edition: 824 pp.
- Louryan, S., Choa-Duterte, M., Lejong, M., & Vanmuylder, N. (2021). Evolution and development of parrot pseudoteeth. *Journal of Morphology*.

- Lubosch, W. (1933). Untersuchungen über die Visceralmuskulatur der Sauropsiden. *Gegenbaurs Morph Jahrb*, 72, 584-666.
- Mackinnon, S. E., & Dellon, A. L. (1995). Fascicular patterns of the hypoglossal nerve. *Journal of reconstructive microsurgery*, 11(03), 195-198.
- Maddin, H. C., Piekarski, N., Sefton, E. M., Hanken, J. (2016). Homology of the cranial vault in birds: new insights based on embryonic fate-mapping and character analysis. *R Soc Open Sci*, 3, 160356.
- Maddin, H. C., Piekarski, N., Reis, R. R., & Hanken, J. (2020). Development and evolution of the tetrapod skull–neck boundary. *Biol Rev*.
- Makovicky, P. J., Norell, M. A., Clark, J. M., & Rowe, T. (2003). Osteology and relationships of *Byronosaurus jaffei* (Theropoda: Troodontidae). *American Museum Novitates*, 2003(3402), 1-32.
- Manor, Y., Koch, C., & Segev, I. (1991). Effect of geometrical irregularities on propagation delay in axonal trees. *Biophysical Journal*, 60(6), 1424-1437.
- Marino, L. (2007). Cetacean brains: how aquatic are they? *The Anatomical Record*, 290, 694-700. doi: 10.1002/ar.20530
- Marsh, O. C. (1884). A new order of extinct Jurassic reptiles (Macelognatha). *The American Journal of Science and Arts, series 3*, 27(160), 341.
- Martill, D. M., Smith, R. E., Longrich, N., & Brown, J. (2021). Evidence for tactile foraging in pterosaurs: a sensitive tip to the beak of *Lonchodraco giganteus* (Pterosauria, Lonchodectidae) from the Upper Cretaceous of southern England. *Cretaceous Research*, 117, 104637.

- Martin, G. R. (2012). Through birds' eyes: Insights into avian sensory ecology. *Journal of Ornithology*, 153(SUPPL. 1), 23–48.
- Mason, M. J. (2016). Structure and function of the mammalian middle ear. I: Large middle ears in small desert mammals. *Journal of Anatomy*, 228(2), 284-299.
- Mastrantonio, B. M., von Baczko, M. B., Desojo, J. B., & Schultz, C. L. (2019). The skull anatomy and cranial endocast of the pseudosuchid archosaur *Prestosuchus chiniquensis* from the Triassic of Brazil. *Acta Palaeontol Pol*, 64.
- Matveyeva, T. N., & Ananjeva, N. B. (1995). The distribution and number of the skin sense organs of agamid, iguanid and gekkonid lizards. *Journal of Zoology*, 235(2), 253-268.
- McDowell, S. B. (1986). The architecture of the corner of the mouth of colubroid snakes. *Journal of Herpetology*, 353-407.
- Megalooikonomou, V., Barnathan, M., Kontos, D., Bakic, P. R., & Maidment, A. D. (2008). A representation and classification scheme for tree-like structures in medical images: analyzing the branching pattern of ductal trees in X-ray galactograms. *IEEE Transactions on Medical Imaging*, 28, 487-493. doi: 10.1109/TMI.2008.929102
- Menco, M. (1980). Qualitative and quantitative freeze-fracture studies on olfactory and nasal respiratory epithelial surfaces of frog, ox, rat, and dog. *Cell and Tissue Research*, 211(1), 5-29.
- Menzel, R., & Lüdicke, M. (1974). Funktionell-anatomische und autoradiographische Untersuchungen am Schnabelhorn von Papageien (Psittaci). *Zool Jahrb Abt Anat Ontog Tiere*, 93, 175–218.

- Monteiro, L. R., Cavalcanti, M. J., & Sommer III, H. J. S. (1997). Comparative ontogenetic shape changes in the skull of Caiman Species (Crocodylia, Alligatoridae). *Journal of Morphology*, 231, 53-62.
- More, H. L., & Donelan, J. M. (2018). Scaling of sensorimotor delays in terrestrial mammals. *Proceedings of the Royal Society B*, 285(1885), 20180613.
- More, H. L., Hutchinson, J. R., Collins, D. F., Weber, D. J., Aung, S. K., & Donelan, J. M. (2010). Scaling of sensorimotor control in terrestrial mammals. *Proceedings of the Royal Society B: Biological Sciences*, 277(1700), 3563-3568.
- Muchlinski, M. N. (2008). The relationship between the infraorbital foramen, infraorbital nerve, and maxillary mechanoreception: Implications for interpreting the paleoecology of fossil mammals based on infraorbital foramen size. *Anatomical Record*, 291(10), 1221–1226.
- Muchlinski, M. N. (2010). A comparative analysis of vibrissa count and infraorbital foramen area in primates and other mammals. *Journal of Human Evolution*, 58(6), 447–473.
- Mukouyama, Y. S., Shin, D., Britsch, S., Taniguchi, M., & Anderson, D. J. (2002). Sensory nerves determine the pattern of arterial differentiation and blood vessel branching in the skin. *Cell*, 109(6), 693-705.
- Müller, G. B., & Alberch, P. (1990). Ontogeny of the limb skeleton in Alligator mississippiensis: developmental invariance and change in the evolution of archosaur limbs. *Journal of Morphology*, 203, 151-164.
- Muller, S. (1838). Waarnemingen over de Indische krokodillen en beschrijving van eene nieuwe soort. *Tijdschrift voor Natuurlijke Geschiedenis en Physiologie*, 5, 61–87.

- Nadon, N. L., Crotzer, D. R., & Stewart, J. R. (1995). Embryonic development of central nervous system myelination in a reptilian species, *Eumeces fasciatus*. *Journal of Comparative Neurology*, 362(3), 433-440.
- Neill, W. T. (1971). *The last of the ruling reptiles: alligators, crocodiles, and their kin*. New York; London: Columbia University Press.
- Nesbitt, S. J. (2011). The early evolution of archosaurs: relationships and the origin of major clades. *Bulletin of the American Museum of Natural History*, 352, 1-292.
- Nicolelis, M. A., Lin, R. C., & Chapin, J. K. (1997). Neonatal whisker removal reduces the discrimination of tactile stimuli by thalamic ensembles in adult rats. *Journal of Neurophysiology*, 78, 1691-1706. doi: 10.1152/jn.1997.78.3.1691
- Nilsson, D. E., Warrant, E. J., Johnsen, S., Hanlon, R., & Shashar, N. (2012). A unique advantage for giant eyes in giant squid. *Current Biology*, 22(8), 683-688.
- Nummela, S. (1995). Scaling of the mammalian middle ear. *Hearing research*, 85(1-2), 18-30.
- O'Brien, H. D., Lynch, L. M., Vliet, K. A., Brueggen, J., Erickson, G. M., & Gignac, P. M. (2019). Crocodylian head width allometry and phylogenetic prediction of body size in extinct crocodyliforms. *Integrative Organismal Biology*, 1(1), obz006.
- Oelrich, T. M. (1956). The anatomy of the head of *Ctenosaura pectinata* (Iguanidae). *Miscellaneous Publications: Museum of Zoology, University of Michigan*, 94, 1-122.
- Oelschlager, H., & Oelschlager, H. (2002). *Encyclopedia of marine mammals*. Academic Press, San Diego.

- Oksanen, J., Blanchet, F. G., Friendly, M., Kindt, R., Legendre, P., McGlinn, D., Minchin, P. R., O'Hara, R. B., Simpson, G. L., Solymos, P., Stevens, H. H., Szoecs, E., & Watner, H. (2007). *vegan*: community ecology package. R package version 2.5-6. (<https://cran.r-project.org/web/packages/vegan>)
- Ollonen, J., Da Silva, F. O., Mahlow, K., & Di-Poï, N. (2018). Skull development, ossification pattern, and adult shape in the emerging lizard model organism *Pogona vitticeps*: a comparative analysis with other squamates. *Frontiers in physiology*, *9*, 278.
- Orejas-Miranda, B., Zug, G. R., Garcia, D. Y., & Achaval, F. (1977). Scale organs of the head of *Leptotyphlops* (Reptilia, Serpentes), a variational study. *Proceedings of the Biological Society of Washington*, *90*, 209 – 213.
- Orme, D., Freckleton, R., Thomas, G., Petzoldt, T., Fritz, S., Isaac, N., & Pearse, W. (2013). *caper*: comparative analysis of phylogenetics and evolution in R. R package version 0.5.2 (<http://CRAN.R-project.org/package=caper>).
- Pagel, M. (1999). Inferring the historical patterns of biological evolution. *Nature*, *401*(6756), 877-884.
- Paradis, E., & Schliep, K. (2019). *ape* 5.0: an environment for modern phylogenetics and evolutionary analyses in R. *Bioinformatics*, *35*, 526-528.
- Park, B. Y., & Saint-Jeannet, J. P. (2010). Induction and segregation of the vertebrate cranial placodes. In *Colloquium series on developmental biology* (Vol. 1, No. 1, pp. 1-83). Morgan & Claypool Life Sciences.
- Parker, A. R. (2011). On the origin of optics. *Optics & Laser Technology*, *43*(2), 323-329.

- Parker, W. K. (1883). On the structure and development of the skull in the Crocodilia. *The Transactions of the Zoological Society of London*, 11(9), 263-310.
- Parrish, J. M. (1994). Cranial osteology of *Longosuchus meadei* and the phylogeny and distribution of the Aetosauria. *Journal of Vertebrate Paleontology*, 14(2), 196-209.
- Pereyra, P. M., Zhang, W., Schmidt, M., & Becker, L. E. (1992). Development of myelinated and unmyelinated fibers of human vagus nerve during the first year of life. *Journal of the Neurological Sciences*, 110(1-2), 107-113.
- Pierce, S. E., & Benton, M. J. (2006). *Pelagosaurus typus* Bronn, 1841 (Mesoeucrocodylia: Thalattosuchia) from the Upper Lias (Toarcian, Lower Jurassic) of Somerset, England. *Journal of Vertebrate Paleontology*, 26(3), 621-635.
- Pelletier, J. D., & Turcotte, D. L. (2000). Shapes of river networks and leaves: are they statistically similar?. *Philosophical Transactions of the Royal Society of London. Series B: Biological Sciences*, 355, 307-311. doi: 10.1098/rstb.2000.0566
- Pennell, M., Eastman, J., Slater, G., Brown, J., Uyeda, J., Fitzjohn, R., Alfaro, M., & Harmon, L. (2014). geiger v2.0: an expanded suite of methods for fitting macroevolutionary models to phylogenetic trees. *Bioinformatics*, 30, 2216-2218.
- Pinheiro, J., Bates, D., DebRoy, S., & Sarkar, D. (2013). nlme: Linear and Nonlinear Mixed Effects Models. R package version 3.1-108.
- Poglayen-Neuwall, I. (1953). Untersuchungen der Kiefermuskulatur und deren Innervation an Krokodilen. *Anat Anz*, 99, 257- 296.

- Porter, W. R., Sedlmayr, J. C., & Witmer, L. M. (2016). Vascular patterns in the heads of crocodylians: blood vessels and sites of thermal exchange. *Journal of Anatomy*, 229, 800-824.
- Price, L. I. (1959). Sobre um crocodilideo notossuquio do Cretacico Brasileiro. Serviço Gráfico do Instituto Brasileiro de Geografia e Estatística. 118, 1-55.
- Prum, R. O., Berv, J. S., Dornburg, A., Field, D. J., Townsend, J. P., Lemmon, E. M., & Lemmon, A. R. (2015). A comprehensive phylogeny of birds (Aves) using targeted next-generation DNA sequencing. *Nature*, 526(7574), 569-573.
- Pyron, R. A., Burbrink, F. T., & Wiens, J. J. (2013). A phylogeny and revised classification of Squamata, including 4161 species of lizards and snakes. *BMC evolutionary biology*, 13(1), 1-54.
- Qureshi, I. Z., & Atkinson, M. E. (2007). Developing chicken trigeminal ganglia show varying patterns of axon outgrowth following ablation in vivo of the maxillary and mandibular target tissues. *Pakistan Journal of Zoology*, 39(6), 389.
- R Core Team (2020). R: A language and environment for statistical computing. R Foundation for Statistical Computing, Vienna, Austria. <https://www.R-project.org/>.
- R Core Team (2021). R: A language and environment for statistical computing. R Foundation for Statistical Computing, Vienna, Austria. <https://www.R-project.org/>.
- Reese, A. M. (1915). *The alligator and its allies*. New York: GP Putnam's Sons.

- Revell, L. J. (2012). Phytools: an R package for phylogenetic comparative biology (and other things). *Methods of Ecology and Evolution*, 3, 217–23. doi: 10.1111/j.2041-210X.2011.00169.x
- Rhinn, M., Miyoshi, K., Watanabe, A., Kawaguchi, M., Ito, F., Kuratani, S., ... & Rijli, F. M. (2013). Evolutionary divergence of trigeminal nerve somatotopy in amniotes. *Journal of Comparative Neurology*, 521(6), 1378-1394.
- Riede, T., Li, Z., Tokuda, I. T., & Farmer, C. G. (2015). Functional morphology of the *Alligator mississippiensis* larynx with implications for vocal production. *Journal of Experimental Biology*, 218, 991-998.
- Rieppel, O. (1993). Studies on skeleton formation in reptiles. V. Patterns of ossification in the skeleton of *Alligator mississippiensis* DAUDIN (Reptilia, Crocodylia). *Zoological Journal of the Linnean Society*, 109, 301-325.
- Romer, A. S. (1956). Osteology of the reptiles. Chicago: The University of Chicago Press,.
- Rosenbluth, J. (1962). The fine structure of acoustic ganglia in the rat. *The Journal of Cell Biology*, 12(2), 329-359.
- Rosenbluth, J., & Palay, S. L. (1961). The fine structure of nerve cell bodies and their myelin sheaths in the eighth nerve ganglion of the goldfish. *The Journal of Cell Biology*, 9(4), 853-877.
- Rothschild, B. M., & Naples, V. (2017). Apparent sixth sense in theropod evolution: The making of a Cretaceous weathervane. *PloS one*, 12(11), e0187064.

- Rowe, T., Brochu, C. A., Colbert, M., Merck, J. W., Kishi, K., Saglamer, E., & Warren, S. (1999). Introduction to Alligator: Digital atlas of the skull. *Journal of Vertebrate Paleontology*, *19*, 1-8.
- Ruebenstahl, A. A. (2019). *Junggarsuchus sloani*, An Early Late Jurassic Crocodylomorph with Crocodyliform Affinities (Doctoral dissertation, The George Washington University).
- Sampson, S. D., & Witmer, L. M. (2007). Craniofacial anatomy of *Majungasaurus crenatissimus* (Theropoda: Abelisauridae) from the late Cretaceous of Madagascar. *Journal of Vertebrate Paleontology*, *27*(S2), 32-104.
- Santos, E., Yanes, C. M., Monzón-Mayor, M., & del Mar Romero-Alemán, M. (2006). Peculiar and typical oligodendrocytes are involved in an uneven myelination pattern during the ontogeny of the lizard visual pathway. *Journal of neurobiology*, *66*(10), 1115-1124.
- Sauret, V., Goatman, K. A., Fleming, J. S., & Bailey, A. G. (1999). Semi-automated tabulation of the 3D topology and morphology of branching networks using CT: application to the airway tree. *Physics in Medicine & Biology*, *44*, 1625. doi: 10.1088/0031-9155/44/7/304
- Säve-Söderbergh, G. (1945). Notes on the trigeminal musculature in non-mammalian tetrapods. *Nova Acta Regiae Societatis Scientiarum Upsaliensis Series IV*, *13*, 1-50.
- Saxod, R. (1996). Ontogeny of the cutaneous sensory organs. *Microscopy Research and Technique*, *34*(4), 313-333.

- Scheetz, R. D. (1999). *Osteology of Orodromeus makelai and the phylogeny of basal ornithopod dinosaurs*. Montana State University.
- Scheidegger, A. E. (1965). The algebra of stream-order numbers. *United States Geological Survey Professional Paper*, 525, 187-189.
- Schmidt, W. (1920). Einiges fiber die Hautsinnesorgane der Agamiden insbesondere von Calotes, nebst Be- merkungen iiber diese Organe bei Gekkonidae und Iguanidae. *Anatomischer Anzeiger*, 53, 11.
- Schneider, C. A., Rasband, W. S., & Eliceiri, K. W. (2012). NIH Image to ImageJ: 25 years of image analysis. *Nature methods*, 9(7), 671-675.
- Schneider, E. R., Gracheva, E. O., & Bagriantsev, S. N. (2016). Evolutionary specialization of tactile perception in vertebrates. *Physiology*, 31, 193-200. doi: 10.1152/physiol.00036.2015
- Schneider, J. G. (1801). *Historiae Amphibiorum naturalis et literariae. Fasciculus secundus continens Crocodilos, Scincos, Chamaesauras, Boas. Pseudoboas, Elapes, Angues. Amphisbaenas et Caecilias*. Frommanni, Jena. 374 pp.
- Schumacher, G. H. (1973). The head muscles and hyolaryngeal skeleton of turtles and Crocodilians. In: Gans C, Parsons TS, editors. *Biology of the Reptilia vol 4*. London: Academic Press. p 101–199
- Schwab, J. A., Young, M. T., Neenan, J. M., Walsh, S. A., Witmer, L. M., Herrera, Y., ... & Brusatte, S. L. (2020). Inner ear sensory system changes as extinct crocodylomorphs transitioned from land to water. *Proceedings of the National Academy of Sciences*, 117(19), 10422-10428.

- Scott, S. A. (1992). The development of peripheral sensory innervation patterns. In: Scott SA, editor. *Sensory Neurons: Diversity, Development, and Plasticity*. Oxford: Oxford University Press. pp 242–263.
- Sellers, K. C. (2021). Function and evolution of the crocodyliform feeding apparatus. PhD dissertation. University of Missouri.
- Sellers, K. C., Middleton, K. M., Davis, J. L., & Holliday, C. M. (2017). Ontogeny of bite force in a validated biomechanical model of the American alligator. *The Company of Biologists*, 220, 2036-2046.
- Sereno, P., Larsson, H. (2009). Cretaceous crocodyliforms from the Sahara. *ZooKeys*, 28:1.
- Shaker, N. A., & El-Bably, S. H. (2015). Morphological and radiological studies on the skull of the Nile crocodile (*Crocodylus niloticus*). *IJAR*, 3:133-140.
- Sherbrooke, W. C., & Nagle, R. B. (1996). Phrynosoma intraepidermal receptor: A dorsal intraepidermal mechanoreceptor in horned lizards (Phrynosoma; Phrynosomatidae; Reptilia). *Journal of Morphology*, 228(2), 145–154.
- Shiino, K. (1914). Studien zur Kenntniss des Wirbeltierkopfes. 1. Das Chondrocranium in Crocodylus mit Berücksichtigung der Gehirnnerven und Kopfgefäße. *Anat Hefte*, 50, 254 -381.
- Shreve, R. L. (1966). Statistical law of stream numbers. *The Journal of Geology*, 74, 17-37. doi: doi.org/10.1086/627137
- Shute, C. C. D., & Bellairs, A. D. A. (1955). The external ear in Crocodylia. In *Proceedings of the Zoological Society of London* (Vol. 124, No. 4, pp. 741-749). Oxford, UK: Blackwell Publishing Ltd.

- Skoura, A., Bakic, P. R., & Megalooikonomou, V. (2013). Analyzing tree-shape anatomical structures using topological descriptors of branching and ensemble of classifiers. *Journal of Theoretical and Applied Computer Science*, 7, 3-19.
- Smaers, J. B., & Mongle, C. S. (2014). evomap: R package for the evolutionary mapping of continuous traits. *GitHub* (<https://github.com/JeroenSmaers/evomap>).
- Soares, D. (2002). An ancient sensory organ in crocodylians. *Nature*, 417, 241-242.
- Sperber, G. H. (2001). *Craniofacial development* (pp. 127). B.C. Decker, Hamilton, Ontario.
- Spielmann, J. A., Lucas, S. G., Rhinehart, L. F., & Heckert, A. B. (2008). *The Late Triassic Archosauromorph Trilophosaurus: Bulletin 43* (Vol. 43). New Mexico Museum of Natural History and Science.
- Stevens, M. (2013). *Sensory ecology, behaviour, and evolution*. Oxford University Press.
- Steventon, B., Mayor, R., & Streit, A. (2014). Neural crest and placode interaction during the development of the cranial sensory system. *Developmental biology*, 389(1), 28-38.
- Stibbe, E. P. (1928). A comparative study of the nictitating membrane of birds and mammals. *Journal of Anatomy*, 62, 159-176.
- Strahler, A. N. (1957). Quantitative analysis of watershed geomorphology. *Eos, Transactions American Geophysical Union*, 38, 913-920. doi: 10.1029/TR038i006p00913
- Sullivan, S. P., McGeachie, F. R., Middleton, K. M., & Holliday, C. M. (2019). 3D muscle architecture of the pectoral muscles of European starling (*Sturnus vulgaris*). *Integrative Organismal Biology*, 1(1), oby010.

- Tan, S. S., & Morriss-Kay, G. (1985). The development and distribution of the cranial neural crest in the rat embryo. *Cell and tissue research*, 240(2), 403-416.
- Thermo Fisher Scientific (2019). User's Guide Avizo Software 2019. Konrad-Zuse-Zentrum für Informationstechnik, Berlin, Germany.
<https://assets.thermofisher.com/TFS-Assets/MSD/Product-Guides/users-guide-avizo-software-2019.pdf>
- Thewissen, J. G., & Nummela, S. (Eds.). (2008). *Sensory evolution on the threshold: adaptations in secondarily aquatic vertebrates*. Univ of California Press.
- Toesca, A. (1996). Central and peripheral myelin in the rat cochlear and vestibular nerves. *Neuroscience letters*, 221(1), 21-24.
- Tsai, H. P., & Holliday, C. M. (2011). Ontogeny of the alligator cartilago transiliens and its significance for sauropsid jaw muscle evolution. *PloS one*, 6.
- Turner, A. H., & Pritchard, A. C. (2015). The monophyly of Susisuchidae (Crocodyliformes) and its phylogenetic placement in Neosuchia. *PeerJ*, 3, e759.
- Turner, A. H., Pritchard, A. C., & Matzke, N. J. (2017). Empirical and Bayesian approaches to fossil-only divergence times: a study across three reptile clades. *PloS one*, 12(2), e0169885.
- Uylings, H. B. M., Smit, G. J., & Veltman, W. A. M. (1975). Ordering methods in quantitative analysis of branching structures of dendritic trees. *Advances in Neurology*, 12, 347-354.
- Uylings, H. B., Van Pelt, J., & Verwer, R. W. (1989). *Topological analysis of individual neurons*. In *Computer Techniques in Neuroanatomy* (pp. 215-239). Springer, Boston, MA. doi: 10.1007/978-1-4684-5691-2_11

- van Buuren, S., & Groothuis-Oudshoorn, K. (2011). mice: Multivariate Imputation by Chained Equations in R. *Journal of Statistical Software*, 45(3), 1-67.
<https://www.jstatsoft.org/v45/i03/>
- Van Hemert, C., Handel, C. M., Blake, J. E., Swor, R. M., & O'Hara, T. M. (2012). Microanatomy of passerine hard-cornified tissues: Beak and claw structure of the black-capped chickadee (*Poecile atricapillus*). *Journal of Morphology*, 273(2), 226-240.
- Venables, W. N., & Ripley, B. D. (2002) *Modern Applied Statistics with S*, Fourth edition. Springer, New York. ISBN 0-387-95457-0,
<https://www.stats.ox.ac.uk/pub/MASS4/>.
- Verwer, R. W., & van Pelt, J. (1986). Descriptive and comparative analysis of geometrical properties of neuronal tree structures. *Journal of Neuroscience Methods*, 18, 179-206. doi: 10.1016/0165-0270(86)90119-6
- Vogel, K. S. (1992). Origins and early development of vertebrate cranial sensory neurons. In *Sensory Neurons: Diversity, Development, and Plasticity*. New York: Oxford University Press. p 171-193.
- Vogl, A. W., Lillie, M. A., Piscitelli, M. A., Goldbogen, J. A., Pyenson, N. D., & Shadwick, R. E. (2015). Stretchy nerves are an essential component of the extreme feeding mechanism of rorqual whales. *Current Biology*, 25, R360-R361.
- von Baczko, M. B., Taborda, J. R., & Desojo, J. B. (2018). Paleoneuroanatomy of the aetosaur *Neoaetosauroides engaeus* (Archosauria: Pseudosuchia) and its paleobiological implications among archosauriforms. *PeerJ*, 6, e5456.

- von Düring, M. (1973). The ultrastructure of lamellated mechanoreceptors in the skin of reptiles. *Zeitschrift für Anatomie und Entwicklungsgeschichte* 143(1), 81-94.
- Wang, S., Stiegler, J., Wu, P., Chuong, C. M., Hu, D., Balanoff, A., ... & Xu, X. (2017). Heterochronic truncation of odontogenesis in theropod dinosaurs provides insight into the macroevolution of avian beaks. *Proceedings of the National Academy of Sciences*, 114(41), 10930-10935.
- Watanabe, A., Fabre, A. C., Felice, R. N., Maisano, J. A., Müller, J., Herrel, A., & Goswami, A. (2019). Ecomorphological diversification in squamates from conserved pattern of cranial integration. *PNAS*, 116, 14688-14697.
- Watanabe, A., Gignac, P. M., Balanoff, A. M., Green, T. L., Kley, N. J., & Norell, M. A. (2019). Are endocasts good proxies for brain size and shape in archosaurs throughout ontogeny?. *Journal of Anatomy*, 234(3), 291-305.
- Watanabe, T., & Yasuda, M. (1970). Comparative and topographical anatomy of the fowl. XXVI. Peripheral course of the trigeminal nerve. *Japanese Journal of Veterinary Science*, 32, 43-57.
- Watkinson, G. B. (1906). The cranial nerves of *Varanus bivittatus*. *Gegenbaurs Morphologisches Jahrbuch*, 35, 450-472.
- Wedin, B. (1953). The origin and development of the extrinsic ocular muscles in the alligator. *Journal of Morphology*, 92, 303-335.
- Wilberg, E. W. (2015). What's in an outgroup? The impact of outgroup choice on the phylogenetic position of Thalattosuchia (Crocodylomorpha) and the origin of Crocodyliformes. *Systematic Biology*, 64(4), 621-637.

- Wilberg, E. W., Turner, A. H., & Brochu, C. A. (2019). Evolutionary structure and timing of major habitat shifts in Crocodylomorpha. *Scientific Reports*, 9, 1-10. doi: 10.1038/s41598-018-36795-1
- Wild, J. M. (2015). The avian somatosensory system: a comparative view. In *Sturkie's Avian physiology* (pp. 55-69). Academic Press.
- Willard, W. A. (1915). *The cranial nerves of Anolis carolinensis*. The Museum.
- Witmer, L. M., & Ridgely, R. C. (2009). New insights into the brain, braincase, and ear region of tyrannosaurs (Dinosauria, Theropoda), with implications for sensory organization and behavior. *The Anatomical Record*, 292(9), 1266–1296.
- Witmer, L. M., & Thomason, J. J. (1995). The extant phylogenetic bracket and the importance of reconstructing soft tissues in fossils. *Functional Morphology in Vertebrate Paleontology*, 1, 19–33.
- Witmer, L. M., Ridgely, R. C., Dufeu, D. L., & Semones, M. C. (2008). Using CT to peer into the past: 3D visualization of the brain and ear regions of birds, crocodiles, and nonavian dinosaurs. In *Anatomical imaging* (pp. 67-87). Springer, Tokyo.
- Wong, M. D., Spring, S., & Henkelman, R. M. (2013). Structural stabilization of tissue for embryo phenotyping using micro-CT with iodine staining. *PloS one*, 8.
- Wylie, D. R., Gutiérrez-Ibáñez, C., & Iwaniuk, A. (2015). Integrating brain, behavior, and phylogeny to understand the evolution of sensory systems in birds. *Frontiers in neuroscience*, 9, 281.

- Xu, H., Dude, C. M., & Baker, C. V. (2008). Fine-grained fate maps for the ophthalmic and maxillomandibular trigeminal placodes in the chick embryo. *Developmental biology*, 317(1), 174-186.
- Yanes, C., Batista, M. P., Trujillo, J. M., Monzon, M., & Marrero, A. (1987). Anterior dorsal ventricular ridge in the lizard: embryonic development. *Journal of Morphology*, 194(1), 55-64.
- Yi, H., Tennant, J. P., Young, M. T., Challands, T. J., Foffa, D., Hudson, J. D., ... & Brusatte, S. L. (2016). An unusual small-bodied crocodyliform from the Middle Jurassic of Scotland, UK, and potential evidence for an early diversification of advanced neosuchians. *Earth and Environmental Science Transactions of the Royal Society of Edinburgh*, 107(1), 1-12.
- Young, B. A., & Wallach, V. (1998). Description of a papillate tactile organ in the Typhlopidae. *African Zoology*, 33(4), 249-253.
- Zusi, R. L., & Livezey, B. C. (2000). Homology and phylogenetic implications of some enigmatic cranial features in galliform and anseriform birds. *Annals of the Carnegie Museum*, 69, 157-193.

Vita

Emily Lessner has never been a product of her environment. She grew up outdoors on land traditionally occupied by the Lenni-Lenape, Nanticoke, and Susquehannock peoples. In the dirt, she discovered her love for the natural world and decided to become a veterinarian. In her undergraduate at Virginia Tech, she did not care for the pre-veterinary crowd and barged towards her other passion, rocks. To her surprise, a paleontology research group was just about to start with the arrival of Drs. Michelle Stocker and Sterling Nesbitt. She was on board, and realizing paleontology was a real career, she began her journey. She was able to spend several seasons at Petrified Forest National Park, where her love and respect for fieldwork blossomed. Her interests in reconstruction of soft tissues and behaviors in fossil animals led her to graduate school at the University of Missouri with Dr. Casey Holliday. There, she and her interests matured only slightly, and if humanity persists, she hopes to pursue a career studying ecological-evolutionary-developmental aspects of sensory systems.